International Journal of
Molecular Sciences

Silver Nano/ Microparticles

Edited by
Bong-Hyun Jun

Printed Edition of the Special Issue Published in
International Journal of Molecular Sciences

www.mdpi.com/journal/ijms

MDPI

Silver Nano/Microparticles

Silver Nano/Microparticles

Modification and Applications 2.0

Editor

Bong-Hyun Jun

MDPI • Basel • Beijing • Wuhan • Barcelona • Belgrade • Manchester • Tokyo • Cluj • Tianjin

Editor
Bong-Hyun Jun
Konkuk University
South Korea

Editorial Office
MDPI
St. Alban-Anlage 66
4052 Basel, Switzerland

This is a reprint of articles from the Special Issue published online in the open access journal *International Journal of Molecular Sciences* (ISSN 1422-0067) (available at: https://www.mdpi.com/journal/ijms/special_issues/Ag-particles).

For citation purposes, cite each article independently as indicated on the article page online and as indicated below:

LastName, A.A.; LastName, B.B.; LastName, C.C. Article Title. *Journal Name* **Year**, *Article Number*, Page Range.

ISBN 978-3-03943-204-2 (Hbk)
ISBN 978-3-03943-205-9 (PDF)

Cover image courtesy of Miye Cho.

Contents

About the Editor

Bong-Hyun Jun is currently Associate Professor at Konkuk University, Republic of Korea. He received his M.S. and Ph.D. degrees from Seoul National University in School of Chemical and Biological Engineering (2009). He has previously worked at Seoul National University (2009–2012) and University of California, Berkeley (2011–2012). He currently serves as Professor at Department of Bioscience and Biotechnology, Konkuk University (2013–present). He has served as a member of the board of directors of the Korean Society of Industrial & Engineering Chemistry (2015–presentent) and Korean Peptide and Protein Society (2013–present). Prof. Jun's work at Konkuk has mainly focused on optical nanoparticle-based sensors for bioapplications.

International Journal of
Molecular Sciences

MDPI

Editorial

Silver Nano/Microparticles: Modification and Applications 2.0

Xuan-Hung Pham, Jaehi Kim and Bong-Hyun Jun *

Department of Bioscience and Biotechnology, Konkuk University, Seoul 143-701, Korea; phamricky@gmail.com (X.-H.P.); susia45@gmail.com (J.K.)
* Correspondence: bjun@konkuk.ac.kr

Received: 12 June 2020; Accepted: 19 June 2020; Published: 20 June 2020

Currently, nano/microparticles are widely used in various fields [1–3]. Silver particles are one of the most vital materials among the various particles, due to their unique optical-physical-chemical properties. The materials have been proposed for various fields, such as bio-sensor, diagnostics, imaging, catalyst, solar cell, and antibacterial [4–14]. In particular, size-dependent unique plasmonic properties make the particles superior in biomedical applications [15–20].

Due to this importance of silver materials, the first version of "silver nano/microparticles: modification and applications" was successfully published last year with 10 outstanding papers [21–30]. This version 2.0 of the Special Issue also provides original contributions detailing the synthesis, modification, and applications of silver materials. Eleven outstanding papers which describe examples of the most recent advances in silver nano/microparticles are included.

The plasmonic properties of silver nanoparticles have been applied to the detection of harmful substances based on surface-enhanced Raman scattering (SERS), due to its non-destructive, rapid, molecular fingerprinting and ultrasensitive and photostable properties [31]. Because histamine intoxication associated with seafood consumption can cause illnesses, Kim-Hung et al. reported facile histamine detection by SERS using a plasmonic silver-gold nanostructure [32]. They successfully detected histamine with SERS using the nanostructure (3.698 ppm LOD). Pham et al. reported the sensitive and quantitative detection of pesticides based on SERS by using an internal standard containing nanostructures [33]. For the study, 4-mercaptobenzoic acid labeled silver-gold nanoparticles were used for a sensitive and quantitative thiram detection, and a range of 240 to 2400 ppb with a detection limit of 72 ppb of thiram was detected.

Silver nanoparticles have great potential as an antibacterial agent. Nakamura et al. reviewed the synthesis and application of silver nanoparticles for the prevention of infection [34]. In particular, they focused on environment friendly synthesis and the suppression of infections in healthcare workers. Nakamura et al. reported that ultraviolet irradiation enhances the microbicidal activity of silver nanoparticles via hydroxyl radicals [35]. They showed that UV irradiation to silver nanoparticles is effective for enhancing their microbicidal activity, due to the antimicrobial activity of reactive hydroxyl radicals which were generated from silver nanoparticles by UV irradiation. The UV irradiation-mediated enhanced production of reactive hydroxyl radicals is generated rapidly from silver nanoparticles. Silver nanowires, which exhibit excellent conductive properties, have been intensively studied for thermal and electronic applications. Mori et al. evaluated the antibacterial and cytotoxicity properties of silver nanowires and their composites with carbon nanotubes for biomedical applications [36]. Li et al. reported a simple, sustainable, and environmentally friendly method for the in situ fabrication of silver nanoparticles in mesoporous TiO_2 films decorated on bamboo via self-sacrificing reduction to synthesize nanocomposites with an efficient antifungal activity [37]. The composite films-endowed bamboo exhibited an excellent antifungal activity to T. viride and P. citrinum. Because of the high biocompatibility, low cost, and ease of manufacture of the poly(methylmethacrylate) (PMMA) resin, it is widely used in medical and dental fields. Matteis et al.

reported that silver nanoparticles added a poly(methyl methacrylate) dental matrix for topographic and antimycotic studies [38].

Since silver nanoparticles are attractive alternatives to plasmonic gold nanoparticles, the controlled synthesis of metal nanoparticles with a defined morphology can be important for such fields as biochemistry, catalysis, biosensors, and microelectronics. Cyclophanes, which have a variety of cyclophane 3D structures and unique redox abilities, can create metal nanoparticles. Padnya et al. summarized the recent advances in the synthesis and stabilization of Ag (0) nanoparticles based on self-assembly of associates with Ag (I) ions with the participation of cyclophanes [39].

Biological molecules have potential for the synthesis of metallic nanoparticles as green and economic methods. Tanaka et al. reported the green synthesis of silver nanoparticles by using peptides [40]. They used array-based screening to identify a list of mineralization peptides with various physicochemical properties. They evaluated the silver nanoparticle mineralization activity of the top 200 gold nanoparticle-binding peptides, and the highest silver nanoparticles synthesis activity was shown in the presence of EE and EXE peptides (E: glutamic acid, and X: any amino acid).

Silver islands films (SIF) can play an important role among plasmonically active platforms. Szalkowski et al. reported silver islands substrates which prepared on demand based on the laser-induced photochemical reduction of silver compounds on a glass substrate [41]. The prepared SIF showed a strong plasmonic activity.

Hybrid systems of photosynthetic pigment–protein complexes with plasmonically active metallic nanostructures can be a useful design for future biomimetic solar cells. Kowalska et al. reviewed SIF for enhancing light harvesting in natural photosynthetic proteins [42]. They presented the results of a variety of photosynthetic complexes upon coupling with SIF structures.

Author Contributions: Conceptualization, X.-H.P., J.K., and B.-H.J., writing, X.-H.P., J.K., and B.-H.J.; supervision, B.-H.J. All authors have read and agreed to the published version of the manuscript.

Funding: This research was funded by the KU Research Professor Program of Konkuk University.

Acknowledgments: This work was supported by the KU Research Professor Program of Konkuk University.

Conflicts of Interest: The authors declare no conflict of interest.

References

1. Yang, S.C.; Luo, X. Mesoporous nano/micro noble metal particles: synthesis and applications. *Nanoscale* **2014**, *6*, 4438–4457. [CrossRef]
2. Agrawal, M.; Gupta, S.; Stamm, M. Recent developments in fabrication and applications of colloid based composite particles. *J. Mater. Chem.* **2011**, *21*, 615–627. [CrossRef]
3. Jun, B.H.; Kang, H.; Lee, Y.S.; Jeong, D.H. Fluorescence-Based Multiplex Protein Detection Using Optically Encoded Microbeads. *Molecules* **2012**, *17*, 2474–2490. [CrossRef]
4. Lee, B.; Roh, S.; Park, J. Current status of micro- and nano-structured optical fiber sensors. *Opt. Fiber Technol.* **2009**, *15*, 209–221. [CrossRef]
5. Hahm, E.; Cha, M.G.; Kang, E.J.; Pham, X.H.; Lee, S.H.; Kim, H.M.; Kim, D.E.; Lee, Y.S.; Jeong, D.H.; Jun, B.H. Multilayer Ag-Embedded Silica Nanostructure as a Surface-Enhanced Raman Scattering-Based Chemical Sensor with Dual-Function Internal Standards. *ACS Appl. Mater. Interfaces* **2018**, *10*, 40748–40755. [CrossRef]
6. Jun, B.H.; Kim, G.; Jeong, S.; Noh, M.S.; Pham, X.H.; Kang, H.; Cho, M.H.; Kim, J.H.; Lee, Y.S.; Jeong, D.H. Silica Core-based Surface-enhanced Raman Scattering (SERS) Tag: Advances in Multifunctional SERS Nanoprobes for Bioimaging and Targeting of Biomarkers. *Bull. Korean Chem. Soc.* **2015**, *36*, 963–978. [CrossRef]
7. Kang, H.; Jeong, S.; Koh, Y.; Cha, M.G.; Yang, J.K.; Kyeong, S.; Kim, J.; Kwak, S.Y.; Chang, H.J.; Lee, H.; et al. Direct Identification of On-Bead Peptides Using Surface-Enhanced Raman Spectroscopic Barcoding System for High-Throughput Bioanalysis. *Sci. Rep.* **2015**, *5*, 10. [CrossRef] [PubMed]
8. Kim, H.M.; Jeong, S.; Hahm, E.; Kim, J.; Cha, M.G.; Kim, K.M.; Kang, H.; Kyeong, S.; Pham, X.H.; Lee, Y.S.; et al. Large scale synthesis of surface-enhanced Raman scattering nanoprobes with high reproducibility and long-term stability. *J. Ind. Eng. Chem.* **2016**, *33*, 22–27. [CrossRef]

9. Rho, W.Y.; Song, D.H.; Yang, H.Y.; Kim, H.S.; Son, B.S.; Suh, J.S.; Jun, B.H. Recent advances in plasmonic dye-sensitized solar cells. *J. Solid State Chem.* **2018**, *258*, 271–282. [CrossRef]
10. Kang, H.; Koh, Y.; Jeong, S.; Jeong, C.; Cha, M.G.; Oh, M.H.; Yang, J.K.; Lee, H.; Jeong, D.H.; Jun, B.H.; et al. Graphical and SERS dual-modal identifier for encoding OBOC library. *Sens. Actuator B-Chem.* **2020**, *303*, 8. [CrossRef]
11. Rho, W.Y.; Kim, H.S.; Chung, W.J.; Suh, J.S.; Jun, B.H.; Hahn, Y.B. Enhancement of power conversion efficiency with TiO2 nanoparticles/nanotubes-silver nanoparticles composites in dye-sensitized solar cells. *Appl. Surf. Sci.* **2018**, *429*, 23–28. [CrossRef]
12. Pham, X.H.; Lee, M.; Shim, S.; Jeong, S.; Kim, H.M.; Hahm, E.; Lee, S.H.; Lee, Y.S.; Jeong, D.H.; Jun, B.H. Highly sensitive and reliable SERS probes based on nanogap control of a Au-Ag alloy on silica nanoparticles. *RSC Adv.* **2017**, *7*, 7015–7021. [CrossRef]
13. Rho, W.Y.; Chun, M.H.; Kim, H.S.; Kim, H.M.; Suh, J.S.; Jun, B.H. Ag Nanoparticle-Functionalized Open-Ended Freestanding TiO2 Nanotube Arrays with a Scattering Layer for Improved Energy Conversion Efficiency in Dye-Sensitized Solar Cells. *Nanomaterials* **2016**, *6*, 117. [CrossRef] [PubMed]
14. Rho, W.Y.; Kim, H.S.; Lee, S.H.; Jung, S.; Suh, J.S.; Hahn, Y.B.; Jun, B.H. Front-illuminated dye-sensitized solar cells with Ag nanoparticle-functionalized freestanding TiO2 nanotube arrays. *Chem. Phys. Lett.* **2014**, *614*, 78–81. [CrossRef]
15. Pham, X.H.; Hahm, E.; Kim, T.H.; Kim, H.M.; Lee, S.H.; Lee, Y.S.; Jeong, D.H.; Jun, B.H. Enzyme-catalyzed Ag Growth on Au Nanoparticle-assembled Structure for Highly Sensitive Colorimetric Immunoassay. *Sci. Rep.* **2018**, *8*, 7. [CrossRef] [PubMed]
16. Jun, B.H.; Kim, G.; Baek, J.; Kang, H.; Kim, T.; Hyeon, T.; Jeong, D.H.; Lee, Y.S. Magnetic field induced aggregation of nanoparticles for sensitive molecular detection. *Phys. Chem. Chem. Phys.* **2011**, *13*, 7298–7303. [CrossRef] [PubMed]
17. Pham, X.H.; Shim, S.; Kim, T.H.; Hahm, E.; Kim, H.M.; Rho, W.Y.; Jeong, D.H.; Lee, Y.S.; Jun, B.H. Glucose Detection Using 4-mercaptophenyl Boronic Acid-incorporated Silver Nanoparticles-embedded Silica-coated Graphene Oxide as a SERS Substrate. *Biochip J.* **2017**, *11*, 46–56. [CrossRef]
18. Pham, X.H.; Hahm, E.; Kang, E.; Ha, Y.N.; Lee, S.H.; Rho, W.Y.; Lee, Y.S.; Jeong, D.H.; Jun, B.H. Gold-silver bimetallic nanoparticles with a Raman labeling chemical assembled on silica nanoparticles as an internal-standard-containing nanoprobe. *J. Alloy. Compd.* **2019**, *779*, 360–366. [CrossRef]
19. Jun, B.H.; Kim, G.; Noh, M.S.; Kang, H.; Kim, Y.K.; Cho, M.H.; Jeong, D.H.; Lee, Y.S. Surface-enhanced Raman scattering-active nanostructures and strategies for bioassays. *Nanomedicine* **2011**, *6*, 1463–1480. [CrossRef]
20. Pham, X.H.; Hahm, E.; Huynh, K.H.; Kim, H.M.; Son, B.S.; Jeong, D.H.; Jun, B.H. Sensitive and selective detection of 4-aminophenol in the presence of acetaminophen using gold-silver core-shell nanoparticles embedded in silica nanostructures. *J. Ind. Eng. Chem.* **2020**, *83*, 208–213. [CrossRef]
21. Lee, S.H.; Jun, B.H. Silver Nanoparticles: Synthesis and Application for Nanomedicine. *Int. J. Mol. Sci.* **2019**, *20*, 865. [CrossRef]
22. Jun, B.H. Silver Nano/Microparticles: Modification and Applications. *Int. J. Mol. Sci.* **2019**, *20*, 609. [CrossRef] [PubMed]
23. Pham, X.H.; Hahm, E.; Kang, E.; Son, B.S.; Ha, Y.; Kim, H.M.; Jeong, D.H.; Jun, B.H. Control of Silver Coating on Raman Label Incorporated Gold Nanoparticles Assembled Silica Nanoparticles. *Int. J. Mol. Sci.* **2019**, *20*, 258. [CrossRef] [PubMed]
24. Kang, E.J.; Baek, Y.M.; Hahm, E.; Lee, S.H.; Pham, X.H.; Noh, M.S.; Kim, D.E.; Jun, B.H. Functionalized beta-Cyclodextrin Immobilized on Ag-Embedded Silica Nanoparticles as a Drug Carrier. *Int. J. Mol. Sci.* **2019**, *20*, 315. [CrossRef]
25. Liu, L.Y.; Cai, R.; Wang, Y.J.; Tao, G.; Ai, L.S.; Wang, P.; Yang, M.R.; Zuo, H.; Zhao, P.; He, H.W. Polydopamine-Assisted Silver Nanoparticle Self-Assembly on Sericin/Agar Film for Potential Wound Dressing Application. *Int. J. Mol. Sci.* **2018**, *19*, 2875. [CrossRef]
26. Radtke, A.; Grodzicka, M.; Ehlert, M.; Muziol, T.M.; Szkodo, M.; Bartmanski, M.; Piszczek, P. Studies on Silver Ions Releasing Processes and Mechanical Properties of Surface-Modified Titanium Alloy Implants. *Int. J. Mol. Sci.* **2018**, *19*, 3962. [CrossRef] [PubMed]
27. Liao, C.Z.; Li, Y.C.; Tjong, S.C. Bactericidal and Cytotoxic Properties of Silver Nanoparticles. *Int. J. Mol. Sci.* **2019**, *20*, 449. [CrossRef]

28. Fehaid, A.; Taniguchi, A. Size-Dependent Effect of Silver Nanoparticles on the Tumor Necrosis Factor -Induced DNA Damage Response. *Int. J. Mol. Sci.* **2019**, *20*, 1038. [CrossRef]
29. Yan, A.; Chen, Z. Impacts of Silver Nanoparticles on Plants: A Focus on the Phytotoxicity and Underlying Mechanism. *Int. J. Mol. Sci.* **2019**, *20*, 1003. [CrossRef]
30. Mo, L.X.; Guo, Z.X.; Yang, L.; Zhang, Q.Q.; Fang, Y.; Xin, Z.Q.; Chen, Z.; Hu, K.; Han, L.; Li, L.H. Silver Nanoparticles Based Ink with Moderate Sintering in Flexible and Printed Electronics. *Int. J. Mol. Sci.* **2019**, *20*, 2124. [CrossRef]
31. Hahm, E.; Jeong, D.; Cha, M.G.; Choi, J.M.; Pham, X.H.; Kim, H.M.; Kim, H.; Lee, Y.S.; Jeong, D.H.; Jung, S.; et al. beta-CD Dimer-immobilized Ag Assembly Embedded Silica Nanoparticles for Sensitive Detection of Polycyclic Aromatic Hydrocarbons. *Sci. Rep.* **2016**, *6*. [CrossRef] [PubMed]
32. Huynh, K.-H.; Pham, X.-H.; Hahm, E.; An, J.; Kim, H.-M.; Jo, A.; Seong, B.; Kim, Y.-H.; Son, B.S.; Kim, J.; et al. Facile Histamine Detection by Surface-Enhanced Raman Scattering Using SiO2@Au@Ag Alloy Nanoparticles. *Int. J. Mol. Sci.* **2020**, *21*, 4048. [CrossRef] [PubMed]
33. Pham, X.H.; Hahm, E.; Huynh, K.H.; Son, B.S.; Kim, H.M.; Jeong, D.H.; Jun, B.H. 4-Mercaptobenzoic Acid Labeled Gold-Silver-Alloy-Embedded Silica Nanoparticles as an Internal Standard Containing Nanostructures for Sensitive Quantitative Thiram Detection. *Int. J. Mol. Sci.* **2019**, *20*, 4841. [CrossRef] [PubMed]
34. Nakamura, S.; Sato, M.; Sato, Y.; Ando, N.; Takayama, T.; Fujita, M.; Ishihara, M. Synthesis and Application of Silver Nanoparticles (Ag NPs) for the Prevention of Infection in Healthcare Workers. *Int. J. Mol. Sci.* **2019**, *20*, 3620. [CrossRef]
35. Nakamura, S.; Ando, N.; Sato, M.; Ishihara, M. Ultraviolet Irradiation Enhances the Microbicidal Activity of Silver Nanoparticles by Hydroxyl Radicals. *Int. J. Mol. Sci.* **2020**, *21*, 3204. [CrossRef]
36. De Mori, A.; Jones, R.S.; Cretella, M.; Cerri, G.; Draheim, R.R.; Barbu, E.; Tozzi, G.; Roldo, M. Evaluation of Antibacterial and Cytotoxicity Properties of Silver Nanowires and Their Composites with Carbon Nanotubes for Biomedical Applications. *Int. J. Mol. Sci.* **2020**, *21*, 2303. [CrossRef]
37. Li, J.P.; Su, M.L.; Wang, A.K.; Wu, Z.X.; Chen, Y.H.; Qin, D.C.; Jiang, Z.H. In Situ Formation of Ag Nanoparticles in Mesoporous TiO2 Films Decorated on Bamboo via Self-Sacrificing Reduction to Synthesize Nanocomposites with Efficient Antifungal Activity. *Int. J. Mol. Sci.* **2019**, *20*, 5497. [CrossRef]
38. De Matteis, V.; Cascione, M.; Toma, C.C.; Albanese, G.; De Giorgi, M.L.; Corsalini, M.; Rinaldi, R. Silver Nanoparticles Addition in Poly(Methyl Methacrylate) Dental Matrix: Topographic and Antimycotic Studies. *Int. J. Mol. Sci.* **2019**, *20*, 4691. [CrossRef]
39. Padnya, P.; Gorbachuk, V.; Stoikov, I. The Role of Calix n arenes and Pillar n arenes in the Design of Silver Nanoparticles: Self-Assembly and Application. *Int. J. Mol. Sci.* **2020**, *21*, 1425. [CrossRef]
40. Tanaka, M.; Saito, S.; Kita, R.; Jang, J.; Choi, Y.; Choi, J.; Okochi, M. Array-Based Screening of Silver Nanoparticle Mineralization Peptides. *Int. J. Mol. Sci.* **2020**, *21*, 2377. [CrossRef]
41. Szalkowski, M.; Sulowska, K.; Jonsson-Niedziolka, M.; Wiwatowski, K.; Niedziolka-Jonsson, J.; Mackowski, S.; Piatkowski, D. Photochemical Printing of Plasmonically Active Silver Nanostructures. *Int. J. Mol. Sci.* **2020**, *21*, 2006. [CrossRef] [PubMed]
42. Kowalska, D.; Szalkowski, M.; Sulowska, K.; Buczynska, D.; Niedziolka-Jonsson, J.; Jonsson-Niedziolka, M.; Kargul, J.; Lokstein, H.; Mackowski, S. Silver Island Film for Enhancing Light Harvesting in Natural Photosynthetic Proteins. *Int. J. Mol. Sci.* **2020**, *21*, 2451. [CrossRef] [PubMed]

International Journal of
Molecular Sciences

MDPI

Article

Facile Histamine Detection by Surface-Enhanced Raman Scattering Using SiO_2@Au@Ag Alloy Nanoparticles

Kim-Hung Huynh [1], Xuan-Hung Pham [1], Eunil Hahm [1], Jaehyun An [1], Hyung-Mo Kim [1], Ahla Jo [1], Bomi Seong [1], Yoon-Hee Kim [1], Byung Sung Son [1], Jaehi Kim [1], Won-Yeop Rho [2] and Bong-Hyun Jun [1,*]

1 Department of Bioscience and Biotechnology, Konkuk University, Seoul 143-701, Korea; huynhkimhung82@gmail.com (K.-H.H.); phamricky@gmail.com (X.-H.P.); greenice@konkuk.ac.kr (E.H.); wogus4067@naver.com (J.A.); hmkim0109@konkuk.ac.kr (H.-M.K.); iamara0421@konkuk.ac.kr (A.J.); bom826@naver.com (B.S.); yoonhees@konkuk.ac.kr (Y.-H.K.); imsonbs@konkuk.ac.kr (B.S.S.); susia45@gmail.com (J.K.)

2 School of International Engineering and Science, Jeonbuk National University, 567 Baekje-daero, Deokjin-gu, Jeonju-si, Jeollabuk-do 54896, Korea; rho7272@jbnu.ac.kr

* Correspondence: bjun@konkuk.ac.kr; Tel.: +82-2-450-0521

Received: 31 March 2020; Accepted: 3 June 2020; Published: 5 June 2020

Abstract: Histamine intoxication associated with seafood consumption represents a global health problem. The consumption of high concentrations of histamine can cause illnesses ranging from light symptoms, such as a prickling sensation, to death. In this study, gold–silver alloy-embedded silica (SiO_2@Au@Ag) nanoparticles were created to detect histamine using surface-enhanced Raman scattering (SERS). The optimal histamine SERS signal was measured following incubation with 125 μg/mL of SiO_2@Au@Ag for 2 h, with a material-to-histamine solution volume ratio of 1:5 and a phosphate-buffered saline-Tween 20 (PBS-T) solvent at pH 7. The SERS intensity of the histamine increased proportionally with the increase in histamine concentration in the range 0.1–0.8 mM, with a limit of detection of 3.698 ppm. Our findings demonstrate the applicability of SERS using nanomaterials for histamine detection. In addition, this study demonstrates that nanoalloys could have a broad application in the future.

Keywords: histamine; fish; gold-silver alloy-embedded silica nanoparticles; surface-enhanced Raman scattering (SERS); reliable and sensitive detection

1. Introduction

Histamine is a common biological substance involved in immune responses, physiological function, and neurotransmission. The consumption of high concentrations of histamine can cause illness ranging from light symptoms, such as a prickling or burning sensation, to serious symptoms, such as erythema, vomiting, diarrhea, headache, angioedema, and urticaria, and even shock or death. Nearly all cases of histamine poisoning are associated with the consumption of fish containing high levels of histidine, which is easily transformed to histamine by decarboxylation if the fish is not correctly stored. Once histamine is produced, it is not easy to completely remove it by heat treatment or freezing. In addition, histamine has no color or odor, which hinders the identification of histamine contamination without noticeable changes in the appearance or smell of the fish [1–5]. According to the European Union (EU) and the U.S. Food and Drug Administration (FDA) standards, the concentration of histamine in fish for

consumption must be <100 and 50 ppm, respectively. Therefore, reliable, rapid detection of histamine in fish is essential for food safety and public health, as well as for the global fish industry. Generally, histamine detection is performed using methods such as high-performance liquid chromatography (HPLC), capillary electrophoresis (CE), enzyme linked immunosorbent assay (ELISA), fluorescence quantification, and ion exchange chromatography [6–11]. Although these methods are very sensitive, they do have some disadvantages; they use hazardous chemicals and require lengthy pretreatment or specific enzymes, which are expensive and strictly produced. In addition, some protocols indirectly detect histamine via histamine derivatives, which can lead to incorrect results [3,6,7].

Surface-enhanced Raman scattering (SERS) is a spectroscopic technique discovered in the 1970s. SERS is an ideal analysis technique, as it can detect single molecules, as well enhance the chemical molecule signal by up to 10^{16}-fold. Compared with other analysis methods, SERS requires simple sample preparation and can use a wide range of excitation frequencies, which enables less energetic excitation, resulting in reduced photodamage. Metal colloids, typically silver or gold colloids in suspension or aggregation, have been broadly used for SERS measurements owing to their strong SERS signal and low toxicity [12–14]. The useful application of SERS has motivated researchers to develop more reliable SERS techniques. Among those techniques under development, nanoalloy materials have been successfully produced. The abundant variety of metallic alloy compositions, structures, and properties, which can consist of bimetallic nanoclusters (Cu-Ag, Cu-Au, Ag-Au, Ni-Pt, and Fe-Ni) or trimetallic nanoclusters (Cu-Au-Pt, Pd-Ag-Fe, Au-Pt-Ag, and Pd-Au-Pt), has created better stability and synergism that has enabled their widespread application in electronics, engineering, and catalysis [15–19].

Currently, SERS is being increasingly applied in the field of food safety for the detection of harmful substances. Several studies have used silver or gold colloids to detect histamine by SERS [1–5]. Compared with other standard methods, such as HPLC, these SERS methods have the advantages of sensitivity, reliability, and easy fabrication; however, precise control of the size and amount of the aggregated particle clusters is difficult because of the heterogeneous formation of the metal particles. The use of a template, such as silica particles or polymer beads, to accumulate silver or gold nanoparticles (NPs) has been widely established in order to control particle size [20–28]. Recently, our group produced an Au-Ag alloy on silica nanoparticles as a highly sensitive and reliable SERS probe that can detect molecular targets at very low concentrations [29–42]. Based on these studies, we investigated histamine detection using an Au-Ag alloy on silica particles as a material for SERS.

2. Results and Discussion

2.1. Characterization of the SiO_2@Au@Ag NPs

The SiO_2@Au@Ag NP material was prepared based on studies conducted by the Pham group revealing that SiO_2@Au@Ag NPs exhibit a high Raman enhancement effect [39,43,44]. Silica NPs were produced using the Stöber method. Subsequently, the surfaces of the silica NPs were covered with Au NPs on which an Ag shell was created.

Figure 1 shows transmission electron microscopy (TEM) images of the nanomaterials. The average diameter of the SiO_2 NPs was 160 nm (1a). SiO_2 NPs covered by Au NPs (2–3 nm) are shown in Figure 1b. The surface of the SiO_2@Au NPs was thoroughly coated with an Ag shell (1c), with clear nanogaps between the Ag NPs, which will provide the best Raman signal [39]. As shown in Figure 1d, while the SiO_2 suspension did not exhibit UV–Vis absorbance in the 300–1000 nm range, the SiO_2@Au NP colloid showed a peak at approximately 520 nm. Once the Ag NPs were embedded onto SiO_2@Au, the absorbance of the SiO_2@Au@Ag suspension showed a wide band from 320 to nearly 800 nm.

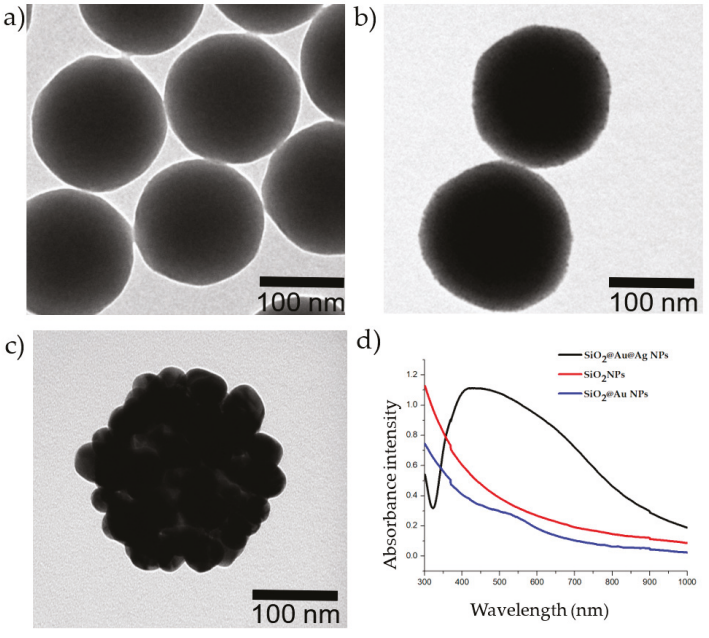

Figure 1. Images of the nanoparticles and UV–Vis absorbance of the nanoparticles. (**a**) Transmission electron microscopy (TEM) image of silica (SiO_2) NPs; (**b**) TEM image of SiO_2@Au NPs; (**c**) TEM image of SiO_2@Au@Ag NPs; (**d**) UV–Vis absorbance of NPs. Red: 1000 μg/mL SiO_2 NPs; blue: 250 μg/mL SiO_2@Au NPs; black: 20 μg/mL SiO_2@Au@Ag NPs.

2.2. Optimization of Histamine Detection

As the SERS signal is affected by many factors, we sought to determine the effect of target volume, incubation time, solvent pH, and material concentration on SERS signal. The SERS spectra of histamine-modified SiO_2@Au@Ag were observed at 850, 1001, 1200, 1258, 1263, 1318, 1353, 1449, 1536, 1603, and 1641 cm^{-1} (Figure S1 and Table S1, Supplementary Materials). The bands at 1641, 1603, 1536, 1353, and 850 cm^{-1} were assigned to ring stretching; the bands at 1258 and 1001 cm^{-1} were assigned to ring bending; the band at 1449 cm^{-1} was assigned to the bending of the CH_2 side chain; the band at 1318 cm^{-1} was assigned to CH_2 wagging; and the bands at 1200 and 1263 cm^{-1} were assigned to ring breathing [45–50]. For simple evaluation, we considered an intensity of wavelength number of 1603 cm^{-1}, which might be due to ring stretching [45–50], as the highest histamine Raman shift peak.

2.2.1. Effect of Target Volume on Histamine Detection

As the SERS signal is affected by the amount of target molecule on the surface of the material, we carried out an experiment in which we incubated 20 μg of SiO_2@Au@Ag NPs (100 μL) with different volumes of 1 mM histamine (100, 500 μL, and 1000 μL); the mean ratio between the volume of the material and histamine was 1:1, 1:5, and 1:10, respectively. As shown in Figure 2, the SERS signal increased with increasing volume, as the amount of histamine absorbed onto the surface of the material increased. Therefore, the SERS signal at a 1:5 and 1:10 ratio was clearer than that at a 1:1 ratio. The 1:5 ratio was chosen for subsequent experiments.

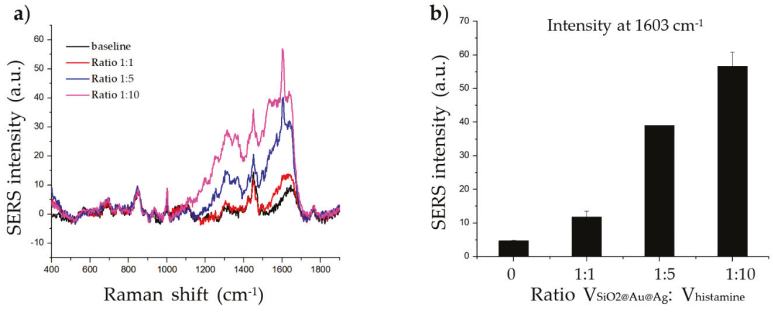

Figure 2. Effect of target volume on histamine detection. (**a**) Raman signal of histamine incubated with SiO_2@Au@Ag nanoparticles (NPs) at three volume ratios (1:1, 1:5, and 1:10) after 2 h. (**b**) The Raman intensity of histamine incubated with SiO_2@Au@Ag NPs at various volume ratios after 2 h (at 1603 cm^{-1}).

2.2.2. Effect of Incubation Time on Histamine Detection

The incubation step allows the target molecule to adsorb onto the surface of the material. To determine the effect of histamine incubation time, histamine was incubated with 20 µg of material for 0, 0.5, 1, 2, 4, 6, and 8 h. As shown in Figure 3, the intensity of the SERS signal increased up to 1 h of incubation. After 1 h, the SERS signal of the histamine gradually increased with further incubation. The signals at wave number 1603 cm^{-1} are clear enough irrespective of experimental incubation time; thus, 2 h of incubation was chosen for subsequent experiments as the intensity at 2 h represents approximately the average of the intensity obtained after incubation for the other time periods.

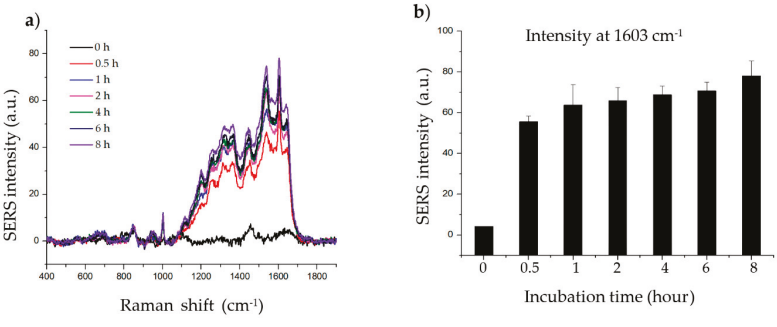

Figure 3. Effect of incubation time on histamine detection. (**a**) Raman signal of histamine incubated with SiO_2@Au@Ag nanoparticles (NPs) after 0.5, 1, 2, 4, 6, and 8 h. (**b**) Raman intensity of histamine incubated with SiO_2@Au@Ag NPs after 0.5, 1, 2, 4, 6, and 8 h (at 1603 cm^{-1}).

2.2.3. Effect of Solvent pH on Histamine Detection

To determine the effect of pH on the SERS signal of the histamine, phosphate-buffered saline-Tween 20 (PBS-T) solvents with various pH values (3, 5, 7, and 9) were created by adjusting the pH with hydrochloric acid (HCl) and sodium hydroxide (NaOH). As shown in Figure 4, the SERS signal of the histamine was strong and clear at all four pH values. However, based on this result, the binding between the histamine and the Ag shell appears to be better in an alkaline environment. Thus, pH 7 was chosen for subsequent experiments as it is near the physiological pH.

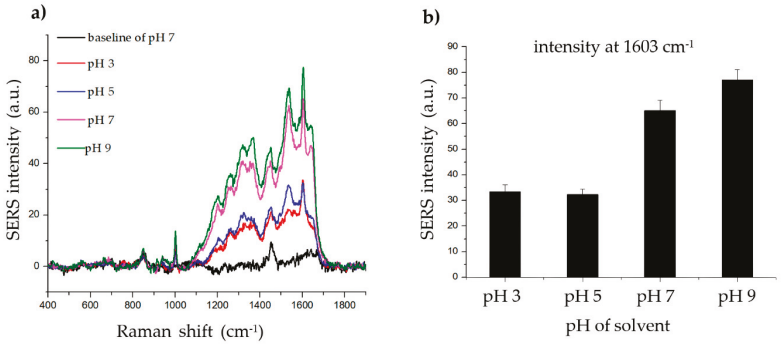

Figure 4. Effect of solvent pH on histamine detection. (**a**) Raman signal of histamine incubated with SiO_2@Au@Ag nanoparticles (NPs) after 2 h in solvents (phosphate-buffered saline-Tween 20 (PBS-T)) with different pH values (3, 5, 7, and 9). (**b**) The Raman intensity of histamine in solvents (PBS-T) with different pH values (3, 5, 7, and 9) (at 1603 cm^{-1}).

2.2.4. Effect of the Material Concentration on the SERS Signal of Histamine

To determine the effect of the material concentration on the SERS signal of histamine, we incubated the same amount of histamine with different concentrations of material (1, 0.5, 0.25, 0.125, and 0.0625 mg/mL) and measured the Raman signal. As shown in Figure 5, the strongest SERS signal was detected when 0.125 mg/mL material was incubated with histamine, while weaker SERS signals were detected at both higher and lower concentrations. These results indicate that the dispersion density of histamine on the surface of the material significantly affected the SERS signal. Although the high and low concentrations of the material did not generate a sufficiently robust SERS signal, any of the concentrations can be used, as the intensities at 1603 cm^{-1} were strong and could be clearly observed.

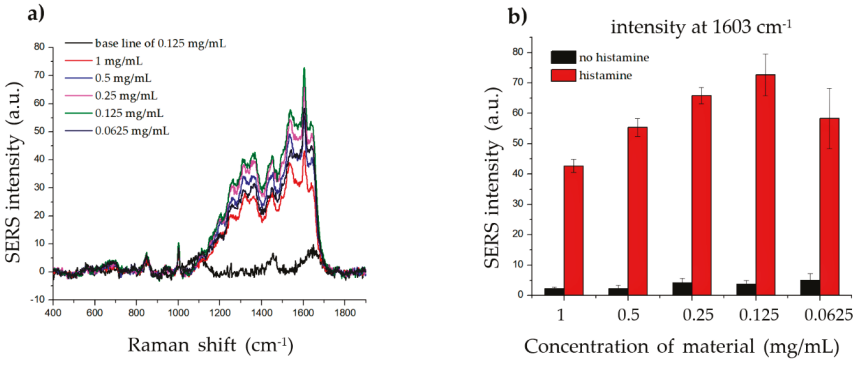

Figure 5. Effect of material concentration on histamine detection. (**a**) The Raman signal of the same concentration of histamine incubated with 1, 0.5, 0.25, 0.125, and 0.0625 mg/mL of SiO_2@Au@Ag nanoparticles (NPs). (**b**) The Raman intensity of histamine for different concentrations of SiO_2@Au@Ag NPs (at 1603 cm^{-1}).

2.3. The Limit of Detection (LOD) of Histamine

To determine the LOD of histamine, we measured the SERS signal at various concentrations of histamine (0.1–0.8 mM) with 20 μg of material (Figure 6a). The intensity at 1603 cm^{-1} increased proportionally with increasing histamine concentration (Figure 6b). The linear calibration formula was determined as y = 37.79951x + 2.89144, R^2 = 0.99081 (x = histamine concentration, y = SERS intensity at 1603 cm^{-1}). The LOD of histamine was 0.033 mM (3.698 ppm) with a signal-to-noise ratio (S/N) = 3, which is considerably lower than the standards described by the FDA (50 ppm) or EU (100 ppm). The LOD of the present method (3.698 ppm) was also comparable to that of existing histamine detection methods such as ELISA (1–17 ppm) [6,8,11], HPLC (0.1–25 ppm) [7,8,10,51], and SERS (5–15 ppm) [2,4,5]. Although the LOD of the present method was not lower than the lowest ELISA and HPLC LODs, it remains useful, as its LOD is lower than the highest LOD values of the other methods. Furthermore, SERS-based methods, including the present method, are suitable for biological applications owing to several advantages, such as low cost, high efficacy, fewer harmful chemicals, non-destructive features, and simple sample preparation. The present method also showed a lower LOD than previous SERS-based histamine detection methods (3.986 vs. 5–15 ppm), owing to the use of Au-Ag alloy NPs instead of Au or Ag NPs. Thus, these results indicate the possible application of this method for histamine detection in fish samples. Additionally, these results also demonstrate a novel SERS-based method using gold-silver alloy-embedded silica NPs for molecular determination.

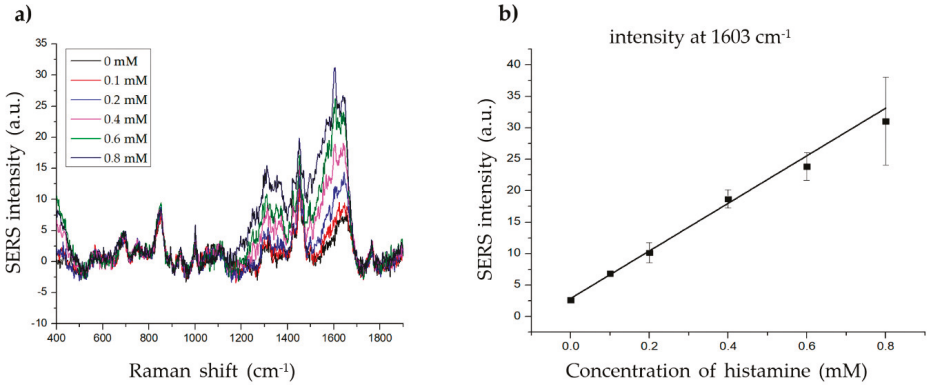

Figure 6. Determining the limit of detection (LOD) of histamine. (**a**) The Raman signal of histamine at different concentrations (0, 0.1, 0.2, 0.4, 0.6, and 0.8 mM). (**b**) The standard linear plot of histamine concentration vs. SERS intensity at 1603 cm^{-1}.

3. Materials and Methods

3.1. Chemicals and Materials

All reagents were used as received from the suppliers without further purification. Tetraethylorthosilicate (TEOS), 3-aminopropyltriethoxysilane (APTS), polyvinylpyrrolidone (PVP) (Mw 40,000), silver nitrate ($AgNO_3$), L-ascorbic acid, Tween 20, tetrakis(hydroxymethyl)phosphonium chloride (THPC), gold (III) chloride trihydrate ($HAuCl_4$), and histamine dihydrochloride were purchased from Sigma-Aldrich (St. Louis, MO, USA). Ethyl alcohol (EtOH) and aqueous ammonium hydroxide (NH_4OH) were purchased from Daejung (Siheung, South Korea). HCl and NaOH were purchased from Samchun (Pyeongtaek, South Korea). Phosphate-buffered saline (PBS; 20×) was purchased from Dyne Bio (Seongnam,

South Korea). Ultrapure water (resistivity 18.2 MΩ×cm) was produced using a Millipore water purification system (EXL water purification, Vivagen Co., Ltd., Seongnam, South Korea).

3.2. Preparation of SiO_2@Au@Ag NPs

The SiO_2@Au@Ag NP material was prepared using silica NPs produced via the Stöber method, with an average diameter of approximately 160 nm. Following amine-functionalization performed by incubating a mixture containing 200 mg of silica NPs, 4 mL of absolute EtOH, 200 µL of APTS, and 40 µL of NH_4OH for 12 h, the silica NPs were incubated with Au NPs (2–3 nm) prepared by reducing $HAuCl_4$ with THPC for 12 h with gentle shaking at 25 °C. The surfaces of the aminated silica NPs were covered with Au NPs. An Ag shell was created on the surface of the SiO_2@Au NPs by reducing $AgNO_3$ in the presence of ascorbic acid and PVP; 200 µL of 200 µg/mL SiO_2@Au@Ag NPs were well dispersed in 9.8 mL of 1 mg/mL PVP solvent and then 20 µL of 10 mM $AgNO_3$ was added, followed by the addition of 20 µL of 10 mM ascorbic acid. This suspension was slowly stirred for 15 min for the reduction of Ag^+ ions to Ag. The reaction was repeated to obtain an $AgNO_3$ concentration of 300 µM. The SiO_2@Au@Ag NPs were collected by centrifugation at 8500 rpm for 15 min. Following several washes with EtOH to remove excess reagent, the SiO_2@Au@Ag NPs were re-dispersed in absolute EtOH to obtain a 200 µg/mL SiO_2@Au@Ag NP solution.

3.3. Histamine Detection

The histamine solution was prepared by dissolving histamine dihydrochloride in PBS-Tween 20 (1%; PBS-T), pH 7. To absorb histamine on the surface of the SiO_2@Au@Ag NPs, 100 µL of a 1 mM histamine solution were incubated with 100 µL of a 200 µg/mL SiO_2@Au@Ag NP suspension for 2 h, followed by centrifugation for 15 min at 11,000 rpm to collect the colloids. The NPs was washed several times with PBS-T (pH 7) to remove excess reagent. The SiO_2@Au@Ag@Histamine NPs were re-dispersed in 100 µL of PBS-T (pH 7) to obtain a 200 µg/mL SiO_2@Au@Ag@Histamine NP suspension. For optimization, each condition, including incubation time, solvent pH, and volume of histamine solution, was changed. The LOD of histamine was determined by varying the concentration of histamine. The control sample (baseline) consisted of only SiO_2@Au@Ag NP material in PBS-T (pH 7) solvent. Each experiment was conducted three times.

3.4. SERS Measurement of SiO_2@Au@Ag@Histamine

The SERS signals were measured using a DXR 2 Raman Microscope System (Thermo Fisher Scientific, Waltham, MA, USA) with a 532-nm laser excitation source and 10× objective lens. Liquid samples were measured in a capillary tube with a laser power of excitation of 10 mW for 5 s. The size of the laser beam spot was approximately 2.0 µm and the sites were randomly selected. The SERS spectra were collected in the 400–1900 cm^{-1} wavenumber range. Each sample was measured three times. The highest peak at wave number 1603 cm^{-1} was selected for analysis.

4. Conclusions

In this study, histamine was successfully detected by SERS using a SiO_2@Au@Ag alloy nanomaterial. The best SERS signal was obtained using an incubation time of 2 h, a material-to-histamine solution volume ratio of 1:5, PBS-T solvent at pH 7, and material concentration of 0.125 mg/mL; using this protocol, the LOD of histamine was 3.698 ppm. To the best of our knowledge, this study is the first to report histamine detection using gold-silver alloy-embedded silica nanoparticles and provides the basis for further research that could be applied to the detection of histamine in real samples. In addition, this study demonstrates that nanoalloys are novel materials that could have a broad application in the future.

Supplementary Materials: Supplementary materials can be found at http://www.mdpi.com/1422-0067/21/11/4048/s1.

Author Contributions: Conceptualization and experimental design, X.-H.P., B.-H.J., W.-Y.R. and K.-H.H.; investigation, K.-H.H., A.J., B.S., and Y.-H.K.; reagents and materials, J.A. and H.-M.K.; data analysis, X.-H.P., B.-H.J., and K.-H.H.; writing, K.-H.H., E.H., J.K. and B.S.S.; supervision, B.-H.J. All authors have read and agreed to the published version of the manuscript.

Funding: This research was funded by Konkuk University, 2017.

Acknowledgments: We wish to thank the Microbial Carbohydrate Resource Bank (MCRB, Seoul, Korea) for their consulting services.

Conflicts of Interest: The authors declare no conflict of interest.

Abbreviations

$AgNO_3$	Silver nitrate
APTS	3-Aminopropyltriethoxysilane
CE	Capillary electrophoresis
ELISA	Enzyme linked immunosorbent assay
EtOH	Ethyl alcohol
EU	European Union
FDA	U.S. Food and Drug Administration
$HAuCl_4$	Gold (III) chloride trihydrate
HCl	Hydrochloric acid
HPLC	High-performance liquid chromatography
LOD	Limit of detection
NaOH	Sodium hydroxide
NH_4OH	Ammonium hydroxide
NPs	Nanoparticles
PBS-T	Phosphate-buffered saline-Tween 20
PVP	Polyvinylpyrrolidone
S/N	Signal to noise ratio
SERS	Surface-enhanced Raman scattering
SiO_2@Au@Ag	Gold–silver alloy-embedded silica
TEM	Transmission electron microscopy
TEOS	Tetraethylorthosilicate
THPC	Tetrakis(hydroxymethyl)phosphonium chloride

References

1. Janči, T.; Valinger, D.; Kljusurić, J.G.; Mikac, L.; Filipec, S.V.; Ivanda, M. Determination of histamine in fish by Surface Enhanced Raman Spectroscopy using silver colloid SERS substrates. *Food Chem.* **2017**, *224*, 48–54. [CrossRef] [PubMed]
2. Chu, B.Q.; Lin, L.; He, Y. Rapid determination of histamine concentration in fish (Miichthys Miiuy) by surface-enhanced Raman spectroscopy and density functional theory. *Int. J. Agric. Biol. Eng.* **2017**, *10*, 252–258.
3. Kolosovas-Machuca, E.S.; Cuadrado, A.; Ojeda-Galván, H.J.; Ortiz-Dosal, L.C.; Hernández-Arteaga, A.C.; Rodríguez-Aranda, M.D.C.; Navarro-Contreras, H.R.; Alda, J.; Gonzalez, F. Detection of histamine dihydrochloride at low concentrations using Raman spectroscopy enhanced by gold nanostars colloids. *Nanomaterials* **2019**, *9*, 211. [CrossRef] [PubMed]
4. Tan, A.; Zhao, Y.; Sivashanmugan, K.; Squire, K.; Wang, A.X. Quantitative TLC-SERS detection of histamine in seafood with support vector machine analysis. *Food Control.* **2019**, *103*, 111–118. [CrossRef] [PubMed]
5. Xie, Z.; Wang, Y.; Chen, Y.; Xu, X.; Jin, Z.; Ding, Y.; Yang, N.; Wu, F. Tuneable surface enhanced Raman spectroscopy hyphenated to chemically derivatized thin-layer chromatography plates for screening histamine in fish. *Food Chem.* **2017**, *230*, 547–552. [CrossRef] [PubMed]

6. Rahimi, E.; Nayebpour, F.; Alian, F. Determination of histamine in canned tuna fish using ELISA method. *Am. Eurasian J. Toxicol. Sci.* **2012**, *4*, 64–66.
7. Nadeem, M.; Naveed, T.; Rehman, F.; Xu, Z. Determination of histamine in fish without derivatization by indirect reverse phase-HPLC method. *Microchem. J.* **2019**, *144*, 209–214. [CrossRef]
8. Muscarella, M.; Magro, S.L.; Campaniello, M.; Armentano, A.; Stacchini, P. Survey of histamine levels in fresh fish and fish products collected in Puglia (Italy) by ELISA and HPLC with fluorimetric detection. *Food Control.* **2013**, *31*, 211–217. [CrossRef]
9. Cinquina, A.; Longo, F.; CaliA; De Santis, L.; Baccelliere, R.; Cozzani, R. Validation and comparison of analytical methods for the determination of histamine in tuna fish samples. *J. Chromatogr. A* **2004**, *1032*, 79–85. [CrossRef]
10. Jinadasa, B.K.K.K.; Jayasinghe, G.; Ahmad, S. Validation of high-performance liquid chromatography (HPLC) method for quantitative analysis of histamine in fish and fishery products. *Cogent Chem.* **2016**, *2*, 1156806. [CrossRef]
11. Manz, G.; Booltink, E. Validation study of a HistaSure (TM) ELISA(Fast Track) for the determination of histamine in fish samples. *J. AOAC Int.* **2014**, *97*, 1601–1614. [CrossRef] [PubMed]
12. Çulha, M.; Cullum, B.; Lavrik, N.; Klutse, C.K. Surface-enhanced Raman scattering as an emerging characterization and detection technique. *J. Nanotechnol.* **2012**, *2012*. [CrossRef]
13. Schlücker, S. Surface-enhanced Raman spectroscopy: Concepts and chemical applications. *Angew. Chem. Int. Ed.* **2014**, *53*, 4756–4795. [CrossRef] [PubMed]
14. Wang, Y.; Yan, B.; Chen, L. SERS tags: Novel optical nanoprobes for bioanalysis. *Chem. Rev.* **2012**, *113*, 1391–1428. [CrossRef]
15. Cai, X.-L.; Liu, C.; Liu, J.; Lu, Y.; Zhong, Y.-N.; Nie, K.; Xu, J.-L.; Gao, X.; Sun, X.-H.; Wang, S.-D. Synergistic effects in CNTs-PdAu/Pt trimetallic nanoparticles with high electrocatalytic activity and stability. *Nano Micro Lett.* **2017**, *9*, 48. [CrossRef]
16. Ferrando, R.; Jellinek, J.; Johnston, R.L. Nanoalloys: From theory to applications of alloy clusters and nanoparticles. *Chem. Rev.* **2008**, *108*, 845–910. [CrossRef] [PubMed]
17. Karthikeyan, B.; Loganathan, B. Rapid green synthetic protocol for novel trimetallic nanoparticles. *J. Nanoparticles* **2013**, *2013*. [CrossRef]
18. Khan, Z. Trimetallic nanoparticles: Synthesis, characterization and catalytic degradation of formic acid for hydrogen generation. *Int. J. Hydrogen Energy* **2019**, *44*, 11503–11513. [CrossRef]
19. Ye, X.; He, X.; Lei, Y.; Tang, J.; Yu, Y.; Shi, H.; Wang, K. One-pot synthesized Cu/Au/Pt trimetallic nanoparticles with enhanced catalytic and plasmonic properties as a universal platform for biosensing and cancer theranostics. *Chem. Commun.* **2019**, *55*, 2321–2324. [CrossRef]
20. Devi, P.; Patil, S.D.; Jeevanandam, P.; Navani, N.K.; Singla, M.L. Synthesis, characterization and bactericidal activity of silica/silver core–shell nanoparticles. *J. Mater. Sci. Mater. Electron.* **2014**, *25*, 1267–1273. [CrossRef]
21. Kandpal, D.; Kalele, S.; Kulkarni, S.K. Synthesis and characterization of silica-gold core-shell (SiO2@Au) nanoparticles. *Pramana* **2007**, *69*, 277–283. [CrossRef]
22. Nghiem, T.H.L.; Le, T.N.; Do, T.H.; Vu, T.T.D.; Do, Q.H.; Tran, H.N. Preparation and characterization of silica–gold core–shell nanoparticles. *J. Nanoparticle Res.* **2013**, *15*. [CrossRef]
23. Pol, V.G.; Gedanken, A.; Calderon-Moreno, J. Deposition of gold nanoparticles on silica spheres: A sonochemical approach. *Chem. Mater.* **2003**, *15*, 1111–1118. [CrossRef]
24. Purdy, S.C.; Muscat, A.J. Coating nonfunctionalized silica spheres with a high density of discrete silver nanoparticles. *J. Nanoparticle Res.* **2016**, *18*, 70. [CrossRef]
25. Roy, S.; Dixit, C.K.; Woolley, R.; O'Kennedy, R.; McDonagh, C. Synthesis and characterization of model silica–gold core–shell nanohybrid systems to demonstrate plasmonic enhancement of fluorescence. *Nanotechnology* **2012**, *23*, 325603. [CrossRef] [PubMed]
26. Tang, S.; Tang, Y.; Zhu, S.; Lu, H.; Meng, X. Synthesis and characterization of silica–silver core–shell composite particles with uniform thin silver layers. *J. Solid State Chem.* **2007**, *180*, 2871–2876. [CrossRef]
27. Zhu, M.; Qian, G.; Hong, Z.; Wang, Z.; Fan, X.; Wang, M. Preparation and characterization of silica–silver core-shell structural submicrometer spheres. *J. Phys. Chem. Solids* **2005**, *66*, 748–752. [CrossRef]

28. Zienkiewicz-Strzałka, M.; Deryło-Marczewska, A.; Kozakevych, R.B. Silica nanocomposites based on silver nanoparticles-functionalization and pH effect. *Appl. Nanosci.* **2018**, *8*, 1649–1668. [CrossRef]
29. Hahm, E.; Cha, M.G.; Kang, E.J.; Pham, X.-H.; Lee, S.H.; Kim, H.-M.; Kim, D.-E.; Lee, Y.-S.; Jeong, D.H.; Jun, B.-H. Multilayer Ag-embedded silica nanostructure as a surface-enhanced Raman scattering-based chemical sensor with dual-function internal standards. *ACS Appl. Mater. Interfaces* **2018**, *10*, 40748–40755. [CrossRef]
30. Hahm, E.; Jeong, D.; Cha, M.G.; Choi, J.M.; Pham, X.H.; Kim, H.M.; Kim, H.; Lee, Y.S.; Jeong, D.H.; Jung, S.; et al. beta-CD dimer-immobilized Ag assembly embedded silica nanoparticles for sensitive detection of polycyclic aromatic hydrocarbons. *Sci. Rep. UK* **2016**, *6*, 26082. [CrossRef]
31. Hahm, E.; Kang, E.J.; Pham, X.H.; Jeong, D.; Jeong, D.H.; Jung, S.; Jun, B.H. Mono-6-deoxy-6-aminopropylamino-beta-cyclodextrin on Ag-embedded SiO2 nanoparticle as a selectively capturing ligand to flavonoids. *Nanomater. Basel* **2019**, *9*, 1349. [CrossRef] [PubMed]
32. Jun, B.H.; Kim, G.; Jeong, S.; Noh, M.S.; Pham, X.H.; Kang, H.; Cho, M.H.; Kim, J.H.; Lee, Y.S.; Jeong, D.H. Silica core-based surface-enhanced Raman scattering (SERS) tag: Advances in multifunctional SERS nanoprobes for bioimaging and targeting of biomarkers. *B Korean Chem. Soc.* **2015**, *3*, 963–978.
33. Kang, E.J.; Baek, Y.M.; Hahm, E.; Lee, S.H.; Pham, X.H.; Noh, M.S.; Kim, D.E.; Jun, B.H. Functionalized beta-cyclodextrin immobilized on Ag-embedded silica nanoparticles as a drug carrier. *Int. J. Mol. Sci.* **2019**, *20*, 315. [CrossRef] [PubMed]
34. Kim, T.H.; Pham, X.-H.; Rho, W.-Y.; Kim, H.-M.; Hahm, E.; Ha, Y.; Son, B.S.; Lee, S.H.; Jun, B.-H. Ag and Ag-Au introduced silica-coated magnetic beads. *Bull. Korean Chem. Soc.* **2018**, *39*, 250–256. [CrossRef]
35. Pham, X.-H.; Hahm, E.; Kang, E.; Na Ha, Y.; Lee, S.H.; Rho, W.-Y.; Lee, Y.-S.; Jeong, D.H.; Jun, B.-H. Gold-silver bimetallic nanoparticles with a Raman labeling chemical assembled on silica nanoparticles as an internal-standard-containing nanoprobe. *J. Alloys Compd.* **2019**, *779*, 360–366. [CrossRef]
36. Pham, X.-H.; Hahm, E.; Kim, H.-M.; Shim, S.; Kim, T.H.; Jeong, D.H.; Lee, J.-Y.; Jun, B.-H. Silver nanoparticle-embedded thin silica-coated graphene oxide as an SERS substrate. *Nanomaterials* **2016**, *6*, 176. [CrossRef]
37. Pham, X.-H.; Hahm, E.; Kim, H.-M.; Son, B.; Jo, A.; An, J.; Thi, T.T.; Nguyen, D.; Jun, B.-H. Silica-coated magnetic iron oxide nanoparticles grafted onto graphene oxide for protein isolation. *Nanomaterials* **2020**, *10*, 117. [CrossRef]
38. Pham, X.-H.; Hahm, E.; Kim, T.H.; Kim, H.-M.; Lee, S.H.; Lee, Y.-S.; Jeong, D.H.; Jun, B.-H. Enzyme-catalyzed Ag growth on Au nanoparticle-assembled structure for highly sensitive colorimetric immunoassay. *Sci. Rep.* **2018**, *8*, 6290. [CrossRef]
39. Pham, X.-H.; Lee, M.; Shim, S.; Jeong, S.; Kim, H.-M.; Hahm, E.; Lee, S.H.; Lee, J.-Y.; Jeong, D.H.; Jun, B.-H. Highly sensitive and reliable SERS probes based on nanogap control of a Au–Ag alloy on silica nanoparticles. *RSC Adv.* **2017**, *7*, 7015–7021. [CrossRef]
40. Pham, X.-H.; Shim, S.; Kim, T.-H.; Hahm, E.; Rho, W.-Y.; Jeong, D.H.; Lee, J.-Y.; Jun, B.-H.; Kim, H.-M. Glucose detection using 4-mercaptophenyl boronic acid-incorporated silver nanoparticles-embedded silica-coated graphene oxide as a SERS substrate. *BioChip J.* **2016**, *11*, 46–56. [CrossRef]
41. Pham, X.-H.; Hahm, E.; Huynh, K.-H.; Kim, H.-M.; Son, B.S.; Jeong, D.H.; Jun, B.-H. Sensitive and selective detection of 4-aminophenol in the presence of acetaminophen using gold–silver core–shell nanoparticles embedded in silica nanostructures. *J. Ind. Eng. Chem.* **2020**, *83*, 208–213. [CrossRef]
42. Shim, S.; Pham, X.-H.; Cha, M.G.; Lee, J.-Y.; Jeong, D.H.; Jun, B.-H. Size effect of gold on Ag-coated Au nanoparticle-embedded silica nanospheres. *RSC Adv.* **2016**, *6*, 48644–48650. [CrossRef]
43. Bastús, N.G.; Merkoçi, F.; Piella, J.; Puntes, V. Synthesis of highly monodisperse citrate-stabilized silver nanoparticles of up to 200 nm: Kinetic control and catalytic properties. *Chem. Mater.* **2014**, *26*, 2836–2846. [CrossRef]
44. Pham, X.-H.; Hahm, E.; Huynh, K.-H.; Son, B.; Kim, H.-M.; Jeong, D.H.; Jun, B.-H. 4-Mercaptobenzoic acid labeled gold-silver-alloy-embedded silica nanoparticles as an internal standard containing nanostructures for sensitive quantitative thiram detection. *Int. J. Mol. Sci.* **2019**, *20*, 4841. [CrossRef]
45. Collado, J.A.; Ramírez, F.J. Vibrational spectra and assignments of histamine dication in the solid state and in solution. *J. Raman Spectrosc.* **2000**, *31*, 925–931. [CrossRef]

46. Davis, K.L.; McGlashen, M.L.; Morris, M.D. Surface-enhanced Raman scattering of histamine at silver electrodes. *Langmuir* **1992**, *8*, 1654–1658. [CrossRef]
47. Itabashi, M.; Shoji, K.; Itoh, K. Raman spectra of copper(II)-histamine (1:2) and nickel(II)-histamine (1:2) aqueous solutions. *Inorg. Chem.* **1982**, *21*, 3484–3489. [CrossRef]
48. Janči, T.; Mikac, L.; Ivanda, M.; Radovčić, N.M.; Medić, H.; Filipec, S.V. Optimization of parameters for histamine detection in fish muscle extracts by surface-enhanced Raman spectroscopy using silver colloid SERS substrates. *J. Raman Spectrosc.* **2016**, *48*, 64–72. [CrossRef]
49. Ramírez, F.J.; Tuñón, I.; Collado, J.A.; Silla, E. Structural and vibrational study of the tautomerism of histamine free-base in solution. *J. Am. Chem. Soc.* **2003**, *125*, 2328–2340. [CrossRef]
50. Torreggiani, A.; Tamba, M.; Bonora, S.; Fini, G. Raman and IR study on copper binding of histamine. *Biopolymers* **2003**, *72*, 290–298. [CrossRef]
51. Peycheva, M.; Yankovska, T.; Stoilova, N. HPLC/FL method for histamine testing in fish. In Proceedings of the Book Days of Veterinary Medicine 2012 3rd International Scientific Meeting, Ohrid, North Macedonia, 2–4 September 2012.

International Journal of
Molecular Sciences

MDPI

Article

4-Mercaptobenzoic Acid Labeled Gold-Silver-Alloy-Embedded Silica Nanoparticles as an Internal Standard Containing Nanostructures for Sensitive Quantitative Thiram Detection

Xuan-Hung Pham [1], Eunil Hahm [1], Kim-Hung Huynh [1], Byung Sung Son [1], Hyung-Mo Kim [1], Dae Hong Jeong [2] and Bong-Hyun Jun [1,*]

[1] Department of Bioscience and Biotechnology, Konkuk University, Seoul 143-701, Korea; phamricky@gmail.com (X.-H.P.); greenice@konkuk.ac.kr (E.H.); huynhkimhung82@gmail.com (K.-H.H.); imsonbs@konkuk.ac.kr (B.S.S.); hmkim0109@konkuk.ac.kr (H.-M.K.)

[2] Department of Chemistry Education, Seoul National University, Seoul 151-742, Korea; jeongdh@snu.ac.kr

* Correspondence: bjun@konkuk.ac.kr; Tel.: +82-2-450-0521

Received: 12 August 2019; Accepted: 26 September 2019; Published: 29 September 2019

Abstract: In this study, SiO_2@Au@4-MBA@Ag (4-mercaptobenzoic acid labeled gold-silver-alloy-embedded silica nanoparticles) nanomaterials were investigated for the detection of thiram, a pesticide. First, the presence of Au@4-MBA@Ag alloys on the surface of SiO_2 was confirmed by the broad bands of ultraviolet-visible spectra in the range of 320–800 nm. The effect of the 4-MBA (4-mercaptobenzoic acid) concentration on the Ag shell deposition and its intrinsic SERS (surface-enhanced Raman scattering) signal was also studied. Ag shells were well coated on SiO_2@Au@4-MBA in the range of 1–1000 μM. The SERS intensity of thiram-incubated SiO_2@Au@4-MBA@Ag achieved the highest value by incubation with 500 μL thiram for 30 min, and SERS was measured at 200 μg/mL SiO_2@Au@4-MBA@Ag. Finally, the SERS intensity of thiram at 560 cm^{-1} increased proportionally with the increase in thiram concentration in the range of 240–2400 ppb, with a limit of detection (LOD) of 72 ppb.

Keywords: ultrasensitive detection; thiram; internal standard; gold–silver-alloy-embedded silica nanoparticles

1. Introduction

The use of pesticides in modern agriculture has improved crop yield and quality by controlling or destroying pests or weeds [1–4]. Although pesticides have diverse benefits, they are also a threat to consumer health because they are toxic to humans and other species [5,6]. When pesticides are used for crops or seeds, their traces could remain in the food [7], and these derivatives are considered to be toxic [8]. Further, pesticides are suspected to be carcinogenic and teratogenic compounds [7]. Therefore, the sensitive detection of a small concentration of these fungicides in soils, water, and foods, as well as their chemical state, is important [7].

Various methods have been proposed for monitoring pesticide residues, such as high-performance liquid chromatography (HPLC), gas chromatography-mass spectrometry (GC-MS), thin-layer chromatography, and enzyme-linked immunosorbent assay [9–13]. Currently, HPLC is the most robust and reliable method for food safety analysis. However, HPLC is time-consuming and expensive; requires a harsh solvent, high power source, bulky and sophisticated operation, complicated multi-step pre-treatment process; and could be dedicated in labs to trained personnel [14,15]. Thus, a fast, simple, highly sensitive, and stable method should be developed for the determination of pesticide residue.

Surface-enhanced Raman scattering (SERS) has been developed as a vibrational spectroscopy technique for various applications because of its non-destructive, rapid, molecular fingerprinting, ultrasensitive, and photostable properties [16–20]. Compared with HPLC-MS, SERS does not require harsh solvents and a high power source, and it is easily compatible with other detection systems [21]. As a result, many studies have focused on the use of different nanoparticles (NPs) as substrates for SERS detection of pesticides, such as silver nanostructures [21–26], gold nanostructures [27–31], and graphene oxide [32,33]. Although these nanostructures could enhance the SERS signal up to 10^{14} times, the practical application of SERS exhibits some technical challenges in the fabrication of reproducible, reliable, and robust SERS-active surfaces.

Recently, internal standards have been used to correct variations of SERS intensity in quantitative SERS assays [34–37]. Among them, the ratiometric SERS indicator-based detection mode of core-shell materials has been successfully developed because it can avoid the competition between the internal standard and the target molecules. However, difficulties in synthesizing an appropriate SERS probe for a specified target limited the application of the ratiometric SERS indicator-based detection mode [37]. Previously, our group reported Au-Ag alloys assembled silica NPs (SiO_2@Au@Ag NPs) as a strong and reliable SERS probe with 4-mercaptobenzoic acid (4-MBA) as an internal standard located between the SiO_2@Au core and the Ag shell. SiO_2@Au@4-MBA@Ag NPs were synthesized by Au seed-mediated Ag growth on the surface of a silica template, followed by incorporating 4-MBA on the surfaces [38–41]. However, their application for SERS detection has not been completely investigated. In this study, we investigated the application of SiO_2@Au@4-MBA@Ag NPs on pesticide detection.

2. Results and Discussion

To prepare SiO_2@Au@4-MBA, silica NPs (ca. 150 nm in diameter) were first functionalized with amine groups by 3-aminopropyltriethoxysilane (APTS) to prepare aminated silica NPs, as shown in Figure 1 [42]. Simultaneously, colloidal Au NPs (3 nm) were prepared using tetrakis(hydroxymethyl)phosphonium chloride (THPC) and incubated with the aminated silica NPs by gentle shaking to prepare Au NPs embedded with SiO_2 (SiO_2@Au NPs), according to the method reported by Pham et al. [38–41]. Subsequently, 4-MBA was introduced on the surface of SiO_2@Au NPs through the strong affinity between thiol groups and Au, and it was used as an internal standard. Finally, the Ag shell was deposited on SiO_2@Au@4-MBA to enhance the Raman signal of RLCs by reducing a silver precursor ($AgNO_3$) in the presence of ascorbic acid (AA) and polyvinylpyrrolidone (PVP) as a stabilizer and structure-directing agent under mild reducing conditions [39]. The silver ions reduced by AA were selectively grown onto SiO_2@Au@4-MBA cores to form the core-shell SiO_2@Au@4-MBA@Ag NPs; this was accompanied by an obvious color change to black. The presence of the Ag shell could also prevent the leakage of 4-MBA from the Au surface and improve the chance of generating numerous hot spots on the silica surface to detect the target molecules.

2.1. Characterizations of SiO_2@Au@4-MBA@Ag NPs

We investigated the characteristics and effect of 4-MBA on the generation of SiO_2@Au@4-MBA@Ag. Figure 2a shows the transmission electron microscopy (TEM) images of SiO_2@Au@4-MBA@Ag. It can be seen that the Ag shell was well coated on its surface. The surface of SiO_2 NPs was decorated with various small Ag NPs. From the TEM images, the average size of the SiO_2@Au@4-MBA@Ag NPs was determined to be 195 ± 10 nm (n = 90). The zeta potential was also used to confirm the presence of Au NPs (Figure 2b). SiO_2 NPs showed a zeta potential of −45 ± 0.1 mV. When the surface of the SiO_2 NP was incubated with APTS, the zeta potential of SiO_2@NH_2 increased to −28 ± 0.6 mV because of the positive property of the NH_2 groups. For all the NH_2 groups, the Au NPs were immobilized on the surface of SiO_2@NH_2 by electrostatic attraction. The surface of the Au NPs was stabilized by THPC; therefore, the zeta potential of SiO_2@Au decreased to −55 ± 6.1 mV. The sizes of SiO_2@Au@4-MBA@Ag NPs increased when the Ag shell was deposited, as shown in Figure 2. The UV-Vis (ultraviolet–visible) spectra of SiO_2@Au@4-MBA@Ag were consistent with the TEM images

(Figure 2b). The suspension of SiO_2 does not show its absorbance in the range of 300–1000 nm. Whereas the maximum peak of SiO_2@Au was at ~520 nm when the Au NPs were immobilized on the surface of SiO_2 NPs, the suspension of SiO_2@Au@4-MBA@Ag NPs showed a broadband from 320 to 800 nm. This indicated the generation of irregular structures in the Ag shell and the creation of hot-spot structures on the surface of SiO_2@Au@4-MBA@Ag NPs, producing a continuous spectrum of resonant multimode [38–41].

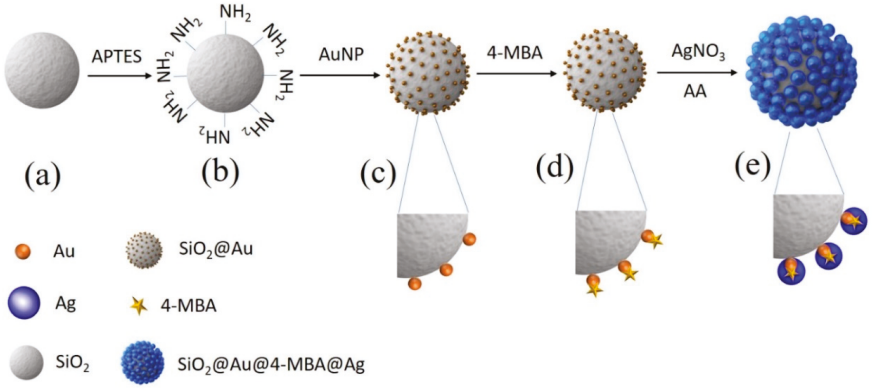

Figure 1. Illustration of preparation of Au@4-MBA@Ag embedded silica nanoparticles (SiO_2@Au@4-MBA@Ag NPs) for surface-enhanced Raman scattering probe. (**a**) Silica NP, (**b**) aminated silica NP, (**c**) Au NPs embedded silica NP, (**d**) Au NPs embedded silica NP incubated with 4-MBA (SiO_2@Au@4-MBA) and (**e**) SiO_2@Au@4-MBA coated with Ag shell by the reduction of silver nitrate in the presence of ascorbic acid and polyvinyl pyrrolidone.

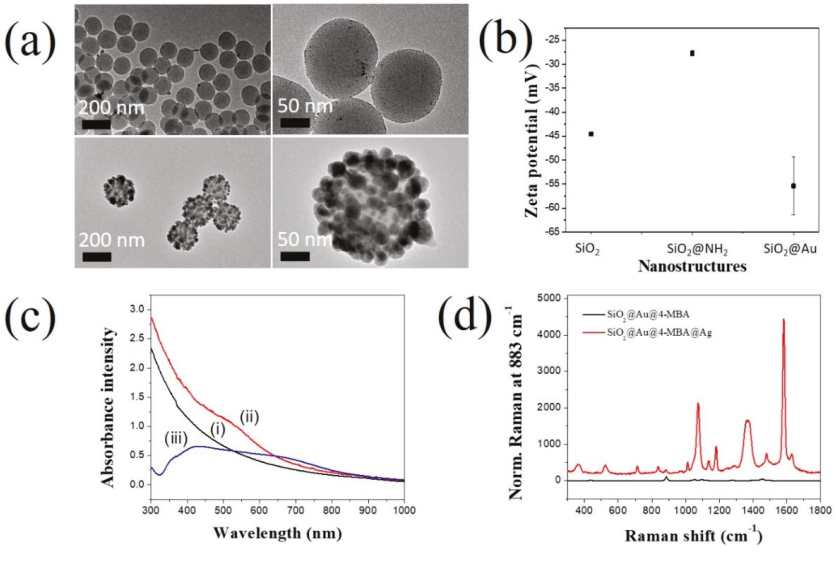

Figure 2. Characteristics of SiO_2@Au@4-MBA@Ag. (**a**) TEM images, (**b**) Zeta potential, (**c**) UV-Vis spectra of (i) 1000 μg/mL SiO_2, (ii) 1000 μg/mL SiO_2@Au@4-MBA, and (iii) 10 μg/mL SiO_2@Au@4-MBA@Ag, and (**d**) Raman spectra of SiO_2@Au@4-MBA and SiO_2@Au@4-MBA@Ag. Error bar represents the average value of three samples.

The Raman signals of SiO_2@Au@4-MBA@Ag NPs were also measured (Figure 2d). The signal of 4-MBA on the surface of SiO_2@Au NPs is unclear. In contrast, SiO_2@Au@4-MBA@Ag exhibited a considerably stronger SERS signal of 4-MBA than SiO_2@Au@4-MBA. In general, the bands of 4-MBA on the surface of SiO_2@Au@4-MBA@Ag were observed at 360, 520, 715, 838, 1012, 1074, 1137, 1180, 1362, 1480, and 1582 cm^{-1} in Figure 2d. For 4-MBA, the peak at about 1074 cm^{-1} was attributed to the aromatic ring vibration possessing the C–S stretching mode, the band at about 1582 cm^{-1} arose from the aromatic ring breathing mode. The less intense band at 1362 cm^{-1} and 840 cm^{-1} were the COO^- stretching mode. Other weak bands at 1137 cm^{-1} and 1179 cm^{-1} corresponding to the C–H deformation modes were also observed. This result is consistent with our previous report [40,41,43]. The reproducibility and repeatability of Raman signals of SiO_2@Au@4-MBA@Ag were showed in Figure S1. The sample was measured three times and repeated three times. The reproducibility and repeatability of Raman signals of SiO_2@Au@4-MBA@Ag were calculated to be 2.7 and 8.1%, respectively. This result was rapidly similar to the size distribution of SiO_2@Au@4-MBA@Ag by TEM analysis.

In addition, the effect of 4-MBA concentration on the SERS signal of SiO_2@Au@4-MBA@Ag NPs was investigated. As previously reported, the density of carboxyl groups on the surface of SiO_2@Au@4-MBA NPs affected the deposition of Ag shell on SiO_2@Au@4-MBA [35,36]. Therefore, the effect of 4-MBA concentration on the SERS signal of SiO_2@Au@4-MBA@Ag is considered in Figure 3. Various concentrations of 4-MBA in the range of 1–1000 μM were incubated with 100 μg of SiO_2@Au@4-MBA, followed by Ag shell deposition of 300 μM $AgNO_3$ in the presence of AA and PVP. All SiO_2@Au@4-MBA@Ag NPs at 4-MBA in the range of 1–1000 μM were coated with Ag shells, as shown in Figure 3a. The Ag shell appears to have been better deposited at low concentrations than high concentrations of 4-MBA. The presence of irregular structures on the Ag shell on the surface of SiO_2@Au@4-MBA@Ag NPs was also confirmed by UV–Vis spectroscopy with a broadband from 320 to 800 nm (Figure 3b). The SERS intensity of SiO_2@Au@4-MBA@Ag NPs for 1–1000 μM 4-MBA clearly differed. The SERS signal of 4-MBA at all bands in Figure 3d increased gradually and became saturated after 100 μM. Therefore, we chose the concentration of 4-MBA concentration as 100 μM for further studies.

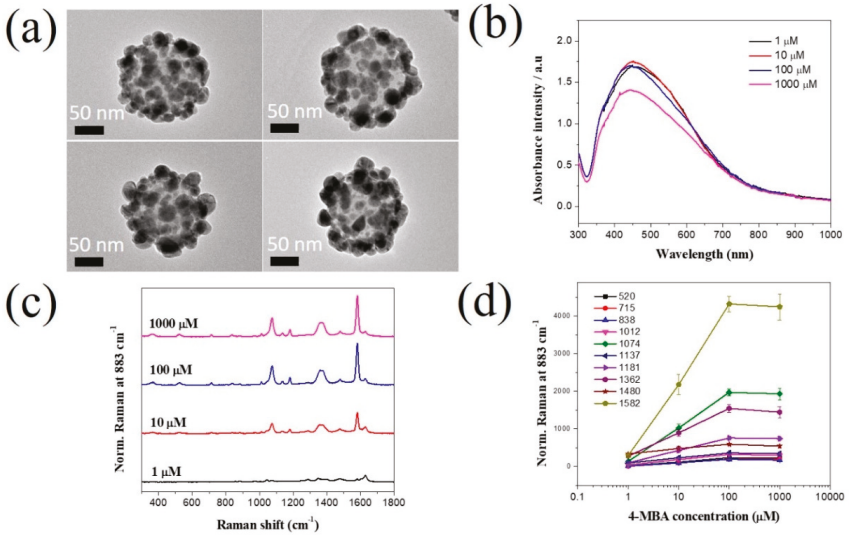

Figure 3. Effect of 4-MBA on SERS signal of SiO_2@Au@4-MBA@Ag NPs at different concentrations in the range of 1 μM–1000 μM. (**a**) TEM images, (**b**) UV-Vis spectra, (**c**) Raman spectra, and (**d**) Raman signal plot of SiO_2@Au@4-MBA@Ag. Error bar represents samples in triplicate.

2.2. Detection of Thiram by SiO_2@Au@4-MBA@Ag NPs

For the application, we chose thiram, a fungicide to prevent fungal diseases in seed and crops, as a pesticide sample in this study. Thiram is the simplest thiuram disulfide and the oxidized dimer of dimethyldithiocarbamate. In literature, the ratio of Raman intensity between a target molecule and an internal standard in quantitative SERS measurement provides more accurate information than the SERS signal of an intrinsic target molecule [31]. In our study, 4-MBA immobilized between the SiO_2@Au core and Ag shell was used as an internal standard to calculate the concentration of thiram. Figure S2 shows the SERS bands of SiO_2@Au@4-MBA@Ag NPs in the presence and absence of thiram. Dominant bands of SiO_2@Au@4-MBA@Ag were observed at 360, 520, 715, 838, 1012, 1074, 1137, 1180, 1362, 1480, and 1582cm^{-1}. When thiram was adsorbed on the surface of SiO_2@Au@4-MBA@Ag NPs, the SERS bands of thiram-incubated SiO_2@Au@4-MBA@Ag NPs was observed at 360, 444, 520, 560, 715, 838, 881, 936, 1015, 1074, 1137, 1181, 1381, 1448, 1480, 151, 1582 cm^{-1}. Thus, several new bands were obtained at 440, 560, 931, 1146, 1381, and 1512 cm^{-1}. According to a previous report by Kang et al., SERS bands of thiram on the Ag surface was observed at 342, 446, 564, 870, 928, 1150, 1386, 1444, 1514 cm^{-1} [25]. Therefore, these bands were attributed to the characteristic bands of thiram [25,41]. The SERS bands of thiram and 4-MBA were partially overlapped; therefore, the SERS signals of thiram-incubated SiO_2@Au@4-MBA@Ag NPs at 360, 881, 1074, 1137, 1181, 1381, 1582 cm^{-1} increased comparing to those of SiO_2@Au@4-MBA@Ag NPs. To calculate the concentration of thiram, the ratio of Raman intensity of bands at 520 cm^{-1} and 560 cm^{-1} were chosen as the characteristic bands of 4-MBA and thiram, respectively.

2.2.1. Optimization of Thiram Detection by SiO_2@Au@4-MBA@Ag NPs

Effect of Employed Power Energy and Laser Lines

In the literature, the power energy has been considered an important factor affecting the SERS signal of target molecules. Therefore, we examined the effect of employed power energy on the SERS signal of thiram detection in the range of 2–10 mW (Figure S3). The SERS intensities of both SiO_2@Au@4-MBA@Au in the presence or absence of thiram increased with the employed power energy. We chose the employed power of 10 mW to detect thiram for further studies. In order to investigate the effect of laser lines on the SERS signal of thiram, we also measured the Raman intensity of thiram-incubated SiO_2@Au@4-MBA@Ag at the laser lines of 532 and 780 nm. As showed in Figure S4 the Raman bands of thiram-incubated SiO_2@Au@4-MBA@Ag using the laser line of 780 nm were broadened and unclear while those using the laser line of 532 nm was clearly obtained. Although UV-Vis absorbance might not be proportionally related to the strength of the SERS signal intensity, when that wavelength of the laser is irradiated to particle, the particles will absorb the laser energy well and it is likely to be connected to a strong SERS signal. Since we have 532 nm wavelength of the laser and the materials well absorbed the 300 nm to 650 nm wavelength with the maximum absorption peak at ~450 nm, we chose the laser line of 532 nm for Raman measurement.

Effect of Target Volume

Other than the power energy of the Raman equipment, the SERS signal was affected by various conditions of the nanomaterials or target concentration. We obtained the SERS signal of SiO_2@Au@4-MBA@Au incubated with various volumes and concentrations of thiram; the results are shown in Figure 4a. The SERS signal at different concentrations of thiram (100, 500, and 1000 μL) was incubated with 20 μg of SiO_2@Au@4-MBA@Ag. The ratio of SERS intensity between 4-MBA and thiram measured by the SERS signal of thiram in the range of 1–100 μM is shown in Figure 4. In Figure 4a, the SERS band ratios of thiram at 560 and 520 cm^{-1} were proportional to the thiram concentration at all thiram volumes. However, the behavior of thiram for each specific volume varied with the concentration. At 100 μL thiram, the SERS band of thiram began increasing at 5 μM, while this ratio increased immediately at 1 μM when 500 μL and 1000 μL thiram were incubated. In addition,

the SERS signal of thiram was almost balanced very early at 5 μM, when 1000 μL thiram was utilized. This is because the quantities of thiram at each volume changed with the thiram concentration, while the surface area of SiO_2@Au@4-MBA@Ag was constant (20 μg). We found that when 100 μL of 5 μM thiram or 500 μL of 1 μM thiram was utilized, the quantity of thiram was calculated to be 0.5 nmol, and the SERS signal of thiram can be observed at 0.5 nm. The SERS signal of thiram was balanced at 5 nmol. The SERS signal of thiram increased steadily and slowly at 500 μM thiram; hence, we chose 500 μL of thiram for further studies.

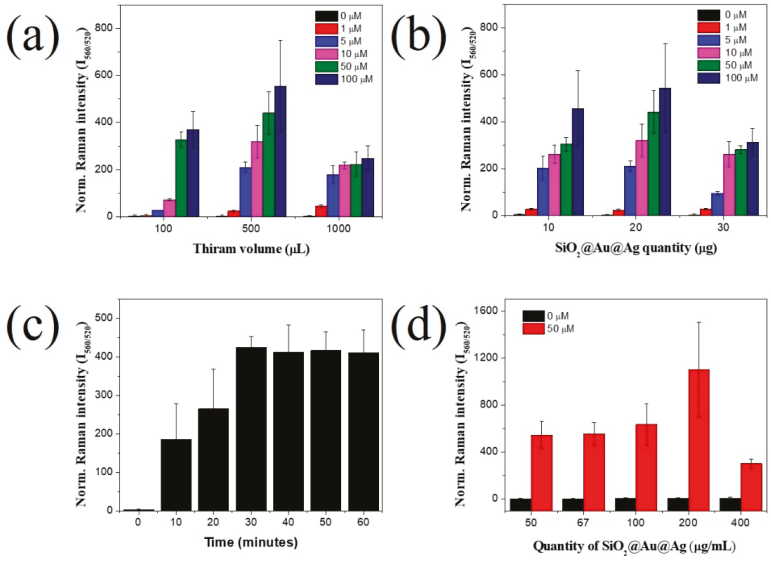

Figure 4. Effect of (**a**) thiram volume, (**b**) quantity of SiO_2@Au@4-MBA@Ag, (**c**) incubation time, and (**d**) dilution of SiO_2@Au@4-MBA@Ag nanoparticles in the presence of 50 uM thiram. Error bar represents the triplicates of samples.

Effect of Quantity of SiO_2@Au@4-MBA@Ag NPs

The effect of SiO_2@Au@4-MBA@Ag quantity is also considered in Figure 4. SiO_2@Au@4-MBA@Ag amounts of 10, 20, and 30 μg were incubated with 500 μL thiram at 1 to 100 μM thiram, and the results are shown in Figure 4b. For the same concentration of thiram, the greater the amount of SiO_2@Au@4-MBA@Ag added to the thiram solution acting as a substrate for thiram detection, the lower the SERS signal of thiram (Figure 4b). It is well known that the efficiency of SERS depends on the density of the target on the surface of nanomaterials [19]. Therefore, when a greater amount of SiO_2@Au@4-MBA@Ag was added, more hot spots were available on the surface of SiO_2@Au@4-MBA@Ag, generating numerous detection sites for thiram, meanwhile, the quantity of thiram was constant. Thus, the density of thiram at the gap or on the surface of SiO_2@Au@4-MBA@Ag decreased, resulting in decreased enhancement of the thiram intensity between two adjacent Au@4-MBA@Ag NPs on the surface of SiO_2@Au@4-MBA@Ag (Figure 4c) [33]. As a result, the intensity of thiram-incubated SiO_2@Au@4-MBA NPs decreased (Figure 4b). For the same concentration of thiram, the greater the amount of SiO_2@Au@4-MBA added, the larger the gap between Au@4-MBA@Ag NPs (Figure 4a).

Effect of Incubation Time of Thiram

Incubation is an important factor that affects the adsorption of target molecules onto the surface of a nanomaterial. Thus, the effect of thiram incubation time on the SERS signal is shown in Figure 4c.

The SERS intensity of thiram-incubated SiO_2@Au@4-MBA@Ag was proportional to the incubation time, and the highest value was achieved at 30 min. The result indicated that thiram was absorbed efficiently on the surface of SiO_2@Au@4-MBA@Ag because of the thiol groups.

Effect of Concentration of Thiram Incubated SiO_2@Au@4-MBA@Ag

According to a previous report, the density of nanomaterials significantly affected the SERS signal. Figure 4d shows the effect of thiram-incubated SiO_2@Au@4-MBA@Ag concentration on the SERS signal of thiram. In the absence of thiram, the SERS signal of SiO_2@Au@4-MBA@Ag NP suspension was insignificantly different; meanwhile, in the presence of thiram, the SERS signal of SiO_2@Au@4-MBA@Ag NPs increased slowly from 50 μg/mL to 100 μg/mL and achieved the highest value at 200 μg/mL. For concentrations greater than 200 μg/mL, the SERS signal of the thiram-incubated SiO_2@Au@4-MBA@Ag NP suspension decreased sharply owing to the low diffraction of the suspension.

2.2.2. Detection of Thiram by SiO_2@Au@4-MBA@Ag NPs

We measured SERS signals at various concentrations of thiram, in the range of 240–24,000 ppb, with 20 μg of the SiO_2@Au@4-MBA@Ag. The bands at 520 cm^{-1} and 560 cm^{-1} were chosen as the characteristic bands of 4-MBA and thiram, respectively. The SERS intensity of thiram at 560 cm^{-1} and the ratios of the Raman intensity of thiram to that of 4-MBA are shown in Figure 5. In Figure 5a, the SERS intensity at 560 cm^{-1} increased with the increase in a thiram concentration lower than 2400 ppb. Whereas the SERS intensity ratio at 560 cm^{-1} and 520 cm^{-1} increased proportionally with the increase in thiram concentration lower than 12,000 ppb (Figure 5b). The calibration curves of thiram showed a linear dependence ($y = 0.344 \times C + 6.625$; $R^2 = 0.95$ (C = thiram concentration, y is SERS signal value on y-axis in Figure 5c)) between the SERS intensity ratio and thiram concentration between 240 ppb and 2400 ppb. The limit of detection of thiram was determined to be 72 ppb (S/N (signal to noise ratio) = 3), which is considerably lower than 288.5 ppb, as in our report [35], and the limit of the detection value is lower than the maximal residue limit recommended by the US (7 ppm) and Canada (0.1 ppm) [44,45].

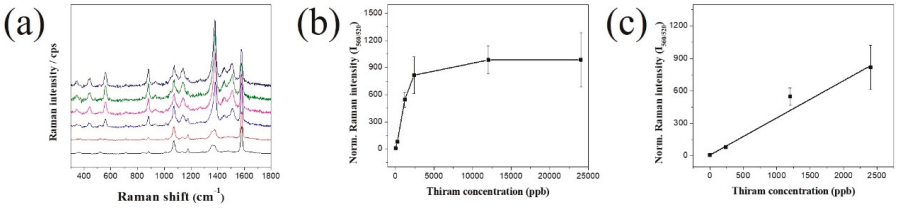

Figure 5. (**a**) Raman signal (different lines from bottom to top represents different thiram concentration: 0, 240, 1200, 2400, 12,000 and 24,000 ppb) and (**b**) Raman intensity ratio at 560 and 520 cm^{-1} and (**c**) calibration curves of thiram-incubated SiO_2@Au@4-MBA@Ag NPs at various concentrations of thiram from 0 to 24,000 ppb. The dynamic linear range of 240 to 2400 ppb with the limit of detection of 72 ppb. Error bar represents an average value of five samples.

3. Materials and Methods

3.1. Chemicals and Reagents

Tetraethylorthosilicate (TEOS), APTS, silver nitrate ($AgNO_3$), chloroauric acid ($HAuCl_4$), THPC, 4-mercaptobenzoic acid (4-MBA), AA, PVP, and thiram were purchased from Sigma-Aldrich (St. Louis, MO, USA) and used without further purification. Ethyl alcohol (EtOH) and aqueous ammonium hydroxide (NH_4OH, 27%) were purchased from Daejung (Siheung, Korea). Ultrapure water (18.2 MΩ cm) was produced using a Millipore water purification system (EXL Water purification, Vivagen Co.,

Ltd., Seongnam, South Korea). Thiram: the toxicity class WHO III (LD_{50} for rabbits >210 mg/kg, Inhalation LC_{50} (4 h) for rats 4.42 mg/kg) [46].

3.2. Preparation of SiO_2@Au@4-MBA

In a previous report, Pham et al. revealed that the SiO_2@Au@Ag NPs possessed a relatively high Raman enhancement effect [38–41]. Au NPs assembled silica nanoparticles (SiO2@Au NPs) were prepared by incubating the Au NP suspension with aminated silica NPs overnight. Subsequently, 1 mL of 100 μM 4-MBA solution in EtOH was added to SiO_2@Au (1.0 mg), and the suspension was stirred vigorously for 1 h at room temperature. The colloids were centrifuged and washed several times with EtOH. The NPs were re-dispersed in 1.0 mL absolute EtOH to obtain 1 mg/mL SiO_2@Au NPs modified with 4-MBA (SiO_2@Au@4-MBA).

3.3. Preparation of SiO_2@Au@4-MBA@Ag NPs

Au@4-MBA@Ag NPs assembled silica NPs were prepared in an aqueous medium via the reduction and deposition of Ag using ascorbic acid onto SiO_2@Au@4-MBA NPs in a polyvinylpyrrolidone (PVP) environment. Briefly, 200 μL of 200 μg/μL SiO_2@Au@4-MBA was dispersed in 9.8 mL of water containing 10 mg PVP, which was kept still for 30 min. Then, 20 μL of 10 mM silver nitrate was added to the suspension, followed by the addition of 20 μL of 10 mM ascorbic acid. This suspension was incubated for 15 min to completely reduce the Ag^+ ions to Ag. The reduction steps were repeated to obtain the desired $AgNO_3$ concentration. SiO_2@Au@4-MBA@Ag NPs were obtained by centrifuging the suspension at 8500 rpm for 15 min, and the NPs were washed several times with EtOH to remove excess reagent. SiO_2@Au@4-MBA@Ag NPs were re-dispersed in 1 mL of absolute EtOH to obtain a 200 μg/mL SiO_2@Au@4-MBA@Ag NP suspension.

3.4. Thiram Detection

To absorb thiram on the surface of SiO_2@Au@4-MBA NPs, 500 μL of 50 μM thiram solution was incubated with 500 μL of 200 μg/mL SiO_2@Au@4-MBA@Ag NPs suspension for 30 min, followed by centrifugation for 15 min at 13,000 rpm to collect the colloids. The prepared NPs were washed several times with EtOH to remove excess reagent. SiO_2@Au@4-MBA@Ag@thiram NPs was re-dispersed in 500 μL of absolute EtOH to obtain a 200 μg/mL SiO_2@Au@4-MBA@Ag@thiram NP suspension.

3.5. SERS Measurement of SiO_2@Au@4-MBA@Ag@thiram

To obtain the surface-enhanced Raman spectrum, the obtained colloids suspensions were measured in a capillary tube. SERS signals were measured using a micro-Raman system with a 532 nm laser excitation source and equipped with an optical microscope (BX41, Olympus, Tokyo, Japan). The SERS signals were collected in a back-scattering geometry using a ×10 objective lens (0.90 NA, Olympus, Shinjuku, Tokyo, Japan). A 532 nm diode-pumped solid-state laser was used as a photo-excitation source, exerting a laser power of 10 mW at the sample. The selected sites were measured randomly, and all SERS spectra were integrated for 5 s. The size of the laser beam spot was approximately 2.0 μm. The SERS spectrum was obtained in the 300–2000 cm^{-1} wavenumber range.

4. Conclusions

We successfully prepared SiO_2@Au@4-MBA@Ag nanomaterials and optimized their conditions for thiram detection. The presence of Au@4-MBA@Ag alloys on the surface of SiO_2 was confirmed by the broad bands in the range of 320 to 800 nm, indicating the generation of bumpy structures on the the Ag shell. The effect of 4-MBA concentration on the SERS signal of SiO_2@Au@4-MBA@Ag NPs was studied. The SERS signal of 4-MBA increased gradually for concentrations under 100 μM. For thiram detection, SiO_2@Au@4-MBA@Ag exhibited a stronger SERS signal of 4-MBA at 360, 520, 715, 838, 1012, 1074, 1137, 1362, 1480, and 1582 cm^{-1}. Meanwhile, several new bands of thiram were obtained at 440,

560, 931, 1146, 1381, and 1512 cm^{-1} when thiram was adsorbed on the surface of SiO_2@Au@4-MBA@Ag NPs. Additionally, the SERS intensities of both SiO_2@Au@4-MBA@Au increased with the employed power energy from 2 to 10 mW. The SERS intensity of the thiram incubated SiO_2@Au@4-MBA@Ag achieved the highest value via incubation with 500 µL thiram for 30 min and measuring SERS at 200 µg/mL SiO_2@Au@4-MBA@Ag. Finally, the SERS intensity of the thiram at 560 cm^{-1} increased proportionally with the increase in thiram concentration in the range of 240 to 2400 ppb with a LOD of 72 ppb. This study provides a thorough understanding of thiram detection, which supports further research and development for strong and reliable SERS probes based on SiO_2@Au@4-MBA@Ag NPs.

Supplementary Materials: Supplementary Materials can be found at http://www.mdpi.com/1422-0067/20/19/4841/s1.

Author Contributions: X.-H.P. and B.-H.J. conceived and designed the experiments; X.-H.P., E.H., H.-M.K., and B.S.S. performed the experiments; X.-H.P., K.-H.H. and E.H. analyzed the data; D.H.J. contributed reagents/materials/analysis tools; X.-H.P. and B.-H.J. wrote the paper; D.H.J. and B.-H.J. supervised.

Funding: This work was supported by the KU Research Professor Program of Konkuk University and funded by Science, ICT & Future Planning (NRF 2016M3A9B6918892) and the Korean Health Technology R&D Project, Ministry of Health & Welfare (HI17C1264).

Conflicts of Interest: The authors declare no conflict of interest. The funders had no role in the design of the study; in the collection, analyses, or interpretation of data; in the writing of the manuscript, or in the decision to publish the results.

References

1. Kumar, P.; Kim, K.-H.; Deep, A. Recent advancements in sensing techniques based on functional materials for organophosphate pesticides. *Biosens. Bioelectron.* **2015**, *70*, 469–481. [CrossRef]
2. Chrimes, A.F.; Khashayar, K.; Paul, R.S.; Arnan, M.; Kourosh, K. Microfluidics and Raman microscopy: Current applications and future challenges. *Chem. Soc. Rev.* **2013**, *42*, 5880–5906. [CrossRef] [PubMed]
3. Chen, L.; Choo, J. Recent advances in surface-enhanced Raman scattering detection technology for microfluidic chips. *ELECTROPHORESIS* **2008**, *29*, 1815–1828. [CrossRef] [PubMed]
4. Damalas, C.A.; Khan, M. Pesticide use in vegetable crops in Pakistan: Insights through an ordered probit model. *Crop Prot.* **2017**, *99*, 59–64. [CrossRef]
5. Johnson, M.K. Trends in Pharmacological Sciences. In *Handbook of Pesticide Toxicology, Vols 1, 2 and 3*; Krieger, R.I., Krieger, W.C., Eds.; Elsevier: Amsterdam, The Netherlands, 1991; Volume 12, pp. 277–278.
6. Gunnell, D.; Eddleston, M.; Phillips, M.R.; Konradsen, F. The global distribution of fatal pesticide self-poisoning: Systematic review. *BMC Public Health* **2007**, *7*, 357. [CrossRef]
7. Sánchez-Cortés, S.; Domingo, C.; García-Ramos, J.V.; Aznárezet, J.A. Surface-Enhanced Vibrational Study (SEIR and SERS) of Dithiocarbamate Pesticides on Gold Films. *Langmuir* **2001**, *17*, 1157–1162. [CrossRef]
8. Ferrer, C.; Lozano, A.; Uclés, S.; Valverde, A.; Fernández-Alba, A.R. European Union proficiency tests for pesticide residues in fruit and vegetables from 2009 to 2016: Overview of the results and main achievements. *Food Control* **2017**, *82*, 101–113. [CrossRef]
9. Sherma, J. Review of thin-layer chromatography in pesticide analysis: 2014–2016. *J. Liq. Chromatogr. Relat. Technol.* **2017**, *40*, 226–238.
10. Watanabe, E.; Miyake, S.; Ito, S.; Baba, K.; Eun, H.; Ishizaka, M.; Endo, S. Reliable enzyme immunoassay detection for chlorothalonil: Fundamental evaluation for residue analysis and validation with gas chromatography. *J. Chromatogr. A* **2006**, *1129*, 273–282. [CrossRef] [PubMed]
11. Kutsanedzie, F.Y.H.; Hao, L.; Yan, S.; Ouyang, Q.; Chen, Q. Near infrared chemo-responsive dye intermediaries spectra-based in-situ quantification of volatile organic compounds. *Sens. Actuators B: Chem.* **2018**, *254*, 597–602. [CrossRef]
12. Chen, Q.; Zhang, C.; Zhao, J.; Ouyang, Q. Recent advances in emerging imaging techniques for non-destructive detection of food quality and safety. *Trac Trends Anal. Chem.* **2013**, *52*, 261–274. [CrossRef]
13. Kutsanedzie, F.Y.H.; Chen, Q.; Hassan, M.M.; Yang, M.; Sun, H.; Rahman, M.H. Near infrared system coupled chemometric algorithms for enumeration of total fungi count in cocoa beans neat solution. *Food Chem.* **2018**, *240*, 231–238. [CrossRef]

14. Sun, F. Analytical methods and recent developments in the detection of melamine. *Trac Trends Anal. Chem.* **2010**, *29*, 1239–1249. [CrossRef]
15. Zheng, J.; He, L. Surface-Enhanced Raman Spectroscopy for the Chemical Analysis of Food. *Compr. Rev. Food Sci. Food Saf.* **2014**, *13*, 317–328. [CrossRef]
16. Schlücker, S. Surface-Enhanced Raman Spectroscopy: Concepts and Chemical Applications. *Angew. Chem. Int. Ed.* **2014**, *53*, 4756–4795. [CrossRef]
17. Wang, Y.; Yan, B.; Chen, L. SERS Tags: Novel Optical Nanoprobes for Bioanalysis. *Chem. Rev.* **2013**, *113*, 1391–1428. [CrossRef] [PubMed]
18. Culha, M.; Klutse, B.; Lavrik, N.; Klutse, C.K. Surface-Enhanced Raman Scattering as an Emerging Characterization and Detection Technique. *J. Nanotechnol.* **2012**, *2012*, 971380. [CrossRef]
19. Jun, B.-H.; Kim, G.; Jeong, S.; Noh, M.S. Silica Core-based Surface-enhanced Raman Scattering (SERS) Tag: Advances in Multifunctional SERS Nanoprobes for Bioimaging and Targeting of Biomarkers#. *Bull. Korean Chem. Soc.* **2015**, *36*, 963–978.
20. Goodacre, R.; Graham, D.; Faulds, K. Recent developments in quantitative SERS: Moving towards absolute quantification. *Trends Anal. Chem.* **2018**, *102*, 359–368. [CrossRef]
21. Dies, H.; Siampani, M.; Escobedo, C.; Docoslis, A. Direct Detection of Toxic Contaminants in Minimally Processed Food Products Using Dendritic Surface-Enhanced Raman Scattering Substrates. *Sensors* **2018**, *18*, 2726. [CrossRef] [PubMed]
22. Dao, T.C.; Luong, T.Q.N.; Cao, T.A.; Kieu, N.M. High-sensitive SERS detection of thiram with silver nanodendrites substrate. *Adv. Nat. Sci. Nanosci. Nanotechnol.* **2019**, *10*, 025012. [CrossRef]
23. Wei, W.; Du, Y.; Zhang, L.; Yang, Y.; Gao, Y. Improving SERS hot spots for on-site pesticide detection by combining silver nanoparticles with nanowires. *J. Mater. Chem. C* **2018**, *6*, 8793–8803. [CrossRef]
24. Sun, H.; Liu, H.; Wu, Y. A green, reusable SERS film with high sensitivity for in-situ detection of thiram in apple juice. *Appl. Surf. Sci.* **2017**, *416*, 704–709. [CrossRef]
25. Kang, J.-S.; Hwang, S.Y.; Lee, C.-J.; Lee, M.-S. SERS of Dithiocarbamate Pesticides Adsorbed on Silver Surface; Thiram. *Bull. Korean Chem. Soc.* **2002**, *23*, 1604–1610.
26. Sánchez-Cortés, S.; Vasina, M.; Francioso, O.; García-Ramos, J.V. Raman and surface-enhanced Raman spectroscopy of dithiocarbamate fungicides. *Vib. Spectrosc.* **1998**, *17*, 133–144. [CrossRef]
27. Yu, Y.; Zeng, P.; Yang, C.; Gong, J.; Liang, R.; Qu, Q.; Zhang, S. Gold-Nanorod-Coated Capillaries for the SERS-Based Detection of Thiram. *Acs Appl. Nano Mater.* **2019**, *2*, 598–606. [CrossRef]
28. Chen, M.; Luo, W.; Liu, Q.; Hao, N.; Zhu, Y.; Liu, M.; Wang, L.; Yang, H.; Chen, X. Simultaneous In Situ Extraction and Fabrication of Surface-Enhanced Raman Scattering Substrate for Reliable Detection of Thiram Residue. *Anal. Chem.* **2018**, *90*, 13647–13654. [CrossRef] [PubMed]
29. Zhao, Y.; Newton, J.N.; Liu, J.; Wei, A. Dithiocarbamate-Coated SERS Substrates: Sensitivity Gain by Partial Surface Passivation. *Langmuir* **2009**, *25*, 13833–13839. [CrossRef] [PubMed]
30. Saute, B.; Premasiri, R.; Ziegler, L.; Narayanan, R. Gold nanorods as surface enhanced Raman spectroscopy substrates for sensitive and selective detection of ultra-low levels of dithiocarbamate pesticides. *Analyst* **2012**, *137*, 5082–5087. [CrossRef]
31. Atanasov, P.A.; Nedyalkov, N.N.; Fukata, N.; Jevasuwan, W.; Subramani, T.; Terakawa, M.; Nakajima, Y. Surface-Enhanced Raman Spectroscopy (SERS) of Mancozeb and Thiamethoxam Assisted by Gold and Silver Nanostructures Produced by Laser Techniques on Paper. *Appl. Spectrosc.* **2019**, *73*, 313–319. [CrossRef]
32. Lai, H.; Xu, F.; Zhang, Y.; Wang, L. Recent progress on graphene-based substrates for surface-enhanced Raman scattering applications. *J. Mater. Chem. B* **2018**, *6*, 4008–4028. [CrossRef]
33. Zhu, C.; Wang, X.; Shi, X.; Yang, F.; Meng, G.; Xiong, Q.; Ke, Y.; Wang, H.; Lu, Y.; Wu, N. Detection of Dithiocarbamate Pesticides with a Spongelike Surface-Enhanced Raman Scattering Substrate Made of Reduced Graphene Oxide-Wrapped Silver Nanocubes. *Acs Appl. Mater. Interfaces* **2017**, *9*, 39618–39625. [CrossRef] [PubMed]
34. Shen, W.; Lin, X.; Jiang, C.; Li, C.; Lin, H.; Huang, J.; Wang, S.; Liu, G.; Yan, X.; Zhong, Q. Reliable Quantitative SERS Analysis Facilitated by Core–Shell Nanoparticles with Embedded Internal Standards. *Angew. Chem. Int. Ed.* **2015**, *54*, 7308–7312. [CrossRef] [PubMed]
35. Kammer, E.; Olschewski, K.; Bocklitz, T.; Rosch, P.; Weber, K.; Cialla, D.; Popp, J. A new calibration concept for a reproducible quantitative detection based on SERS measurements in a microfluidic device demonstrated on the model analyte adenine. *Phys. Chem. Chem. Phys.* **2014**, *16*, 9056–9063. [CrossRef]

36. Zhou, Y.; Ding, R.; Joshi, P.; Zhang, P. Quantitative surface-enhanced Raman measurements with embedded internal reference. *Anal. Chim. Acta* **2015**, *874*, 49–53. [CrossRef] [PubMed]
37. Zhang, X.-Q.; Li, S.-X.; Chen, Z.-P.; Chen, Y.; Yu, R.-Q. Quantitative SERS analysis based on multiple-internal-standard embedded core-shell nanoparticles and spectral shape deformation quantitative theory. *Chemom. Intell. Lab. Syst.* **2018**, *177*, 47–54. [CrossRef]
38. Pham, X.-H.; Lee, M.; Shim, S.; Jeong, S.; Kim, H.-M.; Hahm, E.; Lee, S.H.; Lee, Y.-S.; Jeong, D.H.; Jun, B.-H. Highly sensitive and reliable SERS probes based on nanogap control of a Au-Ag alloy on silica nanoparticles. *RSC Adv.* **2017**, *7*, 7015–7021. [CrossRef]
39. Shim, S.; Pham, X.-H.; Cha, M.G.; Lee, Y.-S.; Jeong, D.H.; Jun, B.-H. Size effect of gold on Ag-coated Au nanoparticle-embedded silica nanospheres. *RSC Adv.* **2016**, *6*, 48644–48650. [CrossRef]
40. Pham, X.-H.; Hahm, E.; Kang, E.; Ha, Y.N.; Lee, S.H.; Rho, W.-Y.; Lee, Y.-S.; Jeong, D.H.; Jun, B.-H. Gold-silver bimetallic nanoparticles with a Raman labeling chemical assembled on silica nanoparticles as an internal-standard-containing nanoprobe. *J. Alloy. Compd.* **2019**, *779*, 360–366. [CrossRef]
41. Pham, X.-H.; Hahm, E.; Kang, E.; Son, B.S.; Ha, Y.; Kim, H.-M.; Jeong, D.H.; Jun, B.-H. Control of Silver Coating on Raman Label Incorporated Gold Nanoparticles Assembled Silica Nanoparticles. *Int. J. Mol. Sci.* **2019**, *20*, 1258. [CrossRef]
42. Stöber, W.; Fink, A.; Bohn, E. Controlled growth of monodisperse silica spheres in the micron size range. *J. Colloid Interface Sci.* **1968**, *26*, 62–69. [CrossRef]
43. Michota, A.; Bukowska, J. Surface-enhanced Raman scattering (SERS) of 4-mercaptobenzoic acid on silver and gold substrates. *J. Raman Spectrosc.* **2003**, *34*, 21–25. [CrossRef]
44. Environmental Protection Agency (EPA). *Reregistration Eligibility Decision for Thiram*; EPA 738-R-04-012; Agency, U.S.E.P.: Washington, DC, USA, 2004; p. 278.
45. Pest Management Regulatory Agency. *Proposed Maximum Residue Limit Ferbam, Thiram and Ziram*; Pest Management Regulatory Agency Health Canada: Ottawa, ON, Cananda, 2019; p. 8.
46. Sharma, V.K.; Aulakh, J.S.; Malik, A.K. Thiram: Degradation, applications and analytical methods. *J. Environ. Monit.* **2003**, *5*, 717–723. [CrossRef] [PubMed]

International Journal of
Molecular Sciences

MDPI

Review

Synthesis and Application of Silver Nanoparticles (Ag NPs) for the Prevention of Infection in Healthcare Workers

Shingo Nakamura [1,*], Masahiro Sato [2], Yoko Sato [1], Naoko Ando [1], Tomohiro Takayama [3], Masanori Fujita [4] and Masayuki Ishihara [1]

1 Division of Biomedical Engineering, National Defense Medical College Research Institute, Saitama 359-8513, Japan
2 Section of Gene Expression Regulation, Frontier Science Research Center, Kagoshima University, Kagoshima 890-8544, Japan
3 Department of Oral and Maxillofacial Surgery, National Defense Medical College Hospital, Saitama 359-8513, Japan
4 Division of Environmental Medicine, National Defense Medical College Research Institute, Saitama 359-8513, Japan
* Correspondence: snaka@ndmc.ac.jp; Tel.: +81-4-2995-1211

Received: 26 June 2019; Accepted: 23 July 2019; Published: 24 July 2019

Abstract: Silver is easily available and is known to have microbicidal effect; moreover, it does not impose any adverse effects on the human body. The microbicidal effect is mainly due to silver ions, which have a wide antibacterial spectrum. Furthermore, the development of multidrug-resistant bacteria, as in the case of antibiotics, is less likely. Silver ions bind to halide ions, such as chloride, and precipitate; therefore, when used directly, their microbicidal activity is shortened. To overcome this issue, silver nanoparticles (Ag NPs) have been recently synthesized and frequently used as microbicidal agents that release silver ions from particle surface. Depending on the specific surface area of the nanoparticles, silver ions are released with high efficiency. In addition to their bactericidal activity, small Ag NPs (<10 nm in diameter) affect viruses although the microbicidal effect of silver mass is weak. Because of their characteristics, Ag NPs are useful countermeasures against infectious diseases, which constitute a major issue in the medical field. Thus, medical tools coated with Ag NPs are being developed. This review outlines the synthesis and utilization of Ag NPs in the medical field, focusing on environment-friendly synthesis and the suppression of infections in healthcare workers (HCWs).

Keywords: antiviral property; healthcare workers (HCWs); medical application; microbicidal property; silver nanoparticles (Ag NPs); cytotoxicity

1. Introduction

Silver is widely used in industrial applications because of its metallic properties, such as conductivity, and in the medical field due to its antimicrobial effect [1]. Silver shows antibacterial activity against various organisms, and this effect is observed even at low concentrations [2]. Berger et al. reported that the growth of *Escherichia coli* (*E. coli*), *Staphylococcus*, *Providencia*, *Serratia*, and *Pseudomonas aeruginosa* is inhibited by the presence of ~1 μg/mL silver ions [1]. Ip et al. reported that several wound-coating materials (wound dressings) that contain silver exert an antibacterial effect against methicillin-resistant *Staphylococcus aureus* (MRSA) [2]. The antibacterial activity of silver is mainly attributed to silver ions, which are released from a silver-containing substance and interact with the thiol groups of enzymes and proteins that support bacterial life, thus affecting cell respiration and killing the cells [3]. When halide ions, such as chloride, are present in the environment, silver ions bind to them and precipitate, losing their water solubility and antibacterial activity. Therefore, the antibacterial activity of

free silver ions is very short when they are used alone [4]. To overcome this issue, silver nanoparticles (Ag NPs) [5], silver-containing fine glass particles [6], and Ag NPs/chitin or chitosan complexes [7–9] have recently been developed. From these compounds, silver ions are gradually released, thereby causing antimicrobial activity.

For a metallic particle to be considered as "nano", its size must be within 1–100 nm [10]. Metallic nanoparticles exhibit specific properties, such as surface plasmon resonance [11]. Such particles have been used for glass decoration because of their specific vivid color, e.g., red from gold nanoparticles and yellow from Ag NPs. In addition, nanoparticles have a large specific surface area with a small amount of metal mass [5]. Metal nanoparticles are commonly synthesized via the reduction of metal salts in a solution [12] or the formation of metal atom aggregates by the heating or vaporization of a metal in inert gas or vacuum [13]. Size-controlled Ag NPs are also synthesized using new environment-friendly synthesis techniques [14]. The surface of Ag NPs in an aqueous environment is oxidized in the presence of oxygen and protons, and silver ions are released as the surface dissolves. Thus, the effective silver ion concentration is maintained in the solution, and the antimicrobial effect will last for a long time [5].

Various applications have been found in the medical field for Ag NPs; for example, they can be used for biosensors, drug delivery systems, and medical devices [15–17]. Because of their wide antibacterial and antiviral spectrum, there are particularly high expectations for the suppression of multidrug-resistant bacteria. For example, Ag NPs are combined with a cationic polymer to produce a bactericidal material. Ag NPs have good applicability and are easily processed because of their low melting point [18]. This review describes representative methods used for synthesizing Ag NPs, focusing on environment-friendly synthesis, their effect on microorganisms and viruses, and their application to medical devices, particularly the suppression of infections in both patients and healthcare workers (HCWs).

2. Synthesis of Ag NPs

Ag NPs have been synthesized using various methods, which can be classified as gas or aerosol, solid, and liquid-phase routes (Figure 1). Both chemical and physical synthesis methods for Ag NPs are well known [19]. In recent years, green synthetic pathways have also been proposed [20]. These green processes reduce the generation of harmful byproducts that damage the environment. They also allow for an efficient resource-saving synthesis.

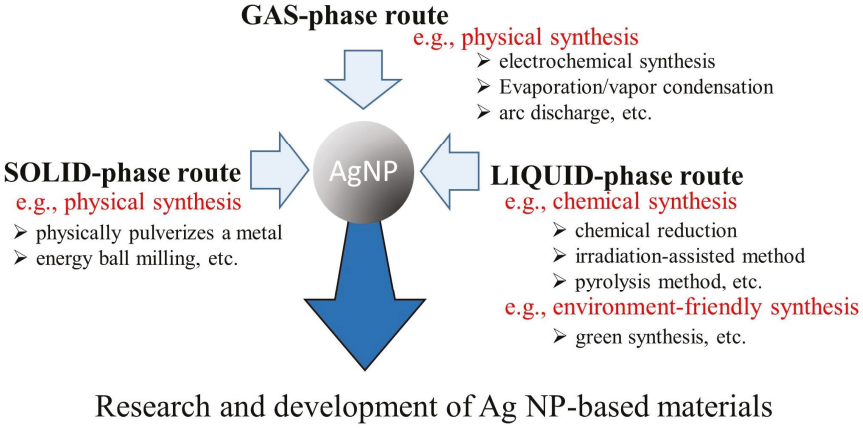

Figure 1. Various methods for silver nanoparticle (Ag NP) synthesis. Ag NPs have been synthesized using various methods that can be classified as solid, liquid, or gas-phase routes.

2.1. Environment-Friendly Synthesis Methods

The green synthesis method based on green chemistry programs is known as the representative environment-friendly synthesis method. To avoid the use or discharge of hazardous chemical substances to a considerable extent during the synthesis of chemical compounds, green chemistry programs were proposed by the Environmental Protection Agency of the United States (EPA) in 1990. Then, in 1998, Anastas and Warner published the "Twelve Principles of Green Chemistry", summarizing the concept of green chemistry [21]. Since then, policies concerning the handling of environment-friendly chemical substances have been announced worldwide. Moreover, green sustainable chemistry advocates for resource savings by recycling, which is not necessarily covered by green chemistry. This consideration has also become widespread in the materials science field, and reports on the green synthesis of Ag NPs have increased. The components of these materials such as nicotinamide adenine dinucleotide (NAD) are capable of reducing Ag salts (silver ions) into Ag NPs. Nicotinamide adenine dinucleotide-dependent reductase can produce Ag NPs by enzymatic reduction; however, the enzymatic reduction rate is often slow [22]. Some biological materials using green synthesis methods using bacteria [23–29], fungi [30–35], and plant [36–42] are shown in Table 1.

Table 1. Some green synthesis methods for synthesizing Ag NPs.

Material	Size (nm)	Note
Bacteria	28–122	*E. coli* [23]
	10–15	*Rhodococcus spp.* [24]
	44–143	*Bacillus thuringiensis* [25]
	38–85	*Ochrobactrum anhtropi* [26]
	8.1–91	*Pantoea ananatis* [27]
	41–68	*Bacillus brevis* [28]
	105	*Bacillus mojavensis* [29]
Fungi	1–20	*Aspergillus terreus* [30]
	8–50	*Pleurotus ostreatus* [31]
	25–50	*Bryophilous rhizoctoni* [32]
	10, 50	*Penicillium fellutanum* [33]
	7	*biomass derived from Aspergillus flavus* [34]
	14, 25	*Penicillium expansum* [35]
plant	9	*Jasminum nervosum* [36]
	10–40	*Artemisia princeps* [37]
	20	*Cassia auriculata* [38]
	34	*Eclipta prostrata* [39]
	20, 30	*Coffea arabica* [40]
	10–60	*Antigonon leptopus* [41]
	25–40	*Fraxinus excelsior* [42]

Among the available green methods of synthesis for Ag NPs, utilization of plant extracts is a rather simple and easy process to produce nanoparticles at large scale relative to bacteria and/or fungi mediated synthesis [43]. Several studies have discussed the synthetic conditions, such as pH and reaction temperature, that promote the synthesis of Ag NPs [16]. With regard to pH, polysaccharides and proteins related to the reaction are denatured under strongly acidic conditions; thus, neutral or slightly alkaline conditions are desirable [44,45]. Regarding the temperature of the reaction system, the amount of reactant consumed remarkably increases at high temperatures, yielding nanoparticles [46].

The diameter of the Ag NPs is known to influence the microbicidal effect [15,17]. The bactericidal activity is stronger when the particle size is smaller [47]. Therefore, an adequate synthesis method is required to generate small-size particles (<10 nm) with small dispersions. Ishihara et al. reported that when synthesizing Ag NPs by common autoclaving using commercially available glass powders containing silver nitrate as a silver ion supplier and glucose as a reducing agent, the particle size can be controlled easily depending on the glucose concentration. Ag NPs of 5 ± 1 nm can be efficiently

synthesized by the method (Figure 2) [14,48]. Moreover, no harmful material was generated by the synthesis method.

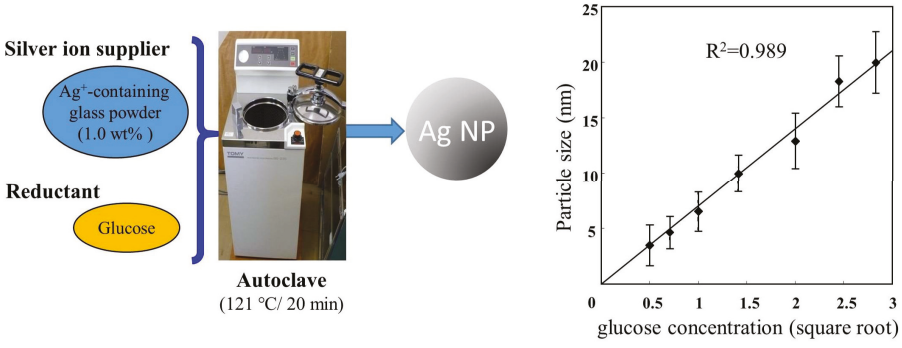

Figure 2. Environment-friendly method for Ag NP synthesis with the diameters control by glucose concentration. We have reported that environment-friendly processes were used to produce small Ag NPs (<10 nm) within a narrow size distribution. The diameters of generated Ag NPs were easily controlled by glucose concentrations [14].

2.2. *Chemical Synthesis Methods*

Some chemical methods for the synthesis of Ag NPs include chemical reduction [12,49–54], electrochemical synthesis [55–57], the irradiation-assisted method [58–61], and the pyrolysis method [62,63], as summarized in Table 2.

Table 2. Some chemical methods for synthesizing Ag NPs.

Method	Size (nm)	Note
Chemical reduction	<50	Hydrogen peroxide was used as reducing agent [12].
	7.6–13.11	Sodium borohydride was used as reducing agent [49].
	7, 29, 89	Gallic acid was used as reducing agent [50].
	<30	Sodium citrate was used as reducing agent [51].
	5, 7, 10, 15, 20, 30, 50, 63, 85, 100	Sodium borohydride and trisodium citrate were used as reducing agent [52].
	9, 11, 24, 30	Hydrazine hydrate and sodium citrate were used as reducing agent [53].
	~5	Sodium borohydride and citrate were used as reducing agent [54].
Electrochemical synthesis	4.8	Dry oxygen-free solvents were used under an argon atmosphere. [55].
	1–18	The film, as a cathode, was ion exchanged to desired Ag contents in $AgNO_3$ solutions and then reduced electrochemically [56].
	30, 46	A platinum was employed as cathode and anode [57].
Irradiation-assisted method	30–120	Dual-beam illumination system (546 nm/440 nm) was used [58].
	2–8	Ag NPs were synthesized with UV (266 nm) irradiation [59].
	50	Ag NPs were synthesized by a microwave irradiation (Cu-Kα; 0.154 nm at 40 kV) [60]
	3–30	Ag NPs containg hydrogels were prepared by radiation crosslinking and reduction, simultaneously [61].
Pyrolysis method	20–300	An argon gas was used under oxygen-free environment [62].
	3–150	All solutions were dispersed by oxygen environment [63].

Among them, chemical reduction is well known and requires two main components: a reducing agent and a silver source for the reaction. Various reagents are used for reducing agents [12,50,51]. Of these, borohydride is the most widely used because of its extremely strong and rapid reducing action [12,64–67]. In addition, Ag NPs synthesized using a co-reduction approach (e.g., sodium borohydride/trisodium citrate [52], hydrazine hydrate/sodium citrate [53], and borohydride/citrate [54]) were reported. Agnihotri et al. reported that Ag NPs were synthesized employing sodium borohydride as a primary reductant and trisodium citrate both as secondary reductant as well as protective agent [52].

In this method, nucleation and growth kinetics during the synthesis process were precisely controlled and Ag NPs of average size 5, 7, 10, 15, 20, 30, 50, 63, 85, and 100 nm were synthesized with good yield and monodispersity. As described, a protective agent is often added to stabilize the produced nanoparticles in a dispersed state. The crystal structure can also be controlled using this protective agent: Rhomboid structures and nanosheets can be produced in addition to the general spherical shape. Silver nitrate, which is chemically stable, easily available, and inexpensive compared to other silver salts [68], can supply silver ions to synthesis systems and is frequently used as the silver source.

Instead of reducing agents, a silver source is also reduced by electrochemical reaction, irradiation-assisted reaction, and pyrolysis reaction. For example, an electrochemical method, which can be used to produce certain transition metal colloids in the nanometer region, was demonstrated for the first time [55]. Ag NPs of ≤ 20 nm can be synthesized using an electrochemical method [55,56]. Using this method, Zhang et al. reported new modification method of ultrathin zeolite film of about 400 nm in thickness; the films are promising candidates for use in membrane applications [56]. Recently, Ag NPs were prepared by an electrochemical method using only polyethylene glycol as a stabilizer and without any other reactant [57]. Interestingly, using irradiation-assisted method, Ag NPs can be extended easily to synthesize relatively monodisperse triangular silver nanocrystals with desired edge lengths in the 30–120 nm range [58] and cubic crystal with 2–8 nm lengths [59]. In addition, irradiation-assisted method contributive to shortening of the synthesis time. According to Manikprabhu and Lingappa, Ag NPs were synthesized rapidly in just 90 s from 20 min by a microwave irradiation method, using pigment as a reducing agent [60]. Zhou et al. reported that nanosilver/gelatin/chitosan hydrogels were prepared by radiation crosslinking and reduction simultaneously, resulting in a stable and homogeneous distribution of Ag NPs in the matrix [61]. To synthesize fine powders by aerosol decomposition, ultrasonic spray pyrolysis has been used; however, a particle size of less than 20 nm has not been reported [62]. Pingali et al. reported that one-step spray pyrolysis of ultrasonically-atomized dilute solutions of metal solutes represents a potentially viable means of generating relatively monodisperse particles, with the capability of obtaining a mean particle size less than 20 nm [62]. Sotiriou et al. also reported that Ag NPs (less than 20 nm) were made and immobilized on nanostructured SiO2 [63].

2.3. Physical Synthesis Methods

Briefly, nanoparticles are synthesized using a physical method that physically pulverizes a metal [22,69,70]. Compared to chemical methods, thin films and the uniformity of nanoparticles distribution can be prepared with the absence of solvent contamination; however, a stable high energy over a long time should be supplied in physical methods to produce a high yield of Ag NPs of uniform size, and require large space for equipment. Evaporation/vapor condensation [22,71,72], arc discharge [73], and energy ball milling [74] are some of the commonly used methods for synthesizing nanoparticles. Tien et al. reported the synthesis of 20–30 nm diameter of Ag NPs via arc discharge with no added surfactants [73]. The fabrication consumes silver rods at a rate of 100 mg/min, yielding metallic silver nanoparticle and ionic silver with concentrations of approximately 11 ppm and 19 ppm, respectively. Nakamura et al. developed a simple and rapid synthesis technique (20-min irradiation), via laser irradiation of an aqueous solution of inorganic ions for nanoparticles synthesis [75]. As a result, antibacterial calcium phosphate sub-microspheres containing Ag NPs expected to be useful in dental healthcare and infection control were produced with one-pot fabrication.

3. Microbicidal Properties of Ag NPs

The mechanisms of the microbicidal activity of Ag NPs have only recently been understood. Sondi and Salopek-Sondi were the first to report the bactericidal ability of Ag NPs against Gram-negative bacteria, using *E. coli.* They revealed that the nanoparticles accumulate in "pits" that are formed in the cell wall; then, the release of free radicals from the Ag NPs damages the cell and annihilates the bacteria [5]. Furthermore, the redox reaction, in which the silver ions are released from Ag NPs, is also

mentioned as one of the factors that damages bacteria [76]. Small Ag NPs (less than 10 nm) releases silver ions from its surface that indicate much higher antibacterial activity than from direct bacterial contact with that surface [77]. Matteis et al. reporeted that the death following the application of Ag NPs is dose-dependent [51]. Silver ions are known to specifically react with the thiol group of cysteine; thus, the metabolic enzymes inside the bacteria are considered to be inhibited. This may be explained either by the formation of new bonds between the silver ions and cysteine residues in the peptide, or by the fact that the ions replace other metal ions already bound to the cysteine, killing the bacteria. The relation between the size of the Ag NPs and the antibacterial effect has also been elucidated, indicating that a smaller diameter results in a higher bactericidal activity [78]. This is likely due to the structure and size of the "pits" on the cell wall, which varies depending on the types of bacteria; smaller Ag NPs can access the "pits" more efficiently than larger Ag NPs [79]. According to Gurunathan et al., in experiments using Ag NPs of 5 nm on average, nanoparticles were more effective than ampicillin or vancomycin against some bacteria [80]. This suggests that Ag NPs are useful against infectious diseases. Ag NPs [81] have a high antibacterial activity against *E. coli* O157: H7 [82], which has a very strong food poisoning effect, and this bactericidal activity is exerted against *Streptococcus pyogenes*, *Salmonella enterica*, *Staphylococcus aureus*, and *Enterococcus faecalis* [83]. Although silver ions show a strong microbicidal activity against prokaryotic cells, particularly Gram-negative bacteria, their activity against Gram-positive bacteria is considered weak. This is explained by the thick cell wall of Gram-positive bacteria. Further, the peptidoglycan in their wall has a significant influence. The affinity between silver ions and the peptidoglycan is very high, and silver ions are presumably trapped in the cell wall and do not reach inside the cell membrane [84]. Furthermore, high temperatures, as well as the presence of chlorine, thiol groups, and oxygen-carrying proteins, strongly influence the presence of silver ions [5]. Thus, the environment in which Ag NPs are used is also an important factor influencing the microbicidal activity of Ag NPs.

4. Antiviral Properties of Ag NPs

Studies on the antiviral action of Ag NPs are far behind those targeting microbicidal properties, and the mechanism of antiviral action is still not well understood. A viral infection is established when the nucleic acids of the virus are introduced into the host cell and then replicated. Ag NPs possibly act on the surface of the virus and physically inhibit the contact with host cells [82,83,85]. Previous studies have demonstrated that the size of the Ag NPs is essential for the manifestation of antiviral effects, similar to the observations in bacteria. According to Speshoc et al., ≤25 nm Ag NPs are effective against arenavirus, inhibiting its replication process [86]. Gaikwad et al. indicate that Ag NPs of 7–20 nm have antiviral effects against herpes simplex virus (HSV) types 1/2 and human parainfluenza virus type-3 [87]. Furthermore, since the antiviral effect decreased with increasing particle diameter, the nanoparticles should be as small as possible. Baram-Pinto et al. reported that Ag NPs inhibit the contact of HSV-1 with the cell surface and prevent infection [88]. Ag NPs are effective against cells already infected with human immunodeficiency virus (HIV) [89]. Ag NPs adhere to the envelope of the HIV virus to prevent cell infection [90]. Mori et al. reported that Ag NPs of ≤ 10 nm were effective against the influenza virus [9,14]. Rogers et al. reported that Ag NPs of approximately 10 nm inhibit Monkeypox virus (MPV), an orthopoxvirus similar to variola virus, infection in vitro [91]. Interestingly, they also reported that larger Ag NPs (25 nm, 55 nm, and 80 nm) promoted an increase in the mean number of MPV plaque-forming unit (PFU)/well when compared to controls. A potential explanation for this may be due to nanoparticle agglomeration, the nanoparticle agglomeration may potentiate or facilitate virus particle interaction or internalization within host cells, leading to an increase in the number of observed PFU. Therefore, particle size of Ag NPs seems very important for antiviral properties of Ag NPs. More studies on the antiviral activity of Ag NPs will possibly be reported in the future.

5. Toxicity of Ag NPs in Humans

Investigations on the toxicity of Ag NPs to the human body have only recently been reported. Recent in vitro studies demonstrate the cytotoxicity of Ag NPs against HaCaT (Human keratinocyte cell line) cells, toxicity data in terms of cell viability revealed a dose-dependent safe profile for low concentrations (<10 μM), whereas higher concentrations were associated with a high rate of cell mortality [92]. The evaluation of cytotoxicity of Ag NPs has been also carried out in other human cellular models such as lung fibroblasts [93], glioblastoma cells [93], and mesenchymal stem cells [94]. Oxidative stress and severe lipid peroxidation have been observed, and they certainly damage proteins [95]. The proposed mechanism by which Ag NPs lead to cytotoxicity has been considered to at least partially be through the induction of reactive oxygen species (ROS) [96]. Overproduction of ROS causes impairments in DNA, lipids, and protein, eventually leading to cell death and progressive aging of an organism [97]. In addition, the cells capture the Ag NPs depending on the surface charge intensity of the nanoparticles [98]; then, their accumulation in the cells likely damages the mitochondrial membrane due to oxidative stress, thereby damaging the DNA [99–101]. Moreover, the induction of cell apoptosis is considered [102]. Thus, knowledge on the toxicity of Ag NPs to several human cells has continued to increase. However, related research mainly focuses on in vitro and animal experiments and is rarely reported. For example, in vivo acute/subacute toxicity data showed no changes in mice health status after intraperitoneal administration. Histological observations of internal organs and the biochemical parameters analyzed together with the other biological observations showed a low toxicity level with no major differences related to control, albeit at skin level a reduced number of mast cells was detected [92]. Hence, further studies on safety to humans are expected in the future [103,104].

6. Applications for Healthcare Workers (HCWs)

"Emerging" infectious diseases (EIDs) can be defined as infections that have newly appeared in a population or have existed but are rapidly increasing in incidence or geographic range [105]. Among recent examples are Ebola Virus Disease (EVD), Middle East Respiratory Syndrome coronavirus (MERS-CoV), Severe Acute Respiratory Syndrome (SARS), infection with MRSA, and Cholera. The HCWs involved during medical treatment of EID patients have a fatal risk of contact infection. The EID outbreak in west Africa had a devastating effect on HCWs. Of the nearly 17,000 cases of EVD in Guinea, Liberia, and Sierra Leone, at least 600 were among HCWs, and more than half of them died [106]. MERS-CoV infection continues to have a high fatality rate, and a large proportion of patients are HCWs (26%) [107].

As described above, Ag NPs have a strong microbicidal activity with a broad spectrum. Furthermore, the mechanism that has been proposed is that Ag NPs yield ROS, leading to oxidative stress [100,101] in addition to the generation of free silver ions [48]. Therefore, Ag NPs will provide useful materials to protect HCWs from the risk of contact infection. To prevent contact infection, HCWs usually wear protective clothing. Pathogenic microbes, which are mainly generated by patients, stay alive on the surfaces of protective clothing. It was necessary to develop an evidence-based protective clothing for HCWs [108]. Especially, there is a risk of infection by incorrect contact when removing the clothing. To overcome that problem, we carried out research with the aim of developing a new microbicidal/antiviral material, using Ag NPs absorbed on a chitin sheet with a nanoscale fiber-like surface structure (Figure 3) [48,109].

The chitin nanofiber sheet (CNFS) used in our study has a nanoscale fiber-like surface structure, with corresponding increases in the available surface area for adsorption of Ag NPs. In addition, the advantages, in terms of biochemical activities, of chitin/chitosan-based materials include anti-infectious activity, the stimulation of angiogenesis/wound repair, and the stabilization/activation of growth factors [110–114]. Recent studies show that the application of CNFS to skin improved the epithelial granular layer and increased granular density, suggesting the potential use of CNFS as a component of skin-protective formulations [31].

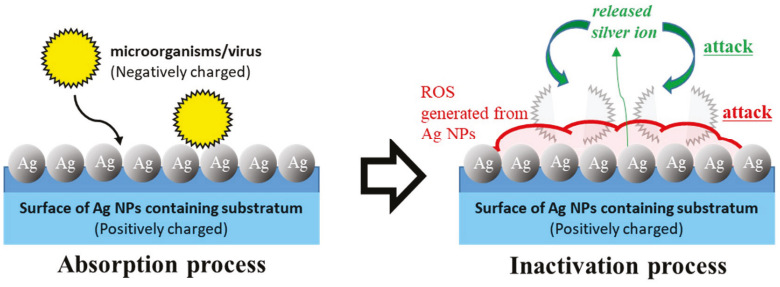

Figure 3. The mechanism for microbicidal and antivirus activities of the Ag NP chitin nanofiber sheet (CNFS). To prevent contact infection of healthcare workers (HCWs), an Ag NP chitin nanofiber sheet (CNFS) was developed, showing strong microbicidal activity against microorganisms/viruses via reactive oxygen species (ROS) and silver ions on the surface of substratum.

We found that negatively charged Ag NPs are efficiently absorbed onto positively charged chitin/chitosan-based materials with a nanoscale fiber-like surface structure (<200 μm), such as CNFS, which also act as stabilizers of the Ag NPs [7,8,109]. Moreover, Ag NPs were able to bind directly to cotton, paper, and cloths with nanoscale fiber-like surface structures (data not published). Materials with immobilized Ag NPs have enhanced microbicidal activities against microbial pathogens and viruses. For example, we confirmed strong microbicidal activities of Ag NPs absorbed on CNFS against bacteria (*E. coli*) and viruses (H1N1 influenza A virus) (Figure 4) [9,48,109]. Thus, the materials have great potential to be used in clothes, plastics, and papers, with various applications such as in doctor/nurse uniforms, security/protection coats, masks, gloves, and counter cloths (Figure 5) [48]. Although we successfully synthesized new microbicidal/antiviral materials using Ag NP technology, further in-depth research will be required to evaluate how long these materials can maintain their stability in terms of microbicidal properties and to evaluate their safety for the human body. The issues of the materials' safety for the human body is especially important, because the potential effects on patients who come into contact with the materials, through their various applications used by HCWs, should also be considered.

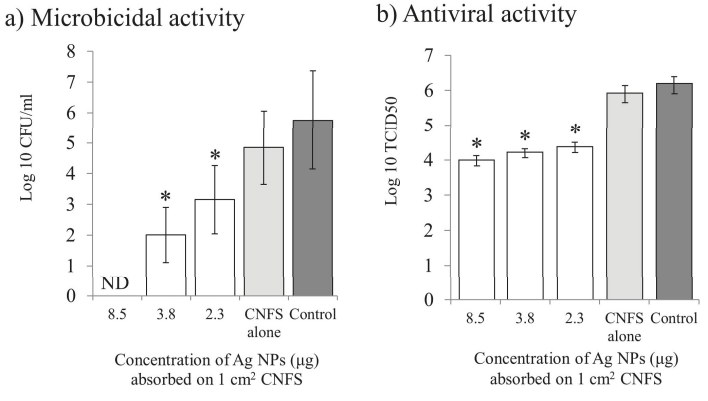

Figure 4. The microbicidal/antiviral activity of materials using Ag NPs/CNFS with various concentration of Ag NPs [48]. The activities of various concentrations of Ag NPs on CNFS against *E. coli* (**a**) and H1N1 Influenza A (**b**). Data are mean value ± standard deviation (n = 6); the asterisk indicates a statistically significant difference ($p < 0.01$) using two-sample t-test vs. control. ND means non-detection. The vertical axis is listed with a common logarithm. For example, with an Ag NP concentration of 8.5 μg/cm^2 in the CNFS in (**b**), there was a reduction of greater than 2 log10 (100-fold) corresponding to a reduction of viral titers by approximately 99%.

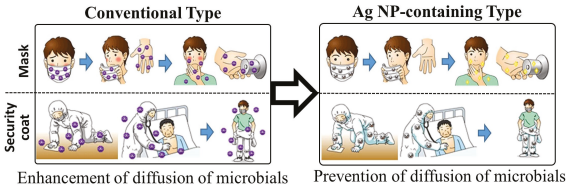

Figure 5. The application of the Ag NP/CNFS complex to protect HCWs. To prevent contact infection of HCWs, we have proposed medical consumables, such as infection-protective coats, masks, and gloves, immobilized Ag NPs.

7. Other Medical Applications

Some of the commercially available silver-based materials already available are shown in Table 3. The range of microbicidal properties of Ag NPs is wider than that of antibiotics, and the appearance of resistant bacteria such as MRSA is rare in Ag NP-based materials [115]. The combination of various materials with Ag NP-based materials has been studied [116–119]. The production of wound dressings and medical catheters coated with Ag NPs has been investigated. However, silver absorbed by the skin causes food poisoning symptoms [120]. Moreover, metal allergies can be triggered if Ag NPs stay in the body for a long time [121]; therefore, care must be taken to avoid their intake.

The skin is the outermost tissue covering the human body and is prone to various stimuli and injuries [122]. Depending on the severity of the physical or chemical injury, the wound may hurt for a long time or even be lethal [123]. When caring for a wound, it is important to prevent it from drying out and to take measures against bacterial infection [124]. Wound dressings are used to maintain a humid environment, and disinfection and antibiotic treatment are measures against infection. Because of the worldwide concern regarding resistant bacteria due to the frequent use of antibiotics, a significant number of studies have been conducted on the development of wound dressings containing materials with antibacterial activity [125]. Wound dressings with Ag NPs are a representative example, and many types are now known. Silver ions are released from the Ag NPs contained in the wound-covering material in order to destroy the bacteria at the wound site [126].

Various types of catheters are used in the medical field; for example, the central venous catheter (CVC) is used intravenously from the body surface, near the main vein in the region of the right atrium for treatment or nutritional supplementation [127–129]. The highest possible attention is thus required to accurately locate the blood vessel and avoid any risk of bacterial infection by the catheter [129]. There is also a risk of septicemia if bacterial infection is caused via a catheter. More than 80% of infectious cases have been caused by MRSA [130]. Catheters coated with Ag NP have been developed to protect patients from such infections [131–133]. Approaches for preventing infections caused by both Gram-negative and Gram-positive bacteria have been reported [128,134–136]. There has been a continuous improvement in catheters coated with Ag NPs, and the development of devices with bactericidal properties and suppressed toxicity to the organism has advanced [129,134,137]. Urinary catheters are also frequently used in hospitals. Usually, these are made of silicone or latex and indwelled in the bladder via the urethra when the patient cannot urinate, e.g., when anesthetized or when the urine volume must be strictly measured [138]. Due to the nature of urinary catheters, bacterial infections in the urinary tract may arise [139]. Gram-negative bacteria, such as *E. coli*, *Enterococcus faecalis*, and *S. epidermidis*, frequently cause such infections [140]. A urinary catheter coated with Ag NPs exhibited hydrophilic properties and prevented the accumulation of proteins and electrolytes, suppressing the formation of biofilms [115].

An example of a typical use of silver materials in modern medicine is the amalgams that have been used in dentistry since the 19th century [141]. Currently, silver is also used in dental prostheses and implants, such as artificial dental roots implanted in the jawbone [142]. Dental implants are often contaminated by a biofilm, resulting in severe inflammatory disorders [143]. To overcome this, various metal dental implants or dental implants coated with metals have been tested, but favorable results were only obtained when using silver [144].

Table 3. Some of the commercially available Ag NP-based materials for clinical use.

Type	Name of Product	Company	Note
Wound dressing material	Acticoat™	Smith & Nephew, Inc., London, UK.	Nanocrystalline silver is used as a dressing to manage wounds by providing broad-spectrum bactericidal activity against over 150 pathogens.
Wound dressing material	PolyMem Silver®	Ferris Mfg. Corp., Texas, USA.	Contains nanocrystalline silver particles, which act on bacteria within the dressing.
External Ventricular Drain Catheter	Silverline® Ventricular Drainage Catheter	Spiegelberg GmbH & Co. KG., Hamburg, DEU.	The special silver additive reduces the possibility of microbial colonization of the product surface.
Drug Delivery Catheter	ON-Q SilverSoaker™	Halyard Health, Inc., Georgia, USA.	The catheter has a silver nanoparticle coating which protects against the formation of infection-causing biofilm.
Endotracheal Tube	Agento® I.C. silver-coated endotracheal tube	C.R. Bard Inc., New Jersey, USA.	With a hydrophilic polymer coating containing silver particles, it was proven to reduce microbiologically confirmed ventilator-associated pneumonia.

8. Conclusion Remarks

Applied research on Ag NPs in the biomedical field has been actively conducted, of which only a portion has been introduced in this review. There are high expectations regarding nanoparticles' use; however, the toxic effect of Ag NPs on living organisms and the related health problems are concerning when their concentration exceeds a certain level [22]. For example, high blood pressure may be caused by Ag NPs [145]. Eliminating silver accumulated in the body is difficult. However, when the silver is present as nanoparticles, the toxicity decreases because they can be eliminated through the urine and hair [146]. However, current knowledge on the toxicity of Ag NPs to humans is based on in vitro tests and animal experiments, and there is no strict consensus about their toxicity. Therefore, the safety of Ag NPs when used for the human body needs further investigation. The microbicidal spectrum of Ag NPs is wide, and there is little concern regarding the rise of resistant bacteria. Recent studies revealed their effect on viruses that were thought to be unaffected by nanoparticles. The application of Ag NPs in the medical field is fascinating, particularly for infectious diseases. Attempts have also been made to impart microbicidal properties to biocompatible medical devices, and Ag NPs are considered to be one of the materials that will contribute to the progress of medical science in the future. In addition, materials based on Ag NP technology are expected to contribute to research into protecting HCWs from various risks, such as contact infection during medical treatments on patients. We expect that Ag NP-based materials will be able to prevent the contact infection of HCWs, besides preventing patient infection.

Author Contributions: S.N. designed and wrote the manuscript. M.S. and M.I. critically revised the manuscript. S.N., Y.S., and N.A. selected and summarized the references carefully. T.T and M.F. collected all the references.

Funding: This research received no external funding.

Acknowledgments: This study was partly supported by a grant (no. 19K22787 for S.N.) from the Ministry of Education, Science, Sports, and Culture, Japan.

Conflicts of Interest: The authors declare no conflict of interest. The funders had no role in the design of the study; in the collection, analyses, or interpretation of data; in the writing of the manuscript, or in the decision to publish the results.

Abbreviations

Ag NPs	silver nanoparticles
CAUTIs	catheter-associated urinary tract infections
CNFS	chitin sheet with nano-scale fiber-like surface structure
CVC	central venous catheter
EID	emerging infectious diseases
EPA	the Environmental Protection Agency of the United States
EVD	ebola virus disease
E. coli	*Escherichia coli*
EG	ethylene glycol
HaCaT	human keratinocyte cell line
HSV	herpes simplex virus
HIV	human immunodeficiency virus
MERS-CoV	middle east respiratory syndrome coronavirus
MPV	monkeypox virus
MRSA	methicillin-resistant Staphylococcus aureus
NAD	nicotinamide adenine dinucleotide
PFU	plaque-forming unit
PVP	polyvinylpyrrolidone
ROS	reactive oxygen species
SARS	severe acute respiratory syndrome
TEM	transmission electron microscopy
UV	ultraviolet
Vis	visible

References

1. Alexander, J.W. History of the medical use of silver. *Surg. Infect.* **2009**, *10*, 289–292. [CrossRef] [PubMed]
2. Ip, M.; Lui, S.L.; Poon, V.K.; Lung, I.; Burd, A. Antimicrobial activities of silver dressings: An in vitro comparison. *J. Med. Microbiol.* **2006**, *55*, 59–63. [CrossRef] [PubMed]
3. Marambio-Jones, C.; Hoek, E.M. A review of the antibacterial effects of silver nanomaterials and potential implications for human health and the environment. *J. Nanopart. Res.* **2010**, *12*, 1531–1551. [CrossRef]
4. Gupta, A.; Maynes, M.; Silver, S. Effects of halides on plasmid-mediated silver resistance in Escherichia coli. *Appl. Environ. Microbiol.* **1998**, *64*, 5042–5045. [PubMed]
5. Sondi, I.; Salopek-Sondi, B. Silver nanoparticles as antimicrobial agent: A case study on E. coli as a model for Gram-negative bacteria. *J. Colloid Interface Sci.* **2004**, *275*, 177–182. [CrossRef] [PubMed]
6. Kawashita, M.; Tsuneyama, S.; Miyaji, F.; Kokubo, T.; Kozuka, H.; Yamamoto, K. Antibacterial silver-containing silica glass prepared by sol-gel method. *Biomaterials* **2000**, *21*, 393–398. [CrossRef]
7. Nguyen, V.Q.; Ishihara, M.; Mori, Y.; Nakamura, S.; Kishimoto, S.; Hattori, H.; Fujita, M.; Kanatani, Y.; Ono, T.; Miyahira, Y.; et al. Preparation of size-controlled silver nanoparticles and chitin-based composites and their antimicrobial activities. *J. Nanomater.* **2013**, *2013*, 693486. [CrossRef]
8. Nguyen, V.Q.; Ishihara, M.; Mori, Y.; Nakamura, S.; Kishimoto, S.; Fujita, M.; Hattori, H.; Kanatani, Y.; Ono, T.; Miyahira, Y.; et al. Preparation of size-controlled silver nanoparticles and chitosan-based composites and their anti-microbial activities. *Biomed. Mater. Eng.* **2013**, *23*, 473–483.
9. Mori, Y.; Ono, T.; Miyahira, Y.; Nguyen, V.Q.; Matsui, T.; Ishihara, M. Antiviral activity of silver nanoparticle/chitosan composites against H1N1 influenza A virus. *Nanoscale Res. Lett.* **2013**, *20*, 93. [CrossRef]
10. Gong, P.; Li, H.; He, X.; Wang, K.; Hu, J.; Tan, W.; Zhang, S.; Yang, X. Preparation and antibacterial activity of Fe_3O_4@ Ag nanoparticles. *Nanotechnology* **2007**, *18*, 285604. [CrossRef]
11. Peiris, S.; McMurtrie, J.; Zhu, H.-Y. Metal nanoparticle photocatalysts: Emerging processes for green organic synthesis. *Catal. Sci. Technol.* **2016**, *6*, 320–338. [CrossRef]
12. Zhang, Q.; Li, N.; Goebl, J.; Lu, Z.; Yin, Y. A systematic study of the synthesis of silver nanoplates: Is citrate a "magic" reagent? *J. Am. Chem. Soc.* **2011**, *133*, 18931–18939. [CrossRef] [PubMed]
13. Tien, D.C.; Tseng, K.H.; Liao, C.Y.; Tsung, T.T. Colloidal silver fabrication using the spark discharge system and its antimicrobial effect on Staphylococcus aureus. *Med. Eng. Phys.* **2008**, *30*, 948–952. [CrossRef] [PubMed]
14. Mori, Y.; Tagawa, T.; Fujita, M.; Kuno, T.; Suzuki, S.; Matsui, T.; Ishihara, M. Simple and environmentally friendly preparation and size control of silver nanoparticles using an inhomogeneous system with silver-containing glass powder. *J. Nanopart. Res.* **2011**, *13*, 2799–2806. [CrossRef]
15. Ngeontae, W.; Janrungroatsakul, W.; Maneewattanapinyo, P.; Ekgasit, S.; Aeungmaitrepirom, W.; Tuntulani, T. Novel potentiometric approach in glucose biosensor using silver nanoparticles as redox marker. *Sens. Actuators B Chem.* **2009**, *137*, 320–326. [CrossRef]
16. Zainal, N.A.; Shukor, S.R.A.; Razak, K.A. Applying the Taguchi Method to Optimise the Size of Silica Nanoparticles Entrapped with Rifampicin for a Drug Delivery System. *J. Eng. Sci.* **2015**, *11*, 9–16.
17. Lee, P.; Meisel, D. Adsorption and surface-enhanced Raman of dyes on silver and gold sols. *J. Phys. Chem.* **1982**, *86*, 3391–3395. [CrossRef]
18. Son, Y.; Yeo, J.; Ha, C.W.; Lee, J.; Hong, S.; Nam, K.H.; Yang, D.-Y.; Ko, S.H. Application of the specific thermal properties of Ag nanoparticles to high-resolution metal patterning. *Thermochim. Acta.* **2012**, *542*, 52–56. [CrossRef]
19. De Matteis, V.; Cascione, M.; Toma, C.C.; Leporatti, S. Silver Nanoparticles: Synthetic Routes, In Vitro Toxicity and Theranostic Applications for Cancer Disease. *Nanomaterials* **2018**, *8*, 319. [CrossRef]
20. Vijayaraghavan, K.; Nalini, S.P. Biotemplates in the green synthesis of silver nanoparticles. *Biotechnol. J.* **2010**, *5*, 1098–1110. [CrossRef]
21. Anastas, P.T.; Warner, J. *Green Chemistry: Theory and Practice*; Oxford University Press: Oxford, UK, 1998.
22. Ge, L.; Li, Q.; Wang, M.; Ouyang, J.; Li, X.; Xing, M.M. Nanosilver particles in medical applications: Synthesis, performance, and toxicity. *Int. J. Nanomed.* **2014**, *9*, 2399–2407.
23. El-Shanshoury, A.E.-R.R.; ElSilk, S.E.; Ebeid, M.E. Extracellular biosynthesis of silver nanoparticles using escherichia coli ATCC 8739, bacillus subtilis atcc 6633, and streptococcus thermophilus esh1 and their antimicrobial activities. *Int. Sch. Res. Not.* **2011**, *2011*, 385480. [CrossRef]

24. Otari, S.V.; Patil, R.M.; Nadaf, N.H.; Ghosh, S.J.; Pawar, S.H. Green synthesis of silver nanoparticles by microorganism using organic pollutant: Its antimicrobial and catalytic application. *Environ. Sci. Pollut. Res. Int.* **2014**, *21*, 1503–1513. [CrossRef]
25. Banu, A.N.; Balasubramanian, C.; Moorthi, P.V. Biosynthesis of silver nanoparticles using Bacillus thuringiensis against dengue vector, Aedes aegypti (Diptera: Culicidae). *Parasitol. Res.* **2014**, *113*, 311–316. [CrossRef] [PubMed]
26. Thomas, R.; Janardhanan, A.; Varghese, R.T.; Soniya, E.V.; Mathew, J.; Radhakrishnan, E.K. Antibacterial properties of silver nanoparticles synthesized by marine Ochrobactrum sp. *Braz. J. Microbiol.* **2015**, *45*, 1221–1227. [CrossRef] [PubMed]
27. Monowar, T.; Rahman, M.S.; Bhore, S.J.; Raju, G.; Sathasivam, K.V. Silver Nanoparticles Synthesized by Using the Endophytic Bacterium Pantoea ananatis are Promising Antimicrobial Agents against Multidrug Resistant Bacteria. *Molecules* **2018**, *23*, 3220. [CrossRef]
28. Saravanan, M.; Barik, S.K.; MubarakAli, D.; Prakash, P.; Pugazhendhi, A. Synthesis of silver nanoparticles from Bacillus brevis (NCIM 2533) and their antibacterial activity against pathogenic bacteria. *Microb. Pathog.* **2018**, *116*, 221–226. [CrossRef] [PubMed]
29. Iqtedar, M.; Aslam, M.; Akhyar, M.; Shehzaad, A.; Abdullah, R.; Kaleem, A. Extracellular biosynthesis, characterization, optimization of silver nanoparticles (Ag NPs) using Bacillus mojavensis BTCB15 and its antimicrobial activity against multidrug resistant pathogens. *Prep. Biochem. Biotechnol.* **2019**, *49*, 136–142. [CrossRef]
30. Li, G.; He, D.; Qian, Y.; Guan, B.; Gao, S.; Cui, Y.; Yokoyama, K.; Wang, L. Fungus-mediated green synthesis of silver nanoparticles using Aspergillus terreus. *Int. J. Mol. Sci.* **2011**, *13*, 466–476. [CrossRef]
31. Devika, R.; Elumalai, S.; Manikandan, E.; Eswaramoorthy, D. Biosynthesis of silver nanoparticles using the fungus Pleurotus Ostreatus and their antibacterial activity. *Open Access Sci. Rep.* **2012**, *12*, 557. [CrossRef]
32. Raudabaugh, D.B.; Tzolov, M.B.; Calabrese, J.P.; Overton, B.E. Synthesis of silver nanoparticles by a bryophilous rhizoctonia species. *Nanomater. Nanotechnol.* **2013**, *3*, 2. [CrossRef]
33. Fahmy, T.A.; Hussein, H.E.-S.; Mostafa, M.E.-H.; Mahmoud, M.E.; Dalia, M.E.-A. Silver Nanoparticlesynthesized by enicillium citreonigrum and usarium moniliforme Isolated from El-Sharkia, Egypt. *Int. J. Sci. Eng. Res.* **2014**, *5*, 181–192.
34. Bhangale, H.; Sarode, K.; Patil, A.; Patil, D. Microbial Synthesis of Silver Nanoparticles Using Aspergillus Flavus and Their Characterization. *>ICATSA 2016:Techno-Societal 2016* **2018**, 463–470.
35. Ammar, H.A.; El-Desouky, T.A. Green synthesis of nanosilver particles by Aspergillus terreus HA1N and Penicillium expansum HA2N and its antifungal activity against mycotoxigenic fungi. *J. Appl. Microbiol.* **2016**, *121*, 89–100. [CrossRef] [PubMed]
36. Lallawmawma, H.; Sathishkumar, G.; Sarathbabu, S.; Ghatak, S.; Sivaramakrishnan, S.; Gurusubramanian, G.; Kumar, N.S. Synthesis of silver and gold nanoparticles using Jasminum nervosum leaf extract and its larvicidal activity against filarial and arboviral vector Culex quinquefasciatus Say (Diptera: Culicidae). *Environ. Sci. Pollut. Res. Int.* **2015**, *22*, 17753–17768. [CrossRef] [PubMed]
37. Gurunathan, S.; Jeong, J.K.; Han, J.W.; Zhang, X.F.; Park, J.H.; Kim, J.H. Multidimensional effects of biologically synthesized silver nanoparticles in Helicobacter pylori, Helicobacter felis, and human lung (L132) and lung carcinoma A549 cells. *Nanoscale Res. Lett.* **2015**, *10*, 35. [CrossRef] [PubMed]
38. Parveen, A.; Rao, S. Cytotoxicity and genotoxicity of biosynthesized gold and silver nanoparticles on human cancer cell lines. *J. Clust. Sci.* **2015**, *26*, 775–788. [CrossRef]
39. Peddi, S.P.; Sadeh, B.A. Structural studies of silver nanoparticles obtained through single-step green synthesis. *Mater. Sci. Eng.* **2015**, *92*, 012004. [CrossRef]
40. Dhand, V.; Soumya, L.; Bharadwaj, S.; Chakra, S.; Bhatt, D.; Sreedhar, B. Green synthesis of silver nanoparticles using coffea arabica seed extract and its antibacterial activity. *Mater. Sci. Eng. C* **2016**, *58*, 36–43. [CrossRef]
41. Ganaie, S.; Abbasi, T.; Abbasi, S. Rapid and green synthesis of bimetallic Au–Ag nanoparticles using an otherwise worthless weed Antigonon leptopus. *J. Exp. Nanosci.* **2016**, *11*, 395–417. [CrossRef]
42. Parveen, M.; Ahmad, F.; Malla, A.M.; Azaz, S. Microwave-assisted green synthesis of silver nanoparticles from Fraxinus excelsior leaf extract and its antioxidant assay. *Appl. Nanosci.* **2016**, *6*, 267–276. [CrossRef]
43. Singh, J.; Dutta, T.; Kim, K.H.; Rawat, M.; Samddar, P.; Kumar, P. 'Green' synthesis of metals and their oxide nanoparticles: Applications for environmental remediation. *J. Nanobiotechnol.* **2018**, *16*, 84. [CrossRef] [PubMed]

44. Chiou, A.-H.; Wu, W.-F.; Chen, D.-Y.; Hsu, C.-Y. The use of the grey-Taguchi method for the optimization of a silicon nanowires array synthesized using electroless Ag-assisted etching. *J. Nanopart. Res.* **2013**, *15*, 1866. [CrossRef]
45. Bhainsa, K.C.; D'souza, S. Extracellular biosynthesis of silver nanoparticles using the fungus Aspergillus fumigatus. *Colloids Surf. B* **2006**, *47*, 160–164. [CrossRef] [PubMed]
46. Morrill, K.; May, K.; Leek, D.; Langland, N.; Jeane, L.D.; Ventura, J.; Skubisz, C.; Scherer, S.; Lopez, E.; Crocker, E.; et al. Spectrum of antimicrobial activity associated with ionic colloidal silver. *J. Altern. Complement. Med.* **2013**, *19*, 224–231. [CrossRef] [PubMed]
47. Liu, H.L.; Dai, S.A.; Fu, K.Y.; Hsu, S.H. Antibacterial properties of silver nanoparticles in three different sizes and their nanocomposites with a new waterborne polyurethane. *Int. J. Nanomed.* **2010**, *5*, 1017–1028.
48. Ishihara, M.; Nguyen, V.Q.; Mori, Y.; Nakamura, S.; Hattori, H. Adsorption of Silver Nanoparticles onto Different Surface Structures of Chitin/Chitosan and Correlations with Antimicrobial Activities. *Int. J. Mol. Sci.* **2015**, *16*, 13973–13988. [CrossRef] [PubMed]
49. Shameli, K.; Ahmad, M.B.; Yunus, W.Z.; Ibrahim, N.A.; Darroudi, M. Synthesis and characterization of silver/talc nanocomposites using the wet chemical reduction method. *Int. J. Nanomed.* **2010**, *5*, 743–751. [CrossRef]
50. Martinez-Castanon, G.; Nino-Martinez, N.; Martinez-Gutierrez, F.; Martinez-Mendoza, J.; Ruiz, F. Synthesis and antibacterial activity of silver nanoparticles with different sizes. *J. Nanopart. Res.* **2008**, *10*, 1343–1348. [CrossRef]
51. De Matteis, V.; Malvindi, M.A.; Galeone, A.; Brunetti, V.; De Luca, E.; Kote, S.; Kshirsagar, P.; Sabella, S.; Bardi, G.; Pompa, P.P. Negligible particle-specific toxicity mechanism of silver nanoparticles: The role of Ag+ ion release in the cytosol. *Nanomedicine* **2015**, *11*, 731–739. [CrossRef]
52. Agnihotri, S.; Mukherji, S.; Mukherji, S. Size-controlled silver nanoparticles synthesized over the range 5–100 nm using the same protocol and their antibacterial efficacy. *RSC Adv.* **2014**, *4*, 3974–3983. [CrossRef]
53. Guzmán, M.G.; Dille, J.; Godet, S. Synthesis of silver nanoparticles by chemical reduction method and their antibacterial activity. *Int. J. Chem. Eng.* **2009**, *2*, 104–111.
54. Pinto, V.V.; Ferreira, M.J.; Silva, R.; Santos, H.A.; Silva, F.; Pereira, C.M. Long time effect on the stability of silver nanoparticles in aqueous medium: Effect of the synthesis and storage conditions. *Colloids Surf. A Phys. Eng. Asp.* **2010**, *364*, 19–25. [CrossRef]
55. Reetz, M.T.; Helbig, W. Size-selective synthesis of nanostructured transition metal clusters. *J. Am. Chem. Soc.* **1994**, *116*, 7401–7402. [CrossRef]
56. Zhang, Y.; Chen, F.; Zhuang, J.; Tang, Y.; Wang, D.; Wang, Y.; Dong, A.; Ren, N. Synthesis of silver nanoparticles via electrochemical reduction on compact zeolite film modified electrodes. *Chem. Commun.* **2002**, *23*, 2814–2815. [CrossRef]
57. Roldán, M.; Pellegri, N.; de Sanctis, O. Electrochemical method for Ag-PEG nanoparticles synthesis. *J. Nanopart. Res.* **2013**, *2013*, 524150. [CrossRef]
58. Jin, R.; Cao, Y.C.; Hao, E.; Métraux, G.S.; Schatz, G.C.; Mirkin, C.A. Controlling anisotropic nanoparticle growth through plasmon excitation. *Nature* **2003**, *425*, 487–490. [CrossRef]
59. Huang, L.; Zhai, M.L.; Long, D.W.; Peng, J.; Xu, L.; Wu, G.Z.; Li, J.Q.; Wei, G.S. UV-induced synthesis, characterization and formation mechanism of silver nanoparticles in alkalic carboxymethylated chitosan solution. *J. Nanopart. Res.* **2008**, *10*, 1193–1202. [CrossRef]
60. Manikprabhu, D.; Lingappa, K. Microwave assisted rapid and green synthesis of silver nanoparticles using a pigment produced by Streptomyces coelicolor klmp33. *Bioinorg. Chem. Appl.* **2013**, *2013*, 341798. [CrossRef]
61. Zhou, Y.; Zhao, Y.; Wang, L.; Xu, L.; Zhai, M.; Wei, S. Radiation synthesis and characterization of nanosilver/gelatin/carboxymethyl chitosan hydrogel. *Radiat. Phys. Chem.* **2012**, *81*, 553–560. [CrossRef]
62. Pingali, K.C.; Rockstraw, D.A.; Deng, S. Silver nanoparticles from ultrasonic spray pyrolysis of aqueous silver nitrate. *Aerosol Sci. Technol.* **2005**, *39*, 1010–1014. [CrossRef]
63. Sotiriou, G.A.; Teleki, A.; Camenzind, A.; Krumeich, F.; Meyer, A.; Panke, S.; Pratsinis, S.E. Nanosilver on nanostructured silica: Antibacterial activity and Ag surface area. *Chem. Eng. J.* **2011**, *170*, 547–554. [CrossRef] [PubMed]
64. Liu, J.; Huang, Z.; Cai, K.; Zhang, H.; Lu, Z.; Li, T.; Zuo, Y.; Han, H. Clean synthesis of an economical 3D nanochain network of PdCu alloy with enhanced electrocatalytic performance towards ethanol oxidation. *Chemistry* **2015**, *21*, 17779–17785. [CrossRef] [PubMed]

65. Evanoff, D.D., Jr.; Chumanov, G. Synthesis and optical properties of silver nanoparticles and arrays. *ChemPhysChem* **2005**, *6*, 1221–1231. [CrossRef] [PubMed]
66. Le, T.P.; Lee, Y.; Hoang, T.T.T.; Park, K.M.; Park, K.D. Catechol-rich gelatin hydrogels in situ hybridizations with silver nanoparticle for enhanced antibacterial activity. *Mater. Sci. Eng. C* **2018**, *92*, 52–60.
67. Begum, R.; Farooqi, Z.H.; Butt, Z.; Wu, Q.; Wu, W.; Irfan, A. Engineering of responsive polymer based nano-reactors for facile mass transport and enhanced catalytic degradation of 4-nitrophenol. *J. Environ. Sci.* **2018**, *72*, 43–52. [CrossRef] [PubMed]
68. Ullah, K.S.; Saleh, T.A.; Wahab, A.; Khan, M.H.U.; Khan, D.; Ullah, K.W.; Rahim, A.; Kamal, S.; Ullah, K.F.; Fahad, S. Nanosilver: New ageless and versatile biomedical therapeutic scaffold. *Int. J. Nanomed.* **2018**, *13*, 733–762. [CrossRef] [PubMed]
69. Wei, L.; Lu, J.; Xu, H.; Patel, A.; Chen, Z.-S.; Chen, G. Silver nanoparticles: Synthesis, properties, and therapeutic applications. *Drug Discov. Today* **2015**, *20*, 595–601. [CrossRef] [PubMed]
70. Asanithi, P.; Chaiyakun, S.; Limsuwan, P. Growth of silver nanoparticles by DC magnetron sputtering. *J. Nanomater.* **2012**, *2012*, 963609. [CrossRef]
71. Iravani, S.; Korbekandi, H.; Mirmohammadi, S.V.; Zolfaghari, B. Synthesis of silver nanoparticles: Chemical, physical and biological methods. *Res. Pharm. Sci.* **2014**, *9*, 385–406.
72. El-Nour, K.M.A.; Eftaiha, A.; Al-Warthan, A.; Ammar, R.A. Synthesis and applications of silver nanoparticles. *Arab. J. Chem.* **2010**, *3*, 135–140. [CrossRef]
73. Tien, D.C.; Tseng, K.H.; Liao, C.Y.; Huang, J.C.; Tsung, T.T. Discovery of ionic silver in silver nanoparticle suspension fabricated by arc discharge method. *J. Alloys. Compd.* **2008**, *463*, 408–411. [CrossRef]
74. Kosmala, A.; Wright, R.; Zhang, Q.; Kirby, P. Synthesis of silver nano particles and fabrication of aqueous Ag inks for inkjet printing. *Mater. Chem. Phys.* **2011**, *129*, 1075–1080. [CrossRef]
75. Nakamura, M.; Oyane, A.; Shimizu, Y.; Miyata, S.; Saeki, A.; Miyaji, H. Physicochemical fabrication of antibacterial calcium phosphate submicrospheres with dispersed silver nanoparticles via coprecipitation and photoreduction under laser irradiation. *Acta Biomater.* **2016**, *46*, 299–307. [CrossRef] [PubMed]
76. Shrivastava, S.; Bera, T.; Roy, A.; Singh, G.; Ramachandrarao, P.; Dash, D. Characterization of enhanced antibacterial effects of novel silver nanoparticles. *Nanotechnology* **2007**, *18*, 225103. [CrossRef]
77. Sotiriou, G.A.; Pratsinis, S.E. Antibacterial activity of nanosilver ions and particles. *Environ. Sci. Technol.* **2010**, *44*, 5649–5654. [CrossRef] [PubMed]
78. Nguyen, V.Q.; Ishihara, M.; Nakamura, S.; Hattori, H.; Ono, T.; Miyahira, Y.; Matsui, T. Interaction of silver nanoparticles and chitin powder with different sizes and surface structures: The correlation with antimicrobial activities. *J. Nanomater.* **2013**, *2013*, 13. [CrossRef]
79. Ramar, M.; Manikandan, B.; Marimuthu, P.N.; Raman, T.; Mahalingam, A.; Subramanian, P.; Karthick, S.; Munusamy, A. Synthesis of silver nanoparticles using Solanum trilobatum fruits extract and its antibacterial, cytotoxic activity against human breast cancer cell line MCF 7. *Spectrochim. Acta A* **2015**, *140*, 223–228. [CrossRef]
80. Gurunathan, S.; Han, J.W.; Kwon, D.N.; Kim, J.H. Enhanced antibacterial and anti-biofilm activities of silver nanoparticles against Gram-negative and Gram-positive bacteria. *Nanoscale Res. Lett.* **2014**, *9*, 373. [CrossRef]
81. Shameli, K.; Ahmad, M.B.; Zargar, M.; Yunus, W.M.; Rustaiyan, A.; Ibrahim, N.A. Synthesis of silver nanoparticles in montmorillonite and their antibacterial behavior. *Int. J. Nanomed.* **2011**, *6*, 581–590. [CrossRef]
82. Karmali, M.A. Factors in the emergence of serious human infections associated with highly pathogenic strains of shiga toxin-producing Escherichia coli. *Int. J. Med. Microbiol.* **2018**, *308*, 1067–1072. [CrossRef] [PubMed]
83. Devi, L.S.; Joshi, S.R. Antimicrobial and synergistic effects of silver nanoparticles synthesized using soil fungi of high altitudes of eastern himalaya. *Mycobiology* **2012**, *40*, 27–34. [CrossRef] [PubMed]
84. Velusamy, P.; Su, C.H.; Venkat Kumar, G.; Adhikary, S.; Pandian, K.; Gopinath, S.C.; Chen, Y.; Anbu, P. Biopolymers Regulate Silver Nanoparticle under Microwave Irradiation for Effective Antibacterial and Antibiofilm Activities. *PLoS ONE* **2016**, *11*, e0157612. [CrossRef] [PubMed]
85. Mehrbod, P.; Motamed, N.; Tabatabaian, M.; Estyar, R.S.; Amini, E.; Shahidi, M.; Kheiri, M. In vitro antiviral effect of "nanosilver" on influenza virus. *DARU J. Pharm. Sci.* **2009**, *17*, 88–93.
86. Speshock, J.L.; Murdock, R.C.; Braydich-Stolle, L.K.; Schrand, A.M.; Hussain, S.M. Interaction of silver nanoparticles with Tacaribe virus. *J. Nanobiotechnol.* **2010**, *8*, 19. [CrossRef] [PubMed]

87. Gaikwad, S.; Ingle, A.; Gade, A.; Rai, M.; Falanga, A.; Incoronato, N.; Russo, L.; Galdiero, S.; Galdiero, M. Antiviral activity of mycosynthesized silver nanoparticles against herpes simplex virus and human parainfluenza virus type 3. *Int. J. Nanomed.* **2013**, *8*, 4303–4314.
88. Baram-Pinto, D.; Shukla, S.; Perkas, N.; Gedanken, A.; Sarid, R. Inhibition of herpes simplex virus type 1 infection by silver nanoparticles capped with mercaptoethane sulfonate. *Bioconjug. Chem.* **2009**, *20*, 1497–1502. [CrossRef] [PubMed]
89. Lara, H.H.; Ayala-Nunez, N.V.; Ixtepan-Turrent, L.; Rodriguez-Padilla, C. Mode of antiviral action of silver nanoparticles against HIV-1. *J. Nanobiotechnol.* **2010**, *8*, 1. [CrossRef]
90. Elechiguerra, J.L.; Burt, J.L.; Morones, J.R.; Camacho-Bragado, A.; Gao, X.; Lara, H.H.; Yacaman, M.J. Interaction of silver nanoparticles with HIV-1. *J. Nanobiotechnol.* **2005**, *3*, 6. [CrossRef]
91. Rogers, J.V.; Parkinson, C.V.; Choi, Y.W.; Speshock, J.L.; Hussain, S.M. A preliminary assessment of silver nanoparticle inhibition of monkeypox virus plaque formation. *Nanoscale Res. Lett.* **2008**, *3*, 129–133. [CrossRef]
92. Stensberg, M.C.; Wei, Q.; McLamore, E.S.; Porterfield, D.M.; Wei, A.; Sepulveda, M.S. Toxicological studies on silver nanoparticles: Challenges and opportunities in assessment, monitoring and imaging. *Nanomedicine* **2011**, *6*, 879–898. [CrossRef] [PubMed]
93. Vazquez-Munoz, R.; Borrego, B.; Juarez-Moreno, K.; Garcia-Garcia, M.; Mota Morales, J.D.; Bogdanchikova, N.; Huerta-Saquero, A. Toxicity of silver nanoparticles in biological systems: Does the complexity of biological systems matter? *Toxicol. Lett.* **2017**, *276*, 11–20. [CrossRef] [PubMed]
94. El Mahdy, M.M.; Eldin, T.A.; Aly, H.S.; Mohammed, F.F.; Shaalan, M.I. Evaluation of hepatotoxic and genotoxic potential of silver nanoparticles in albino rats. *Exp. Toxicol. Pathol.* **2015**, *67*, 21–29. [CrossRef] [PubMed]
95. Pinzaru, I.; Coricovac, D.; Dehelean, C.; Moaca, E.A.; Mioc, M.; Baderca, F.; Sizemore, I.; Brittle, S.; Marti, D.; Calina, C.D.; et al. Stable PEG-coated silver nanoparticles-A comprehensive toxicological profile. *Food Chem. Toxicol.* **2018**, *111*, 546–556. [CrossRef] [PubMed]
96. Majeed, S.; Danish, M.; Zahrudin, A.H.B.; Dash, G.K. Biosynthesis and characterization of silver nanoparticles from fungal species and its antibacterial and anticancer effect. *Karbala Int. J. Mod. Sci.* **2018**, *4*, 86–92. [CrossRef]
97. Dakal, T.C.; Kumar, A.; Majumdar, R.S.; Yadav, V. Mechanistic Basis of Antimicrobial Actions of Silver Nanoparticles. *Front. Microbiol.* **2016**, *7*, 1831. [CrossRef] [PubMed]
98. Wu, F.; Harper, B.J.; Harper, S.L. Differential dissolution and toxicity of surface functionalized silver nanoparticles in small-scale microcosms: Impacts of community complexity. *Environ. Sci. Nano* **2017**, *4*, 359–372. [CrossRef]
99. Senthil, B.; Devasena, T.; Prakash, B.; Rajasekar, A. Non-cytotoxic effect of green synthesized silver nanoparticles and its antibacterial activity. *J. Photochem. Photobiol. B* **2017**, *177*, 1–7. [CrossRef]
100. Kora, A.J.; Sashidhar, R. Biogenic silver nanoparticles synthesized with rhamnogalacturonan gum: Antibacterial activity, cytotoxicity and its mode of action. *Arab. J. Chem.* **2018**, *11*, 313–323. [CrossRef]
101. Kinoda, J.; Ishihara, M.; Hattori, H.; Nakamura, S.; Fukuda, K.; Yokoe, H. Cytotoxicity of Silver Nanoparticle and Chitin-Nanofiber Sheet Composites Caused by Oxidative Stress. *Nanomaterials* **2016**, *6*, 189. [CrossRef]
102. Sudha, A.; Jeyakanthan, J.; Srinivasan, P. Green synthesis of silver nanoparticles using Lippia nodiflora aerial extract and evaluation of their antioxidant, antibacterial and cytotoxic effects. *Res. Effic. Technol.* **2017**, *3*, 506–515. [CrossRef]
103. Burdusel, A.C.; Gherasim, O.; Grumezescu, A.M.; Mogoanta, L.; Ficai, A.; Andronescu, E. Biomedical Applications of Silver Nanoparticles: An Up-to-Date Overview. *Nanomaterials* **2018**, *8*, 681. [CrossRef] [PubMed]
104. Akter, M.; Sikder, M.T.; Rahman, M.M.; Ullah, A.; Hossain, K.F.B.; Banik, S.; Hosokawa, T.; Saito, T.; Kurasaki, M. A systematic review on silver nanoparticles-induced cytotoxicity: Physicochemical properties and perspectives. *J. Adv. Res.* **2018**, *9*, 1–16. [CrossRef] [PubMed]
105. Morse, S.S. Factors in the emergence of infectious diseases. *Emerg. Infect. Dis.* **1995**, *1*, 7–15. [CrossRef] [PubMed]
106. Green, A. Remembering health workers who died from Ebola in 2014. *Lancet* **2014**, *384*, 2201–2206. [CrossRef]
107. Al-Tawfiq, J.A.; Memish, Z.A. Middle East respiratory syndrome coronavirus in the last two years: Health care workers still at risk. *Am. J. Infect. Control* **2019**. [CrossRef] [PubMed]
108. Clement, R. Is it time for an evidence based uniform for doctors? *BMJ* **2012**, *345*, e8286. [CrossRef] [PubMed]

109. Nguyen, V.Q.; Ishihara, M.; Kinoda, J.; Hattori, H.; Nakamura, S.; Ono, T.; Miyahira, Y.; Matsui, T. Development of antimicrobial biomaterials produced from chitin-nanofiber sheet/silver nanoparticle composites. *J. Nanobiotechnol.* **2014**, *12*, 49. [CrossRef] [PubMed]
110. Ishihara, M.; Nakanishi, K.; Ono, K.; Sato, M.; Saito, Y.; Yura, H.; Matsui, T.; Hattori, H.; Uenoyama, M.; Kurita, A. Photocrosslinkable chitosan as a dressing for wound occlusion and accelerator in healing process. *Biomaterials* **2002**, *23*, 833–840. [CrossRef]
111. Nakamura, S.; Nambu, M.; Ishizuka, T.; Hattori, H.; Kanatani, Y.; Takase, B.; Kishimoto, S.; Amano, Y.; Aoki, H.; Kiyosawa, T.; et al. Effect of controlled release of fibroblast growth factor-2 from chitosan/fucoidan micro complex-hydrogel on in vitro and in vivo vascularization. *J. Biomed. Mater. Res. A* **2008**, *85*, 619–627. [CrossRef]
112. Kiyozumi, T.; Kanatani, Y.; Ishihara, M.; Saitoh, D.; Shimizu, J.; Yura, H.; Suzuki, S.; Okada, Y.; Kikuchi, M. Medium (DMEM/F12)-containing chitosan hydrogel as adhesive and dressing in autologous skin grafts and accelerator in the healing process. *J. Biomed. Mater. Res.* **2006**, *79*, 129–136. [CrossRef] [PubMed]
113. Ishihara, M.; Fujita, M.; Obara, K.; Hattori, H.; Nakamura, S.; Nambu, M.; Kiyosawa, T.; Maehara, T. Controlled releases of FGF-2 and paclitaxel from chitosan hydrogels and their subsequent effects on wound repair, angiogenesis, and tumor growth. *Curr. Drug. Deliv.* **2006**, *3*, 351–358. [CrossRef] [PubMed]
114. Masuoka, K.; Ishihara, M.; Asazuma, T.; Hattori, H.; Matsui, T.; Takase, B.; Kanatani, Y.; Fujita, M.; Saito, Y.; Yura, H.; et al. Interaction of chitosan with fibroblast growth factor-2 and its protection from inactivation. *Biomaterials* **2005**, *26*, 3277–3284. [CrossRef] [PubMed]
115. Lu, H.; Liu, Y.; Guo, J.; Wu, H.; Wang, J.; Wu, G. Biomaterials with Antibacterial and Osteoinductive Properties to Repair Infected Bone Defects. *Int. J. Mol. Sci.* **2016**, *17*, 334. [CrossRef] [PubMed]
116. Nam, S.; Condon, B.D.; Delhom, C.D.; Fontenot, K.R. Silver-cotton nanocomposites: Nano-design of microfibrillar structure causes morphological changes and increased tenacity. *Sci. Rep.* **2016**, *6*, 37320. [CrossRef] [PubMed]
117. Zheng, Y.; Cai, C.; Zhang, F.; Monty, J.; Linhardt, R.J.; Simmons, T.J. Can natural fibers be a silver bullet? Antibacterial cellulose fibers through the covalent bonding of silver nanoparticles to electrospun fibers. *Nanotechnology* **2016**, *27*, 055102. [CrossRef] [PubMed]
118. Ghorbani, P.; Soltani, M.; Homayouni-Tabrizi, M.; Namvar, F.; Azizi, S.; Mohammad, R.; Moghaddam, A.B. Sumac silver novel biodegradable nano composite for bio-medical application: Antibacterial activity. *Molecules* **2015**, *20*, 12946–12958. [CrossRef]
119. Sim, W.; Barnard, R.T.; Blaskovich, M.A.T.; Ziora, Z.M. Antimicrobial Silver in Medicinal and Consumer Applications: A Patent Review of the Past Decade (2007–2017). *Antibiotics* **2018**, *7*, 93. [CrossRef]
120. Trop, M.; Novak, M.; Rodl, S.; Hellbom, B.; Kroell, W.; Goessler, W. Silver-coated dressing acticoat caused raised liver enzymes and argyria-like symptoms in burn patient. *J. Trauma* **2006**, *60*, 648–652. [CrossRef]
121. Hirai, T.; Yoshioka, Y.; Izumi, N.; Ichihashi, K.; Handa, T.; Nishijima, N.; Uemura, E.; Sagami, K.; Takahashi, H.; Yamaguchi, M.; et al. Metal nanoparticles in the presence of lipopolysaccharides trigger the onset of metal allergy in mice. *Nat. Nanotechnol.* **2016**, *11*, 808–816. [CrossRef]
122. You, C.; Li, Q.; Wang, X.; Wu, P.; Ho, J.K.; Jin, R.; Zhang, L.; Shao, H.; Han, C. Silver nanoparticle loaded collagen/chitosan scaffolds promote wound healing via regulating fibroblast migration and macrophage activation. *Sci. Rep.* **2017**, *7*, 10489. [CrossRef] [PubMed]
123. Zulkifli, F.H.; Hussain, F.S.J.; Zeyohannes, S.S.; Rasad, M.; Yusuff, M.M. A facile synthesis method of hydroxyethyl cellulose-silver nanoparticle scaffolds for skin tissue engineering applications. *Mater. Sci. Eng. C Mater. Biol. Appl.* **2017**, *79*, 151–160. [CrossRef] [PubMed]
124. Gong, C.P.; Li, S.C.; Wang, R.Y. Development of biosynthesized silver nanoparticles based formulation for treating wounds during nursing care in hospitals. *J. Photochem. Photobiol. B* **2018**, *183*, 137–141. [CrossRef] [PubMed]
125. Negut, I.; Grumezescu, V.; Grumezescu, A.M. Treatment Strategies for Infected Wounds. *Molecules* **2018**, *23*, 2392. [CrossRef] [PubMed]
126. Yang, Y.; Hu, H. A review on antimicrobial silver absorbent wound dressings applied to exuding wounds. *J. Microb. Biochem. Technol.* **2015**, *7*, 228–233.
127. Heilman, S.; Silva, L. Silver and titanium nanoparticles used as coating on polyurethane catheters. *J. Nano Res.* **2017**, *47*, 17–23. [CrossRef]

128. Thomas, R.; Mathew, S.; Nayana, A.R.; Mathews, J.; Radhakrishnan, E.K. Microbially and phytofabricated Ag NPs with different mode of bactericidal action were identified to have comparable potential for surface fabrication of central venous catheters to combat Staphylococcus aureus biofilm. *J. Photochem. Photobiol. B* **2017**, *171*, 96–103. [CrossRef]
129. Wu, K.; Yang, Y.; Zhang, Y.; Deng, J.; Lin, C. Antimicrobial activity and cytocompatibility of silver nanoparticles coated catheters via a biomimetic surface functionalization strategy. *Int. J. Nanomed.* **2015**, *10*, 7241–7252.
130. Kumar, C.G.; Sujitha, P. Green synthesis of Kocuran-functionalized silver glyconanoparticles for use as antibiofilm coatings on silicone urethral catheters. *Nanotechnology* **2014**, *25*, 325101. [CrossRef]
131. Cui, Z.; Wang, B.; Zhong, Z.; Sun, Y.; Sun, Q.; Yang, G.; Bian, L. Impact of antibiotic- and silver-impregnated external ventricular drains on the risk of infections: A systematic review and meta-analysis. *Am. J. Infect. Control* **2015**, *43*, e23–e32. [CrossRef]
132. Atkinson, R.A.; Fikrey, L.; Vail, A.; Patel, H.C. Silver-impregnated external-ventricular-drain-related cerebrospinal fluid infections: A meta-analysis. *J. Hosp. Infect.* **2016**, *92*, 263–272. [CrossRef]
133. Konstantelias, A.A.; Vardakas, K.Z.; Polyzos, K.A.; Tansarli, G.S.; Falagas, M.E. Antimicrobial-impregnated and -coated shunt catheters for prevention of infections in patients with hydrocephalus: A systematic review and meta-analysis. *J. Neurosurg.* **2015**, *122*, 1096–1112. [CrossRef] [PubMed]
134. Thomas, R.; Soumya, K.R.; Mathew, J.; Radhakrishnan, E.K. Inhibitory effect of silver nanoparticle fabricated urinary catheter on colonization efficiency of Coagulase Negative Staphylococci. *J. Photochem. Photobiol. B* **2015**, *149*, 68–77. [CrossRef] [PubMed]
135. Jishma, P.; Narayanan, R.; Snigdha, S.; Thomas, R.; Radhakrishnan, E. Rapid degradative effect of microbially synthesized silver nanoparticles on textile dye in presence of sunlight. *Biocatal. Agric. Biotechnol.* **2018**, *14*, 410–417. [CrossRef]
136. Ballo, M.K.; Rtimi, S.; Pulgarin, C.; Hopf, N.; Berthet, A.; Kiwi, J.; Moreillon, P.; Entenza, J.M.; Bizzini, A. In Vitro and In Vivo Effectiveness of an Innovative Silver-Copper Nanoparticle Coating of Catheters to Prevent Methicillin-Resistant Staphylococcus aureus Infection. *Antimicrob. Agents Chemother.* **2016**, *60*, 5349–5356. [CrossRef] [PubMed]
137. Mala, R.; Annie, A.A.; Celsia, A.S.R.; Geerthika, S.; Kiruthika, N.; VazagaPriya, C.; Srinivasa, K.K. Foley catheters functionalised with a synergistic combination of antibiotics and silver nanoparticles resist biofilm formation. *IET Nanobiotechnol.* **2017**, *11*, 612–620. [CrossRef] [PubMed]
138. Jamal, M.; Ahmad, W.; Andleeb, S.; Jalil, F.; Imran, M.; Nawaz, M.A.; Hussain, T.; Ali, M.; Rafiq, M.; Kamil, M.A. Bacterial biofilm and associated infections. *J. Chin. Med. Assoc.* **2018**, *81*, 7–11. [CrossRef] [PubMed]
139. Dayyoub, E.; Frant, M.; Pinnapireddy, S.R.; Liefeith, K.; Bakowsky, U. Antibacterial and anti-encrustation biodegradable polymer coating for urinary catheter. *Int. J. Pharm.* **2017**, *531*, 205–214. [CrossRef]
140. Stickler, D. Bacterial biofilms and the encrustation of urethral catheters. *Biofouling* **1996**, *9*, 293–305. [CrossRef]
141. Noronha, V.T.; Paula, A.J.; Duran, G.; Galembeck, A.; Cogo-Muller, K.; Franz-Montan, M.; Duran, N. Silver nanoparticles in dentistry. *Dent. Mater.* **2017**, *33*, 1110–1126. [CrossRef]
142. Correa, J.M.; Mori, M.; Sanches, H.L.; da Cruz, A.D.; Poiate, E.J.; Poiate, I.A. Silver nanoparticles in dental biomaterials. *Int. J. Biomater.* **2015**, *2015*, 485275. [CrossRef] [PubMed]
143. Kejlova, K.; Kasparkova, V.; Krsek, D.; Jirova, D.; Kolarova, H.; Dvorakova, M.; Tomankova, K.; Mikulcova, V. Characteristics of silver nanoparticles in vehicles for biological applications. *Int. J. Pharm.* **2015**, *496*, 878–885. [CrossRef] [PubMed]
144. Divakar, D.D.; Jastaniyah, N.T.; Altamimi, H.G.; Alnakhli, Y.O.; Muzaheed; Alkheraif, A.A.; Haleem, S. Enhanced antimicrobial activity of naturally derived bioactive molecule chitosan conjugated silver nanoparticle against dental implant pathogens. *Int. J. Biol. Macromol.* **2018**, *108*, 790–797. [CrossRef] [PubMed]
145. Ramirez-Lee, M.A.; Aguirre-Banuelos, P.; Martinez-Cuevas, P.P.; Espinosa-Tanguma, R.; Chi-Ahumada, E.; Martinez-Castanon, G.A.; Gonzalez, C. Evaluation of cardiovascular responses to silver nanoparticles (Ag NPs) in spontaneously hypertensive rats. *Nanomedicine* **2018**, *14*, 385–395. [CrossRef] [PubMed]
146. DiVincenzo, G.D.; Giordano, C.J.; Schriever, L.S. Biologic monitoring of workers exposed to silver. *Int. Arch. Occup. Environ. Health* **1985**, *56*, 207–215. [CrossRef] [PubMed]

International Journal of
Molecular Sciences

MDPI

Article

Ultraviolet Irradiation Enhances the Microbicidal Activity of Silver Nanoparticles by Hydroxyl Radicals

Shingo Nakamura [1,*], Naoko Ando [1], Masahiro Sato [2] and Masayuki Ishihara [1]

[1] Division of Biomedical Engineering, National Defense Medical College Research Institute, Saitama 359-8513, Japan; naoandokoro@gmail.com (N.A.); ishihara@ndmc.ac.jp (M.I.)
[2] Section of Gene Expression Regulation, Frontier Science Research Center, Kagoshima University, Kagoshima 890-8544, Japan; masasato@m.kufm.kagoshima-u.ac.jp
* Correspondence: snaka@ndmc.ac.jp; Tel.: +81-4-2995-1211

Received: 8 April 2020; Accepted: 29 April 2020; Published: 30 April 2020

Abstract: It is known that silver has microbicidal qualities; even at a low concentration, silver is active against many kinds of bacteria. Silver nanoparticles (AgNPs) have been extensively studied for a wide range of applications. Alternately, the toxicity of silver to human cells is considerably lower than that to bacteria. Recent studies have shown that AgNPs also have antiviral activity. We found that large amounts of hydroxyl radicals—highly reactive molecular species—are generated when AgNPs are irradiated with ultraviolet (UV) radiation with a wavelength of 365 nm, classified as ultraviolet A (UVA). In this study, we used electron spin resonance direct detection to confirm that UV irradiation of AgNPs produced rapid generation of hydroxyl radicals. As hydroxyl radicals are known to degrade bacteria, viruses, and some chemicals, the enhancement of the microbicidal activity of AgNPs by UV radiation could be valuable for the protection of healthcare workers and the prevention of the spread of infectious diseases.

Keywords: healthcare workers; hydroxyl radical; medical application; microbicidal activity; silver nanoparticles (AgNPs); ultraviolet (UV) irradiation

1. Introduction

The microbicidal effects of silver have widely been known and are even apparent at low concentrations. Silver has antibacterial action against a wide range of species, and its toxicity to human cells is considerably lower than that toward bacteria [1–5]. Berger et al. [1] reported that approximately 1 μg/mL of silver ions is effective for suppressing the growth of many types of bacteria, including *Escherichia coli* (*E. coli*), Staphylococci, Providencia, Serratia, and *Pseudomonas aeruginosa*. Ip et al. [2] demonstrated that several silver ion-containing vulneraries covering materials exhibited antibacterial activity against methicillin-resistant *Staphylococcus aureus*. Although the details of the mechanism by which silver produces its antibacterial activity remains largely unknown, the production of silver ions is thought to be one of the main factors [6]. Silver ions react with enzymes that require thiol (–SH) groups for the cysteine residue of their active sites; such enzymes are succinate dehydrogenase and nicotinamide adenine dinucleotide (NADH)-cytochrome b, which inhibit the metabolic pathways needed for the survival of bacteria [7].

"Nano" metallic particles are defined as those with sized 1 to 100 nm [8]. Metallic nanoparticles exhibit a size-specific property known as surface plasmon resonance (SPR) [9]. Due to their lager surface area, silver nanoparticles (AgNPs) enable the continuous release of silver ions at low concentrations, producing antibacterial action against a wide range of species [10]. Recently, AgNPs have also been shown to have antiviral activity. The size of the AgNPs is essential to their antiviral effects, as AgNPs act on the surface of the virus and physically inhibit contact with host cells [11–13]. Lara et al. [14] demonstrated that AgNPs of less than 10 nm preferentially adsorb the envelope of

human immunodeficiency virus-1 (HIV-1) and prevent the viral infection of host cells. Gaikwad et al. [15] reported that AgNPs of 7–20 nm exhibited antiviral effects against herpes simplex virus types 1 and 2, and human parainfluenza virus type 3.

We previously reported on the possibility of using AgNPs to prevent infection of healthcare workers [16]. In this report, we describe a novel, convenient method for the synthesis of AgNPs of controlled size and demonstrate that chitin or chitosan-based materials act as excellent stabilizers of the AgNPs [17–19]. These composite materials, when coated with AgNPs, can exhibit strong microbicidal activity [20] and virus inactivation activity against the influenza A virus subtype H1N1 [21]. In addition to generating free silver ions, it has been suggested that AgNPs may yield reactive oxygen species (ROS), leading to oxidative stress [22]. Thus, the AgNPs could be widely used as antibacterial and antiviral materials in a variety of fields using clothing (doctor and nurse uniforms, security protection coats, masks, and counter cloths), plastics (gloves), and papers. We suggest that AgNPs may be valuable materials, owing to their bactericidal activity, when the levels of ROS produced from AgNPs are well-controlled.

Metal nanoparticles, including AgNPs, exhibit a property known as SPR. The absorption and scattering of light by AgNPs is highly efficient. The excitation of metal atoms on a metal surface stimulated by photons with a specific wavelength causes a collective oscillation of conduction electrons. SPR-based absorption spectroscopy depends on the size, shape, and composition of the metal surface, and on changes in response to alterations of the metal surface [23]. This approach can be applied to the detection of structural changes caused by the adsorption of substances onto metals, and several biosensing devices employ this principle. In this study, we investigated the generation of radicals following ultraviolet (UV) irradiation of AgNPs and the effect of the generated radicals as bactericides. Taking this phenomenon as a hint, we hypothesized that radicals are generated when AgNPs are irradiated with specific wavelengths of UV radiation that cause rapid oscillations in electron density and collisions in subsequent low-energy ion atoms.

2. Results and Discussion

2.1. UV Irradiation-Induced Generation of Radicals

The silver nanoparticles used in this study were prepared using a method we previously reported [20]. The resulting AgNPs exhibited a maximum absorption at 390 nm (Figure 1), which concurs with a previous report [17–19], and particle sizes were ~5 nm [17–19,24]. To produce UV radiation, we used a universal handy-type UV lamp frequently employed for the detection of ethidium bromide-stained DNA in agarose gel electrophoresis. The UV that the lamp was able to generate has a wavelength of 365 nm, putting it in the range of UVA (320 to 400 nm), which is safer than other types of UV radiation (i.e., UVC and UVB). UVB (280 to 320 nm) can cause a variety of damaging effects in various biological cells, whereas UVC (200 to 280 nm) is very hazardous to most organisms [25,26].

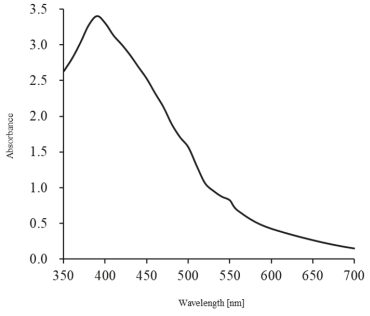

Figure 1. UV–Vis spectra of silver nanoparticles (AgNPs) used in this study. UV–Vis spectra from AgNPs in suspension peaked at 390 nm, which is considered as a representative pattern of the spherical AgNPs [17–19].

We first examined whether hydroxyl radicals are generated when a solution containing AgNPs is subjected to UV irradiation. Hydroxyl radicals were detected when a UV-irradiated solution was subjected to an electron paramagnetic resonance (EPR) analysis (Figure 2A). We measured the amounts of hydroxyl radicals in solutions of AgNPs by varying the time of UV irradiation from 0 to 30 min. The presence of hydroxyl radicals was discernible after adding AgNPs to Dulbecco's modified phosphate-buffered saline without Ca^{2+} and Mg^{2+}, pH 7.2 (PBS) ("0 min required for UV irradiation" in Figure 2B). Similar observations were made by Zhang et al. [27], who detected the presence of oxidative stress in natural samples, observing small amounts of hydroxyl radicals in aqueous AgNPs solutions. We observed UV irradiation-mediated enhanced production of hydroxyl radicals from AgNPs. The proportion of hydroxyl radicals increased as UV irradiation continued for up to 1 min and subsequently plateaued (Figure 2B). The amounts of hydroxyl radicals generated by UV irradiation for 1 and 3 min did not differ significantly. The lifespan of hydroxyl radicals generated was very short, at around 30 s (Figure 2C).

There are several possible mechanisms underlying the generation of hydroxyl radicals induced by UV irradiation of AgNPs. An SPR-mediated collective oscillation of conduction electrons may be generated on the surface of UV-irradiated AgNPs, leading to local generation of an enhanced electric field. Homolytic cleavage, a process in which the covalent bonds of water surrounding AgNPs are broken, may occur in response to the collective oscillation of conduction electrons, resulting in the generation of unpaired electrons as well as radicals. Unfortunately, the current results do not support this hypothesis, and further analysis is required to elucidate the mechanism of action.

As described in the Introduction, some reports claim that AgNPs yield ROS, which act as oxidative stressors to kill various types of bacteria [28–31]. However, these reports appear to rely on the indirect action of Ag, in which antibacterial activity might be elicited through oxidized peripheral substances or modified materials. Electron paramagnetic resonance spectroscopy is considered one of the standard methods for the quantification of ROS; however, the equipment is very expensive [32]. To our knowledge, there has only been one report indicating that this equipment is useful to detect radicals [27]. In this study, we demonstrated the usefulness of an EPR spectroscopy-based direct detection approach. Our present study differs from the experiments of Zhang et al. [27], who explored the mechanism by which ROS exerts microbicidal activity. We observed a 1.7-fold enhanced production of hydroxyl radicals when AgNPs were irradiated for 0.5 min, and 4.5-fold enhanced production when AgNPs were UV-irradiated for 1 min (Figure 2B). The increased levels of hydroxyl radicals should reflect enhanced microbicidal activity of AgNPs.

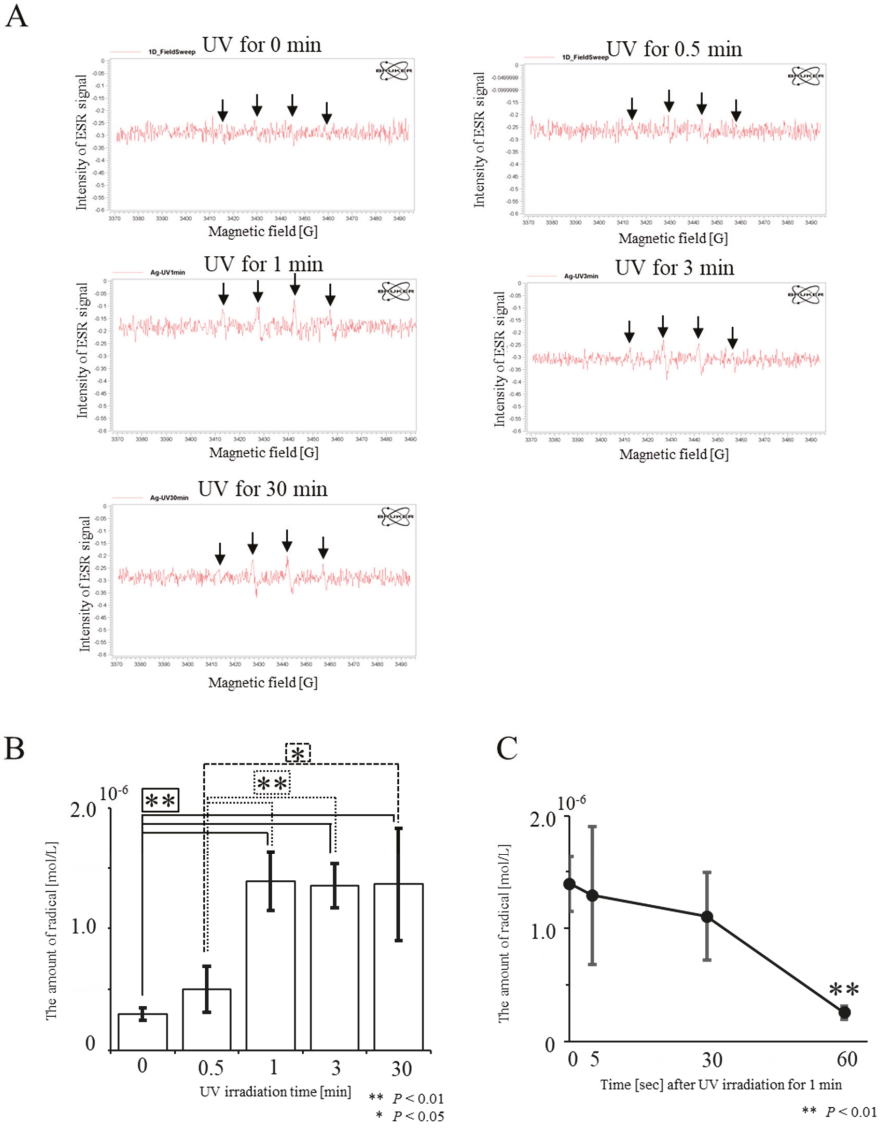

Figure 2. Detection of hydroxyl radicals from UV-irradiated AgNPs using electron paramagnetic resonance (EPR) spectroscopy for the detection of radicals. (**A**) Raw data obtained from AgNPs UV-irradiated for 0, 0.5, 1, 3, or 30 min. In "UV for 0 min", a very weak peak for hydroxyl radicals is apparent. Four peaks for hydroxyl radicals, indicated by arrows, are discernible in the UV-irradiation groups. (**B**) Evaluation of the amount of hydroxy radicals produced after UV irradiation of AgNPs. The amount of hydroxyl radicals was determined using software solution (Xenon) provided by the Bruker Corporation, from the raw data shown in A. There is no significant difference between "UV for 1 min" and "UV for 3 min". Experiments were repeated three times on different days. (**C**) Time-dependent decrease in the amounts of hydroxyl radicals generated after "UV for 1 min" at 30 s and thereafter the amount of hydroxyl radicals decreases rapidly.

2.2. Antibacterial Activity of UV-Irradiated AgNPs

We investigated whether UV-irradiated AgNPs inhibit the survival of the bacterium *E. coli*. Experiments were carried out using two approaches: In the first set of experiments, solutions containing AgNPs were UV-irradiated, and then mixed with *E. coli* prior to seeding onto agar plates (Figure 3). In the second approach, agar plates that had their surface coated with AgNPs were irradiated with UV and plated with *E. coil* (Figure 4).

In the first approach, PBS or PBS-containing AgNPs (PBS/AgNPs) was subjected to UV irradiation for 0, 1, or 3 min, after which, each solution was mixed with *E. coli* prior to plating onto agar plates. After overnight incubation at 37 °C, the number of *E. coli* colonies growing on plates coated with the AgNPs, which had been UV-irradiated for 1 min (Figure 3A-e,B), was significantly lower than that of untreated *E. coli* colonies ("UV irradiation for 1 min" in Figure 3A-b,B). Similar results were observed when UV irradiation was performed for 3 min ("UV irradiation for 3 min" in Figure 3A-f,B). The number of *E. coli* colonies grown in the "AgNPs" group that had not been irradiated was lower than that of those grown in the "PBS" group (PBS vs. AgNPs in Figure 3A-a,d,B). When *E. coli* were grown on plates coated with PBS, the number of *E. coli* colonies was not significantly different, even after UV irradiation for 3 min (Figure 3A-a–c,B). These results indicate that the antibacterial effects of AgNPs were significantly enhanced after exposure to UV for 1 min. This experimental system was modeled on sterilization by spraying chemicals. In this context, radicals generated from AgNPs after UV irradiation could be an alternative to the use of chemicals.

In the second approach, in an experimental group designated as "AgNPs/UV", *E. coli* were first plated onto agar plate surfaces pre-coated with AgNPs, after which the surfaces were subjected to UV exposure for 1 min ("AgNPs/UV" group). As controls, *E. coli* were first plated onto agar plate surfaces pre-coated with PBS, after which the surfaces were subjected to UV exposure for 1 min (the "PBS/UV" group) or were not UV-irradiated (the "PBS" group). As an additional control, *E. coli* were plated onto agar plates pre-coated with AgNPs, which were not subsequently UV-irradiated ("AgNPs" group). In the AgNPs/UV group, the growth of *E. coli* was suppressed (Figure 4A-a) compared with that of *E. coli* colonies in the other groups (a vs. c and d in Figure 4A,B). There were statistical differences between the PBS and AgNPs/UV groups ($P = 0.0009$) and between the PBS/UV and AgNPs/UV groups ($P = 0.002$) (Figure 4B). Additionally, as in the first experiment, the number of *E. coli* colonies in the AgNPs was lower than that of "PBS" group ($P = 0.009$; b vs. d in Figure 4A,B). These results suggest that the generation of radicals from AgNPs is accelerated after UV irradiation, leading to increased toxicity against *E. coli*. In this study, AgNPs were transiently kept under dry conditions, which was different from the situation in the first approach. As bacteria live in an environment enriched with water, the radicals provided by AgNPs might affect their survival. Alternatively, the survival of bacteria may be influenced by direct contact with AgNPs in the absence of water. In any event, complex materials coated with AgNPs can bring effective bactericidal effects.

Our results indicate that UV irradiation of materials coated with AgNPs produces increased antibacterial activity. The UV radiation used in this study was produced by a universal handy-type UV lamp capable of generating UV of 365 nm, which is within the range of UVA (320 to 400 nm) and is safer than other types of rays such as UVC (200 to 280 nm). UVC is highly biotoxic, in addition to its strong bactericidal action. In contrast, UVA is not only known to be involved in reducing skin elasticity and promoting aging, but also facilitates the exchange of intracellular substances, leading to promotion of cell's metabolism [26]. Ninety-nine percent of UV rays reaching the earth's surface from the sun are UVA. This is advantageous, especially when people wearing AgNP-coated protective clothing and medical masks continue to work outside without removing the clothes or masks, because their sterility can be maintained. This UV-enhanced AgNP-based microbicidal system is also useful for protecting against infection in case of occasional unintended contact when healthcare workers change clothes.

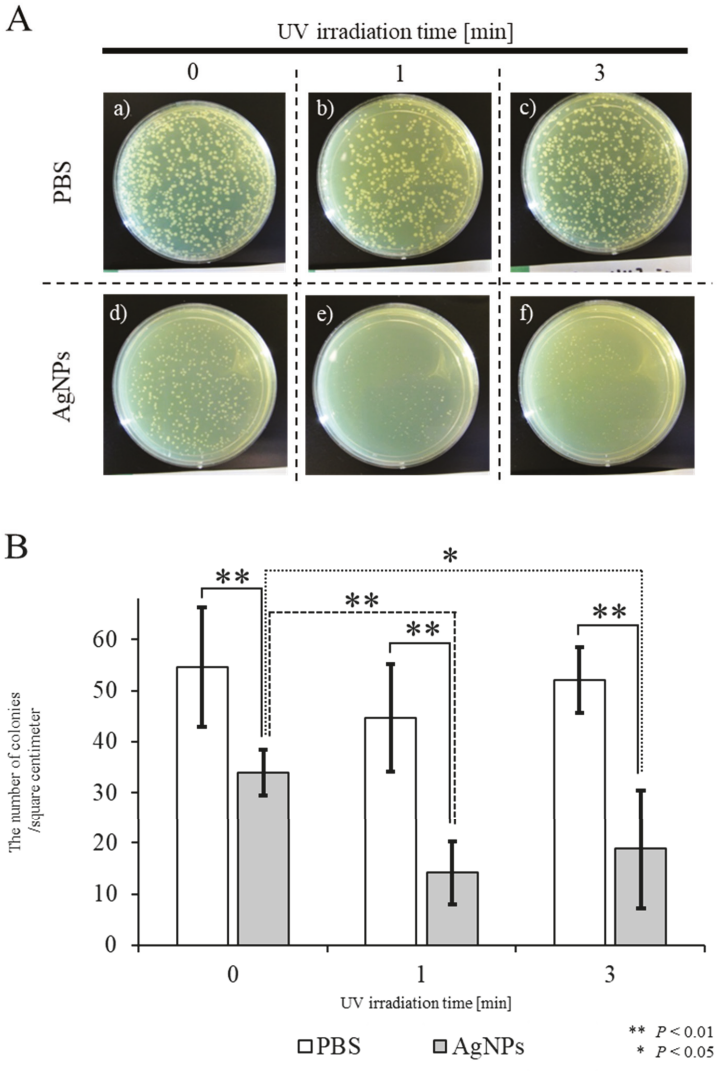

Figure 3. Bactericidal effects of UV-irradiated AgNPs on the survival of *E. coli*. (**A**) Appearance of *E. coli* colonies on agar plates after overnight incubation at 37 °C. Aqueous solutions of PBS or solutions containing AgNPs were subjected to UV irradiation for 0, 1, or 3 min, then each solution was mixed with *E. coli* prior to plating on agar plates. (**B**) Quantitation of colony numbers in each group. In the control PBS groups, shown as white columns, there was no difference in the survival of *E. coli* with or without UV irradiation. In the experimental groups, shown as gray columns, there was a slight decrease in the number of colonies after incubation with non-UV-irradiated AgNPs (designated as "UV for 0 min"). A significant decrease in the number of colonies was observed when *E. coli* were incubated with AgNPs UV-irradiated for one or three min, designated as "UV for 1 min" and "UV for 3 min", respectively. Experiments were repeated three times on different days.

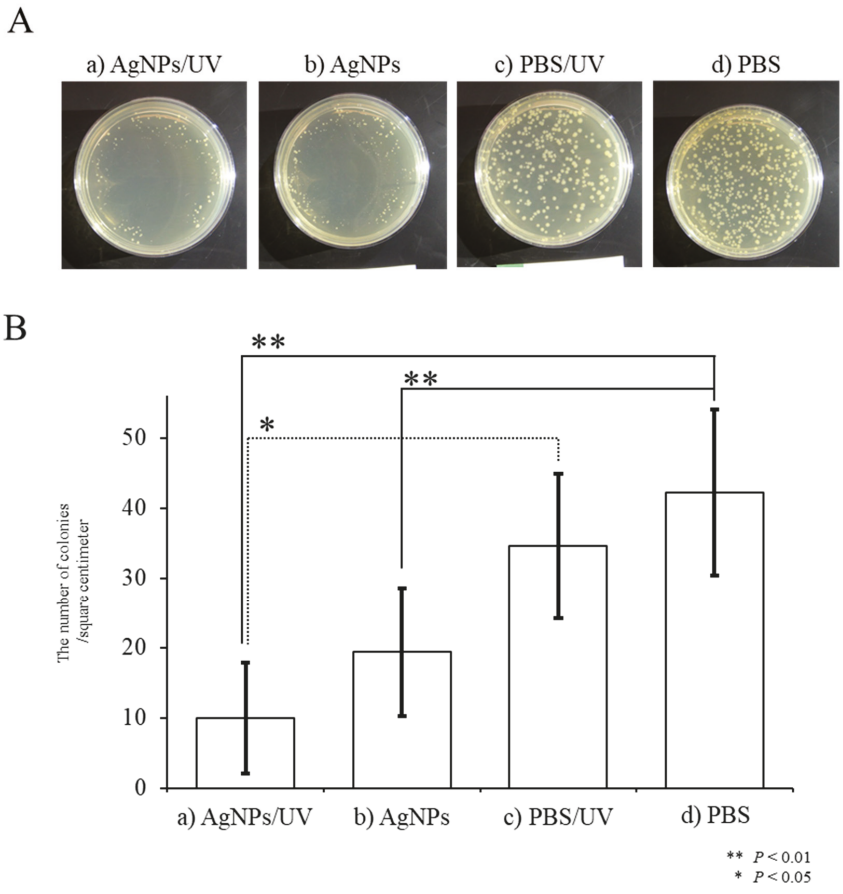

Figure 4. Bactericidal effects of hydroxyl radicals generated in situ on the survival of *E. coli*. (**A**) Appearance of *E. coli* colonies on agar plates after overnight incubation at 37 °C. A solution containing AgNPs was plated onto the surface of agar plates. Then, *E. coli* were seeded onto the surface of agar plates pre-coated with AgNPs, and the surface was subjected to UV exposure for one min (designated as "AgNPs/UV") or were not irradiated (designated as "AgNPs"). Alternatively, *E. coli* were plated onto non-coated agar plates, and then the surfaces were either subjected to UV exposure for one min (designated as "PBS/UV") or were not irradiated (designated as "PBS"). (**B**) Quantitation of colony numbers in each group. The presence of AgNPs reduced the number of *E. coli* colonies. The growth of *E. coli* was significantly suppressed when a plate was UV-irradiated for one min. Experiments were repeated three times on different days.

3. Materials and Methods

3.1. Preparation of AgNPs

A suspension of AgNPs (approximately 5 nm, 10 ng/μL, and pH7.2) was prepared as previously described [20,24]. One gram of silver-containing glass powder was dispersed in 100 mL of an aqueous solution of 0.8 wt% glucose in a 500 mL glass vial. The mixture was autoclaved at 121 °C at 200 kPa for 20 min, and then gradually cool to room temperature (~25 °C). The mixture was then centrifuged at 1500 rpm for 10 min at 25 °C, and the AgNPs were collected from the supernatant. To confirm the

existence of the AgNPs, UV–Vis spectrometer analysis was performed. The AgNPs were stored in the dark at 4 °C.

3.2. Measurement of Radicals from UV-Irradiated AgNPs

Fifty microliters (10 ng/μL) of the AgNPs was subjected to UV (365 nm) irradiation for 0.5, 1, 3, or 30 min. UV irradiation was performed using a Handheld UV Lamp (UVGL-58; Analytik Jena, CA, USA), which is generally used for the detection of DNA. After irradiation with UV, 10 μL of radical trapping reagent 5,5-dimethyl-1-pyrroline N-oxide (DMPO) (#LM-2110; Dojindo Laboratories, Kumamoto, Japan) was added to each sample followed by gentle mixing. Subsequently, the mixture was transferred to a 50 μL calibrated pipet (#2-000-050; Drummond Scientific Company, Pennsylvania, USA) and analyzed using a benchtop EPR (EMX-nano, Bruker Corporation, Massachusetts, USA) together with its proprietary software solution (Xenon). In this study, all experiments were performed in the same area where there was no external light.

3.3. Bactericidal Activity of UV-Irradiated AgNPs

The bactericidal activity of the UV-irradiated AgNPs was evaluated as previously reported [18], with a few modifications. *E. coli* (DH5; Takara Bio Inc., Shiga, Japan) were pre-cultured in 2 mL of LB medium and grown at 37 °C for 6 h until reaching an optical density at 600 nm (OD600) of 0.260. The *E. coli* cultures were diluted ten-fold with LB broth, and 100 μL of the diluted *E. coli* suspension was used in each study.

To examine the system that generates radicals in an aqueous solution from AgNPs and then sterilizes *E. coli* with the radicals, 30 μL of AgNP solution was irradiated using UV at a wavelength of 365 nm for either 1 or 3 min, then added immediately to the diluted *E. coli* suspensions. After 1 min, the mixture was plated onto agar plates and subsequently cultured overnight in a 37 °C incubator.

To investigate the bactericidal effect of the AgNP-coated plates on *E. coli*, 100 μL of AgNPs was plated on agar and left to air dry for 5 min at room temperature (~25 °C). The diluted *E. coli* suspension was then plated on agar and subjected to UV irradiation with a wavelength of 365 nm for 1 min. The culture plate was then incubated overnight at 37 °C.

After incubation, the plates were photographed (Cyber-shot; SONY Corp., Tokyo, Japan) and the number of colonies per square centimeter was counted. Bactericidal activity was evaluated from the number of colonies. As a control, PBS solution was used instead of AgNPs. The treatment with AgNPs after sterilization using an autoclave was performed on a clean bench. Aseptic conditions were stringently maintained during the plating of *E. coli* onto agar plates.

3.4. Statistical Analysis

The amount of hydroxyl radicals and the number of colonies in each examination are presented as mean ± standard deviation. Statistical analysis was performed using an unpaired *t*-test and one-way factorial analysis of variance. Scheffe's post hoc test was used for multiple comparisons. The *p*-values were calculated using the JMP14 for Windows software (SAS Institute Inc., North Carolina, USA). A *p*-value of less than 0.05 was considered to indicate statistical significance. Values of *p* less than 0.001 are marked with a double asterisk those less than 0.05 with a single asterisk.

4. Conclusions

AgNPs have been shown to have bactericidal action. In this study, we demonstrated that UV irradiation of AgNPs is effective at enhancing their activity. This bactericidal effect is attributable to the UV irradiation-mediated enhanced production of highly reactive hydroxyl radicals generated from AgNPs. The method of UV irradiation is very simple. The UV radiation used in this study was UVA, which is safer for humans than UVC rays and has stronger bactericidal activity. Although challenges persist regarding the effects of AgNPs on human health and the elucidation of the molecular mechanisms underlying the generation of radicals, our findings would contribute to the development of

medical materials for further protection against infection. For the practical use of AgNPs, investigating the effects of particle size, formulation, and the stabilizers (added for preventing aggregation of particles) on the behavior of nanometals might be important. Furthermore, if the behavior of nanometals is associated with SPR, the efficiency for radical generation may increase by changing the wavelength of the UV. Biosafety issues and environmental safety concerning AgNPs have also been a subject for discussion [22,33]. These concerns must be carefully addressed before putting AgNPs to practical use. Hydroxyl radicals, renowned as powerful oxidizing agents, are likely to be effective against viruses, bacteria, and in the degradation of chemicals. Therefore, our system may be valuable for the protection of healthcare workers from infection with pathogens such as COVID-19 and SARS, and in the prevention of outbreaks of similar diseases.

Author Contributions: S.N. conceived and designed the study, drafted the manuscript, and revised the manuscript; N.A. performed all experiments and created figures; M.S. was involved in providing some experimental ideas and critically revised the manuscript; M.I. revised the manuscript. All authors have read and agreed to the published version of the manuscript.

Acknowledgments: This study was partly supported by JSPS KAKENHI (no. 19K22787 for S.N.).

Conflicts of Interest: The founding sponsors had no role in the design of the paper.

Abbreviations

AgNPs	silver nanoparticles
COVID-19	coronavirus disease 2019
DMPO	5,5-dimethyl-1-pyrroline N-oxide
E. coli	*Escherichia coli*
EPR	electron paramagnetic resonance
HIV-1	human immunodeficiency virus-1
HSV	herpes simplex virus
MRSA	methicillin-resistant *Staphylococcus aureus*
NADH	nicotinamide adenine dinucleotide
PBS	Dulbecco's modified phosphate-buffered saline without Ca^{2+} and Mg^{2+}, pH 7.2
ROS	reactive oxygen species
SARS	severe acute respiratory syndrome
SPR	surface plasmon resonance
UV	ultraviolet
UVA	ultraviolet A (320 to 400 nm)
UVB	ultraviolet B (280 to 320 nm)
UVC	ultraviolet C (200 to 280 nm)

References

1. Berger, T.J.; Spadaro, J.A.; Chapin, S.E.; Becker, R.O. Electrically generated silver ions: Quantitative effects on bacterial and mammalian cells. *Antimicrob. Agents Chemother.* **1976**, *9*, 357–358. [CrossRef] [PubMed]
2. Ip, M.; Lui, S.L.; Poon, V.K.; Lung, I.; Burd, A. Antimicrobial activities of silver dressings: An in vitro comparison. *J. Med. Microbiol.* **2006**, *55*, 59–63. [CrossRef] [PubMed]
3. Silvestry-Rodriguez, N.; Sicairos-Ruelas, E.E.; Gerba, C.P.; Bright, K.R. Silver as a disinfectant. *Rev. Environ. Contam. Toxicol.* **2007**, *191*, 23–45. [CrossRef] [PubMed]
4. Alexander, J.W. History of the medical use of silver. *Surg. Infect.* **2009**, *10*, 289–292. [CrossRef]
5. Liao, C.; Li, Y.; Tjong, S.C. Bactericidal and cytotoxic properties of silver nanoparticles. *Int. J. Mol. Sci.* **2019**, *20*, 449. [CrossRef] [PubMed]
6. Marambio-Jones, C.; Hoek, E.M.V. A review of the antibacterial effects of silver nanomaterials and potential implications for human health and the environment. *J. Nanopart. Res.* **2010**, *12*, 1531–1551. [CrossRef]
7. Chou, K.-S.; Lu, Y.-C.; Lee, H.-H. Effect of alkaline ion on the mechanism and kinetics of chemical reduction of silver. *Mater. Chem. Phys.* **2005**, *94*, 429–433. [CrossRef]

8. Gong, P.; Li, H.; He, X.; Wang, K.; Hu, J.; Tan, W.; Zhang, S.; Yang, X. Preparation and antibacterial activity of Fe3O4@Ag nanoparticles. *Nanotechnology* **2007**, *18*, 285604. [CrossRef]
9. Peiris, S.; McMurtrie, J.; Zhu, H.-Y. Metal nanoparticle photocatalysts: Emerging processes for green organic synthesis. *Catal. Sci. Technol.* **2016**, *6*, 320–338. [CrossRef]
10. Sondi, I.; Salopek-Sondi, B. Silver nanoparticles as antimicrobial agent: A case study on E. coli as a model for Gram-negative bacteria. *J. Colloid. Interface Sci.* **2004**, *275*, 177–182. [CrossRef]
11. Mehrbod, P.; Motamed, N.; Tabatabaian, M.; Soleimani Estyar, R.; Amini, E.; Shahidi, M.; Kheiri, M.T. In vitro antiviral effect of "nanosilver" on influenza virus. *DARU J. Pharm. Sci.* **2009**, *17*, 88–93.
12. Devi, L.S.; Joshi, S.R. Antimicrobial and synergistic effects of silver nanoparticles synthesized using soil fungi of high altitudes of eastern himalaya. *Mycobiology* **2012**, *40*, 27–34. [CrossRef] [PubMed]
13. Karmali, M.A. Factors in the emergence of serious human infections associated with highly pathogenic strains of shiga toxin-producing Escherichia coli. *Int. J. Med. Microbiol.* **2018**, *308*, 1067–1072. [CrossRef]
14. Lara, H.H.; Ayala-Nuñez, N.V.; Ixtepan-Turrent, L.; Rodriguez-Padilla, C. Mode of antiviral action of silver nanoparticles against HIV-1. *J. Nanobiotechnol.* **2010**, *8*, 1. [CrossRef] [PubMed]
15. Gaikwad, S.; Ingle, A.; Gade, A.; Rai, M.; Falanga, A.; Incoronato, N.; Russo, L.; Galdiero, S.; Galdiero, M. Antiviral activity of mycosynthesized silver nanoparticles against herpes simplex virus and human parainfluenza virus type 3. *Int. J. Nanomed.* **2013**, *8*, 4303–4314. [CrossRef]
16. Nakamura, S.; Sato, M.; Sato, Y.; Ando, N.; Takayama, T.; Fujita, M.; Ishihara, M. Synthesis and application of silver nanoparticles (Ag NPs) for the prevention of infection in healthcare workers. *Int. J. Mol. Sci.* **2019**, *20*, 3620. [CrossRef]
17. Nguyen, V.Q.; Ishihara, M.; Mori, Y.; Nakamura, S.; Kishimoto, S.; Fujita, M.; Hattori, H.; Kanatani, Y.; Ono, T.; Miyahira, Y.; et al. Preparation of size-controlled silver nanoparticles and chitosan-based composites and their anti-microbial activities. *Biomed. Mater. Eng.* **2013**, *23*, 473–483. [CrossRef]
18. Nguyen, V.Q.; Ishihara, M.; Kinoda, J.; Hattori, H.; Nakamura, S.; Ono, T.; Miyahira, Y.; Matsui, T. Development of antimicrobial biomaterials produced from chitin-nanofiber sheet/silver nanoparticle composites. *J. Nanobiotechnol.* **2014**, *12*, 49. [CrossRef]
19. Ishihara, M.; Nguyen, V.Q.; Mori, Y.; Nakamura, S.; Hattori, H. Adsorption of silver nanoparticles onto different surface structures of chitin/chitosan and correlations with antimicrobial activities. *Int. J. Mol. Sci.* **2015**, *16*, 13973–13988. [CrossRef]
20. Mori, Y.; Tagawa, T.; Fujita, M.; Kuno, T.; Suzuki, S.; Matsui, T.; Ishihara, M. Simple and environmentally friendly preparation and size control of silver nanoparticles using an inhomogeneous system with silver-containing glass powder. *J. Nanopart. Res.* **2011**, *13*, 2799–2806. [CrossRef]
21. Mori, Y.; Ono, T.; Miyahira, Y.; Nguyen, V.Q.; Matsui, T.; Ishihara, M. Antiviral activity of silver nanoparticle/chitosan composites against H1N1 influenza A virus. *Nanoscale Res. Lett.* **2013**, *8*, 93. [CrossRef] [PubMed]
22. Kinoda, J.; Ishihara, M.; Hattori, H.; Nakamura, S.; Fukuda, K.; Yokoe, H. Cytotoxicity of silver nanoparticle and chitin-nanofiber sheet composites caused by oxidative stress. *Nanomaterials* **2016**, *6*, 189. [CrossRef] [PubMed]
23. Jayasmita, J.; Mainak, G.; Tarasankar, P. Enlightening surface plasmon resonance effect of metal nanoparticles for practical spectroscopic application. *RSC Adv.* **2016**, *89*, 86174–86211. [CrossRef]
24. Nguyen, V.Q.; Ishihara, M.; Nakamura, S.; Hattori, H.; Ono, T.; Miyahira, Y.; Matsui, T. Interaction of silver nanoparticles and chitin powder with different sizes and surface structures: The correlation with antimicrobial activities. *J. Nanomater.* **2013**, *2013*, 1–9. [CrossRef]
25. Hollosy, F. Effects of ultraviolet radiation on plant cells. *Micron (Oxford, England: 1993)* **2002**, *33*, 179–197. [CrossRef]
26. Surjadinata, B.B.; Jacobo-Velazquez, D.A.; Cisneros-Zevallos, L. UVA, UVB and UVC light enhances the biosynthesis of phenolic antioxidants in fresh-cut carrot through a synergistic effect with wounding. *Molecules* **2017**, *22*, 668. [CrossRef]
27. Zhang, L.; Wu, L.; Si, Y.; Shu, K. Size-dependent cytotoxicity of silver nanoparticles to Azotobacter vinelandii: Growth inhibition, cell injury, oxidative stress and internalization. *PLoS ONE* **2018**, *13*, e0209020. [CrossRef]
28. Quinteros, M.A.; Cano Aristizabal, V.; Dalmasso, P.R.; Paraje, M.G.; Paez, P.L. Oxidative stress generation of silver nanoparticles in three bacterial genera and its relationship with the antimicrobial activity. *Toxicol. In Vitro* **2016**, *36*, 216–223. [CrossRef]

29. Dabrowska-Bouta, B.; Sulkowski, G.; Struzynski, W.; Struzynska, L. Prolonged exposure to silver nanoparticles results in oxidative stress in cerebral myelin. *Neurotox. Res.* **2019**, *35*, 495–504. [CrossRef]
30. Gasmalla, H.B.; Lu, X.; Shinger, M.I.; Ni, L.; Chishti, A.N.; Diao, G. Novel magnetically separable of Fe3O4/Ag3PO4@WO3 nanocomposites for enhanced photocatalytic and antibacterial activity against Staphylococcus aureus (S. aureus). *J. Nanobiotechnol.* **2019**, *17*, 58. [CrossRef]
31. Lee, B.; Lee, M.J.; Yun, S.J.; Kim, K.; Choi, I.H.; Park, S. Silver nanoparticles induce reactive oxygen species-mediated cell cycle delay and synergistic cytotoxicity with 3-bromopyruvate in Candida albicans, but not in Saccharomyces cerevisiae. *Int. J. Nanomed.* **2019**, *14*, 4801–4816. [CrossRef] [PubMed]
32. Li, M.; Yin, J.J.; Wamer, W.G.; Lo, Y.M. Mechanistic characterization of titanium dioxide nanoparticle-induced toxicity using electron spin resonance. *J. Food. Drug Anal.* **2014**, *22*, 76–85. [CrossRef] [PubMed]
33. Oliveira, E.; Santos, H.M.; Garcia-Pardo, J.; Diniz, M.; Lorenzo, J.; Rodríguez-González, B.; Capelo, J.L.; Lodeiro, C. Synthesis of functionalized fluorescent silver nanoparticles and their toxicological effect in aquatic environments (Goldfish) and HEPG2 cells. *Front. Chem.* **2013**, *1*, 29. [CrossRef] [PubMed]

International Journal of
Molecular Sciences

MDPI

Article

Evaluation of Antibacterial and Cytotoxicity Properties of Silver Nanowires and Their Composites with Carbon Nanotubes for Biomedical Applications

Arianna De Mori [1], Richard S. Jones [1], Matteo Cretella [1], Guido Cerri [2], Roger R. Draheim [1], Eugen Barbu [1], Gianluca Tozzi [3] and Marta Roldo [1,*]

[1] School of Pharmacy and Biomedical Science, University of Portsmouth, St Michael's Building, White Swan Road, PO1 2DT, Portsmouth, UK; arianna.demori@port.ac.uk (A.D.M.); richard.jones1@port.ac.uk (R.S.J.); matteo.cretella@port.ac.uk (M.C.); roger.draheim@port.ac.uk (R.R.D.); eugen.barbu@port.ac.uk (E.B.)

[2] Department of Architecture, Design and Urban Planning—GeoMaterials Lab, University of Sassari, Via Piandanna 4, 07100 Sassari, Italy; gcerri@uniss.it

[3] Zeiss Global Centre, School of Engineering, University of Portsmouth, Anglesea Building, Anglesea Road, PO1 3DJ Portsmouth, UK; gianluca.tozzi@port.ac.uk

* Correspondence: marta.roldo@port.ac.uk

Received: 11 March 2020; Accepted: 25 March 2020; Published: 26 March 2020

Abstract: In this work, we prepared silver nanowires (AgNWs) via the polyol method in the presence or absence of single wall carbon nanotubes (CNTs) and tested their physicochemical, antibacterial and cytotoxic properties. Results showed that the introduction of CNTs lead to the formation of AgNWs at lower temperature, but the final product characteristics of AgNWs and AgNWs-CNT were not significantly different. AgNWs exhibited antibacterial properties against all the studied bacterial species via the formation of oxygen reactive species (ROS) and membrane damage. Furthermore, AgNWs exhibited a dose-dependent and time-dependent toxicity at concentrations ≥ 10 μg/mL. Fibroblasts appeared to be more resistant than human colorectal adenocarcinoma (Caco-2) and osteoblasts to the toxicity of AgNWs. The cytotoxicity of AgNWs was found to be related to the formation of ROS, but not to membrane damage. Overall, these results suggest that AgNWs are potential antibacterial agents against *E. coli*, *S. aureus*, MRSA and *S. saprophyticus*, but their dosage needs to be adjusted according to the route of administration.

Keywords: silver nanowires; nanomaterials; biocompatibility

1. Introduction

Silver has been known for centuries for its antimicrobial properties against a wide range of microorganisms. In the 1980s the first findings on the unique properties of nanoparticles (NPs) were published, researchers started to investigate novel applications for silver nanomaterials in electronic, optical and biomedical fields. In order to satisfy specific needs, several morphologies have been developed, including silver nanospheres, nanocubes, nanorods, nanotriangles and nanowires.

Silver nanowires (AgNWs) are one-dimensional silver structures and are currently being intensively studied for thermal and electronic applications due to their excellent conductive properties [1–3]. Despite the fact that the antibacterial and cytotoxic properties of other silver nanoparticles have been widely explored [4–8] and medical devices loaded with silver nanopoarticles have been developed, research on AgNW antibacterial properties, mechanisms of action and possible biomedical applications is still scarce [9]. So far we know that AgNWs are potential antibacterial agents against *E. coli* and *S. aureus*, but we know little about how they exert their action. Visnapuu et al., for instance, stated that the toxicity of AgNWs against *E. coli* was due to dissolved Ag^+ ions rather than to

a direct effect of the silver nanostructures [10]. Cui and Liu, instead, highlighted that *E. coli* is more sensitive than *S. aureus* to the action of AgNWs, determining their toxicity was a consequence of both AgNW-induced bacterial disruption and the induction of ROS generation [11].

In the development of AgNWs containing commercial products, we must be considerate of the fact that nanowires can be released into the environment during manufacturing, use or disposal; thus, there is a compelling need to understand the short- and long-term toxicity of these materials in humans [12]. Other high-aspect ratio materials, such as asbestos or carbon nanotubes, have indeed been shown to be actively absorbed into eukaryotic cells, causing different types of damage [13]. As the respiratory route is one of the major access routes linked to occupational exposure to AgNWs, the majority of studies have so far focused on the possible damages through this route. Schinwald et al. found that AgNWs longer than ≥14 μm or ≥ 5 μm were able to induce pleural inflammation, in vivo and in vitro, respectively [14]. Further studies have also highlighted that AgNWs can enter and accumulate in epithelial cells, interstitial sites, airway smooth muscle cells, the vascular endothelium, the pleural membrane and macrophages. Stoehr et al. compared the cytotoxicity of AgNWs (length: 1.5–25 μm; diameter 100–160 nm) and Ag nanospheres (30 nm) against human alveolar epithelial cells (A549), finding that whereas no effects were observed for the spherical particles, significantly reduced cell viability and increased LDH release were induced by AgNWs [15]. A recent review on the safety of nanosilver has highlighted that, at the nanoscale, silver nanowires are safer than silver nanoparticles due to their hindered cellular uptake [16].

In light of this diverse evidence, and in particular, the results considering different routes of administration, this study aimed to investigate the in vitro antibacterial properties of AgNWs obtained via two synthetic methods (soft template and heterogeneous method) tested against *E. coli, S. aureus,* MRSA and *S. saprophyticus*. Moreover, the internalization, cytotoxicity and possible mechanisms of action of AgNWs against human osteoblasts (hFOB 1.19), human skin fibroblasts (Hs27) and human colorectal adenocarcinoma (Caco-2) were studied in order to assess future potential applications such as inclusion in bone implants or in wound dressings for skin and mucosa.

2. Results

2.1. AgNW Physicochemical Characterisation

2.1.1. UV-vis and TEM Characterization

AgNWs were synthesized via the polyol method using PVP as a soft template, and AgNWs-CNT were synthesized with the same method in the presence of carbon nanotubes (CNTs) in order to evaluate whether the addition of CNTs influenced the morphological, physical and biological properties of the AgNWs. AgNWs-CNT-mix (physical mixture of AgNWs and CNTs) was used as a control to investigate whether any potential difference between AgNWs in AgNWs-CNT was due to the mere presence of CNTs or if they had an effect when introduced in the synthetic procedure. The UV-Vis spectra of AgNWs and AgNWs-CNT at low temperatures showed a peak at 410 nm, indicative of the formation of nucleation sites with the initial presence of silver nanoparticles and nanorods (Figure 1A–B). A shift towards lower wavenumbers and the formation of a double peak (350 and 380 nm) were observed as the temperature increased, indicating the formation of longer structures such as nanowires [17]. The shift was observed at lower temperatures when the synthesis of AgNWs was performed in the presence of CNTs; this could be due to the excellent heat conductivity of CNTs that can affect the reaction kinetics. Nanoparticles were also observed by TEM (Figure 1C–F); images confirmed the successful formation of AgNWs under both synthetic conditions. However, in both cases, other types of nanoparticles, such as nanospheres and nanorods, were visualized. Moreover, the amount of CNTs found in AgNWs-CNT appeared significantly inferior to that in the AgNWs-CNT-mix. Interestingly, in both AgNWs-CNT and AgNWs-CNT-mix samples, the smaller particles tended to align along the surface of CNTs (Figure 1G–H). A size analysis was performed based on SEM images (Figures S1 and S2); average lengths were 5.23 μm (± 1.5), 5.21 μm (± 2.7)

and 5.04 µm (± 1.7), for AgNWs, AgNWs-CNT and AgNWs-CNT-mix, respectively. Average diameters were 73.70 nm (± 25.79), 67.04 nm (± 25.23) and 68.54 nm (± 17.47) for AgNWs, AgNWs-CNT and AgNWs-CNT-mix, respectively. One-way ANOVA showed no significant difference in lengths and diameters across all three materials ($p > 0.05$).

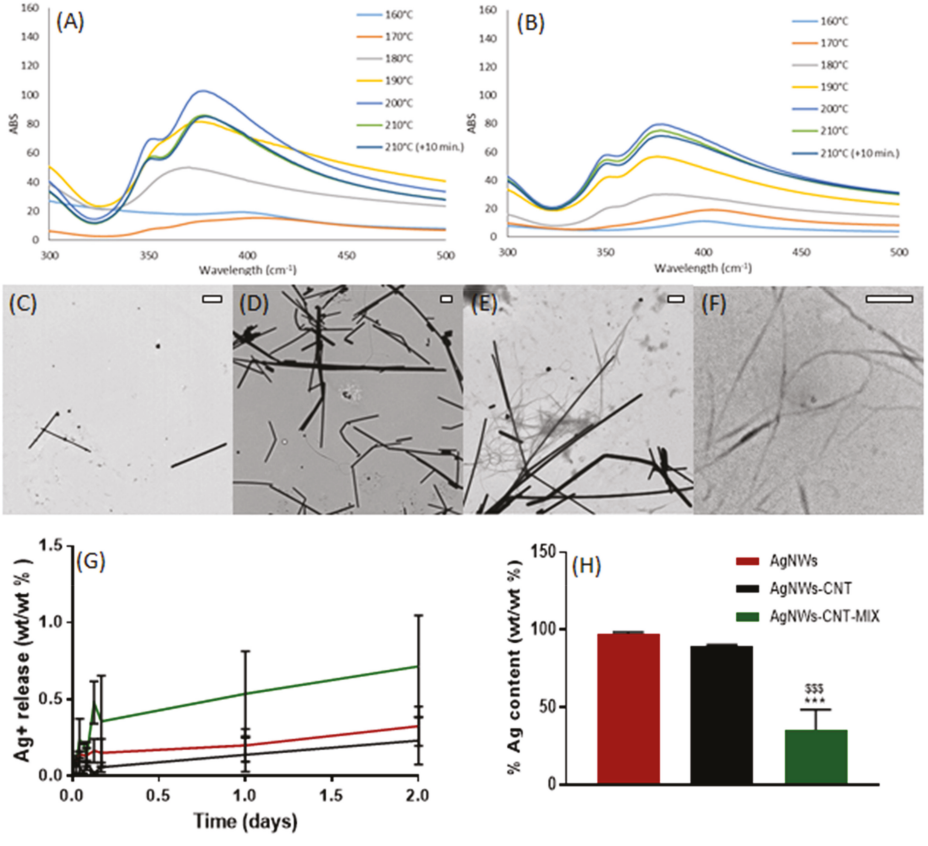

Figure 1. Physicochemical characterization of synthesized products. UV-spectra of (**A**) AgNWs and (**B**) of AgNWs-CNT at different temperatures during the synthesis reaction. TEM images of (**C**) AgNWs (scale bar 500 nm), (**D**) AgNWs-CNT (scale bar 500 nm), (**E**) AgNWs-CNT-mix (scale bar 500 nm) and (**F**) CNTs (scale bar 500 nm). (**G**) Silver release from AgNWs, AgNWs-CNT and AgNWs-CNT-mix measured by ICP-OES and expressed as wt/wt%. (**H**) Silver contents measured by ICP-OES in AgNWs, AgNWs-CNT and AgNWs-CNT-mix ($n = 3$). One-way ANOVA returned $p < 0.05$; Post-hoc Tukey's multicomparison test, *** $p = 0.001$ when comparing all the formulations to AgNWs, and $^{\$\$\$}$ $p = 0.003$ when comparing AgNWs-CNT to AgNWs-CNT-mix.

2.1.2. Total Silver Content and Ag^+ Release

The total Ag content in each of the products and the cumulative Ag^+ released over time were determined. The total silver content found in AgNWs (97.33 ± 1.14 wt/wt%) was higher than that in AgNWs-CNT (89.11 ± 1.25 wt/wt%), but not significantly different (one-way ANOVA, $p > 0.05$, Figure 1H); this explains the observation of only a few CNTs in the TEM images (Figure 1C–E). The amount of Ag in AgNWs-CNT-mix was significantly inferior to the other two batches (35.27 ± 5.33 wt/wt%) ($p < 0.001$), as expected. The release of Ag^+ from AgNWs, AgNWs-CNT and AgNWs-CNT-mix

(Figure 1G) started immediately in the aqueous solution and its concentration increased over time. After 30 min, the concentration of Ag^+ in suspension was ca. 0.31 ± 0.04 ppm from AgNWs, 0.22 ± 0.17 ppm from AgNWs-CNT and 0.09 ± 0.02 ppm from AgNWs-CNT-mix. After 2 days, the percentage of Ag^+ released was of ca. 0.32 wt/wt% from AgNWs, 0.23 wt/wt% from AgNWs-CNT and 0.71 wt/wt% from AgNWs-CNT-mix (one-way ANOVA $p > 0.05$), corresponding to 1.15 ± 0.39, 0.95 ± 0.53 and 0.92 ± 0.81 ppm, respectively.

2.1.3. XRD, Photoluminescence and ζ-Potential Analyses

The X-ray diffraction (XRD) pattern of AgNWs (Figure 2A) corresponds to the structure of metallic silver; in particular, the sharp peaks at 2θ values of 38.1°, 44.3°, 64.4° and 77.3° refer to the reticular planes (111), (200), (220) and (311), and are typical of AgNWs [18]. Furthermore, the (111)/(200) peak ratio was 3.7, indicating the formation of well-elongated AgNWs [19]. Minimal trace impurity of AgCl can be seen at a 2θ value of 32.1° and 46.2° [20].

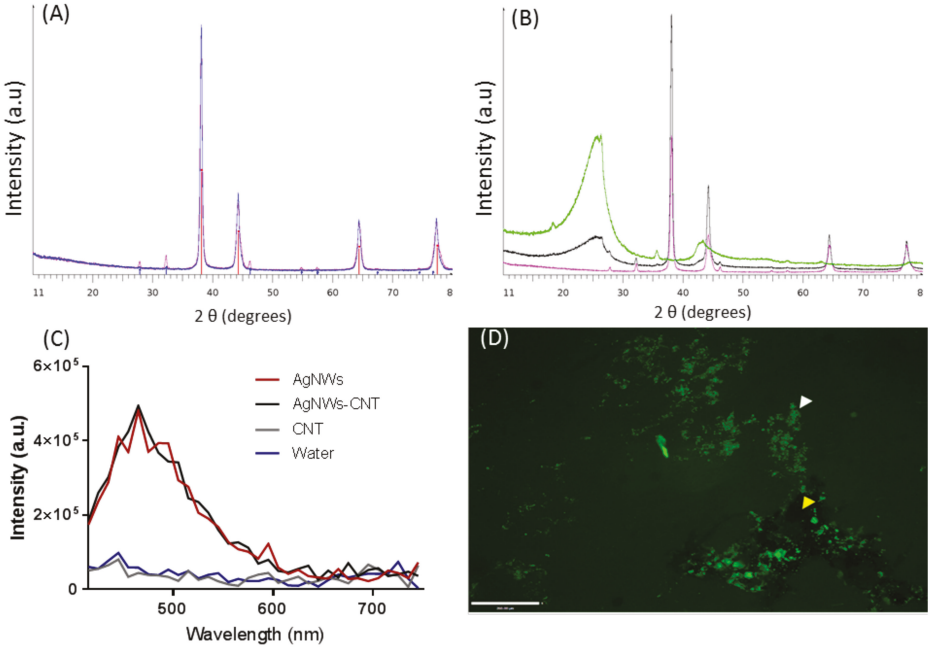

Figure 2. XRD pattern and fluorescence spectra. (**A**) XRD pattern of AgNWs (pink) and AgNWs-CNT (blue); red bars: Ag, PDF No. 04-0783; blue bars: AgCl, PDF n. 31-1238. (**B**) XRD pattern of AgNWs (violet), AgNWs-CNT-mix (black) and CNTs (green). (**C**) The emission fluorescence peaks of AgNWs (red), AgNWs-CNT-mix (black), CNTs (grey) and water (blue). (**D**) Fluorescence microscope image of AgNWs-CNT in water; the white arrow indicates AgNWs, and the yellow arrow indicates CNTs (scale bar 200 μm).

Superimposed patterns of AgNWs and AgNWs-CNT confirmed that the two synthetic processes led to similar products. The (111)/(200) intensity ratio of AgNWs-CNT was 3.2. The XRD profile of CNTs (Figure 2B) showed broad peaks at 2θ angles of ≈26°, ≈43° and ≈57°, corresponding to the (002) plane of graphite and to the (111) and (200) reflections of carbon, respectively [21]; these peaks also featured in AgNWs-CNTs-mix. The (111)/(200) intensity ratio of AgNWs-CNT-mix was found to be 3.2, similar to AgNWs-CNT. The fluorescence emission of AgNWs, AgNWs-CNT and CNTs aqueous solutions was also investigated. Excitation at wavelengths between 390 and 400 nm led to fluorescence

emission between 450 and 600 nm with lambda maxima at 465 nm, corresponding to the blue-green emitting region. The luminescence emission from silver clusters and silver nanoparticles of different dimensions has previously been described [22,23], but not entirely understood. This phenomenon could be related to the number and position of surface plasmon resonance (SPR), which in turn depends on the size and shape of silver clusters.

Surface zeta potential (ζ) was found to be negative for all the preparations (AgNWs −12.43 ± 1.23 mV; AgNWs-CNT −18.24 ± 5.92 mV; AgNWs-CNT-mix −19.8 ± 7.66 mV); the values indicated that electrostatically stable suspensions cannot be obtained in water without the use of a suspending agent [10].

2.2. Antibacterial Properties

2.2.1. Minimum Inhibitory Concentration (MIC) and Minimum Bactericidal Concentration (MBC)

The potential bacteriostatic and bactericidal activities of the synthesized materials were tested against four different bacterial species: *E. coli*, *S. aureus*, MRSA and *S. saprophyticus*. In order to compare the activity of AgNWs, AgNWs-CNT, AgNWs-CNT-mix and ionic silver (as $AgNO_3$), the MIC and MBC values obtained were normalized to the amount of Ag present in each material.

All studied materials inhibited or stopped cell growth within the tested concentration range, except for single-wall carbon nanotubes-COOH (tested as control), which did not show any antibacterial response (Table 1). All preparations were less efficient than $AgNO_3$ in both inhibiting cell growth and in promoting cell death apart from *S. saprophyticus* that was highly sensitive to all treatments. Normalized MIC and MBC values of AgNWs, AgNWs-CNT and AgNWs-CNT-mix were not statistically different from each other ($p > 0.05$) against all the different bacterial species; only *S. aureus* AgNWs-CNT-mix showed a lower efficacy ($p < 0.001$). Overall, *S. saprophyticus* was found to be the most sensitive strain against silver nanowires, whereas MRSA was the most resistant. The MIC values found in this study for *E. coli* and *S. aureus* were higher than those reported by Cui and Liu for AgNWs (28 and 35 μg/mL to *E. coli* and *S. aureus*, respectively) [11] and Hong et al. (> 100 μg/mL against *E. coli*) [24]; this can be explained considering the differences in initial bacterial density, nanowire dimensions and methods adopted for the MIC and MBC determination [25].

2.2.2. Bacterial Growth Kinetics

In order to study how the bacterial growth kinetics were influenced by different concentrations of studied materials, growth was followed by measuring $OD._{600nm}$ in LB medium (Figure 3, Figures S3 and S4). Seemingly for MIC and MBC studies, CNTs did not appear to influence bacterial growth kinetics (Figure S3). AgNWs affected both the lag phase (100 μg/mL, $p < 0.05$) and the time to reach the stationary phase (50 μg/mL, $p < 0.05$) of *E. coli* (Figure 3A and Figure S5). MRSA showed a significantly longer lag phase than the control only in the presence of AgNWs 100 μg/mL ($p < 0.01$) but no effect on the time to reach the stationary phase (Figure 3E and Figure S5). *S. aureus* (Figure 3C) was more sensitive than MRSA and *E. coli* to the action of AgNWs: all the tested concentrations, except for 12.5 μg/mL, produced longer lag phases (25 μg/mL $p < 0.001$; 50 and 100 μg/mL $p < 0.0001$). The time to reach the stationary phase was statistically longer for concentrations equal to or higher than 50 μg/mL ($p < 0.05$). The lag phase duration of *S. saprophyticus* (Figure 3G and Figure S5) was increased for the two lowest concentrations (12.5 μg/mL $p < 0.01$ and 25 μg/mL $p < 0.05$), whereas no growth was found for the higher concentrations of nanowires, and the time to reach the stationary phase was significantly longer even for the lowest tested concentration. *E. coli* was more sensitive to AgNWs-CNT (Figure 3A and Figure S5) than AgNWs: its lag phase (12.5 μg/mL, $p < 0.05$, whereas 25, 50 and 100 μg/mL had a $p < 0.0001$) and the time to reach stationary phase were also significantly longer for the lowest concentration. Seemingly, *S. aureus* (Figure 3D) was more sensitive to the action of AgNWs-CNT than AgNWs with decreased growth at all concentrations tested and no growth at the highest concentration. No difference in the time to reach the stationary phase was found for

concentrations 12.5 and 25 µg/mL in comparison to the control (Figure S5). MRSA (Figure 3F) growth was affected by AgNWs-CNT at all concentrations. No effect on the time to reach the stationary phase was observed. *S. saprophyticus* lag phase (Figure 3H and Figure S5) was affected for the two lowest concentrations ($p < 0.05$), and no growth was observed for the higher concentrations. The time to reach the stationary phase of *S. saprophyticus* was statistically longer for the 25 µg/mL concentration than for the control. For all the studied nanowires and bacterial strains, whenever the stationary phase was reached, no statistical difference in OD values was found among treated and untreated bacteria (Figure S5). The ability of AgNWs to retard cell growth was further demonstrated by fluorescence imaging (Figure S6).

Table 1. MIC and MBC values (mg/mL) for AgNWs, AgNWs-CNT, AgNWs-CNT-mix, $AgNO_3$ and CNTs. Data are reported as the mean ± SD ($n \geq 3$). One-way ANOVA results are reported in the table. The post hoc Tukey multiple comparisons test results are shown with *when compared to Ag+ and with $when compared to AgNW-CNT-mix. $^{*,\$}$ $p < 0.05$; $^{**,\$\$}$ $p < 0.01$, $^{***,\$\$\$}$ $p < 0.001$ and $^{****,\$\$\$\$}$ $p < 0.0001$.

Microorganism	Material	MIC (mg/mL)	MBC (mg/mL)	MBC/MIC
E. coli Anova MIC p < 0.0001 MBC p < 0.0001	AgNWs	0.42 ± 0.26 *	1.16 ± 0.27 $^{\$\$}$	**2.8**
	AgNWs-CNT	0.53 ± 0.54 $^{*\$\$\$}$	1.38 ± 0.55 ***	**2.6**
	AgNWs-CNT-mix	0.49 ± 0.07 ***	0.99 ± 0.16 ***	**2.0**
	$AgNO_3$	0.01 ± 0.00	0.17 ± 0.05	17
	CNTs	> 3.00	> 3.00	-
S. aureus Anova MIC p < 0.0001 MBC p < 0.05	AgNWs	0.36 ± 0.24 $^{\$\$\$}$	1.55 ± 0.63	4.3
	AgNWs-CNT	0.28 ± 0.24 $^{\$\$\$}$	1.05 ± 0.80	**2.9**
	AgNWs-CNT-mix	0.44 ± 0.12	0.77 ± 0.16**	**1.8**
	$AgNO_3$	0.01 ± 0.00 $^{\$\$\$}$	0.1 ± 0.00	10
	CNTs	> 3.00	> 3.00	-
MRSA Anova MIC p < 0.01 MBC p < 0.0001	AgNWs	1.07 ± 0.40 *	2.53 ± 0.53 ****	**2.4**
	AgNWs-CNT	0.85 ± 0.85 *	2.00 ± 0.44 ****$^{\$\$}$	**2.4**
	AgNWs-CNT-mix	0.67 ± 0.14 *	> 3.00 ****	-
	$AgNO_3$	0.01 ± 0.00	0.07 ± 0.05	7
	CNTs	> 3.00	> 3.00	-
S. saprophyticus Anova MIC p < 0.05 n.s.	AgNWs	0.25 ± 0.21	0.66 ± 0.42	**2.7**
	AgNWs-CNT	0.08 ± 0.00	0.72 ± 0.60	9
	AgNWs-CNT-mix	0.08 ± 0.06	0.46 ± 0.36	5.8
	$AgNO_3$	0.01 ± 0.00	0.01 ± 0.00	**1**
	CNTs	> 3.00	> 3.00	-

2.2.3. Leakage of Proteins From Bacteria

Cui and Liu reported that AgNWs could cause the leakage of cytoplasmic contents, such as DNA and proteins, from *E. coli* [11]. This phenomenon may be due to several alterations in bacterial cells, such as the inhibition of the activity of membranous enzymes or DNA damage. In the present study, a bicinchoninic acid (BCA) assay was used to determine whether AgNWs obtained by the two methods induced the release of proteins in the extracellular liquid. All the bacterial species tested showed an increased release of proteins in comparison to the control (Figure 4A–H). Moreover, this effect was dose-dependent, but no difference was found between 1 or 24 h after treatment, except for *S. saprophyticus*. A higher amount of proteins leaked out of *E. coli* compared to *S. aureus*

and MRSA, suggesting that gram-negative bacteria are more sensitive than gram-positive bacteria to the action of AgNWs on the integrity of the membrane. This is justified by the barrier function of the thicker peptidoglycan found in gram-positive bacteria and is in agreement with previous studies [26]. No statistical difference was found between AgNWs and AgNWs-CNT, when comparing the same concentrations. SEM images confirmed the cell membrane damage caused by AgNWs, particularly in *E. coli* (Figure S8).

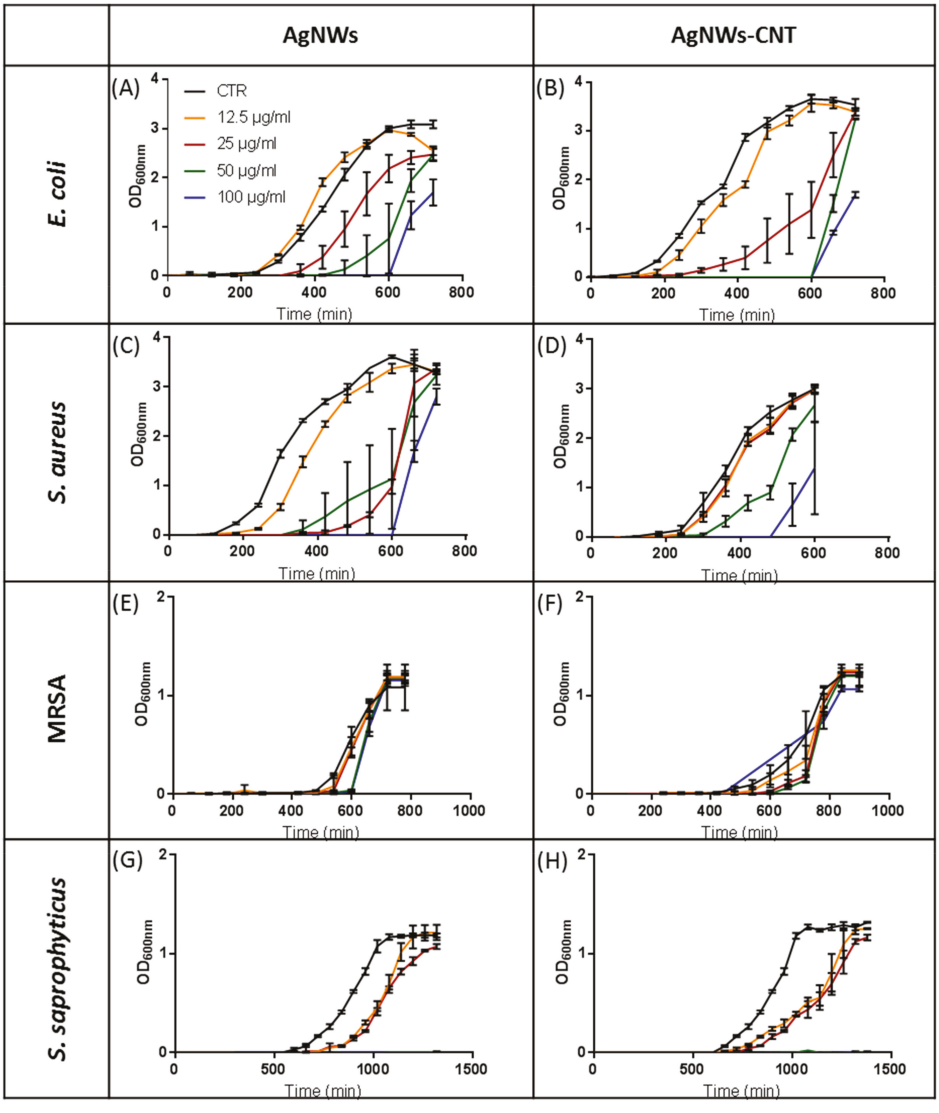

Figure 3. Growth curves of bacteria with different concentrations of AgNWs (**A**,**C**,**E**,**G**) and AgNWs-CNT (**B**,**D**,**F**,**H**). Results are reported as the mean ± SD (n = 3).

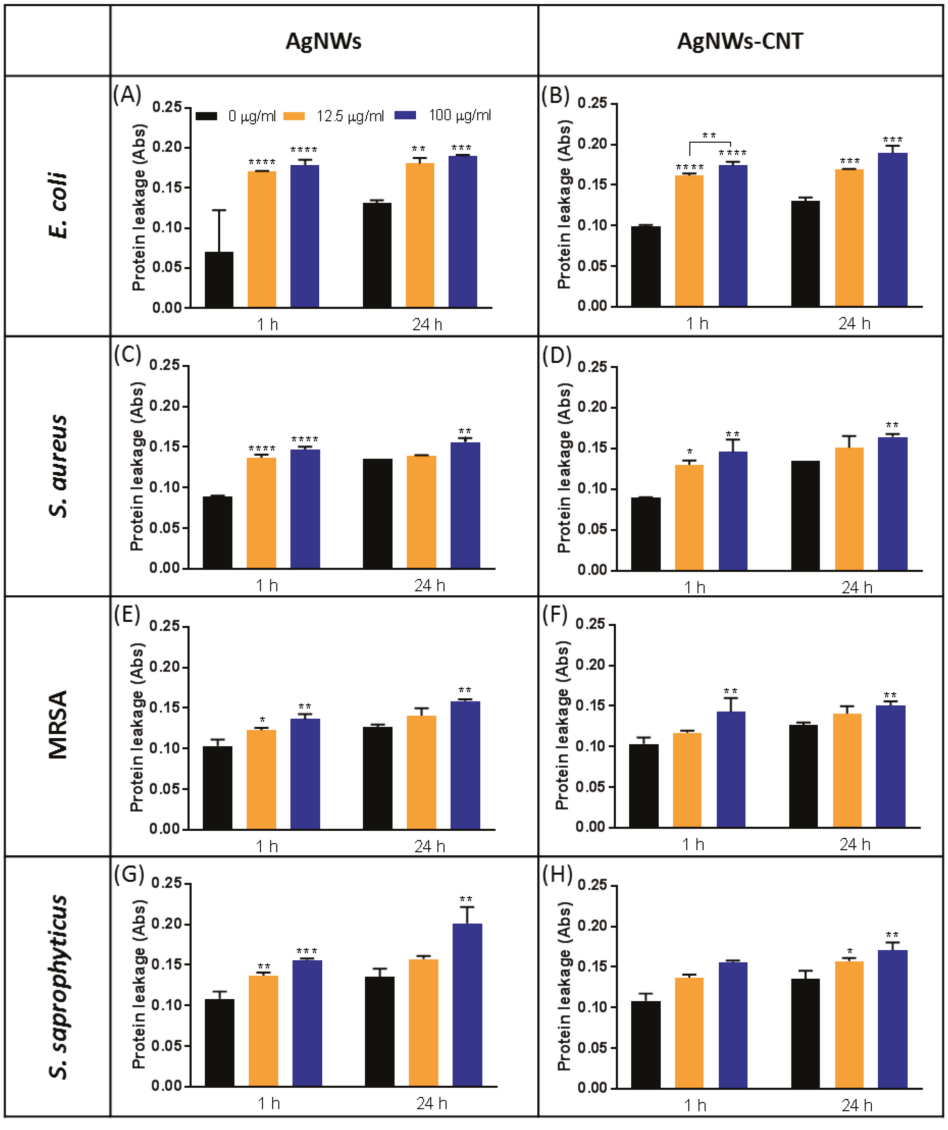

Figure 4. Absorbance relative to protein release after 1 and 24 h of treatment for *E. coli* (**A**,**B**), *S. aureus* (**C**,**D**), MRSA (**E**,**F**) and *S. saprophyticus* (**G**,**H**) treated with 12.5 or 100 µg/mL of AgNWs or AgNWs-CNT. Data are presented as the mean ± SD (n = 4). The one-way ANOVA performed on all the samples showed significantly different releases for both AgNWs and AgNWs-CNT ($p < 0.05$). Results of the post-hoc Tukey multicomparison test are shown in the graphs (* indicates $p < 0.05$, ** indicates $p < 0.01$, *** indicates $p < 0.001$ and **** indicates $p < 0.0001$).

2.2.4. ROS Generation From Bacteria

Previous studies suggested that oxidative stress plays a crucial role in the mechanism of toxicity of silver nanoparticles versus bacterial cells. In this work, extracellular ROS production was quantified 24 h after treatment with nanowires (Figure 5A–H). ROS were produced when *S. aureus* and *E. coli* were

treated with all types of metallic nanoparticles in a dose-dependent manner, as previously reported for other types of AgNPs [27].

MRSA did not show significantly increased ROS generation, similar to *S. saprophyticus* treated with AgNWs; but when *S. saprophyticus* was treated with AgNWs-CNT, there was a statistically significant increase in ROS at concentrations equal to or higher to 25 μg/mL. On the contrary, AgNWs were found to produce statistically more ROS than AgNWs-CNT in *E. coli* and *S. aureus* (unpaired two tailed *t*-test for: a) *E. coli*: 100 $p < 0.05$; 12.5 μg/mL, $p < 0.01$; b) *S. aureus:* 100 μg/mL, $p < 0.05$). See Figure S7 for data obtained for all concentrations tested.

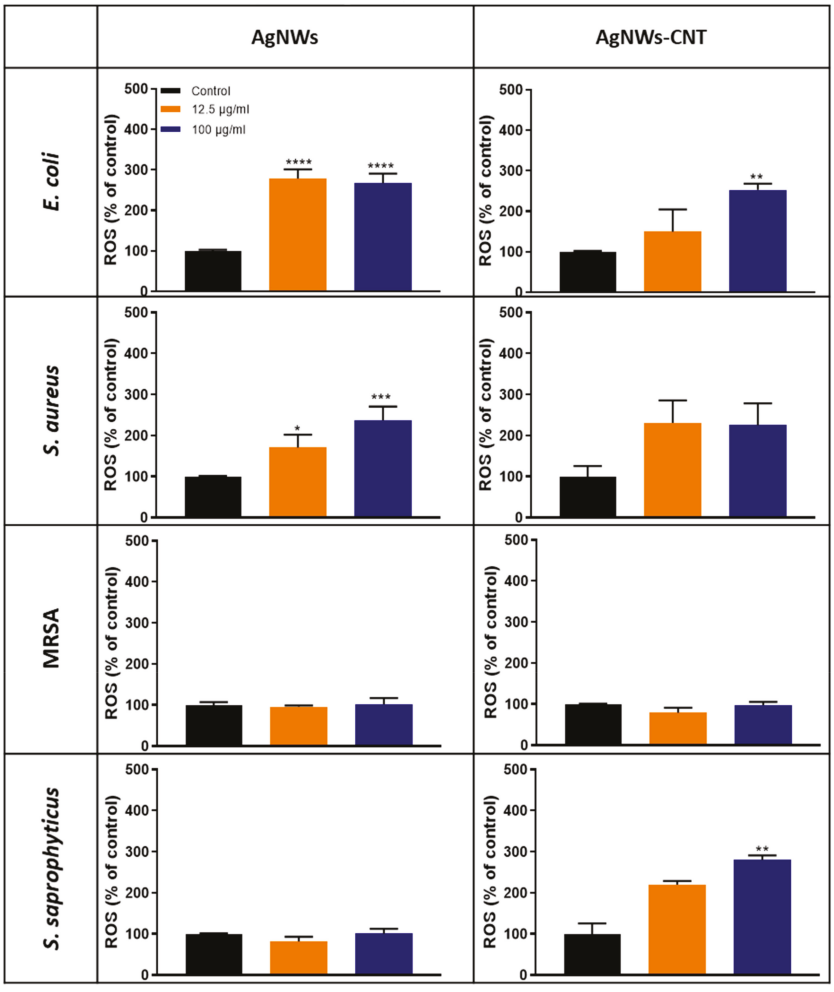

Figure 5. ROS production (% of the control) from bacterial cells, 24 h from treatment. *E. coli* (**A**,**B**), *S. aureus* (**C**,**D**), MRSA (**E**,**F**) and *S. saprophyticus* (**G**,**H**) treated with 12.5 and 100 μg/mL of AgNWs or AgNWs-CNT. Data are presented as the mean ± SD ($n = 3$). The one-way ANOVA performed on all the samples showed significantly different ROS production for both AgNWs and AgNWs-CNT ($p < 0.05$) for some of the bacterial strains. Results of the post-hoc Tukey multicomparison test are shown in the graphs (* indicates $p < 0.05$, ** indicates $p < 0.01$, *** indicates $p < 0.001$ and **** indicates $p < 0.0001$).

2.3. Cytotoxicity Studies

The toxicity of the two types of AgNWs was tested against three cell lines: osteoblasts (hFOB 1.19), human foreskin fibroblasts (Hs27) and Caco-2 cells (Figure 6A–F). These cell lines were chosen to mimic three possible routes of exposure such as the application of treatments to bone, skin and the digestive system, respectively [28]. No signs of acute toxicity were observed, as after 2 h of treatment, no cell line showed a significant decrease in cell viability ($p > 0.05$). After 24 h of exposure, fibroblasts were the more robust cells as their viability did not show a significant decrease with increasing doses of AgNWs and AgNWs-CNTs. Caco-2 cells were the most sensitive, with a significant decrease in viability at doses of 25 µg/mL of AgNWs ($p < 0.001$) and 10 µg/mL of AgNWs-CNTs ($p < 0.001$).

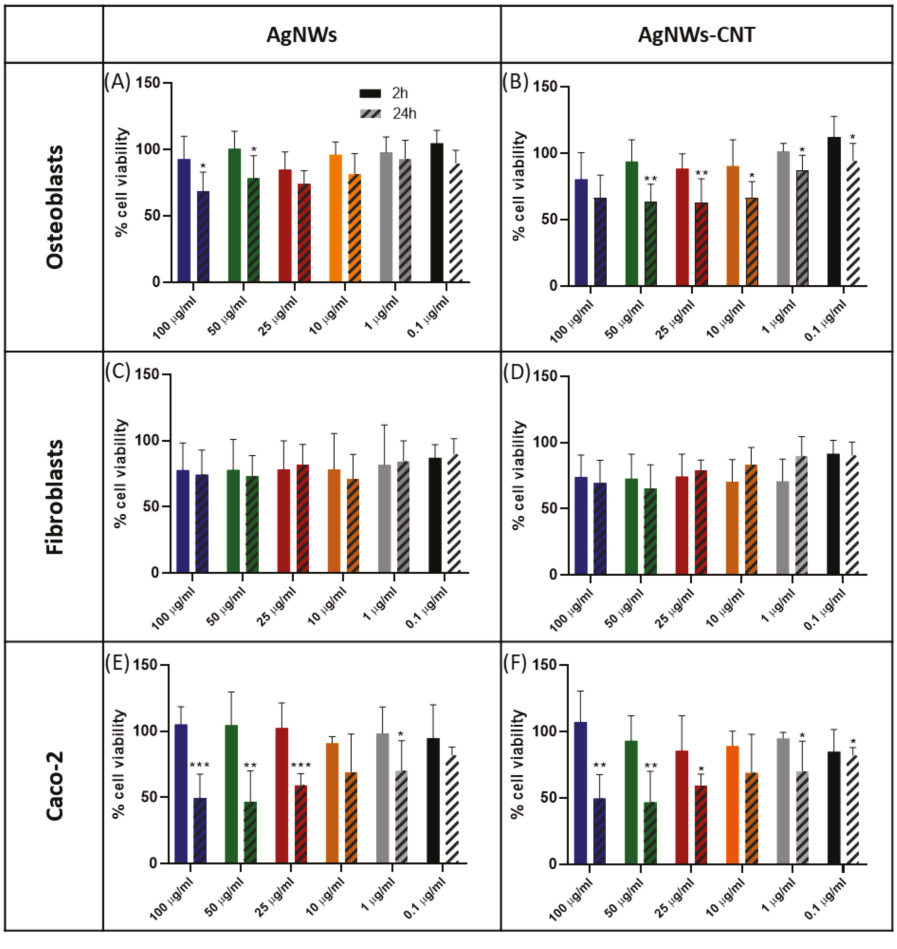

Figure 6. Cytotoxicity observed in different types of cell lines after 2 and 24 h of treatment. Osteoblasts (**A**,**B**), fibroblasts (**C**,**D**), Caco-2 (**E**,**F**). Data are presented as the mean ± SD ($n > 3$). The one-way ANOVA performed on all samples showed significantly different viability for AgNWs and AgNWs-CNT (* indicates $p < 0.05$, ** indicates $p < 0.01$, *** indicates $p < 0.001$ and **** indicates $p < 0.0001$).

2.3.1. Oxidative Stress in Eukaryotic Cells

Several studies have shown that AgNPs induce the production of ROS in mammalian cells [29,30]. Results of the present study (Figure 7A–F) confirmed that ROS induced by AgNWs and AgNWs-CNT

are an important factor in promoting toxicity, but once again, the effect is specific to the cell line treated. Fibroblasts presented the lowest level of ROS produced when treated with AgNWs-CNTs and with no significant effect when treated with AgNWs. Osteoblasts were the most sensitive to the AgNW treatment, with a higher level of ROS detected. Caco-2 cells presented a wider range of variability that caused non-significant differences when compared to the control. CNTs were tested as a control and induced no significant ROS production in any of the cell lines (Figure S9). Few other studies are available for AgNWs; Sweeney et al. reported that AgNWs (72 nm × 1.5 µm) could induce a significant increase in ROS production in human type-I epithelial-like cells (TT1), both after 4 (≥25 µg/mL) and 24 h treatment (≥ 10 µg/mL) [31].

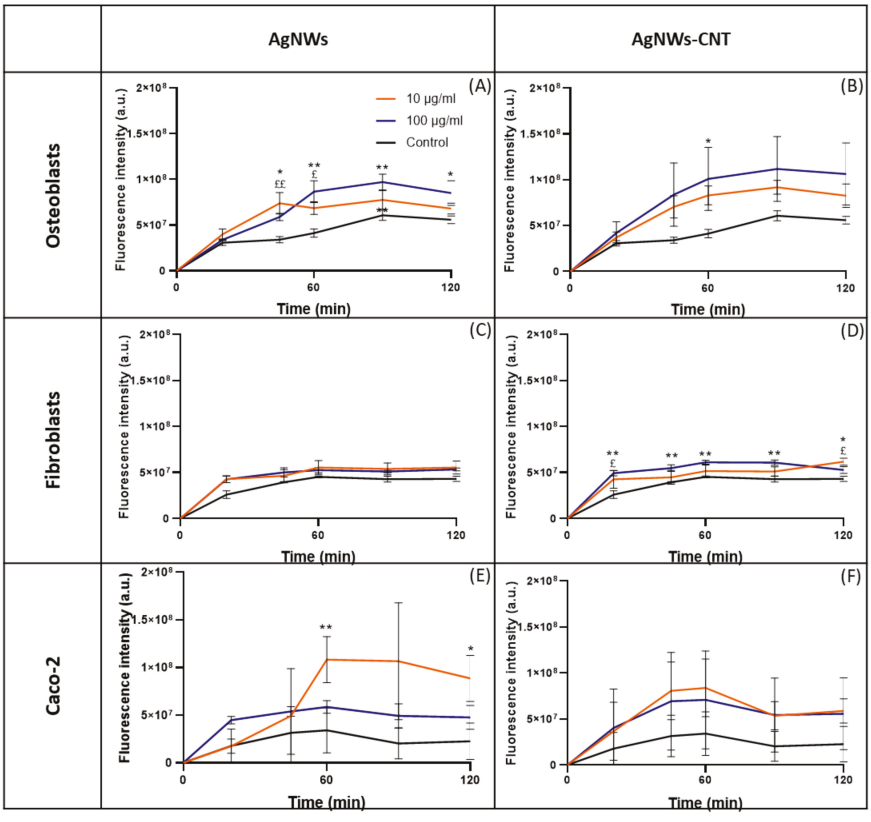

Figure 7. Time course of ROS production in different cell lines: osteoblasts (**A**,**B**), fibroblasts (**C**,**D**) and Caco-2 (**E**,**F**) treated with AgNWs or AgNWs-CNT for 15 min. One-way ANOVA returned $p < 0.05$. Data are reported as the mean ± SD ($n = 3$). Results of the post-hoc Tukey multicomparison test are shown in the graph: *was used to compare 100 with 0 µg/mL (* indicates $p < 0.05$ and ** indicates $p < 0.01$); $ was used to compare 10 with 0 µg/mL ($ indicates $p < 0.05$ and $$ indicates $p < 0.01$).

2.3.2. Membrane Damage Evaluation

Membrane integrity was assessed by measuring extracellular lactate dehydrogenase (LDH, Figure 8). No significant toxicity was observed after 24 h for any of the concentrations tested in comparison to the spontaneous LDH release (0 µg/mL) ($p > 0.05$).

2.3.3. Silver Uptake

Previous studies have reported that AgNWs are taken up and accumulate in different types of lung cells, such as alveolar type-I and type-II epithelial cells [31]. In our work, we wanted to find out if AgNWs are also taken up in other cell lines and at which concentration. Cells were treated with Ag^+, AgNWs or AgNWs-CNT for 24 h. Concentrations up to 10 µg/mL were tested as they caused no relevant differences in toxicity to osteoblasts after 24 h of exposure (Figure 9).

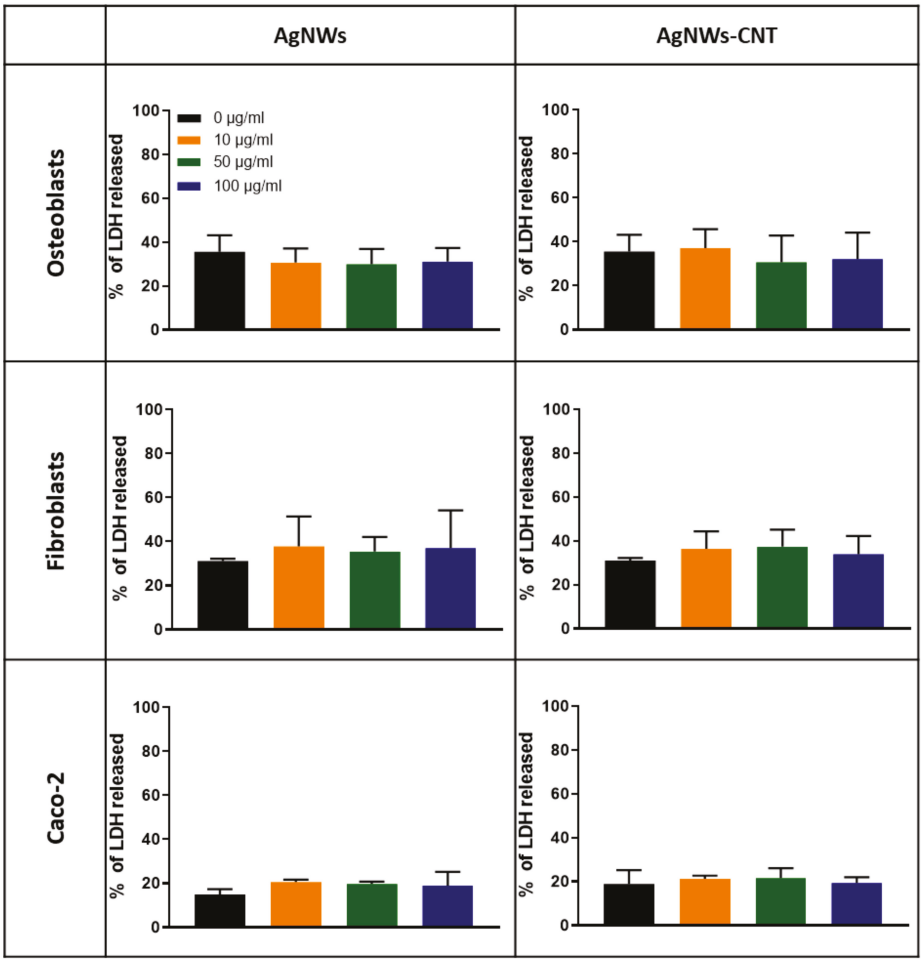

Figure 8. Percentage LDH release from osteoblasts, fibroblasts and Caco-2 after 24 h of exposure to different concentrations of AgNWs or AgNWs-CNTs. The one-way ANOVA calculated among the different concentrations of each test did not show statistical differences ($p > 0.05$). Data are reported as the mean ± SD ($n = 3$).

AgNWs were up taken by all cell lines more efficiently than Ag^+ (Tukey's multicomparison test showed $p < 0.0001$) and in a concentration-dependent manner. A similar behavior was found with mammalian kidney cells (Pk15) for silver nanoparticles of different sizes (ca. 13.8–61.2 µm) by Milic et al. [32]. We hypothesized that as there is no specific transporter for Ag^+, it has to compete for transporters with other ionic species, and the amount of Ag that entered in the cells was inferior

in comparison to AgNWs that can enter by endocytosis. Results of ICP-OES were confirmed by fluorescence microscopy for osteoblasts (Figure 10), where AgNWs accumulated either close to the membrane (Figure 10F) or within the cytoplasm (Figure 10F–I).

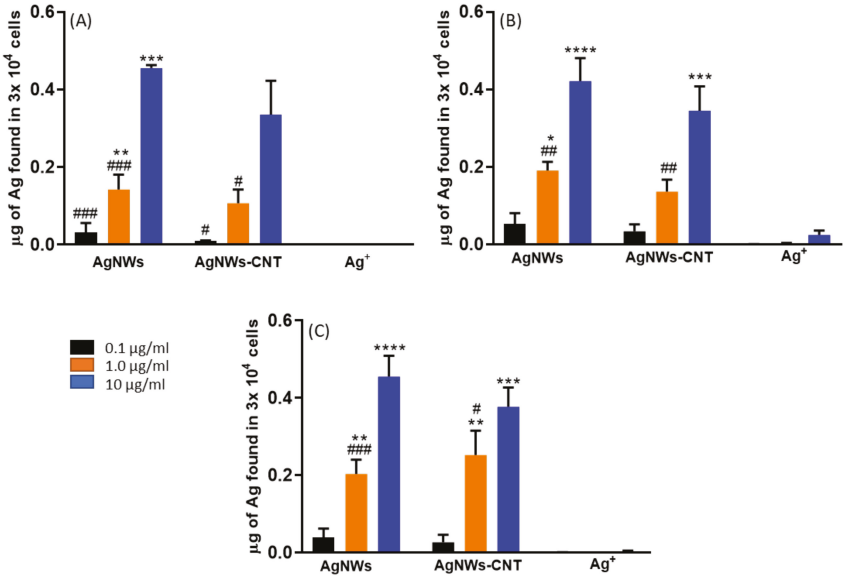

Figure 9. Uptake of silver by (**A**) osteoblasts, (**B**) fibroblasts and (**C**) Caco-2 treated with AgNWs, AgNWs-CNT and $AgNO_3$. Data are expressed as the mean ± SD ($n = 3$). One way Anova indicated at least $p < 0.05$ for all samples tested apart from $AgNO_3$. Results of the post-hoc Tukey multicomparison test are shown in the graph (symbol *compared to 0.1 and # compared to 10 µg/mL).

3. Discussion

The present study aimed to investigate both the antibacterial efficacy and the eukaryotic cytocompatibility of silver nanowires in vitro, as well as to test the effect of silver nanowire composite materials in combination with carbon nanotubes (based on previous reports of enhanced activity of silver nanowires combined with graphene) [11]. In this work, AgNWs-CNT-mix (a physical mixture of AgNWs and CNTs) was used as a control to further investigate the role of CNTs in the synthesis and properties of the composite material. Silver nanowires were successfully synthesized both in the presence and in absence of carbon nanotubes using the soft template method, as confirmed by UV-VIS, XRD and EM imaging. The average size (ca. 70 nm in diameter and 5 µm in length) and silver content in both materials were similar. In the soft template synthesis of AgNWs, a coordination complex is formed between silver ions and PVP through donation of lone-pair electrons of oxygen and nitrogen atoms of PVP to sp orbitals of the metallic silver reduced by glycerol [33]. We hypothesized that –COOH groups of CNTs can interact with Ag^+, forming the first nucleation centers for the growth of silver nanowires. TEM images supported the theory that nucleation centers form on the surface of carbon nanotubes and lead to the formation of nanowires along the axis of CNTs. Furthermore, size and silver content data suggest that whereas CNTs might have played a role in the nucleation and reduction of heat required in the synthesis (as seen on UV-Vis spectra), they are not chemically bound to AgNWs, and as a consequence, they are removed during the purification process. The release of Ag^+ from the nanowires was also studied; the silver ion concentration was higher than 0.1 ppb (minimum effective concentration [34]) already after 30 min, suggesting that these nanomaterials are potential platforms for Ag^+ controlled release for antibacterial purposes. In fact, even though $AgNO_3$

is a more potent antibacterial agent than AgNWs, free silver ions may not act in the long term, as they can be easily washed away by physiological fluids, whereas silver nanowires can act as reservoirs and allow for a sustained release of therapeutic doses [35].

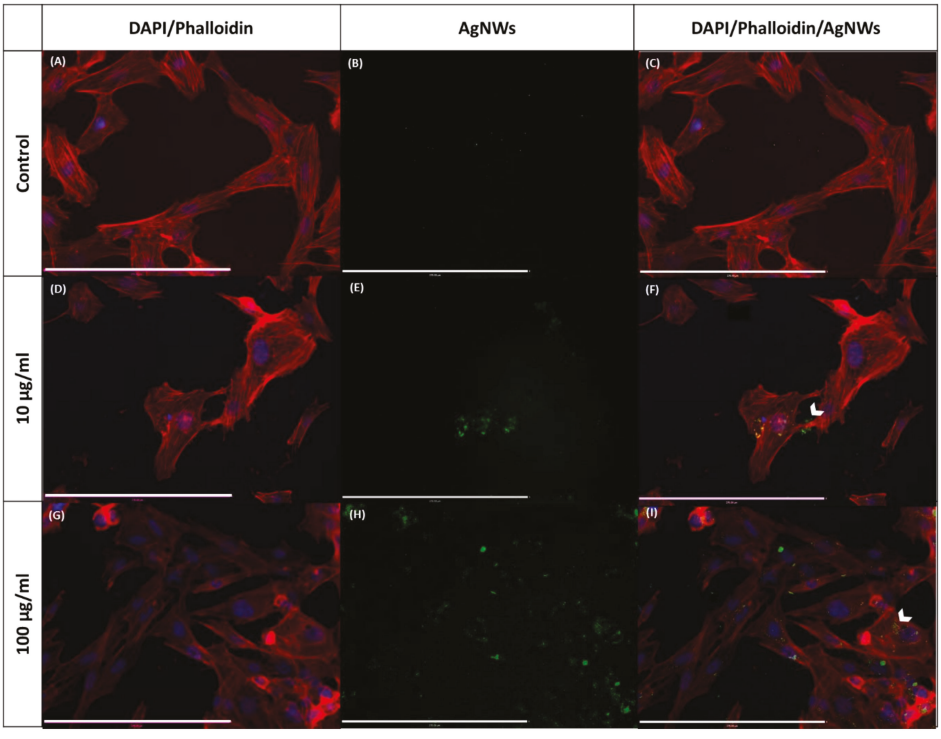

Figure 10. Phalloidin Dylight 550- and DAPI-stained osteoblast cells at 24 h of incubation with AgNWs (10 and 100 µg/mL). (**A**,**D**) and (**G**): merged images of Phalloidin (staining F-actin) and DAPI (staining nuclei) of osteoblasts. (**B**,**E**) and (**H**): AgNWs excited at 495 nm and emitting at 519 nm. (**C**,**F**) and (**I**): merged images of Phalloidin/DAPI/AgNWs. Scale bar 270 µm.

As MIC and MBC values appeared to be similar among AgNWs, AgNWs-CNT and AgNWs-CNT-mix, we could assume that the three preparations had similar antibacterial properties (with no effect due to the presence of CNTs). Moreover, as reported by Cavassin et al., in order to reduce the selection of resistant microorganisms, antimicrobials should present an MBC/MIC ratio ≤4; this was found to be the case with AgNWs against all bacteria tested, apart from *S. aureus* for which the value was 4.3 [36]. In our study, we showed that AgNWs had a bactericidal effect against all the isolates, except for MRSA. The antibacterial activity of AgNWs and AgNWs-CNTs was tested in suspension, and the growth kinetics of all the bacterial strains tested were affected by the treatment but in different ways. Similar results were observed by Cui et Liu, who described the influence of increasing concentrations of AgNWs on *E. coli* growth [11]. However, whereas they showed growth inhibition at concentrations higher than 25 µg/mL, in the present study, none of the concentrations used could inhibit cell growth in the same time frame. Variations in the results can be due to microbial strains, but also to physicochemical characteristics of the AgNW suspension, for instance, the presence of PVP [37]. In our study, MRSA was found to be the least sensitive, whereas *S. saprophyticus* was the most susceptible. These results indicate that it is not possible to explain the species sensitivity to silver nanoparticles in terms of bacterial classification (gram-positive and gram-negative), but that there

are more specific differences among species [37]. MRSA has been previously described as susceptible to AgNPs, with evident membrane damage shown by TEM images; the damage was attributed to charge interaction between positively charged nanoparticles and negatively charged peptidoglycan, and only the smaller particles (dia. < 20 nm) were observed to enter the cells [38]. In the case of AgNWs, the negative charge and longer length might hinder the interaction with MRSA and reduce efficacy. In this regard, we previously observed that the combination of AgNWs with the positively charged polymer chitosan had a synergistic effect on AgNW efficacy against MRSA [39]. The mechanism of bacterial toxicity was further investigated with a focus on membrane damage and ROS production. The bacterial toxicity of AgNWs was mainly mediated through oxidative stress, in the case of *E. coli* and *S. aureus*, whereas the ROS levels in MRSA were not significantly changed at the tested concentrations, supporting the theory that MRSA could present more efficient antioxidant mechanisms than *E. coli* and *S. aureus*. In this regard, Grinholc et al. found that MRSA was more resistant than *S. aureus* to photodynamic inactivation, a therapeutic means based on the generation of ROS. The exact reason for this difference was not identified, but evidence led to excluding that it was related to the multidrug resistance mechanisms developed by MRSA [40]. When tested on human cell lines, silver nanowires did not show acute toxicity. A significant decrease in cell viability was observed only after prolonged treatment, as previously described [41]. This toxicity could be reduced if the silver nanowires are formulated as part of a device, such as a wound healing dressing or a bone regeneration scaffold. This was shown by Verma et al., who found that silver nanowire toxicity was greatly reduced when not tested as free wires but as part of a thin film [41]. No evidence of membrane damage was observed for any of the cell lines tested. Gliga et al. previously observed that LDH release from human lung cells (BEAS-2) depended on the dimensions of the AgNPs. Testing particles of 10, 40 and 75 nm, they found no significant LDH release for the NPs ≥ 40 nm diameter [42]. Thus, we hypothesize that AgNWs may cause less membrane damage than other AgNPs due to their size. In conclusion, we did not observe any advantage of the use of carbon nanotubes to form AgNW composites. We confirmed the potential use of AgNWs as slow release reservoirs of silver ions. The use of silver nanowires for biomedical applications could be advantageous in applications where a slow and sustained release is required, and embedding of AgNWs in delivery platforms such as wound healing bandages can be used as a strategy to reduce potential cytotoxicity.

4. Materials and Methods

4.1. Materials

2′,7′-Dichlorofluorescin diacetate (≥97%), acetone, agar, chitosan from shrimp shells with low viscosity (degree of deacetylation ~85%, calculated by H^1-NMR), dimethyl sulfoxide anhydrous, (≥99.9%), glutaraldehyde solution, hexamethyldisilazane (≥99%), sodium chloride, octaldehyde (99%), poly(vinylpyrrolidone) powder (55 kDa), phosphate-buffered saline tablets, a silver standard for AAS, sodium cacodylate trihydrate, trypsin-EDTA 0.25% solution, tryptone enzymatic digest from casein, Triton™ X-100 and yeast extract for microbiology were purchased from Sigma–Aldrich (Irvine, UK). Ethanol, glycerol (99%), hydrochloric acid (37%), isopropanol, L-(+)-lactic acid (90 %) and sodium borohydride were purchased from Acros Organics (Geel, Belgium). 3-(4, 5-dimetheylthiazol-2)-2, 5 diphenyl tetrazolium bromide (MTT), 4′,6-diamidino-2-phenylindole dihydrochloride (DAPI), dimethylformamide, DMEM (high glucose, with GlutaMAX™ and pyruvate), fetal bovine serum (FBS), Hank's Balanced Salt Solution (HBSS), HPLC-grade water, methanol, nitric acid (70%), penicillin/streptomycin solution, phalloidin dylight 550, Pierce ™ BCA Protein Assay and silver nitrate were purchased from Fisher (Loughborough, UK). Single-wall carbon nanotubes-COOH OD 1–4 nm (SW-CNTs) were purchased from Cheaptubes.com (Grafton, VT). Corning DMEM/F12 (with L-glutamine and 15 mM HEPES) was purchased from Scientific Laboratory Supplies (UK).

4.2. Synthesis and Characterization of AgNWs

4.2.1. Synthesis of AgNWs and Composites

AgNWs were synthesized via the polyol method, as previously described [43]. AgNWs-CNT were synthetized in the presence of CNTs with a slightly modified method. After complete dissolution of PVP in glycerol, 5.8 mg of carbon nanotubes was added and sonicated for 2 h to favor dispersion. After sonication, the synthetic procedure was the same as that used for AgNWs. The reaction progress was monitored by UV-Vis in the wavelength range of 300–600 nm (Thermo Scientific Nicolet Evolution 100 UV-Visible Spectrophotometer, Loughborough, UK). As a control, a physical mixture of CNTs and AgNWs (AgNWs-CNT mix) was prepared. Briefly, *N*-octyl-*O*-sulphate chitosan (NOSC, 10 mg, synthetized as previously described [44]) was dissolved in 10 mL of purified water before the addition of 12.5 mg of CNTs. The sample was sonicated for 4 h. Then, 40 mL of deoxygenated water and 2 g of PVP were added to the mixture. The mixture was then heated and maintained at 80 ∘C for 30 min. AgNWs in deoxygenated water (10 mL, 1.5 mg/mL) were then added to the reaction mixture; this was stirred at 800 rpm for 6 h in the dark. The sample was then centrifuged at 2880 g for twenty minutes and the supernatant removed. This step was repeated twice. The solid pellet obtained was then washed and stored as previously described [43].

4.2.2. Characterization of AgNWs and Composites

Freeze-dried samples were suspended in deionized water at a concentration of 0.1 mg/mL; suspensions were dropped onto TEM grids (Agar scientific square mesh TEM support grids—copper) and allowed to dry at room temperature and pressure; no further treatment was applied. Dry grids were stored in sealed Petri dishes in a desiccator until analysis with an FEI CM120 BioTwin transmission electron microscope. The crystal structure of the samples was determined with a Bruker D2-Phaser diffractometer. Instrumental parameters were as follows: CuKα radiation, 30kV, 10 mA, LynxEye PSD detector with an angular opening of 5°, 2θ range 10°–80°, step size 0.020°, time per step 1 s, spinner 7.5 rpm. The alignment of the instrument was calibrated using an international standard (NIST 1976b). A low-background silicon crystal specimen holder (Bruker) was used. The analyses were performed at 26 ± 2°C. The XRD patterns were evaluated using Bruker EVA 14.2 (DIFFRAC^{plus} Package) software coupled with the database PDF-2 (ICDD). The total silver content and silver release were determined after digesting the freeze-dried samples in an equal volume of MilliQ water and 70% nitric acid. The volume of digested samples was brought up to 20 mL with MilliQ water. Finally, the solutions containing CNTs were filtered five times by a glass microfiber filter (GF/D). The silver content was determined by an inductively coupled plasma optical emission (ICP-OES) spectrometer (Spectroblue OEP-TI, Ametek, Germany) equipped with an ASX-520 autosampler. External calibration was performed by analysis of a blank and five solutions of dissolved $AgNO_3$ standard in 2% HNO_3 ranging from 0 to 100 µg L^{-1}. The charged Ag ions were measured at two wavelengths (328.068 and 328.289 nm), and the results were averaged. The ICP-OES was equipped with Spectro Smart Analyzer software (vs. 6.01.0943). The set parameters for the analysis were as follows: 1450 W for plasma power, 30 rpm for pump speed, 13 L/min for coolant flow and 0.75 L/min for nebulizer flow. Ag^+ release from nanoparticles was determined as previously reported [43]. In order to determine whether either AgNWs or CNTs possessed any autofluorescence, freeze-dried NPs were suspended in deionized water and sonicated to provide a homogeneous suspension. Samples were excited at different wavelengths (390, 488, 550, 570, 633 and 670 nm), and the respective emission spectra were recorded. Images of the suspensions were then acquired by fluorescence microscopy (Zeiss Axio Imager Z1). Surface zeta potentials were measured using a Malvern Zetasizer (Nano ZS, Malvern, UK). Nanoparticles were suspended by sonication in deionized water. On average, twelve measurements per samples were carried out. The selected refractive index for silver nanoparticles was 1.333.

4.3. Antibacterial Activity

4.3.1. Bacterial Culture Preparation

The antibacterial activity of AgNWs was examined by a suspension assay against gram-negative *E.coli (ATCC 25922)* and gram-positive *S. aureus (ATCC 25923),* methicillin-resistant *S. aureus (ATCC 12403) and S. saprophyticus (ATCC 15305).* The bacteria were transferred from −80 °C (30% glycerol) into 5 mL of fresh sterile LB by a sterile toothpick and incubated (at 37 °C and 200 rpm) until the bacterial suspension was cloudy (1 day for *E.coli* and *S. aureus*, 2 days for MRSA and 3 days for *S. saprophyticus*) (MaxQ™ 8000, Thermo Scientific). Then, 50 µL of the bacterial suspension was transferred into 5 mL of fresh sterile LB, and the bacteria were further incubated at 37 °C until the suspension was newly cloudy (1 day for *E. coli*, *S. aureus* and *MRSA* and 2 days for *S. saprophyticus*).

4.3.2. Preparation of Stock Solutions of Antibacterial/Cytotoxic Agents

Stock suspensions (10 mg/mL) of NPs were prepared in deionized water and were then diluted in the appropriate medium. $AgNO_3$ was dissolved in water in order to obtain an Ag^+ concentration of 10 mg/mL. All suspensions and the silver nitrate solutions were sonicated for 2 h in order to obtained homogenous preparations.

4.3.3. Determination of the Minimum Inhibitory Concentration (MIC) and Minimum Bactericidal Concentration (MBC)

Bacterial suspensions were prepared as described above. Samples were tested at a range of concentrations (10, 100, 200, 500, 750, 1000, 1500, 2000 and 3000 µg/mL) against bacterial suspensions (10^7 CFU/mL) to a final volume of 150 µL in 96 well plates. Medium with only bacteria served as a negative control. Then, the plates were incubated at 37 °C for 24 h with gentle shaking (60 rpm). The absorbance was read at 600 nm using the appropriate blank suspensions/solutions. MIC was determined through spectrophotometry as the lowest concentration visibly inhibiting the bacterial growth. MBC was determined by transferring 25 µL samples from each well onto a LB agar plate. After overnight incubation (12 h), the total number of colonies appearing on the culture plate was assessed. The MBC was determined as the concentration at which there was no microbial growth. All experiments were performed in duplicate.

4.3.4. Bacterial Growth Kinetics

The effect of the prepared samples on bacterial growth kinetics was assessed as previously described [43].

4.3.5. Protein Leakage From Bacteria

Bacteria were grown as described above and then centrifuged (13,000 g for 5 min), and the pellets were suspended in sterile PBS (pH 7.4) to a final concentration of 0.6 CFU/mL in the presence of two concentrations of samples to be tested: 12.5 and 100 µg/mL. Bacteria were incubated at 37 °C and 200 rpm. After 1 and 24 h incubation, 1 mL of sample was taken from each test tube and centrifuged (13,000 g for 5 min). The supernatant was then stored at −20 °C until further analysis. The bicinchoninic assay (Pierce ™ BCA Protein Assay) was carried out according to the manufacturer's instructions. Briefly, 25 µL samples were mixed with 200 µL of working solution. Sample absorbance was read at 562 nm after two hours of incubation at 37 °C. The experiment was carried out in duplicate.

4.3.6. Extracellular ROS Production

To determine levels of ROS generated, a fluorescent probe was used; 2, 7- dichlorofluorescein diacetate (DCFH-DA) is converted to highly fluorescent 2, 7- dichlorofluorescein (DCF) in the presence of reactive oxygen species (H_2O_2, $HO^\bullet$ and $ROO^\bullet$). Initially, the DCFH-DA probe was suspended in

DMSO at a 10 mM concentration before being diluted with LB medium to create a 100 μM working solution. After 24 h of incubation of bacteria with the test samples, 1 mL samples were removed and centrifuged at 1300 rpm for 1 min. The supernatant (40 μL) was removed and incubated with 60 μL of the fluorescent probe for 30 min in the dark at 37 °C. Using an excitation wavelength of 485 nm and an emission wavelength of 520 nm, the fluorescence of the samples was read on a bench top fluorimeter (Agilent Cary Eclipse).

4.4. Cytotoxicity Studies

4.4.1. Cell Culture

Human fetal osteoblasts (hFOB 1.19), human foreskin fibroblasts (Hs27) and human colorectal adenocarcinoma cells (Caco-2) were purchased from ATCC®. hFOB were maintained at 37 °C in 5% CO_2 in a flask in Dulbecco's Modified Eagle's Ham/F12 medium (with L-glutamine and 12 mM HEPES) containing 10% fetal bovine serum (FBS) and 1% penicillin/streptomycin (P/S). Hs27 were maintained under the same physical conditions but using DMEM (high glucose, with GlutaMAX™ and pyruvate), 10% FBS and 1% P/S. Caco-2 cells were maintained at 37 °C in 5% CO_2 in MEM containing 10% FBS, 1% P/S, 2 mM L-glutamine and 1% non-essential amino acids (NEAA). Cell lines were used between passage 4 and 12.

4.4.2. Cell Viability

Cell viability was evaluated by the MTT [3-(4, 5-dimetheylthiazol-2)-2, 5 diphenyl tetrazolium bromide] colorimetric technique. Briefly, 5000 cells/ well were plated in a 96-well plate with 100 μL of complete medium and incubated overnight to permit cell attachment. Stock suspensions of test samples in complete medium were sonicated for 4 h at 40 Hz. Aliquots of initial AgNW suspensions were added to the cell medium to final concentrations of 0.1, 1, 10, 25, 50 and 100 μg/mL. After 24 h of incubation, 100 μL of treatments were added to each well containing cells and incubated for 2 and 24 h. At these time points, the treatments were removed and cells were treated with 100 μL of complete medium containing MTT (0.5 mg/mL). The cells were incubated for 4 h in a 5% CO_2 incubator for reduction of MTT by metabolically active cells. The reagent was removed, and the purple formazan crystal inside the cells was solubilized with 100 μL of DMSO. The formazan content was quantified by spectrophotometry at a wavelength of 570 nm (SpectraMax® i3x, Molecular Devices). DMSO served as a blank. The experiments were carried out at least in triplicate.

4.4.3. Cell Membrane Integrity

To evaluate cell membrane integrity, the lactate dehydrogenase (LDH) leakage assay was performed. Cells were plated at 10,000 cells/well. Then, cells were treated with nanoparticles in complete medium containing 2% FBS (as the serum may interfere with the assay). Spontaneous activity and maximum LDH activity were used as controls. The assay was carried out according to the manufacturer's instructions (Pierce ™ LDH cytotoxicity assay). The absorbance was read at 490 and 680 nm. The absorbance read at 680 nm (background) was subtracted from the 490 nm absorbance before the calculation of LDH release.

4.4.4. Intracellular ROS Production

Cells were plated in a sterile black 96-well plate at 25,000 cells/well in 100 μL of medium. Cells were incubated for 24 h; then, the medium was removed, and the cells were washed once with sterile HBSS containing Ca and Mg. Cells were further incubated with DCFH-DA 28 μM in HBSS for 45 min. After washing with HBSS, the cells were treated with the complete medium (2% FBS), containing the test samples, for desired periods of time. Fluorescence was measured as described in Section 4.3.6.

4.4.5. Silver Uptake by Cells

Cells were plated at 30,000 cells/well (1 mL medium) in a 24-well plate and incubated for 24 h, as described above. Cells were exposed to nanoparticles at different concentrations (1 mL). After 24 h of exposure, the medium was removed, and the cells were gently washed twice with cold PBS to remove loosely attached Ag ions and/or NPs from the cell membrane. To each well, HPLC grade water (600 µL) was added, and then 70% HNO_3 (600 µL). The nanoparticles were then digested for 20 min, and the solutions were brought to 21 mL with HPLC grade water. Controls were made with just cells. The silver content was determined by an inductively coupled plasma optical emission (ICP-OES) spectrometer (Spectroblue OEP-TI, Ametek, Germany) equipped with an ASX-520 autosampler. External calibration was performed by analysis of a blank and five solutions of dissolved Ag in 2% HNO3 ranging from 0 to 100 µg L^{-1}. The charged Ag ions were measured at two wavelengths (328.068 and 328.289 nm), and the results were averaged. The ICP-OES was equipped with SPECTRO SMART ANALYZER software (vs. 6.01.0943). The set parameters for the analysis were 1450 W for plasma power, 30 rpm for pump speed, 13.00 L/min for coolant flow and 0.75 L/min for nebulizer flow.

4.4.6. Fluorescence Imaging of AgNW Uptake

Cells were seeded on coverslips at a cell density of 10000 cells/well in 24-well plates (300 µL of medium). After overnight incubation at 37 °C and 5% CO_2, cells were treated with AgNWs. At scheduled time points, cells on coverslips were fixed directly with paraformaldehyde (4%) in PBS (pH 7.4) for 15 min, washed with PBS, permeabilized for 10 min in 0.1% Triton X-100/PBS, washed twice with PBS, blocked with 2% bovine serum albumin (BSA) in PBS for 1 h, washed twice with PBS, stained with Phalloidin Dylight 550 in PBS (2 units/mL, stock solution 300 units/mL in methanol) for 1 h (300 µL, at room temperature), washed twice with PBS, stained with DAPI 2 µg/mL in PBS for 10 min and finally rinsed again with PBS. Coverslips were mounted on glass slides using PermaFluor Aqueous Mounting Medium. Samples were kept protected from light until imaging. Photos were taken with a fluorescence microscope (Zeiss Axio Imager Z1) equipped with a Hamamatsu HR camera and a color AxioCam MRc camera. Images were processed by Volocity 6.3 software.

Supplementary Materials: Supplementary materials can be found at http://www.mdpi.com/1422-0067/21/7/2303/s1.

Author Contributions: Conceptualization, A.D.M. and M.R.; methodology, A.D.M., G.C. and R.R.D.; formal analysis, A.D.M.; investigation, A.D.M., R.S.J., M.C. and G.C.; resources, M.R.; data curation, A.D.M., G.C., R.R.D. and M.R.; writing—original draft preparation, A.D.M.; writing—review and editing, A.D.M., E.B. and M.R.; visualization, A.D.M. and M.R.; supervision, E.B., G.T., R.R.D. and M.R.; funding acquisition, M.R. All authors have read and agreed to the published version of the manuscript.

Funding: This research received no external funding.

Acknowledgments: This project was supported by the University of Portsmouth Research and Innovation Development Fund and the Institute of Biology and Biomedical Science (IBBS). The authors wish to thank Linley Hastewell and Torquil Jackson for their assistance with analytical techniques.

Conflicts of Interest: The authors declare no conflict of interest.

Abbreviations

AgNWs	Silver nanowires
AgNWs-CNT	Silver nanowires prepared in the presence of carbon nanotubes
AgNWs-CNT-mix	Silver nanowire and carbon nanotube physical mixture
CNTs	Carbon nanotubes
ROS	Reactive oxygen species

References

1. Park, J. Functional Fibers, Composites and Textiles Utilizing Photothermal and Joule Heating. *Polymers* **2020**, *12*, 189. [CrossRef]
2. Jung, J.; Cho, H.; Yuksel, R.; Kim, D.; Lee, H.; Kwon, J.; Lee, P.; Yeo, J.; Hong, S.; Unalan, H.E.; et al. Stretchable/flexible silver nanowire Electrodes for energy device applications. *Nanoscale* **2019**, *11*, 20356–20378. [CrossRef]
3. Sohn, H.; Park, C.; Oh, J.-M.; Kang, S.W.; Kim, M.-J. Silver Nanowire Networks: Mechano-Electric Properties and Applications. *Materials* **2019**, *12*, 2526. [CrossRef]
4. Bonilla-Gameros, L.; Chevallier, P.; Sarkissian, A.; Mantovani, D. Silver-based antibacterial strategies for healthcare-associated infections: Processes, challenges, and regulations. An integrated review. *Nanomedicine* **2019**, *24*, 102142. [CrossRef]
5. Kalantari, K.; Mostafavi, E.; Afifi, A.M.; Izadiyan, Z.; Jahangirian, H.; Rafiee-Moghaddam, R.; Webster, T.J. Wound dressings functionalized with silver nanoparticles: promises and pitfalls. *Nanoscale* **2020**, *12*, 2268–2291. [CrossRef]
6. Bi, Y.; Marcus, A.K.; Robert, H.; Krajmalnik-Brown, R.; Rittmann, B.E.; Westerhoff, P.; Ropers, M.-H.; Mercier-Bonin, M. The complex puzzle of dietary silver nanoparticles, mucus and microbiota in the gut. *J. Toxicol. Environ. Health. B. Crit. Rev.* **2020**, *23*, 69–89. [CrossRef]
7. Abdalla, S.S.I.; Katas, H.; Azmi, F.; Busra, M.F.M. Antibacterial and Anti-Biofilm Biosynthesised Silver and Gold Nanoparticles for Medical Applications: Mechanism of action, Toxicity and Current Status. *Curr. Drug Deliv.* **2020**, *17*, 88–100. [CrossRef]
8. Slepicka, P.; Slepickova Kasalkova, N.; Siegel, J.; Kolska, Z.; Svorcik, V. Methods of Gold and Silver Nanoparticles Preparation. *Materials* **2019**, *13*, 1. [CrossRef]
9. Jones, R.; Draheim, R.R.; Roldo, M. Silver Nanowires: Synthesis, Antibacterial Activity and Biomedical Applications. *Appl. Sci.* **2018**, *8*, 673. [CrossRef]
10. Visnapuu, M.; Joost, U.; Juganson, K.; Künnis-Beres, K.; Kahru, A.; Kisand, V.; Ivask, A. Dissolution of silver nanowires and nanospheres dictates their toxicity to escherichia coli. *Biomed Res. Int.* **2013**, *2013*, 819252. [CrossRef]
11. Cui, J.; Liu, Y. Preparation of graphene oxide with silver nanowires to enhance antibacterial properties and cell compatibility. *RSC Adv.* **2015**, *5*, 85748–85755. [CrossRef]
12. Silva, R.M.; Xu, J.; Saiki, C.; Anderson, D.S.; Franzi, L.M.; Vulpe, C.D.; Gilbert, B.; Van Winkle, L.S.; Pinkerton, K.E. Short versus long silver nanowires: A comparison of in vivo pulmonary effects post instillation. *Part. Fibre Toxicol.* **2014**, *11*, 52. [CrossRef]
13. Tomatis, M.; Turci, F.; Ceschino, R.; Riganti, C.; Gazzano, E.; Martra, G.; Ghigo, D.; Fubini, B. High aspect ratio materials: role of surface chemistry vs. length in the historical "long and short amosite asbestos fibers". *Inhal. Toxicol.* **2010**, *22*, 984–998. [CrossRef]
14. Schinwald, A.; Murphy, F.A.; Prina-Mello, A.; Poland, C.A.; Byrne, F.; Movia, D.; Glass, J.R.; Dickerson, J.C.; Schultz, D.A.; Jeffree, C.E.; et al. The threshold length for fiber-induced acute pleural inflammation: shedding light on the early events in asbestos-induced mesothelioma. *Toxicol. Sci.* **2012**, *128*, 461–470. [CrossRef]
15. Stoehr, L.C.; Gonzalez, E.; Stampfl, A.; Casals, E.; Duschl, A.; Puntes, V.; Oostingh, G.J. Shape matters: effects of silver nanospheres and wires on human alveolar epithelial cells. *Part. Fibre Toxicol.* **2011**, *8*, 36. [CrossRef]
16. Rezvani, E.; Rafferty, A.; McGuinness, C.; Kennedy, J. Adverse effects of nanosilver on human health and the environment. *Acta Biomater.* **2019**, *94*, 145–159. [CrossRef]
17. Xiong, Y.; Xie, Y.; Wu, C.; Yang, J.; Li, Z.; Xu, F. Formation of Silver Nanowires Through a Sandwiched Reduction Process. *Adv. Mater.* **2003**, *15*, 405–408. [CrossRef]
18. Cui, L.; Du, Z.; Zou, W.; Li, H.; Zhang, C. The in situ growth of silver nanowires on multi-walled carbon nanotubes and their application in transparent conductive thin films. *RSC Adv.* **2014**, *4*, 27591–27596. [CrossRef]
19. Bari, B.; Lee, J.; Jang, T.; Won, P.; Ko, S.H.; Alamgir, K.; Arshad, M.; Guo, L.J. Simple hydrothermal synthesis of very-long and thin silver nanowires and their application in high quality transparent electrodes. *J. Mater. Chem. A* **2016**, *4*, 11365–11371. [CrossRef]
20. Moreno, I.; Navascues, N.; Arruebo, M.; Irusta, S.; Santamaria, J. Facile preparation of transparent and conductive polymer films based on silver nanowire/polycarbonate nanocomposites. *Nanotechnology* **2013**, *24*, 275603. [CrossRef]

21. Mugadza, T.; Antunes, E.; Nyokong, T. Synthesis of single-walled carbon nanotubes by the pyrolysis of a compression activated iron(II) phthalocyanine/phthalocyanine metal-free derivative/ferric acetate mixture. *J. Chem. Sci.* **2015**, *127*, 1191–1199. [CrossRef]
22. Clayton, D.A.; Benoist, D.M.; Zhu, Y.; Pan, S. Photoluminescence and Spectroelectrochemistry of Single Ag Nanowires. *ACS Nano* **2010**, *4*, 2363–2373. [CrossRef]
23. Sarkar, R.; Kumbhakar, P.; Mitra, A.K.; Ganeev, R.A. Synthesis and photoluminescence properties of silver nanowires. *Curr. Appl. Phys.* **2010**, *10*, 853–857. [CrossRef]
24. Hong, X.; Wen, J.; Xiong, X.; Hu, Y. Shape effect on the antibacterial activity of silver nanoparticles synthesized via a microwave-assisted method. *Environ. Sci. Pollut. Res.* **2016**, *23*, 4489–4497. [CrossRef]
25. Qais, F.A.; Shafiq, A.; Khan, H.M.; Husain, F.M.; Khan, R.A.; Alenazi, B.; Alsalme, A.; Ahmad, I. Antibacterial Effect of Silver Nanoparticles Synthesized Using *Murraya koenigii* (L.) against Multidrug-Resistant Pathogens. *Bioinorg. Chem. Appl.* **2019**, *2019*, 4649506. [CrossRef]
26. Hwan, S.; Lee, H.-S.; Ryu, D.-S.; Choi, S.-J.; Lee, D.-S. Antibacterial Activity of Silver-Nanoparticles Against Staphylococcus Aureus and Escherichia Coli. *Korean J. Microbiol. Biotechnol.* **2011**, *39*, 77–85.
27. Quinteros, M.A.; Cano Aristizabal, V.; Dalmasso, P.R.; Paraje, M.G.; Paez, P.L. Oxidative stress generation of silver nanoparticles in three bacterial genera and its relationship with the antimicrobial activity. *Toxicol. In Vitro* **2016**, *36*, 216–223. [CrossRef]
28. Böhmert, L.; Niemann, B.; Thünemann, A.F.; Lampen, A. Cytotoxicity of peptide-coated silver nanoparticles on the human intestinal cell line Caco-2. *Arch. Toxicol.* **2012**, *86*, 1107–1115. [CrossRef]
29. Avalos, A.; Haza, A.I.; Mateo, D.; Morales, P. Cytotoxicity and ROS production of manufactured silver nanoparticles of different sizes in hepatoma and leukemia cells. *J. Appl. Toxicol.* **2014**, *34*, 413–423. [CrossRef]
30. Lee, Y.-H.; Cheng, F.-Y.; Chiu, H.-W.; Tsai, J.-C.; Fang, C.-Y.; Chen, C.-W.; Wang, Y.-J. Cytotoxicity, oxidative stress, apoptosis and the autophagic effects of silver nanoparticles in mouse embryonic fibroblasts. *Biomaterials* **2014**, *35*, 4706–4715. [CrossRef]
31. Sweeney, S.; Theodorou, I.G.; Zambianchi, M.; Chen, S.; Gow, A.; Schwander, S.; Zhang, J.J.; Chung, K.F.; Shaffer, M.S.P.; Ryan, M.P.; et al. Silver nanowire interactions with primary human alveolar type-II epithelial cell secretions: contrasting bioreactivity with human alveolar type-I and type-II epithelial cells. *Nanoscale* **2015**, *7*, 10398–10409. [CrossRef] [PubMed]
32. Milić, M.; Leitinger, G.; Pavičić, I.; Zebić Avdičević, M.; Dobrović, S.; Goessler, W.; Vinković Vrček, I. Cellular uptake and toxicity effects of silver nanoparticles in mammalian kidney cells. *J. Appl. Toxicol.* **2015**, *35*, 581–592. [CrossRef] [PubMed]
33. Mao, H.; Feng, J.; Ma, X.; Wu, C.; Zhao, X. One-dimensional silver nanowires synthesized by self-seeding polyol process. *J. Nanoparticle Res.* **2012**, *14*, 887. [CrossRef]
34. Kumar, R.; Münstedt, H. Silver ion release from antimicrobial polyamide/silver composites. *Biomaterials* **2005**, *26*, 2081–2088. [CrossRef] [PubMed]
35. Wiglusz, R.J.; Kedziora, A.; Lukowiak, A.; Doroszkiewicz, W.; Strek, W. Hydroxyapatites and europium(III) doped hydroxyapatites as a carrier of silver nanoparticles and their antimicrobial activity. *J. Biomed. Nanotechnol.* **2012**, *8*, 605–612. [CrossRef] [PubMed]
36. Cavassin, E.D.; de Figueiredo, L.F.P.; Otoch, J.P.; Seckler, M.M.; de Oliveira, R.A.; Franco, F.F.; Marangoni, V.S.; Zucolotto, V.; Levin, A.S.S.; Costa, S.F. Comparison of methods to detect the in vitro activity of silver nanoparticles (AgNP) against multidrug resistant bacteria. *J. Nanobiotechnology* **2015**, *13*, 64. [CrossRef]
37. Agnihotri, S.; Mukherji, S.; Mukherji, S. Size-controlled silver nanoparticles synthesized over the range 5–100 nm using the same protocol and their antibacterial efficacy. *RSC Adv.* **2014**, *4*, 3974–3983. [CrossRef]
38. Romero-Urbina, D.G.; Lara, H.H.; Velázquez-Salazar, J.J.; Arellano-Jiménez, M.J.; Larios, E.; Srinivasan, A.; Lopez-Ribot, J.L.; Yacamán, M.J. Ultrastructural changes in methicillin-resistant Staphylococcus aureus induced by positively charged silver nanoparticles. *Beilstein J. Nanotechnol.* **2015**, *6*, 2396–2405. [CrossRef]
39. De Mori, A.; Di Gregorio, E.; Kao, A.P.; Tozzi, G.; Barbu, E.; Sanghani-Kerai, A.; Draheim, R.R.; Roldo, M. Antibacterial PMMA Composite Cements with Tunable Thermal and Mechanical Properties. *ACS Omega* **2019**, *4*, 19664–19675. [CrossRef]
40. Grinholc, M.; Rapacka-Zdonczyk, A.; Rybak, B.; Szabados, F.; Bielawski, K.P. Multiresistant strains are as susceptible to photodynamic inactivation as their naïve counterparts: protoporphyrin IX-mediated photoinactivation reveals differences between methicillin-resistant and methicillin-sensitive Staphylococcus aureus strains. *Photomed. Laser Surg.* **2014**, *32*, 121–129. [CrossRef]

41. Verma, N.K.; Conroy, J.; Lyons, P.E.; Coleman, J.; O'Sullivan, M.P.; Kornfeld, H.; Kelleher, D.; Volkov, Y. Autophagy induction by silver nanowires: A new aspect in the biocompatibility assessment of nanocomposite thin films. *Toxicol. Appl. Pharmacol.* **2012**, *264*, 451–461. [CrossRef]
42. Gliga, A.R.; Skoglund, S.; Wallinder, I.O.; Fadeel, B.; Karlsson, H.L. Size-dependent cytotoxicity of silver nanoparticles in human lung cells: the role of cellular uptake, agglomeration and Ag release. *Part. Fibre Toxicol.* **2014**, *11*, 11. [CrossRef]
43. De Mori, A.; Hafidh, M.; Mele, N.; Yusuf, R.; Cerri, G.; Gavini, E.; Tozzi, G.; Barbu, E.; Conconi, M.; Draheim, R.; et al. Sustained Release from Injectable Composite Gels Loaded with Silver Nanowires Designed to Combat Bacterial Resistance in Bone Regeneration Applications. *Pharmaceutics* **2019**, *11*, 116. [CrossRef]
44. Roldo, M.; Power, K.; Smith, J.R.; Cox, P.A.; Papagelis, K.; Bouropoulos, N.; Fatouros, D.G. N-Octyl-O-sulfate chitosan stabilises single wall carbon nanotubes in aqueous media and bestows biocompatibility. *Nanoscale* **2009**, *1*, 366–373. [CrossRef]

International Journal of
Molecular Sciences

MDPI

Article

In Situ Formation of Ag Nanoparticles in Mesoporous TiO_2 Films Decorated on Bamboo via Self-Sacrificing Reduction to Synthesize Nanocomposites with Efficient Antifungal Activity

Jingpeng Li [1,2], Minglei Su [2], Anke Wang [1], Zaixing Wu [1], Yuhe Chen [1,*], Daochun Qin [2,*] and Zehui Jiang [2]

[1] Key Laboratory of High Efficient Processing of Bamboo of Zhejiang Province, Engineering Technology Research Center for Building and Decorating Materials of Bamboo State Forestry Administration, China National Bamboo Research Center, Hangzhou 310012, China; lijp@caf.ac.cn (J.L.); wang_anke@126.com (A.W.); jansonwu@126.com (Z.W.)

[2] International Center for Bamboo and Rattan, Beijing 100102, China; suminglei1122@163.com (M.S.); jiangzehui@icbr.ac.cn (Z.J.)

* Correspondence: yuhec@sina.com (Y.C.); qindc@icbr.ac.cn (D.Q.)

Received: 8 October 2019; Accepted: 3 November 2019; Published: 5 November 2019

Abstract: We developed a novel green approach for the in situ fabrication of Ag NPs in mesoporous TiO_2 films via the bamboo self-sacrificing reduction of $Ag(NH_3)_2^+$ ions, which can inhibit fungal growth on the bamboo surface. Mesoporous anatase TiO_2 (MT) films were first synthesized on bamboo via a hydrothermal method. Then, Ag NPs with a 5.3 nm mean diameter were incorporated into the pore channels of optimal MT/bamboo (MTB) samples at room temperature without the addition of reducing agents, such that the Ag NPs were almost entirely embedded into the MT films. Our analysis indicated that the solubilized lignin from bamboo, which is rich in oxygen-containing functional groups, serves as a green reductant for reducing the $Ag(NH_3)_2^+$ ions to Ag NPs. Antifungal experiments with *Trichoderma viride* under dark conditions highlighted that the antifungal activity of the Ag/MT/bamboo samples were greater than those of naked bamboo, MTB, and Ag/bamboo, suggesting that these hybrid nanomaterials produce a synergistic antifungal effect that is unrelated to photoactivity. The inhibition of *Penicillium citrinum* effectively followed a similar trend. This newly developed bamboo protection method may provide a sustainable, eco-friendly, and efficient method for enhancing the antifungal characteristics of traditional bamboo, having the potential to prolong the service life of bamboo materials, particularly under dark conditions.

Keywords: bamboo; Ag/TiO_2 nanocomposites; self-sacrificing reduction; antifungal activity

1. Introduction

Bamboo is a widely used material in furniture, construction, and commodities trading owing to its renewability, easy processability, high strength-to-weight ratio, and negative carbon footprint [1]. However, bamboo, which is rich in nutrients, such as starch, saccharides, proteins, and aliphatics, and low in toxic constituents, is easily susceptible to attack by a variety of microorganisms such as fungi, bacteria, and insects. Such mildew-based attacks can impair its durability and cause the bamboo materials to lose their value during storage, transport, and even in their final usage [2]. Over 10% of the global annual bamboo output is damaged by microbiological attack, which greatly limits the usefulness of bamboo products, resulting in massive economic and bamboo resource losses [3]. Numerous methods have been employed to overcome this mildew problem by prolonging the service life of bamboo and adding value to bamboo products. Traditional bamboo protection

methods against fungi include microwave and high-temperature treatments [4,5], which could sterilize and decrease the starch and sugar contents of the bamboo. Furthermore, chemical mold-resistant agents, including pentachlorophenol, alkaline copper quaternary compounds [6], chromated copper arsenate [7], chitosan–copper complex [8], and camphor leaf extract [9], have been used to prevent fungal growth in bamboo products. However, the use of various fungicidal chemicals has been banned or restricted owing to drawbacks such as their potential toxicity, leaching and environmental concerns, and unpleasant odor. Therefore, it is desirable to develop novel, effective, and non-toxic antifungal agents for bamboo materials.

Nanotechnological advances have permitted the development of nanosized metal oxides or their composites, such as TiO_2 [10], ZnO [11], Fe^{3+}-TiO_2 [12], and ZnO/TiO_2 [13,14], to mitigate fungal growth in bamboo, as outlined in our previous research. However, numerous limitations and shortcomings remain, such as the poor antifungal ability to single-phase materials, the need for ultraviolet/visible (UV/VIS) light, poor adhesion, and leaching resistance. For example, TiO_2 coatings can combine strongly with the bamboo matrix, but single-phase TiO_2 is not able to achieve significant fungal resistance unless it is either combined with co-biocides or in the absence of UV light. Although ZnO/TiO_2 nanocomposites exhibit excellent antifungal activity under dark conditions, leaching resistance has become an urgent problem because nanosized ZnO was hardly incorporated into the TiO_2 matrix that coated the bamboo substrate. Previous studies have proven that Ag nanoparticles (NPs), as well as Ag nanocomposites or Ag NP-based materials, exhibit potent antimicrobial efficacy against bacteria, viruses, and fungi with low toxicity for humans and animals [15–17]. The incorporation of Ag NPs into various matrices, such as cellulose-based materials [18], organic polymer complexes [19], polymer-inorganic hybrid matrices [20], and inorganic hybrid matrices [16], has recently been investigated to extend their utility in practical antimicrobial applications, particularly in inorganic hybrid matrices with mesoporous structures. Ag-containing materials that are formed by embedding Ag NPs within mesoporous nanomaterials may protect the Ag NPs from aggregation and allow for the slow release of Ag ions; as such, these materials are predicted to be more effective as an antibacterial agent than conventional Ag NPs [16,21]. Ag NPs are generally prepared via three major approaches: UV irradiation reduction [22], thermal decomposition [23], and chemical reduction [24], with chemical reduction being the most widely used method. However, this synthesis process requires the addition of reducing agents, such as sodium borohydride, hydrazine hydrate, aldehydes, or stabilizing agents, all of which have undesirable environmental impacts and require additional steps during synthesis.

The bamboo cell wall primarily comprises cellulose, hemicellulose, and lignin. Lignin is a complex phenolic polymer that comprises methoxylated phenylpropane substructures with many functional groups, such as hydroxyl, carbonyl, and aldehyde groups [25,26]; these groups can act as reductive functional groups for metal NP synthesis [27,28]. However, an exhaustive literature search indicates there is currently no report that discusses the preparation of Ag NPs by using bamboo as this reducing agent. In this study, a novel green approach was developed for the in situ fabrication of Ag NPs in mesoporous anatase TiO_2 (MT) films via the bamboo self-sacrificing reduction of $Ag(NH_3)_2^+$ ions. Various characterization techniques, including X-ray diffraction (XRD), Brunauer–Emmett–Teller (BET) analysis, X-ray photoelectron spectroscopy (XPS), scanning electron microscopy (SEM), high-resolution transmission electron microscopy (HRTEM), and Fourier transform infrared spectroscopy (FTIR) were employed to study surface properties such as the film microstructure, crystalline structure, surface area, and pore size. Furthermore, the mechanism for the in situ reduction of the Ag NPs in the pore channel of the MT films was investigated. This method was conducted without the use of chemical reducing or stabilizing agents such as sodium borohydride, hydrazine hydrate, and aldehydes, and could yield a highly dispersed arrangement of small Ag NPs in the MT films. These Ag-TiO_2 composite films endowed the bamboo with excellent antifungal activity; consequently, the growth of *Trichoderma viride* (*T. viride*) and *Penicillium citrinum* (*P. citrinum*) were effectively inhibited owing to a synergistic antifungal effect that was unrelated to photoactivity. The adhesion and long-term stability

of these Ag-TiO_2 composite films on the bamboo surface were studied using Scotch tape and 2 months lab-exposure tests. Additionally, the antifungal mechanism was explored.

2. Results

2.1. Overview of Material Synthesis

The schematics of the ATMB synthesis procedure and its antifungal activity are illustrated in Figure 1. Previous studies have shown that the hydroxyl groups in the bamboo substrate can react with certain metal oxides, such as TiO_2 [10], ZnO [11], and γ-Fe_2O_3 [29], and that bamboo is hydrophilic, with numerous active hydroxyl groups. The existence of numerous R–OH groups as active sites promoted the formation of R−O−Ti linkages between the bamboo surface and TiO_2 NPs. The nucleated TiO_2 layer on the bamboo substrate could serve as the seed layer to boost the homogeneous condensation of TiO_2 NPs. The Ti−OH groups existing on the surface of previous TiO_2 could further promote the growth of TiO_2 NPs by acting as active sites for subsequent particle growth through olation and oxolation, leading to the formation of Ti−O−Ti linkages. Finally, the MT films were formed on the bamboo surface. The positively charged $Ag(NH_3)_2^+$ was quickly drawn to the negatively charged TiO_2 surface, which was covered by F^- or OH groups owing to an attractive electrostatic force. Previous studies have shown that liquid ammonia can be used for solubilizing lignin, resulting in the extraction of lignin from lignocellulose [30,31]. The metal precursors can be in situ reduced to metal NPs using various functional groups, such as the hydroxyl, carbonyl, and aldehyde groups in lignin. The MTB samples were immersed in an $Ag(NH_3)_2OH$ solution, with the $Ag(NH_3)_2^+$ ions in the $Ag(NH_3)_2OH$ solution being slowly reduced by lignin and forming Ag NPs in the pore channel of MT films on the bamboo surface. The Ag NPs retained great mechanical stability even after the Scotch tape test, owing to the strong binding between the Ag NPs and TiO_2 matrix. Fungal growth was inhibited by the strong antifungal properties of the resultant AMTB samples.

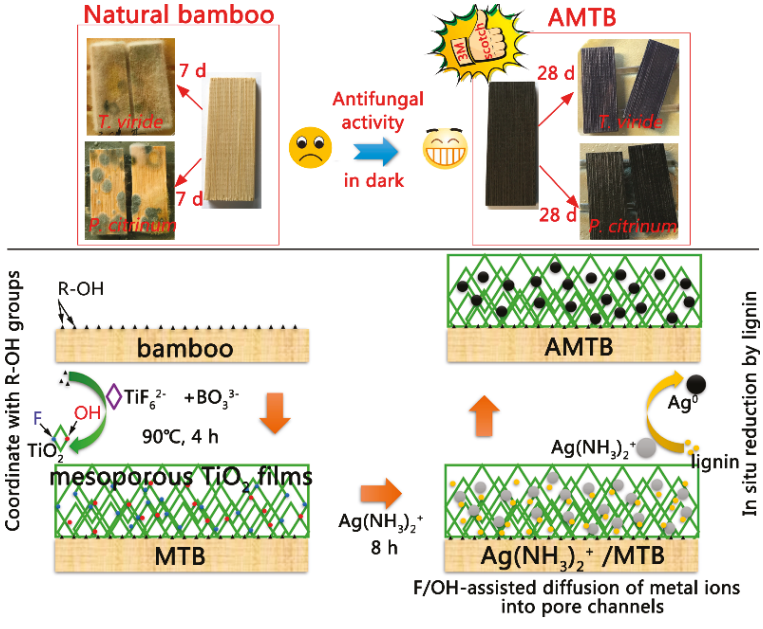

Figure 1. Schematic of the Ag NP-decorated mesoporous anatase TiO_2 film-coated bamboo (AMTB) synthesis procedure and its antifungal activity owing to which fungal growth was inhibited for the two tested fungi. MTB: mesoporous anatase TiO_2 film-coated bamboo.

2.2. The Optimized Synthesis of MTB

XRD and BET analyses were conducted to optimize the MTB synthesis process by determining the structural changes in the MT films on the bamboo surface at different growth times. Three characteristic broad peaks at 2θ = 16°, 22°, and 35° were associated with the crystalline diffraction of cellulose in bamboo (Figure 2a). Five new peaks were observed at 2θ = 25.3°, 37.8°, 48.0°, 53.9°, and 62.7° in the MTB samples, which were attributed to the diffraction peaks of the (101), (004), (200), (105), and (204) planes of anatase TiO_2 structures [10]. The intensity of the anatase diffraction peaks increased as the growth time increased from 2 to 4 h; however, there was no obvious increase between 4 and 6 h. No impurity peaks were detected from this pattern, confirming that high-purity TiO_2 films could be deposited on hydrophilic bamboo via a hydrothermal method.

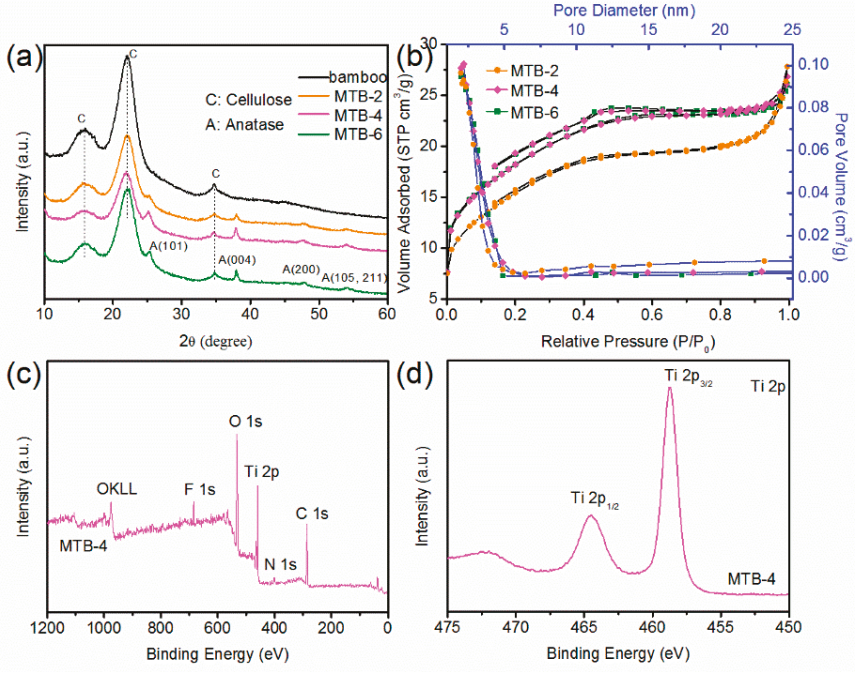

Figure 2. (**a**) XRD spectra of bamboo, MTB-2, MTB-4, and MTB-6. (**b**) N_2 adsorption–desorption isotherm and pore-size distributions of MTB-2, MTB-4, and MTB-6. (**c**) X-ray photoelectron spectroscopy (XPS) survey spectra of MTB-4. (**d**) XPS spectrum of Ti 2p.

The pore structure and surface area of the samples were characterized using the N_2 adsorption–desorption isotherms (Figure 2b), with specific surface areas of 55.8, 66.4, and 65.0 $m^2\ g^{-1}$ calculated for samples MTB-2, MTB-4, and MTB-6, respectively, by the multi-point BET method (Table 1). The pore-size analyses from the N_2 adsorption branch revealed that the pore diameter decreased from 3.1 to 2.5 nm as the growth time increased; however, the total pore volume was not observed to change. These results indicated that the growth time of the MT films on bamboo was optimum at 4 h.

Furthermore, the chemical compositions and valence of the MTB-4 sample were confirmed via XPS analysis, with the survey spectra revealing the presence of O, Ti, F, N, and C (Figure 2c), which was consistent with previous results. It should be noted that the presence of F in MTB-4 suggests the adsorbed F^- ions played for a role in the formation of Ag NPs in the pore channel of the MT films. The Ti $2p_{1/2}$ and $2p_{3/2}$ core levels of MTB-4 were approximately 464.6 and 458.9 eV, respectively, as

shown in Figure 2d. A binding energy difference of 5.7 eV was measured between the Ti $2p_{3/2}$ and $2p_{1/2}$ peaks of both samples, indicating that Ti was primarily in the +4-valence state (Ti^{4+}).

Table 1. Summary of the surface area and pore properties of the MTB samples.

Sample	S_{BET}/m^2 g^{-1}	d_P/nm	V_P/cm^3 g^{-1}
MTB-2	55.8	3.1	0.04
MTB-4	65.4	2.5	0.04
MTB-6	65.0	2.5	0.04

2.3. Synthesis and Microstructure Characterization of AMTB

An example SEM image of naked bamboo, which comprises numerous large parenchyma cells, is shown in Figure 3a; the bamboo microstructure was the only other substance observed in the image. The MT films that were self-assembled with nanosized TiO_2 particles were uniformly deposited on the bamboo surface after the 4 h hydrothermal reaction at 90 °C (Figure 3b). A large number of nanosized particles were observed on the anatase films, with these NPs introduced via the bamboo self-sacrificing reduction of $Ag(NH_3)_2^+$ ions, as shown in Figure 3c. Furthermore, the structural state of the nanosized particles was characterized via XRD, with the AMTB samples exhibiting characteristic peaks that matched JCPDS card 36-1451; this indicated that the Ag NPs had face-centered cubic structures (Figure 3d) [32]. Note that the original color of the MTB samples became black–brown owing to the plasmon absorption of Ag NPs (Figure 1). Only the anatase crystal phase and cellulose were observed in the XRD spectra. Cross-sections of the AMTB samples were investigated using EDS to survey the doping depth of the Ag NPs in the MT films (Figure 3e), with the EDS results confirming the presence of Ag (15.52% Ag), indicating that numerous Ag NPs were embedded into the MT films. Furthermore, a small amount of C may have come from the bamboo component (e.g., lignin) that was solubilized in liquid ammonia and involved in the reduction of $Ag(NH_3)_2^+$ ions. These results were supported by the FTIR analyses. XPS analysis was conducted to further determine the composition of the sample surfaces, with a narrow Ag 3d peak detected in the AMTB sample (Figure 3f), which was indicative of a major Ag^0 component (368.2 eV for Ag^0 $3d_{5/2}$ and 374.2 eV for Ag^0 $3d_{3/2}$) that corresponded to the Ag NPs [33]. The F 1s peak in the AMTB sample decreased compared with that of the MTB sample owing to the consumption of F^- ions during the Ag NP synthesis (Figure 3g). The F^- ions on the TiO_2 surface could combine with the $Ag(NH_3)_2^+$ ions through electrostatic attraction, contributing to the formation of Ag NPs. These results indicated that MT films were successfully doped with Ag NPs.

The detailed structure of the AMTB sample and the Ag NP distribution in the MT films were further revealed via TEM, HRTEM, high-angle annular dark-field scanning TEM (HAADF–STEM), and element mapping measurements. The TEM image revealed that a high density of small particles with good dispersity was incorporated into the three-dimensional MT films (Figure 4a). The relatively dark regions in the HRTEM image were attributed to the intertwining of Ag NPs (average diameter of 5.3 nm) with the TiO_2 films (Figure 4b). The lattice fringe spacing was 0.23 nm, which corresponded to the (111) plane of the face-centered-cubic Ag crystals. These results were consistent with the XRD results in Figure 3d. The diameter of the Ag NPs was in the 2−13 nm range (Figure 4c). The STEM analysis results are shown in Figure 4d–h. The bright spots in the HAADF image corresponded to isolated Ag atoms that remained in the MT films (Figure 4d), with a uniform distribution of Ag atoms in the AMTB sample (Figure 4e–h), which suggested that Ag NPs were successfully incorporated into the pore channels of the MT films.

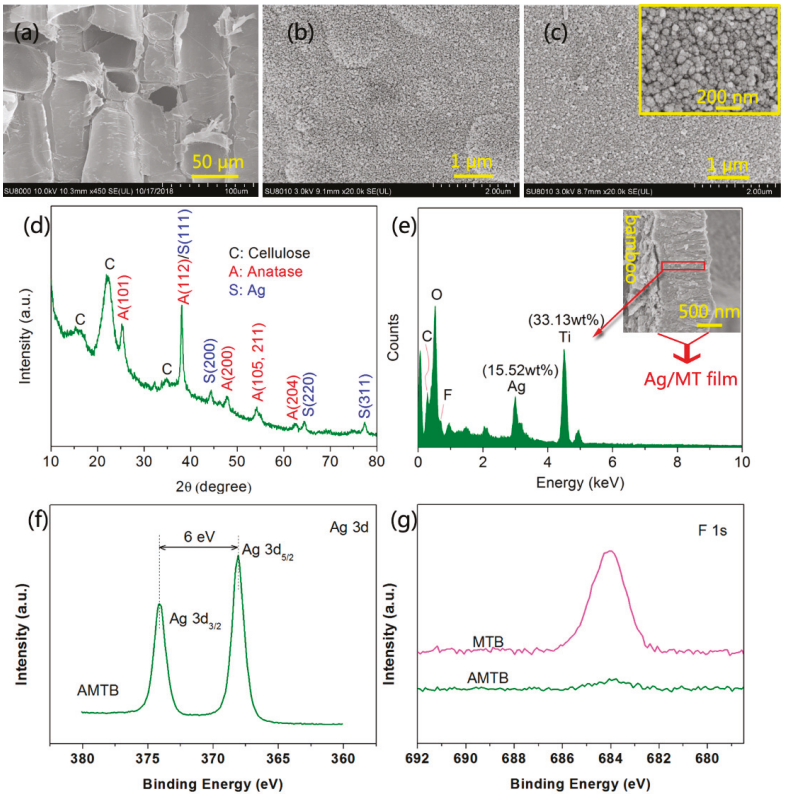

Figure 3. SEM images of (**a**) naked bamboo, (**b**) MTB, and (**c**) AMTB samples (The inset shows the corresponding high-magnification image of each sample). (**d**) XRD spectrum of an AMTB sample. (**e**) The energy-dispersive X-ray spectroscopy (EDS)spectrum of an AMTB sample (The inset is the cross section). (**f**) Ag 3d region of an AMTB sample. (**g**) F 1s region of the MTB and AMTB samples.

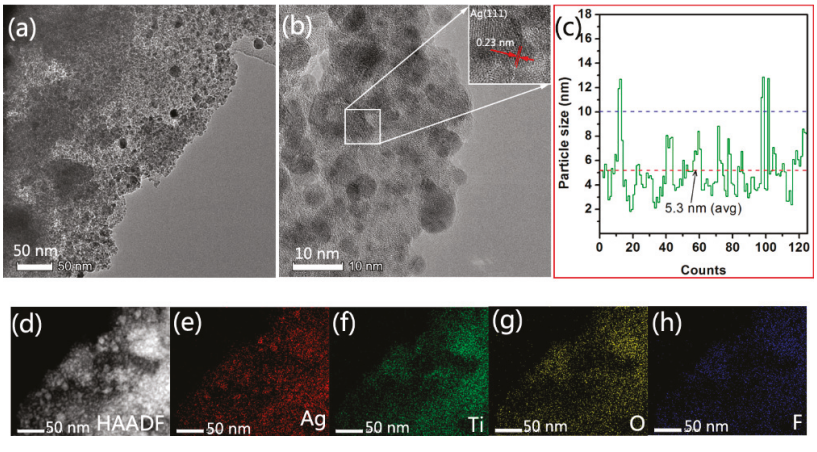

Figure 4. Typical (**a**) TEM and (**b**) high-resolution transmission electron microscopy (HRTEM) images, (**c**) Ag NP size distribution, (**d**) high-angle annular dark-field scanning TEM (HAADF–STEM) image, and (**e**–**h**) elemental mapping analysis of the AMTB samples.

2.4. AMTB Formation Mechanism

The FTIR spectra of naked bamboo, MTB, and AMTB were compared to investigate the AMTB formation mechanism (Figure 5). The naked bamboo absorption band at 3368 cm^{-1} was attributed to the O–H stretching vibration of the intramolecular hydrogen bond. The peak at 2912 cm^{-1} could be assigned to C–H group's stretching vibrations. The other bands were typical bands of cellulose, hemicellulose, and lignin, as follows [11,34]: 1735 cm^{-1} for unconjugated C=O in hemicellulose, 1604 and 1508 cm^{-1} for the aromatic skeleton vibrations of lignin, 1459 cm^{-1} for the CH_3 deformation in lignin and CH_2 bending in xylan, 1425 cm^{-1} for the HCH and OCH in-plane bending vibrations of lignin, 1375 cm^{-1} for the CH deformation vibration of cellulose, 1330 cm^{-1} for the C−H bending of cellulose, 1250 cm^{-1} for the C−O stretching of hemicellulose and lignin, 1163 cm^{-1} for the C−O stretching of cellulose, 1046 cm^{-1} for C−O stretching, 897 cm^{-1} for C−H deformation in hemicellulose and cellulose, and 833 cm^{-1} for the benzene ring C−H bending of lignin.

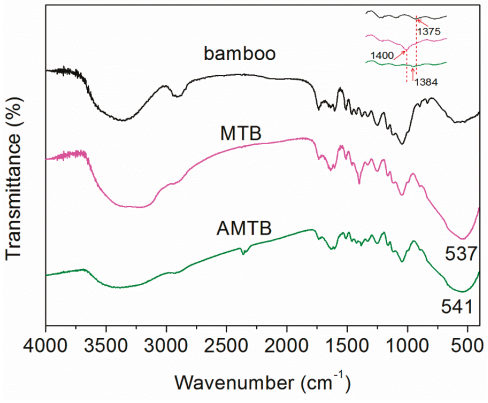

Figure 5. FTIR spectra of naked bamboo, MTB, and AMTB.

A broad band was observed in the 3000–3600 cm^{-1} wavelength range of the MTB spectrum after TiO_2 deposition, which was assigned to the stretching modes of the O−H and N−H bonds [35]. The concomitant appearance of new N−H bands at lower frequencies (3221 cm^{-1}) indicated that numerous R–OH groups served as active sites and reacted with the precursor to immobilize particles on the bamboo surface. The band intensity of the C–H stretching vibration (2888–2947 cm^{-1}) was significantly decreased after hydrothermal treatment. Additionally, a similar reduced band intensity was observed at 1735 cm^{-1}, which corresponded to the C=O stretching vibration. Conversely, the primary bands in the MTB samples were at 537 cm^{-1}, which were attributed to the Ti−O stretching and Ti−O−Ti bridging stretching modes [36]. The peak located at 1400 cm^{-1} was due to the bending vibrations of the N−H bonds in the NH_4^+ ions [37], which was significantly decreased after impregnation in $Ag(NH_3)_2^+$ solution. The observed decreases in the O−H (3384 cm^{-1}), C–H (2888–2947 cm^{-1}), and C=O bonds (1735 cm^{-1}) in the AMTB samples in combination with the existence of –CHO groups in bamboo indicated that these groups participated in the redox reaction with the $Ag(NH_3)_2^+$ solution. These results were further supported by the FTIR spectrum of the AB sample (Figure S2). Previous studies have shown that the abundant oxygen-containing functional groups in natural cotton could be utilized to reduce silver nitrate to Ag NPs on the cotton surface [38]; furthermore, they found that the peak –OH intensity at approximately 3400 cm^{-1} decreased, indicating that some groups, such as hydroxyl, carbonyl, and aldehyde, were involved in the reduction reaction. However, the $Ag(NH_3)_2^+$ solution in the pore channel of the MT films was not in direct contact with the bamboo substrate in our work; as such, the oxygen-containing functional groups in bamboo were not directly involved in the reduction reaction. However, the $Ag(NH_3)_2^+$ solution was still reduced to Ag NPs in the pore

channel of the MT films without adding reducing agents. A new absorption band at 1384 cm^{-1} in the AMTB spectrum was attributed to C–N group stretching vibrations. Owen et al. [31] also reported that ammonia easily penetrates into the wood structure, which causes many of the oxygen linkages that hold the cellulose and hemicellulose polymer chains together to break down. The isolated lignin could react with ammonia to form ammonium salts. A typical lignin UV spectrum was observed at 294 nm, indicating that some lignin was solubilized in ammonia solution, as shown in Figure S3. [39] These ammonium salts in solution could potentially play a crucial role in reducing the $Ag(NH_3)_2^+$ ions to Ag NPs in the pore channel of the MT films. The AMTB sample was successfully fabricated via the direct bamboo self-sacrificing reduction of $Ag(NH_3)_2^+$ ions in the TiO_2 matrix.

2.5. Antifungal Activity of AMTB

2.5.1. Inhibition of *T. viride* Spores

The antifungal activity of naked bamboo, MTB, AB, and AMTB and their ability to inhibit *T. viride* spores are shown in Figure 6. The test specimens were supported by a U-shaped glass rod (4 mm diameter) on the mycelia-covered PDA substrates and had no direct contact with the spores. We can clearly see that the naked bamboo was entirely covered with mycelia after incubation for 7 days (Figure 6a2,a3), indicating that naked bamboo had no resistance to *T. viride*. A small number of mycelia were directly observed on the MTB sample surface after incubation for 28 days (Figure 6b2), with its optical microscope image illustrating that it was completely covered with mycelia (Figure 6b3), similar to that observed for natural bamboo. However, the fungal growth was much more robust in the naked bamboo. Mycelia can grow well in the bamboo in the AB sample after incubation for 28 days, even though many nanosized Ag particles were coated on the bamboo surface (Figure 6c2,c3). These results indicated that the AB samples possessed a poor resistance to *T. viride.* Both the MTB and AB samples had very limited antifungal activity under dark conditions. Conversely, we did not observe mycelia on the AMTB sample surface (Figure 6d2,d3), which indicated that the antifungal activity of the AMTB sample was greater than that of both the MTB and AB samples. These observations suggest that the Ag-TiO_2 hybrid materials produce a synergistic antifungal effect that is unrelated to photoactivity.

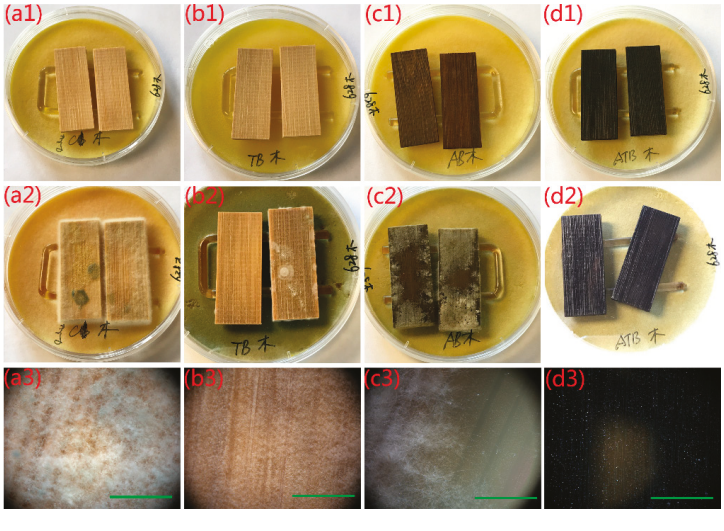

Figure 6. Antifungal properties of (**a1–a3**) naked bamboo, (**b1–b3**) MTB, (**c1–c3**) Ag/bamboo (AB), and (**d1–d3**) AMTB to inhibit *Trichoderma viride* growth. Incubation period: (**a1–d1**) 0 days, (**a2**) 7 days, (**b2–d2**) 28 days. The optical microscope images in (**a3–d3**) correspond to the samples in (**a2–d2**). Scale bars: 1 mm.

2.5.2. Inhibition of *P. citrinum* Spores

P. citrinum was also chosen to confirm the aforementioned conclusion and verify the antifungal activity of the as-prepared samples in the same assays. Multiple fungus clusters were observed on the surface of the naked bamboo after incubation for 7 days (Figure 7a2,a3). The bamboo surface was almost entirely covered with mycelia in the optical microscope image, indicating that the natural bamboo had no resistance to *P. citrinum*. The MTB sample also had poor resistance to *P. citrinum* (Figure 7b2,b3) after incubation for 28 days, similar to its poor resistance to *T. viride.* However, the AB sample showed better antifungal activity than the naked bamboo and MTB samples, as *P. citrinum* mycelia failed to cover the entire surface of the AB sample after incubation for 28 days (Figure 7c2,c3). The area of fungal infection reached 35% (average) at the end of the 28 days incubation period. This also indicated that the antifungal activity of the AB samples for *P. citrinum* was more effective than that for *T. viride*. The AMTB sample exhibited efficient antifungal activity for *P. citrinum* after incubation for 28 days in dark conditions, with no mycelia observed on the AMTB sample surface (Figure 7d2,d3).

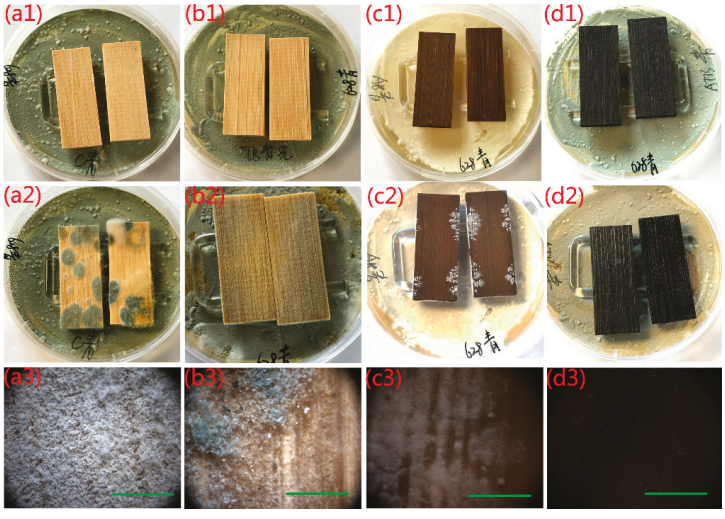

Figure 7. Antifungal properties of (**a1–a3**) naked bamboo, (**b1–b3**) MTB, (**c1–c3**) AB, and (**d1–d3**) AMTB to inhibit *Penicillium citrinum* growth. Incubation period: (**a1–d1**) 0 days, (**a2**) 7 days, (**b2–d2**) 28 days. The corresponding optical microscope images in (**a3–d3**) correspond to the samples in (**a2–d2**). Scale bars: 1 mm.

The antifungal activity of the naked bamboo, MTB, AB, and AMTB samples during the 28 days incubation period are shown in Figure 8. The naked bamboo was seriously infected with both *T. viride* and *P. citrinum*, with the surface infection value reaching ratings of 2.2 and 2.8 on day 4, and 4 and 4 on day 8, respectively. There was a marked improvement in the antifungal activity of the MTB sample against *T. viride* and *P. citrinum* compared with that for naked bamboo. The fungal growth on the MTB surface was slower than that on the naked bamboo surface, with the surface infection value of the MTB sample possessing a 0 rating after 14 days. However, fungi spores began to germinate and grew rapidly after 14 days, with surface infection values reaching ratings of 4 (*T. viride*) and 3.4 (*P. citrinum*) on day 24. The AB sample initially became infected with *T. viride* and *P. citrinum* on days 8 and 12, respectively. The surface infection value for *T. viride* reached a rating of 4 on day 20, whereas it only reached 1.4 for *P. citrinum* at the end of the experiment. The antifungal activity of the AB samples to *P. citrinum* was therefore more effective than that to *T. viride*. Conversely, the surface infection values of

the AMTB samples possessed 0 ratings for both *T. viride* and *P. citrinum* at the end of the experiment, indicating that the AMTB samples displayed effective resistance to fungal growth.

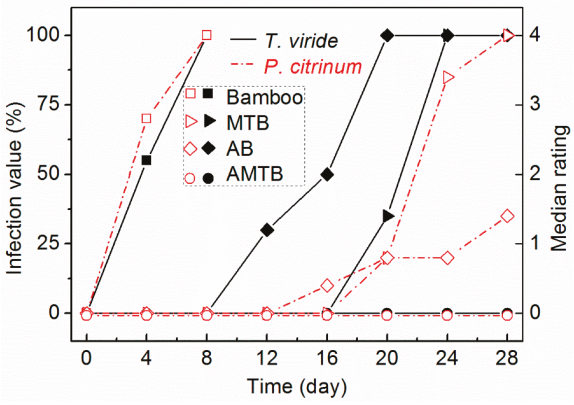

Figure 8. Fungal growth curves for two fungal species (*T. viride* and *P. citrinum*) cultured on naked bamboo, MTB, AB, and AMTB.

2.6. Exploration of the Antifungal Mechanism

Recent studies have indicated that the mechanism responsible for the activation of the biocidal properties of Ag/TiO_2 nanocomposites was rather complicated. The reasons for the enhanced antimicrobial effect of Ag/TiO_2 hybrids in the absence of UV light are still not completely understood. Their enhanced antimicrobial qualities originated from the light-mediated generation of reactive oxygen species, release of toxic silver ions, and cell membrane damage through their contact with the Ag NPs. Li et al. [40] reported that hybrid Ag/TiO_2 nanocomposites possessed stronger bactericidal activity than pure Ag and pure TiO_2 under UV light. It is well known that the doping of Ag NPs on TiO_2 enhances the photocatalytic activity of TiO_2, resulting in the enhanced generation of reactive oxygen species. They also suggested that the release of Ag^+ ions was not the dominant inactivation mechanism for the Ag/TiO_2 nanocomposites [40]. Jin et al. [41] reported a similar observation, where the Ag^+ ions released from Ag_2O/TNBs did not contribute to the bactericidal effects of Ag_2O/TNBs in dark conditions. However, another study also showed that the Ag^+ ion release rates from the Ag/TiO_2 nanocomposites were much higher than those from the Ag NPs, resulting in better bactericidal activity [42]. Furthermore, previous studies have suggested that the enhanced antimicrobial activity of nanocomposites may be due to their large surface-to-volume ratio. However, the BET surface area of the TiO_2 particles decreased owing to Ag NP modification (Table S1). A comparison of the BET surface area and antifungal activity suggested that the surface area was not the main factor contributing to the enhanced antifungal effect. Perkas et al. [43] reported that nanocomposites with smaller-sized Ag NPs incorporated in titania possessed higher antibacterial properties. Esfandiari et al. [44] reported a similar observation, noting that the bactericidal capacity was dependent on the size characteristics of the Ag/TiO_2 coating. Here, numerous Ag NPs that were 50–100 nm in diameter were similarly prepared on the MTB surface via a silver-mirror reaction (Figure S4a). Some *T. viride* mycelia were observed on its surface after incubation for 28 days (Figure S4c), revealing a much poorer antifungal activity than that of the AMTB samples. We believe this could be attributed to the small particle size of the self-sacrificing reduction-derived AMTB (2−10 nm) compared with that of the silver-mirror-reaction-derived AMTB (50−100 nm). The ATMB antifungal activity was greater than those for the MTB and AB samples in the absence of light, suggesting that the Ag/TiO_2 hybrid materials produced a synergistic antifungal effect that was unrelated to photoactivity.

2.7. Stability Evaluation

The Scotch tape test, which was based on ASTM D3359-02 standard, was applied to determine the stability and durability of the Ag-incorporated MT films on the bamboo surface. Scotch tape was pressed against the AMTB sample and subsequently peeled off. Optical images of the AMTB surface before and after 15 peeling attempts are shown in Figure 9, with no obvious damage or detachment of the films after the test. However, slight black particles were observed on the 3M Scotch tape after the first peeling attempt (Figure S5), but this did not affect the antifungal activity of the test AMTB samples. No mycelia were observed on the AMTB surface after incubation for 28 days, indicating the films had good adhesion after the Scotch tape test. Furthermore, the antifungal activity of the AMTB samples after exposure in the lab environment for two months was measured to determine the long-term stability of the AMTB samples. Mycelia failed to cover the AMTB sample surface after incubation for 28 days, indicating that the AMTB samples also retained good long-term stability.

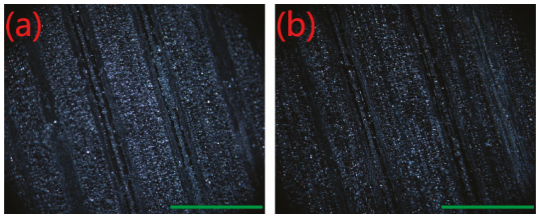

Figure 9. Optical microscope images of the AMTB surfaces during the Scotch tape tests: (**a**) original surface; (**b**) after 15 peeling tests. Scale bars: 1 mm.

3. Conclusions

We have introduced a simple, sustainable, and environmentally friendly method for the in situ fabrication of Ag NPs into mesoporous TiO_2 films via bamboo self-sacrificing reduction. The mesoporous anatase TiO_2 films provided sufficient active sites (F or OH groups) for the $Ag(NH_3)_2{}^+$ ions diffusing into its pore channels. The solubilized lignin from bamboo, which is rich in oxygen-containing functional groups, served as a green reductant for reducing the $Ag(NH_3)_2{}^+$ to Ag NPs in the pore channels. Natural bamboo was not only used as a reductant to nucleate the Ag precursors but also as a support to immobilize the Ag-TiO_2 composite films. These Ag-TiO_2 composite films endowed the bamboo with excellent antifungal activity with which *T. viride* and *P. citrinum* was inhibited, with this synergistic antifungal effect being unrelated to photoactivity. Furthermore, the high antifungal activity was found to be dependent on the size of the Ag NPs. Moreover, the Scotch tape and 2 months lab-exposure tests indicated that the Ag-TiO_2 composite films on the bamboo surface had good adhesion and long-term stability. The use of bamboo as an environmentally friendly and sustainable material with abundant functional groups could serve as a general support to produce metal/bamboo functional materials for a broader range of catalytic and environmental remediation applications.

4. Materials and Methods

4.1. Materials

Air-dried moso bamboo (*Phyllostachys edulis* (Carr.) J.Houz.) specimens (50 (longitudinal) × 20 (tangential) × 5 mm (radial)) were derived from Zhejiang YoYu Corporation (Anji, China). Ammonium hexafluorotitanate ($(NH_4)_2TiF_6$), boracic acid (H_3BO_3), silver nitrate ($AgNO_3$), and ammonia solution (NH_4OH, 25%–28%) were purchased from Aladdin Chemistry Co., Ltd. (Shanghai, China). All the chemicals used in this experiment were of analytical reagent grade. Potato dextrose agar (PDA; 1 L of water, 6 g of potato, 20 g of dextrose, and 20 g of agar, pH = 5.6) was obtained from Qingdao Hope Bio-Technology Co., Ltd. (Qingdao, China). Deionized water (DI water) was prepared with a

Milli-Q Advantage A10 water purification system (Millipore, Bedford, MA, USA) and used throughout the experiments.

4.2. Preparation of the Ag NP-Decorated MT Film-Coated Bamboo (AMTB) Samples

The MT films were synthesized on the bamboo surface through a modified procedure outlined in our previous work [13]. A $(NH_4)_2TiF_6$ and H_3BO_3 solution was first mixed and transferred into a 50 mL Teflon-lined autoclave that contained a bamboo specimen without pH adjustment, and then oven-heated at 90 °C for 2, 4, and 6 h. The resultant MT film-coated bamboo (MTB) samples were then dried overnight at 60 °C. Ag NPs were embedded into the MTB samples by immersing the dried MTB samples in 0.1 M $Ag(NH_3)_2OH$ solution for 8 h at room temperature using fresh $Ag(NH_3)_2OH$ solution that was prepared via the dropwise addition of ammonia solution into aqueous $AgNO_3$ solution until the brown precipitate was dissolved, producing a clear solution. The impregnation of Ag NPs onto the MTB sample surface was deemed successful when the sample turned black–brown. Finally, the resultant Ag NP-decorated MTB (AMTB) samples were washed repeatedly with DI water and oven-dried at 50 °C for 24 h. Ag/bamboo (AB) samples were also prepared following the same Ag impregnation procedure.

4.3. Characterization

XRD patterns were acquired using a Bruker AXS D8 Advance diffractometer (Bruker, Billerica, MA, USA) with a Cu Kα (1.5406 Å) radiation source that operated at 40 kV voltage and 40 mA current. The BET surface areas were measured from the N_2 adsorption–desorption isotherms that were acquired using a Micromeritics ASAP 2020 surface analyzer (Micromeritics, Norcross, GA, USA), with the pore-size distribution curves calculated from the adsorption branch of the isotherm. XPS measurements were acquired using a Thermo ESCALAB 250Xi spectrometer (Thermo Scientific, Waltham, MA, USA) with an Al Kα X-ray source. SEM images and EDS spectra were obtained using a field-emission SEM (Hitachi SU8010, Tokyo, Japan). Structural analysis was conducted via TEM/HRTEM (TF20, Jeol 2100F, 200kV; JEOL, Tokyo, Japan). FTIR analysis was conducted using an FTIR spectrometer (Nicolet Magna 550; GMI, Ramsey, MN, USA) in the 4000–400 cm^{-1} range with KBr pellets. The UV/VIS diffuse reflectance spectra were recorded using a UV-2550 spectrophotometer (Shimadzu, Japan) in the 250–600 nm range.

4.4. Antifungal Test

The antifungal tests of the as-prepared samples were conducted on the basis of Chinese Standard GB/T 18261-2013. *T. viride* and *P. citrinum* were used during all the experiments because they are common fungi that are found in infected bamboo. The fungi spores were obtained from the BeNa Culture Collection (BNCC, Beijing, China) and needed to be activated before use. The activated fungi spores with approximately 1×10^6 CFU/mL (CFU: colony forming unit) were inoculated onto each PDA plate at 25 °C and 95% relative humidity for 7 days until sporulation. The as-prepared samples and U-shaped glass rod was sterilized using an autoclave steam sterilizer at 121 °C and 0.1 MPa for 30 min (MLS-3750; Sanyo, Osaka, Japan) prior to inoculation. A sterilized U-shape glass rod (4 mm diameter) was placed on the PDA substrate, which was covered with mycelium, and two specimens were placed separately onto the glass rod, as shown in Figure S1. Then, the dishes were placed into a climate chamber (BIC-400; Boxun, Shanghai, China), where temperature and relative humidity were fixed at 25 °C and 95%, respectively. The tests were conducted for 28 days. The as-prepared samples (bamboo, MTB, AB, and AMTB) were used for the antifungal tests in the absence of light irradiation. All of the experiments were performed in sextuplet, with the mean values provided in the paper. The fungi control effectiveness was calculated as follows: 0 rating indicated no fungal growth on the sample surface, 1 indicated a surface infection area of less than one-quarter, 2 indicated a surface infection area between one-quarter and one-half, 3 indicated a surface infection area between one-half

and three-quarters, and 4 indicated a surface infection area of greater than three-quarters. Lower infection values represented better antifungal treatment and vice versa.

4.5. Stability Evaluation

The mechanical durability and long-term stability of the ATMB samples were conducted via the Scotch tape test, which was based on ASTM D3359-02 standard, and the 2 months exposure test in a lab environment. Scotch tape was pressed against the AMTB substrate and subsequently peeled off, with the peeling test repeated up to 15 times. Another group of AMTB samples was exposed in the lab environment for 2 months. Then, these two groups of samples were incubated in a climate chamber for 28 days at 25 °C and 95% relative humidity in dark conditions.

Supplementary Materials: The following are available online at http://www.mdpi.com/1422-0067/20/21/5497/s1.

Author Contributions: Conceptualization, J.L., Y.C., and D.Q.; formal analysis, M.S. and Z.W.; investigation, J.L., M.S., A.W., and Z.J.; methodology, J.L.; resources, Y.C. and D.Q.; writing—original draft, J.L.

Funding: The work was financially supported by the Fundamental Research Funds for the Central Non-Profit Research Institution of CAF (CAFYBB2017MA023).

Acknowledgments: The authors would like to thank Teacher Rong from Zhejiang University for support of the SEM analysis, Teacher Qiu from CBRC for the support of the BET analysis, and Teacher Zhang from Shiyanjia Lab for support of the TEM analysis (http://www.Shiyanjia.com).

Conflicts of Interest: The authors declare no conflict of interest.

References

1. Chang, F.-C.; Chen, K.-S.; Yang, P.-Y.; Ko, C.-H. Environmental benefit of utilizing bamboo material based on life cycle assessment. *J. Clean. Prod.* **2018**, *204*, 60–69. [CrossRef]
2. Prosper, N.K.; Zhang, S.; Wu, H.; Yang, S.; Li, S.; Sun, F.; Goodell, B. Enzymatic biocatalysis of bamboo chemical constituents to impart antimold properties. *Wood Sci. Technol.* **2018**, *52*, 619–635. [CrossRef]
3. Wu, Z.; Huang, D.; Wei, W.; Wang, W.; Wang, X.; Wei, Q.; Niu, M.; Lin, M.; Rao, J.; Xie, Y. Mesoporous aluminosilicate improves mildew resistance of bamboo scrimber with CuBP anti-mildew agents. *J. Clean. Prod.* **2019**, *209*, 273–282. [CrossRef]
4. Cheng, D.; Jiang, S.; Zhang, Q. Mould resistance of Moso bamboo treated by two step heat treatment with different aqueous solutions. *Eur. J. Wood Wood Prod.* **2013**, *71*, 143–145. [CrossRef]
5. Kang, F.; Yu, C.; Huang, Q.; Wei, Y.; Zhang, R.; Fei, Y. Advances in application of microwave technology to pest quarantine. *Plant Prot.* **2009**, *6*, 36–39.
6. Hastrup, A.C.S.; Iii, F.G.; Clausen, C.A.; Bo, J. Tolerance of Serpula lacrymans to copper-based wood preservatives. *Int. Biodeter. Biodegr.* **2005**, *56*, 173–177. [CrossRef]
7. Guo, H.; Bachtiar, E.V.; Ribera, J.; Heeb, M.; Schwarze, F.W.M.R.; Burgert, I. Non-biocidal preservation of wood against brown-rot fungi with TiO_2/Ce Xerogel. *Green Chem.* **2018**, *20*, 1375–1382. [CrossRef]
8. Sun, F.; Ma, L.; Chen, A.; Duan, X. Mould-resistance of bamboo treated with the compound of chitosan-copper complex and organic fungicides. *J. Wood Sci.* **2012**, *58*, 51–56. [CrossRef]
9. Xu, G.; Wang, L.; Liu, J.; Hu, S. Decay resistance and thermal stability of bamboo preservatives prepared using camphor leaf extract. *Int. Biodeter. Biodegr.* **2013**, *78*, 103–107. [CrossRef]
10. Li, J.; Hui, Y.; Wu, Z.; Jin, W.; Sheng, H.; Jian, J.; Li, N.; Bao, Y.; Huang, C.; Chen, Z. Room temperature synthesis of crystalline anatase TiO_2 on bamboo timber surface and their short-term antifungal capability under natural weather conditions. *Colloid. Surface. Asp.* **2016**, *508*, 117–123. [CrossRef]
11. Li, J.; Wu, Z.; Bao, Y.; Chen, Y.; Huang, C.; Li, N.; Sheng, H.; Chen, Z. Wet chemical synthesis of ZnO nanocoating on the surface of bamboo timber with improved mould-resistance. *J. Saudi Chem. Soc.* **2017**, *21*, 920–928. [CrossRef]
12. Li, J.; Ren, D.; Wu, Z.; Huang, C.; Yang, H.; Chen, Y.; Hui, Y. Visible-light-mediated antifungal bamboo based on Fe-doped TiO_2 thin films. *RSC Adv.* **2017**, *7*, 55131–55140. [CrossRef]
13. Ren, D.; Li, J.; Bao, Y.; Wu, Z.; He, S.; Wang, A.; Guo, F.; Chen, Y. Low-temperature synthesis of flower-like ZnO microstructures supported on TiO_2 thin films as efficient antifungal coatings for bamboo protection under dark conditions. *Colloid. Surface. Ase.* **2018**, *555*, 381–388. [CrossRef]

14. Ren, D.; Li, J.; Xu, J.; Wu, Z.; Chen, Y. Efficient Antifungal and Flame-Retardant Properties of ZnO-TiO_2-Layered Double-Nanostructures Coated on Bamboo Substrate. *Coatings* **2018**, *8*, 341. [CrossRef]
15. Ales, P.; Milan, K.; Renata, V.; Robert, P.; Jana, S.; Vladimír, K.; Petr, H.; Radek, Z.; Libor, K. Antifungal activity of silver nanoparticles against *Candida* spp. *Biomater.* **2009**, *30*, 6333–6340.
16. Liong, M.; France, B.; Bradley, K.A.; Zink, J.I. Antimicrobial Activity of Silver Nanocrystals Encapsulated in Mesoporous Silica Nanoparticles. *Adv. Mater.* **2010**, *21*, 1684–1689. [CrossRef]
17. Svitlana, C.; Matthias, E. Silver as antibacterial agent: Ion, nanoparticle, and metal. *Angew. Chem. Int. Edit.* **2013**, *44*, 1636–1653.
18. Mohammad, K.A.; Yazdanshenas, M.E. Superhydrophobic antibacterial cotton textiles. *J. Colloid Inter. Sci.* **2010**, *351*, 293–298.
19. Kim, M.; Byun, J.W.; Shin, D.S.; Lee, Y.S. Spontaneous formation of silver nanoparticles on polymeric supports. *Mater. Res. Bull.* **2009**, *44*, 334–338. [CrossRef]
20. Shah, M.S.A.S.; Nag, M.; Kalagara, T.; Singh, S.; Manorama, S.V. Silver on PEG-PU-TiO_2 Polymer Nanocomposite Films: An Excellent System for Antibacterial Applications. *Chem. Mater.* **2008**, *20*, 2455–2460. [CrossRef]
21. Tian, Y.; Qi, J.; Zhang, W.; Cai, Q.; Jiang, X. Facile, one-pot synthesis, and antibacterial activity of mesoporous silica nanoparticles decorated with well-dispersed silver nanoparticles. *ACS Appl. Mater. Interfaces* **2014**, *6*, 12038–12045. [CrossRef] [PubMed]
22. Lu, Q.; Lu, Z.; Lu, Y.; Lv, L.; Ning, Y.; Yu, H.; Hou, Y.; Yin, Y. Photocatalytic synthesis and photovoltaic application of Ag-TiO_2 nanorod composites. *Nano. Lett.* **2013**, *13*, 5698–5702. [CrossRef] [PubMed]
23. Gao, H.; Liu, L.; Luo, Y.-f.; Jia, D.-m. In-situ preparation of epoxy/silver nanocomposites by thermal decomposition of silver–imidazole complex. *Mater. Lett.* **2011**, *65*, 3529–3532. [CrossRef]
24. Yu, B.; Zhou, Y.; Li, P.; Tu, W.; Tang, L.; Ye, J.; Zou, Z. Photocatalytic reduction of CO_2 over Ag/TiO_2 nanocomposites prepared with a simple and rapid silver mirror method. *Nanoscale* **2016**, *8*, 11870–11874. [CrossRef]
25. Xin, T.; Zhou, Z.K.; Gang, L.; Shen, B.; Kang, P.D.; Jian, L.; Qi, L.; Pei, F.X. High-Value Utilization of Lignin to Synthesize Ag Nanoparticles with Detection Capacity for Hg^{2+}. *ACS Appl. Mater. Interfaces* **2014**, *6*, 16147–16155.
26. El Mansouri, N.E.; Salvadó, J. Analytical methods for determining functional groups in various technical lignins. *Ind. Crop. Prod.* **2007**, *26*, 116–124. [CrossRef]
27. Chen, F.; Gong, A.S.; Zhu, M.; Chen, G.; Lacey, S.D.; Feng, J.; Li, Y.; Wang, Y.; Dai, J.; Yao, Y. Mesoporous, Three-Dimensional Wood Membrane Decorated with Nanoparticles for Highly Efficient Water Treatment. *ACS Nano* **2017**, *11*, 4275–4282. [CrossRef]
28. Ji, T.; Long, C.; Schmitz, M.; Bao, F.S.; Zhu, J. Hierarchical Macrotube/Mesopore Carbon Decorated with Mono-dispersed Ag Nanoparticles as Highly Active Catalyst. *Green Chem.* **2015**, *17*, 2515–2523. [CrossRef]
29. Jin, C.; Yao, Q.; Li, J.; Fan, B.; Sun, Q. Fabrication, superhydrophobicity, and microwave absorbing properties of the magnetic γ-Fe_2O_3/bamboo composites. *Mater. Design* **2015**, *85*, 205–210. [CrossRef]
30. Strassberger, Z.; Prinsen, P.; van der Klis, F.; van Es, D.S.; Tanase, S.; Rothenberg, G. Lignin solubilisation and gentle fractionation in liquid ammonia. *Green Chem.* **2015**, *17*, 325–334. [CrossRef]
31. Owen, N.L.; Pawlak, Z. An infrared study of the effect of liquid ammonia on wood surfaces. *J. Mol. Struct.* **1989**, *198*, 435–449. [CrossRef]
32. Zhang, P.; Shao, C.; Zhang, Z.; Zhang, M.; Mu, J.; Guo, Z.; Liu, Y. In situ assembly of well-dispersed Ag nanoparticles (AgNPs) on electrospun carbon nanofibers (CNFs) for catalytic reduction of 4-nitrophenol. *Nanoscale* **2011**, *3*, 3357–3363. [CrossRef] [PubMed]
33. Wang, S.; Gong, Q.; Zhu, Y.; Liang, J. Preparation and photocatalytic properties of silver nanoparticles loaded on CNTs/TiO_2 composite. *Appl. Surf. Sci.* **2009**, *255*, 8063–8066. [CrossRef]
34. Cai, Q.; Fan, Z.; Chen, J.; Guo, W.; Ma, F.; Sun, S.; Hu, L.; Zhou, Q. Dissolving process of bamboo powder analyzed by FT-IR spectroscopy. *J. Mol. Struct.* **2018**, *1171*, 639–643. [CrossRef]
35. Li, J.; Ren, D.; Wu, Z.; Xu, J.; Bao, Y.; He, S.; Chen, Y. Flame retardant and visible light-activated Fe-doped TiO_2 thin films anchored to wood surfaces for the photocatalytic degradation of gaseous formaldehyde. *J. Colloid Interf. Sci.* **2018**, *530*, 78–87. [CrossRef]
36. Liu, S.; Sun, X.; Li, J.G.; Li, X.; Xiu, Z.; Huo, D. Synthesis of Dispersed Anatase Microspheres with Hierarchical Structures via Homogeneous Precipitation. *Eur. J. Inorg. Chem.* **2009**, *2009*, 1214–1218. [CrossRef]

37. Liu, S.; Wang, W.; Chen, J.; Li, J.-G.; Li, X.; Sun, X.; Dong, Y. Foamed single-crystalline anatase nanocrystals exhibiting enhanced photocatalytic activity. *J. Mater. Chem. A* **2015**, *3*, 17837–17848. [CrossRef]
38. Li, Z.; Jia, Z.; Ni, T.; Li, S. Green and facile synthesis of fibrous Ag/cotton composites and their catalytic properties for 4-nitrophenol reduction. *Appl. Surf. Sci.* **2017**, *426*, 160–168. [CrossRef]
39. Tolba, R.; Tian, M.; Wen, J.; Jiang, Z.-H.; Chen, A. Electrochemical oxidation of lignin at IrO_2-based oxide electrodes. *J. Electroanal. Chem.* **2010**, *649*, 9–15. [CrossRef]
40. Li, M.; Noriega-Trevino, M.E.; Nino-Martinez, N.; Marambio-Jones, C.; Wang, J.; Damoiseaux, R.; Ruiz, F.; Hoek, E.M. Synergistic bactericidal activity of Ag-TiO_2 nanoparticles in both light and dark conditions. *Environ. Sci. Technol.* **2011**, *45*, 8989–8995. [CrossRef]
41. Jin, Y.; Dai, Z.; Liu, F.; Kim, H.; Tong, M.; Hou, Y. Bactericidal mechanisms of Ag_2O/TNBs under both dark and light conditions. *Water Res.* **2013**, *47*, 1837–1847. [CrossRef] [PubMed]
42. Liu, C.; Geng, L.; Yu, Y.; Zhang, Y.; Zhao, B.; Zhang, S.; Zhao, Q. Reduction of bacterial adhesion on Ag-TiO_2 coatings. *Mater. Lett.* **2018**, *218*, 334–336. [CrossRef]
43. Perkas, N.; Lipovsky, A.; Amirian, G.; Nitzan, Y.; Gedanken, A. Biocidal properties of TiO_2 powder modified with Ag nanoparticles. *J. Mater. Chem. B* **2013**, *1*, 5309–5316. [CrossRef]
44. Esfandiari, N.; Simchi, A.; Bagheri, R. Size tuning of Ag-decorated TiO_2 nanotube arrays for improved bactericidal capacity of orthopedic implants. *J. Biomed. Mater. Res. A* **2014**, *102*, 2625–2635. [CrossRef]

International Journal of
Molecular Sciences

MDPI

Article

Silver Nanoparticles Addition in Poly(Methyl Methacrylate) Dental Matrix: Topographic and Antimycotic Studies

Valeria De Matteis [1,*], Mariafrancesca Cascione [1,*], Chiara Cristina Toma [1], Giovanni Albanese [2], Maria Luisa De Giorgi [1], Massimo Corsalini [3] and Rosaria Rinaldi [1]

1 Department of Mathematics and Physics "Ennio De Giorgi", University of Salento, 73100 Lecce (LE), Italy; chiara.toma@unisalento.it (C.C.T.); Marialuisa.degiorgi@unisalento.it (M.L.D.G.); Ross.rinaldi@unisalento.it (R.R.)

2 U.O.C. of Plastic Surgery and Burns Center, Department of Oral Hygiene Clini, Hospital "A. Perrino", 72100 Brindisi (BR), Italy; giannialbanese69@libero.it

3 Dental School, Interdisciplinary Department of Medicine, University of Bari "Aldo Moro", 70124 Bari (Ba), Italy; massimo.corsalini@uniba.it

* Correspondence: valeria.dematteis@unisalento.it (V.D.M.); mariafrancesca.cascione@unisalento.it (M.C.)

Received: 2 August 2019; Accepted: 19 September 2019; Published: 21 September 2019

Abstract: The widespread use of nanoparticles (NPs) in medical devices has opened a new scenario in the treatment and prevention of many diseases and infections owing to unique physico-chemical properties of NPs. In this way, silver nanoparticles (AgNPs) are known to have a strong antimicrobial activity, even at low concentrations, due to their ability to selectively destroy cellular membranes. In particular, in the field of dental medicine, the use of AgNPs in different kinds of dental prosthesis matrixes could be a fundamental tool in immunodepressed patients that suffer of different oral infections. *Candida albicans* (*C. albicans*), an opportunistic pathogenic yeast with high colonization ability, is one of the causative agents of oral cavity infection. In our work, we added monodispersed citrate-capping AgNPs with a size of 20 nm at two concentrations (3 wt% and 3.5 wt%) in poly(methyl methacrylate) (PMMA), the common resin used to develop dental prostheses. After AgNPs characterization, we evaluated the topographical modification of PMMA and PMMA with the addition of AgNPs by means of atomic force microscopy (AFM), showing the reduction of surface roughness. The *C. albicans* colonization on PMMA surfaces was assessed by the Miles and Misra technique as well as by scanning electron microscopy (SEM) at 24 h and 48 h with encouraging results on the reduction of yeast viability after AgNPs exposure.

Keywords: silver nanoparticles; *Candida albicans*; poly(methyl methacrylate); dental prostheses

1. Introduction

In the last century, several materials have been employed in dental and mandibular prosthetic reconstructions. Among the others, poly(methylmethacrylate) (PMMA) resin is widely used in medical and dental fields as a matrix in different kinds of removable or implantable devices due to its high biocompatibility, low cost, and ease of manufacture [1,2].

Nevertheless, clinical evidence has shown that dental prosthetic devices, mainly based on PMMA resins, undergo a proliferation of *C. albicans* infections [3–5], which affects their lifetime. Indeed, *C. albicans* is a pleomorphic *fungus* that is commensal of gastrointestinal microbiota [5] and, in case of immunodeficiency, the frequency of candidiasis can increase [6–8].

In order to eradicate *C. albicans* infections, several protocols for the periodic chemical cleaning of prostheses have been proposed; however these solutions are not definitive and, in addition, the

treatment repetition causes damage to prosthesis surfaces, eventually compromising the longevity of implants [9–13].

Moving from these observations, structural modifications of PMMA matrices at nanoscale could be a possible strategy to improve their performance; in particular, resin implementation with NPs offers many advantages. Metal NPs, such as gold NPs (AuNPs) or titanium dioxide NPs (TiO_2NPs), as well as mesoporous silica NPs (MSN), have been added to different kinds of biomaterials, such as PMMA-based matrices [14].

Lee et al. [15] employed MSN (2.5 wt%) as additive in PMMA obtaining a microbial reduction of 20–30% compared to the control samples, but this result needs to be improved.

Recently, Kim et al. [16] used carbon nanotubes (CNT) (0.25/2 wt%) as an additive in PMMA finding a reduction of *C. albicans*, *S. aureus*, and *S. mutans* adhesions of 35–95%. However, there are many concerns about the use of CNTs for clinical purposes [17]. AgNPs are the most used nanomaterial in different commercial products [18–20] and they are strong antibacterial [21] and antimycotic agents [22,23] as well as an anticancer tool [24,25] through their plasmonic features [26,27]. The exact mechanism of AgNPs toxicity is still unclear despite much evidence that has suggested it is their ability to release silver ions (Ag^+) [28], stimulating molecular pathways that induce cell death [29]. Regarding the antimycotic properties, their activity against *C. albicans* has been demonstrated [30,31]. Panácek et al. [32] synthetized AgNPs by modified Tollens route, showing the antimycotic ability of NPs through an antiproliferation effect, even at low concentration (0.21 mg/mL). Similar results were obtained by Kim et al. [33]: AgNPs exhibited a strong inhibition activity on *C. albicans* that was greater than fluconazole, the drug usually used against the yeast. The antibacterial and antifungal activities of AgNPs support their employment in the biomedical field for prostheses and implants; in fact, the *C. albicans* infection is particularly aggressive on device surfaces due to their ability to develop biofilms on different materials (biological or inert) [34]. Roe et al. [35] showed the anti-growth ability of AgNPs on *C. albicans* in plastic catheters. Similar results were obtained by Hassan et al. [36], in comparison with the antifungal drugs grisofulvin, and itraconazole. In dental prostheses, AgNPs could reduce the oropharyngeal candidiasis which spreads in immune compromised individuals [37].

In our work we synthetized monodispersed citrate capped-AgNPs, having a mean size of 20 nm, and we added them in PMMA acrylic resin at two different concentrations (3 wt% and 3.5 wt%).

The morphology of PMMA matrices enriched with AgNPs were characterized in terms of roughness by atomic force microscopy (AFM). Our results showed a strong reduction of roughness parameter, affecting the colonization and the proliferation of yeast, as confirmed by the Miles and Misra test and SEM analysis.

2. Results and Discussion

The use of PMMA is widespread in dental and esthetic industries due to its low cost, but its surface porosity leads to several disadvantages [38]. Indeed, the dimensional instability of this material during the conventional heat-curing phase increases the number of pores in PMMA matrix becoming a suitable surface for microorganisms [39]. In addition, the hydrophobicity of PMMA contributes to increase *C. albicans* colonization [39,40]. In this work, we synthetized and characterized citrate capped-AgNPs, adding them to PMMA acrylic resin in order to improve its characteristics.

The morphology of AgNPs were characterized by TEM: They exhibited a spherical size of 20 ± 3 nm (Figure 1a), as showed on size distribution graph performed on 270 AgNPs (Figure 1b). The size of NPs was confirmed by DLS measurements: The hydrodynamic radius was compatible with the mean size values noticed in TEM acquisitions (19 ± 2) nm (Figure 1c).

UV measurements on AgNPs dispersed in ultrapure water showed the peak in UV region at ~400 nm of wavelength (Figure 1d). The surface charge was measured by ζ-potential measurements, showing the negative surface charge of NPs (−55 ± 2 mV), due to the citrate capping contribution (Figure 1e).

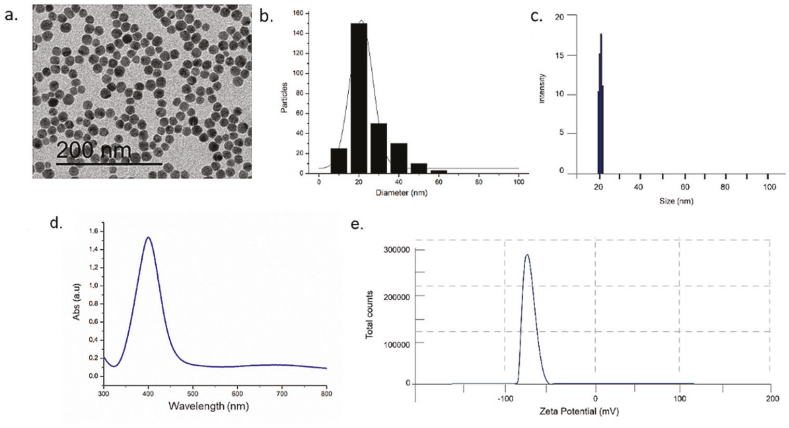

Figure 1. Characterizations of silver nanoparticles (AgNPs) in water: Representative TEM image (**a**), size distribution measured on 270 AgNPs and fitted with a normal function (solid line) (**b**), DLS (**c**), UV–vis (**d**) and ζ-potential measurement (**e**).

After NPs characterizations, we analyzed the morphology of PMMA-based resin, with and without AgNPs addition, at two concentrations (C1: 3 wt% and C2: 3.5 wt%). We retain that dental material architecture affects not only their performance, but also influences microbiological susceptibility.

In general, subjects wearing dental prostheses show an acidic and anaerobic oral environment, due to the adhesion between the oral mucosa and the prosthesis that is deprived of oxygen and saliva [41,42]. In addition, any small trauma on the mucosa caused by dental tools increases the permeability of *C. albicans* to invade the surrounding tissues [43]. In subjects suffering oral stomatitis and immunodeficiency, the *C. albicans* colonies produce acid proteinase and phospholipase on the surface prosthesis that promoted the adherence of the growing yeast, inducing several types of damage [44]. In this way, the Van der Waals and electrostatic forces between the yeast (that has a negative surface charge) and the surface play an important role [45]: Indeed, these forces promoted the adhesion that can be strong or less dependent on surface topography and chemistry [46]. Therefore, chemical modification of the surface charge of PMMA is important to prevent *C. albicans* adhesion. The addition of negative charged AgNPs reduced the roughness and yeast colonization on PMMA.

At the two tested AgNPs concentrations (C1: 3 wt% and C2: 3.5 wt%), a little color change (from pink to dark pink/beige) of the PMMA resins, as consequence of AgNPs addition, was observed and compared to the untreated PMMA (Figure 2a–c).

In order to quantify topographical differences of PMMA due to the presence of AgNPs, the surfaces roughness was measured by means of AFM. Topographic images (Figure 2d–f), clearly showed a flatter surface when AgNPs were implemented in PMMA in a dose dependent manner.

In fact, the PMMA surface was irregular and a lot of scratches and valleys were visualized (as indicated by a colorimetric scale associated to height of the sample); on the contrary, the presence of AgNPs in the matrix reduced sharp height alterations.

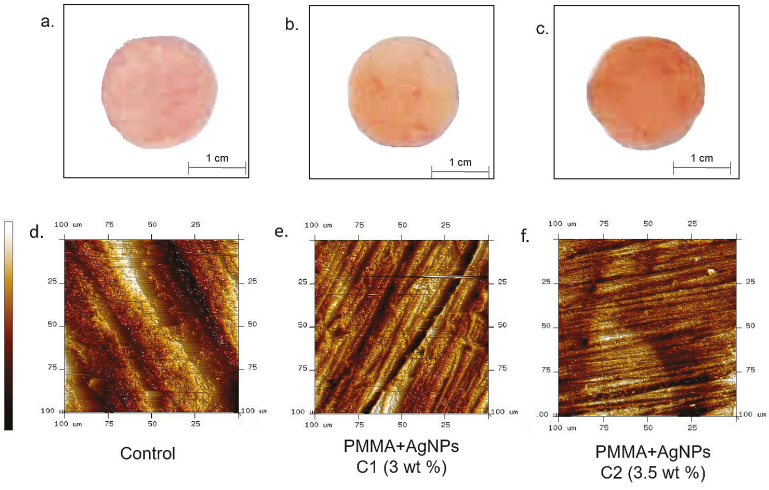

Figure 2. Images acquired by camera of poly(methyl methacrylate) (PMMA) without NPs added (control) (**a**); PMMA + AgNPs C1 (3 wt%) (**b**) and PMMA + AgNPs C2 (3.5 wt%) (**c**): The color became darker with increasing concentrations of the NPs. AFM topographical acquisitions of PMMA without NPs added (control) (**d**); PMMA + AgNPs C1 (3 wt%) (**e**) and PMMA + AgNPs C2 (3.5 wt%) (**f**).

The topographical changes due to AgNP treatments were evident in cross-section profiles of PMMA surface (Figure 3a–c): Images showed flatter profiles after AgNP addition in dose dependent manner. This effect was quantified in terms of roughness (Rq) parameter.

These data were also confirmed from a quantitative point of view: Rq surface values of untreated PMMA changed from 123 ± 15 nm to 61 ± 6 nm and to 41 ± 3 nm, after AgNP addition at C1 and C2, respectively. Some experimental evidence reported how the ability of *C. albicans* to invade surfaces was related to roughness [47]; consequently, a smooth surface could decrease yeast colonization (Figure 3d).

Several investigators have shown that the radiation or the chemotherapy treatment in some kinds of cancers result in saliva pH change toward acidity and an increased incidence of *C. albicans* [48]. Some of these alterations have been recorded in patients with endstage renal disease [49] and diabetes [50]. In this environment, AgNPs have undergone a degradation process: The effect was particularly evident in acidic conditions [28]. For this reason, we tested the Ag^+ degradation from PMMA–AgNPs C2 samples at seven pH points (from 4.5 to 7.5) up to 48 h. As showed in Figure 4, the effect was time and pH dependent: When pH values were lowered, the effect was stronger. For example, after 48 h, the Ag^+ release was 35×10^{-5}% for pH 4.5 in comparison with 0.48×10^{-5}% at pH 7.5. However, the concentration of ions released from PMMA was very low and it was not considered toxic to human cells [28]. The disruption of *C. albicans* instead occurred even at slight Ag^+ concentration [51–53].

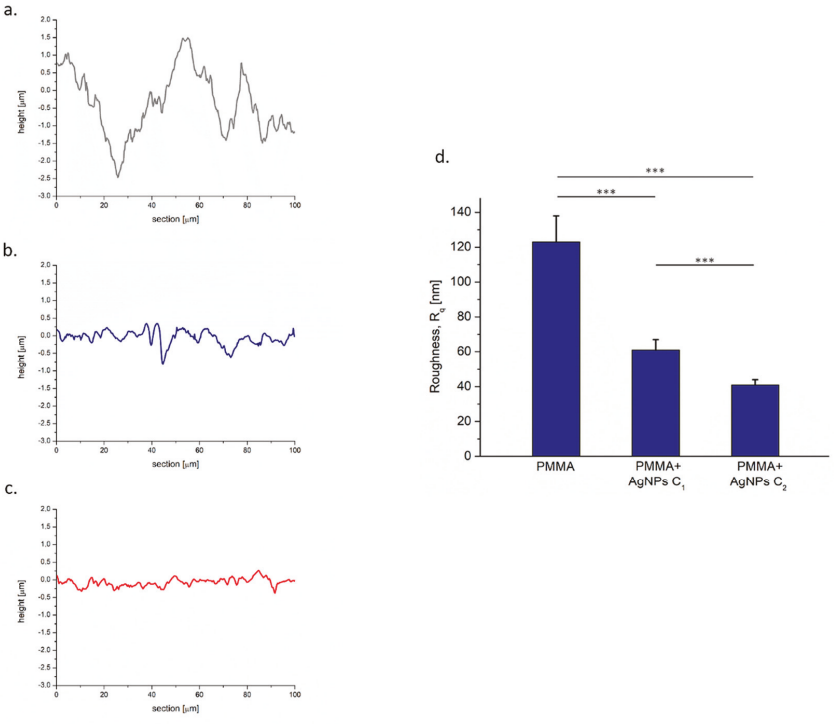

Figure 3. Representative cross-section profiles of PMMA surfaces without NPs added (**a**), PMMA + AgNPs C1 (3 wt%) (**b**) and PMMA + AgNPs C2 (3.5 wt%) (**c**). Roughness Rq values (nm) quantified on PMMA surfaces without NPs added (**a**), PMMA + AgNPs C1 (3 wt%) (**b**) and PMMA + AgNPs C2 (3.5 wt%) (**c**). (**d**) Data reported were calculated as average ± SD on three independent experiments, and the statistical significance respect to the control was represented (*** p-value < 0.005).

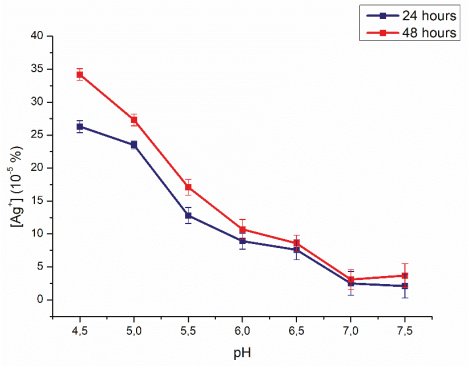

Figure 4. Effects of pH on Ag^+ release from PMMA–AgNPs C2 (3.5 wt%). NP degradation was evaluated at pH 4.5, 5, 5.5, 6, 6.5, 7.5, and 7 up to 48 h.

When AgNPs were added to PMMA, these not only filled up the pores of the matrix, as reported by AFM analysis, but also probably made the PMMA surface electrically negative, due to their citrate

capping. Moving from these observations, we speculated that AgNPs features could reduce the *C. albicans* colonization, so we carried out proliferation and adhesion tests.

The Miles and Misra plate assay [54] was performed to assess the number of viable *C. albicans* CFU on PMMA, with and without the addition of AgNPs, at two tested concentrations (Figure 5). As reported, after 24 h of incubation, the CFU/mL were ($2.6 \times 10^6 \pm 0.6$) for PMMA–Ag C1 (3 wt%) and ($1.8 \times 10^6 \pm 0.03$) for PMMA–Ag C2 (3.5 wt%), respectively, whereas for the control PMMA we recorded ($4 \times 10^6 \pm 0.58$) CFU/mL.

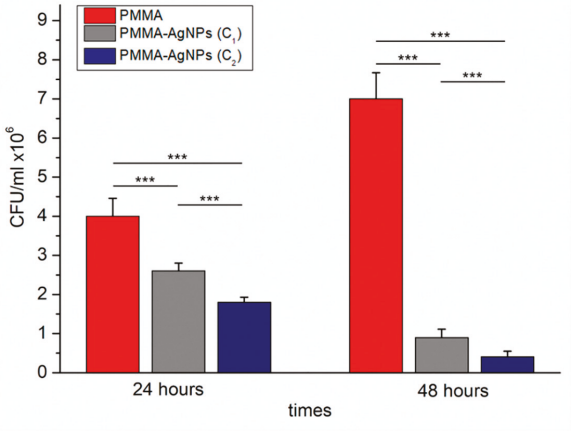

Figure 5. Viability of *C. albicans* on PMMA–AgNPs C1 (3 wt%) and PMMA–AgNPs C2 (3.5 wt%) were assessed by colony forming units (CFU) counts (the Miles and Misra test) after 24 h and 48 h of incubation. PMMA without AgNPs were also included as negative control. Data reported were calculated as average ± SD on three independent experiments, and the statistical significance respect to the control was represented (*** p-value < 0.005).

Extending the time of incubation from 24 h to 48 h, the reduction of viability was more evident: when AgNPs were added in PMMA at higher concentration C2, CFU/mL was only ($0.41 \times 10^6 \pm 0.43$), whereas on the PMMA without NPs (control) the CFU/mL was ($7 \times 10^6 \pm 1.03$). Similar value was recorded for the blank: CFU/mL was ($7.73 \times 10^6 \pm 1.09$), which referred to the CFU/mL of *C. albicans* grown in standard conditions for 48 h. Our data confirmed the antimicrobial properties of AgNPs against *C. albicans* in agreement with previous works [30,55].

We analyzed the ability of yeast to adhere on dental materials using PMMA–AgNPs C2 matrices and incubating them with *C. albicans* for 24 h 48 h. In details, at 48 h we assessed the surfaces of resins with and without AgNPs by SEM analysis (Figure 6). At time 0, little and isolated *C. albicans* colonies were found on the PMMA surface (data not shown), whereas, after 24 h, densely-packed yeast cells covering the entire surface were observed, using three different magnifications (2000×, 1000×, and 500×). At the same time point, the PMMA samples with AgNP addition showed a reduction of colonies that was evident after 48 h. We speculated that the reduction of colonization was mainly due to PMMA surface modifications exerted by AgNPs but also to AgNPs toxicity effects against microorganisms.

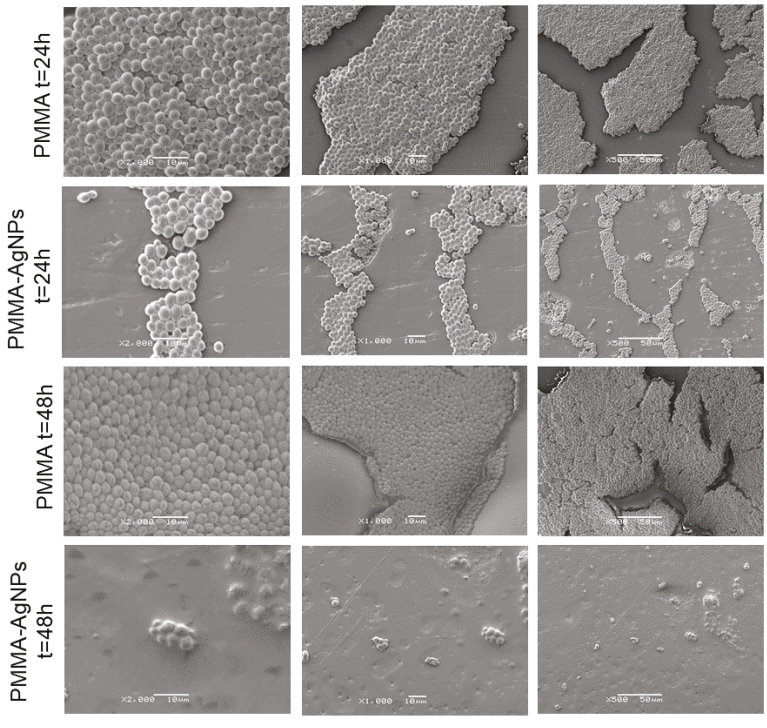

Figure 6. Representative SEM images at 3 magnifications (×2000, ×1000, ×500) of PMMA without NPs and after the addition of PMMA–AgNPs C2 (3.5 wt%) at different time points (24 h and 48 h).

The SEM acquisitions were used to assess the circularity of *C. albicans*. In general, the circularity parameter compares an object to a circle and it ranges from 0 to 1 (for a perfect circle) [56]. In our case, the loss of circularity corresponded to an increase of yeast mortality [57]. The morphology of control *C. albicans*, examined by SEM, exhibited homogeneous and regular cell surface both to 24 h and 48 h. Treated cells, in particular at 48 h, started to assume an abnormal appearance, reducing their circularity (Figure 6). This represented a first step that occurred at short times (24 and 48 h): in fact, at longer times the toxicity can be visualized due to the assumption of an irregular morphology, as demonstrated in previous studies [32,58,59].

The circularity of *C. albicans* growth on PMMA was 0.91 ± 0.05 at 24 h and 0.92 ± 0.04 at 48 h. After the addition of AgNPs (C2), the circularity values were reduced from 0.85 ± 0.06 to 0.81 ± 0.08 at 24 and 48 h, respectively (Figure 7).

In order to establish the percentage of area covered by yeast on pure PMMA and PMMA–AgNPs C2, we used the software ImageJ (Figure 8). After 24 h of *C. albicans* incubation, the area covered by the microorganism was 66% ± 4% on the PMMA surface; it decreased to 36% ± 2% of coverage when the yeast was exposed to PMMA–AgNPs C2. After 48 h, the control colonization value 90% ± 3% was drastically reduced after AgNP addition, becoming 6% ± 1%. We speculated that the reduction of *C. albicans* adhesion on dental resins affected biofilm formation and influenced yeast viability [60,61].

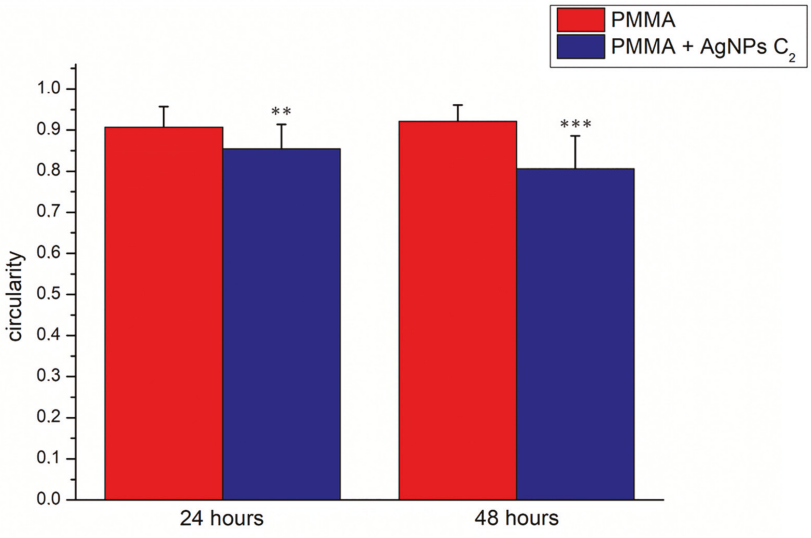

Figure 7. Histogram reported the mean values and their respective standard deviation of *C. albicans* circularity measured by ImageJ software on SEM acquisitions. The statistical significance of results respect to control cells was evaluated by *t*-test, and reported in histograms (** $p < 0.01$ and *** $p < 0.005$).

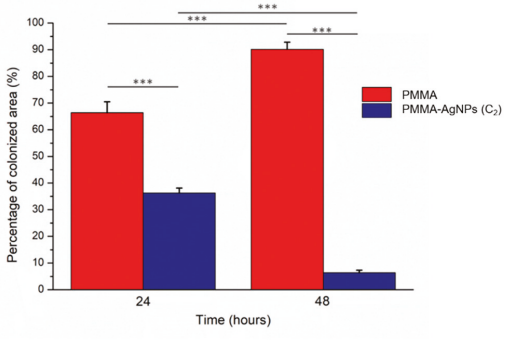

Figure 8. Histograms reported the colonization assay experiments of *C. albicans* on PMMA and PMMA–AgNPs C2 substrates. The analysis was conducted by ImageJ software on SEM acquisitions. The colonized area (**e**) was expressed as a percentage rate of the *C. albicans* covered area respect to entire acquired surface at two time points (24 and 48 h). Data reported were calculated as average ± SD on three independent experiments, and the values were considered statistically significant respect to control for *p*-value < 0.05 (<0.05, <0.01 *, and <0.005 ***).

The obtained results indicated that the implementation with AgNPs improved the performance of PMMA in prosthetic devices. In fact, we found that PMMA/AgNPs composite material had superficial structures that inhibited the colonization and viability of *C. albicans*. Currently, the development of *C. albicans* infections represents one of the main limitations to the duration of dental implants; for this reason, we strongly believe that the achievements of our work could have great impact in the biomedical and dentistry fields because they provide a preventative strategy for candidal biofilms formation on the denture surfaces.

3. Materials and Methods

3.1. Synthesis of AgNPs

AgNPs were obtained following the route described in [28]. Briefly, $AgNO_3$ (0.592 mM final concentration) aqueous solution was added to trisodium citrate (1.36 mM) and tannic acid (2.9 μM) and boiled at 120 °C. Then, the solution was cooled at room temperature and centrifuged at 6000× *g* for 45 min. AgNPs were collected and stored in the dark at 4 °C.

3.2. Transmission Electron Microscope (TEM), Dynamic Light Scattering (DLS), ζ-Potential, UV–vis Measurements (UV–Vis)

TEM images were recorded by a JEOL Jem 1011 microscope operating at an accelerating voltage of 100 kV. TEM samples were prepared by dropping a dilute solution of AgNPs in water on carbon-coated copper grids (Formvar/Carbon 300 Mesh Cu). Microscopy observations were made by means of a Scanning Electron Microscope (SEM, JEOL JSM-6480LV operating at an accelerating voltage of 10 kV, JEOL USA, Inc., Peabody, MA, USA). The sample was prepared by dropping a solution of AgNPs in water on monocrystalline silicon wafer. DLS and ζ-Potential measurements were performed on a Zetasizer Nano ZS90 (Malvern, Worcestershire, UK). Measurements were made at 25 °C in milliQ water and in cell culture medium used for cell experiments after 48 h of incubation. The optical absorbance spectra of AgNPs in water was measured with a Cary 300 UV–vis spectrophotometer (Varian, Palo Alto Palo Alto, California, USA) at a resolution of 1 nm using 5 mm path length quartz cuvettes.

3.3. Inductively Coupled Plasma Atomic Emission Spectrometer (ICP-AES)

To quantify the metal content of NPs, after centrifuge in water, a little amount of solution was collected and digested by the addition of a solution of HNO_3 10% (*v*/*v*) over night. Afterwards, after dilution of ultrapure water, the amount of free ions was measured by ICP-AES (Varian Vista AX spectrometer, Palo Alto, California, USA).

The evaluation of AgNP ions release was performed at 37 °C at specific pH conditions ranged from 4.5 to 7.5. Acidic pH points (4.5, 5, 5.5, 6, 6.5) were prepared adding HCl to MilliQ water, whereas pH 7.5 was obtained adding NaOH. In each solution, three replicates of PMMA–AgNPs C2 were added. The ions release was analyzed at 24 h and 48 h. At each time points the solutions were collected and digested by the addition of of HNO_3 10% (*v*/*v*), and the number of free ions was measured by ICP-AES.

3.4. Synthesis of PMMA Resin/ AgNPs Composite Material

3 wt% and 3.5 wt% of AgNPs were added to 5 g of powder Resin Paladon 65 (Kulzer) and manually mixed using a steel spatula. After 3 min, the resin turned from a semi-liquid state to a semi-viscous phase and was pour slowly into silicon molds (80 shore). Then, the samples were inserted into a polymerization machine (Pentatlon 205, Effegi Brega, Sarmato, PC - Italy) for 30 min at 100 °C of temperature and 5 atm of pressure.

After polymerization, all the samples were treated after polymerization as follows:

a. Stitch—with a multi-blade tungsten carbide bur mounted on a rotating instrument (50,000 rpm);
b. Finishing—obtained in two-step: The first, using a thin abrasive cloth (75 microns) mounted on a spindle and, the second with a fine-grain finishing cutter (50 microns) mounted on a rotating instrument (50,000 rpm);
c. Polishing—also obtained in two stages, the first, by using a cotton cloth brush mounted on a laboratory cleaner with water and pumice powder, and the second step with a dry cotton canvas and polishing liquid for resins (Dentaurum, Ispringen, Deutschland).

3.5. Atomic Force Microscopy (AFM) Analysis

The experiments were conducted by means of an advanced scanning probe microscope (Bioscope Catalyst, Bruker Inc., Santa Barbara, CA, USA), implemented on an inverted optical microscope (Zeiss Observer Z1, Zeiss, Jena, Germany). The whole system is placed on an insulating base to minimize effects of environmental mechanical vibrations on measurements. The experiments were performed using a V-shaped Bruker's Sharp Microlever (MSNL, Bruker Inc., USA), that consists in high sensitivity Silicon Nitride cantilever. The topographic images were acquired on 50 × 50 µm scan area at resolution of 512*512. The images were analyzed by NanoScope Analysis software (Bruker Inc., USA) in order to quantify roughness parameters, and thus evaluate porosity at surface level. The roughness was expressed as Rq. In details, Rq was calculated as root mean square of height fluctuations respect to mean height value obtained by all data image, previously treated with a second order plane fit and with a second order flattening for deleting every bow and minimizing tridimensionality effects. To obtain a more accurate estimate of local roughness, Rq value was reckoned as the mean value of 20 selected areas of 3 × 3 um.

3.6. Microbiological Tests

3.6.1. *C. albicans* Culture Conditions

For the preparation of the *C. albicans* suspensions, the cells were inoculated in Sabouraud dextrose broth (SDB) (Oxoid, Hampshire, UK), incubated for 18 h at 37 °C with shaking at 150 rpm and cultivated as working stock. In order to perform the experiments, yeast cells were harvested by centrifugation at 3000× *g* for 10 min and then washed twice with phosphate-buffered saline (PBS, pH 7.0); finally, cell density was adjusted to 1×10^7 cells/mL in SDB.

3.6.2. *C. albicans* Viability Analysis by Colony Forming Units (CFU)

CFU analysis was performed to test the effect of PMMA/AgNPs composite materials against *C. albicans*. PMMA resins, with AgNPs (3% and 3.5%) or without them as negative control, were incubated with 1 mL of yeast cell suspension (1×10^7 cells/mL) for 24 and 48 h, then the Miles and Misra technique was employed [54]. Serial dilutions of *C. albicans* grown in presence of dental resins were plated on SDB agar Petri dishes and incubated at 37 °C for 24 h. Colonies were manually counted and the CFU was calculated using the following formula: CFU = Number of Colonies Counted/[Amount plated (in mL) × the dilution].

3.6.3. *C. albicans* Adhesion Test

Initial adhesion and colonization of *C. albicans* on the surface of the samples were evaluated by adherence assays. The discs of dental materials with AgNPs (3.5 wt%) were placed in a 24-well tissue culture plate (Corning, St. Louis, MO, USA), and 1 mL of the yeast cell suspension (1×10^7 cells/mL) was added. Resins without AgNPs represented negative control. The samples were incubated with *C. albicans* suspension at 37 °C for 24 and 48 h respectively. Then, dental materials were gently washed with sterile PBS to remove non-adherent cells, while remaining adherent cells were fixed by immersion in methanol (50% *v*/*v*) for 2 min and then left to dry.

3.6.4. Analysis of *C. albican* Adhesion by Scanning Electron Microscopy (SEM) Acquisitions

After fixation, the samples were coated with gold (10 nm) and examined in a scanning electron microscope (SEM) JEOL JSM-6480LV (JEOL USA, Inc., Peabody, MA, USA) with a magnification up to 2000× operating at a maximum accelerating voltage of 20 kV. After SEM acquisitions, the yeast-free area in the captured images was manually traced and quantified using ImageJ public domain software (NIH) and its specific tools. Circularity values were obtained as means calculated on 20 *C. albicans* cells and statistically analyzed by means of a paired two-tailed *t*-test.

Data reported were calculated as average ± SD on three independent experiments, and the values were considered statistically significant with respect to control for p-value < 0.05 (<0.05 *, <0.01 ** and <0.005 ***).

4. Conclusions

Nowadays, PMMA represents suitable material for fabrication of full denture structures and removable devices, thanks to its intrinsic material properties and its high biocompatibility. Nevertheless, PMMA dental prostheses are subject to the colonization of *C. albicans*, inducing the development of serious oral infections. In this experimental work, we demonstrated how AgNP addition in acrylic resin matrix decreases the surface roughness, reducing the viability of *C. albicans* as consequence of a reduction of its ability to adhere and colonize PMMA dental prostheses. The results obtained open new perspectives in dentistry and they could be useful to increase the performance of the removable prosthesis by improving the patients' quality of life by reducing oral infections.

Author Contributions: V.D.M. conceived and designed the experimental activity, V.D.M. synthetized and characterized the nanomaterials. V.D.M., M.C. (Mariafrancesca Cascione), C.C.T., G.A. performed the experiments in cells; M.C. (Mariafrancesca Cascione) performed AFM analysis, V.D.M., M.C. (Mariafrancesca Cascione), C.C.T., wrote paper. M.L.D.G performed the SEM analysis. V.D.M., M.C. (Mariafrancesca Cascione), C.C.T., M.C. (Massimo Corsalini), R.R. edited and drafted the work. V.D.M., M.C. (Mariafrancesca Cascione), C.C.T., M.C. (Massimo Corsalini), R.R. analyzed and explained the experimental data. M.C. (Massimo Corsalini) and R.R. supervised work.

Funding: This research received no external funding.

Acknowledgments: V.D.M and MF.C. kindly acknowledges Programma Operativo Nazionale (PON) Ricerca e Innovazione 2014-2020 Asse I "Capitale Umano", Azione I.2, Avviso "A.I.M: Attraction and International Mobility CUP F88D18000070001. The authors kindly acknowledge Maria Teresa Zorzetto, biologist leader at Clinic Microbiology Laboratories P.O "Antonio Perrino" Brindisi (BR), Italy.

Conflicts of Interest: The authors declare no conflict of interest.

References

1. Cuijpers, V.M.; Jaroszewicz, J.; Anil, S.; Al Farraj Aldosari, A.; Walboomers, X.F.; Jansen, J.A. Resolution, sensitivity, and in vivo application of high-resolution computed tomography for titanium-coated polymethyl methacrylate (PMMA) dental implants. *Clin. Oral Implant. Res.* **2014**, *25*, 359–365. [CrossRef] [PubMed]
2. Frazer, R.Q.; Byron, R.T.; Osborne, P.B.; West, K.P. PMMA: An essential material in medicine and dentistry. *J. Long Term Eff. Med. Implant.* **2005**, *15*, 629–639. [CrossRef]
3. Pereira, T.; Del Bel Cury, A.A.; Cenci, M.S.; Rodrigues-Garcia, R.C.M. In vitro Candida colonization on acrylic resins and denture liners: Influence of surface free energy, roughness, saliva, and adhering bacteria. *Int. J. Prosthodont.* **2007**, *20*, 308–310.
4. Altarawneh, S.; Bencharit, S.; Mendoza, L.; Curran, A.; Barrow, D.; Barros, S.; Preisser, J.; Loewy, Z.G.; Gendreau, L.O.S. Clinical and histological findings of denture stomatitis as related to intraoral colonization patterns of Candida albicans, salivary flow, and dry mouth. *J. Prosthodont.* **2013**, *22*, 13–22. [CrossRef] [PubMed]
5. Dantas, S.; Lee, K.K.; Raziunaite, I.; Schaefer, K.; Wagener, J.; Yadav, B.; Gow, N.A. Cell biology of Candida albicans – host interactions. *Curr. Opin. Microbiol.* **2016**, *34*, 111–118. [CrossRef] [PubMed]
6. Low, C.; Rotstein, C. Emerging fungal infections in immunocompromised patients. *F1000 Med. Rep.* **2011**, *8*, 1–8. [CrossRef]
7. Yapar, N. Epidemiology and risk factors for invasive candidiasis. *Ther. Clin. Risk. Manag.* **2014**, *13*, 95–105. [CrossRef]
8. Davidson, L.; Mihai, G.N.; Kullberg, B.J. Patient Susceptibility to Candidiasis—A Potential for Adjunctive Immunotherapy. *J. Fungi* **2018**, *4*, 9. [CrossRef]
9. Salvia, A.C.R.D.; dos Santos Matilde, F.; Rosa, F.C.S.; Kimpara, E.T.; Jorge, A.O.C.; Balducci, I.; Koga-Ito, C.Y. Disinfection protocols to prevent cross-contamination between dental offices and prosthetic laboratories. *J. Infect. Public Health* **2013**, *6*, 377–382. [CrossRef]

10. De Rezende Pinto, L.; Rodriguez Acosta, E.J.T.; Távora, F.F.F.; Da Silva, P.M.B.; Porto, V.C. Effect of repeated cycles of chemical disinfection on the roughness and hardness of hard reline acrylic resins. *Gerodontology* **2010**, *27*, 147–153. [CrossRef]
11. Ma, T.; Johnson, G.H.; Gordon, G.E. Effects of chemical disinfectants on the surface characteristics and color of denture resins. *J. Prosthet. Dent.* **1997**, *77*, 197–204. [CrossRef]
12. Peracini, A.; Davi, L.R.; de Queiroz Ribeiro, N.; de Souza, R.F.; da Silva, C.H.L.; Paranhos, H.D.F.O. Effect of denture cleansers on physical properties of heat-polymerized acrylic resin. *J. Prosthodont. Res.* **2010**, *54*, 78–83. [CrossRef] [PubMed]
13. Davi, L.R.; Peracini, A.; de Queiroz Ribeiro, N.; Soares, R.B.; Da Silva, C.H.L.; de Freitas Oliveira Paranhos, H.; De Souza, R.F. Effect of the physical properties of acrylic resin of overnight immersion in sodium hypochlorite solution. *Gerodontology* **2010**, *27*, 297–302. [CrossRef] [PubMed]
14. Wang, W.; Liao, S.; Zhu, Y.; Liu, M.; Zhao, Q.; Fu, Y. Recent Applications of Nanomaterials in Prosthodontics. *J. Nanomater.* **2015**, *2015*, 3. [CrossRef]
15. Lee, J.H.; El-Fiqi, A.; Jo, J.K.; Kim, D.A.; Kim, S.C.; Jun, S.K.; Lee, H.H. Development of long-term antimicrobial poly (*Methyl methacrylate*) by incorporating mesoporous silica nanocarriers. *Dent. Mater.* **2016**, *32*, 1564–1574. [CrossRef]
16. Kim, K.I.; Kim, D.A.; Patel, K.D.; Shin, U.S.; Kim, H.W.; Lee, J.H.; Lee, H.H. Carbon nanotube incorporation in PMMA to prevent microbial adhesion. *Sci. Rep.* **2019**, *9*, 4921. [CrossRef]
17. Mohanta, D.; Patnaik, S.; Sood, S.; Das, N. Carbon nanotubes: Evaluation of toxicity at biointerfaces. *J. Pharm. Anal.* **2019**. [CrossRef]
18. Dargo, H.; Ayaliew, A.; Kassa, H. Synthesis paradigm and applications of silver nanoparticles (AgNPs), a review. *Sustain. Mater. Technol.* **2017**, *13*, 18–23. [CrossRef]
19. El-Nour, K.M.A.; Eftaiha, A.A.; Al-Warthan, A.; Ammar, R.A. Synthesis and applications of silver nanoparticles. *Arab. J. Chem.* **2010**, *3*, 135–140. [CrossRef]
20. Matteis VDe Cascione, M.; Toma, C.C.; Leporatti, S. Silver Nanoparticles: Synthetic Routes, In Vitro Toxicity and Theranostic Applications for Cancer Disease. *Nanomaterials* **2018**, *85*, 319. [CrossRef]
21. Salomoni, R. Antibacterial effect of silver nanoparticles in Pseudomonas aeruginosa. *Nanotechnol. Sci. Appl.* **2017**, *10*, 115–121. [CrossRef] [PubMed]
22. Xia, Z.; Ma, Q.; Li, S.; Zhang, D. ScienceDirect the antifungal effect of silver nanoparticles on Trichosporon asahii. *J. Microbiol. Immunol. Infect.* **2016**, *49*, 182–188. [CrossRef] [PubMed]
23. Kim, S.W.; Jung, J.H.; Lamsal, K.; Kim, Y.S.; Min, J.S.; Lee, Y.S. Antifungal Effects of Silver Nanoparticles (AgNPs) against Various Plant Pathogenic Fungi. *Mycobiology* **2012**, *40*, 53–58. [CrossRef] [PubMed]
24. Ding, J.; Chen, G.; Chen, G.; Guo, M. One-Pot Synthesis of Epirubicin-Capped Silver Nanoparticles and Their Anticancer Activity against Hep G2 Cells. *Pharmaceutics* **2019**, *11*, 123. [CrossRef] [PubMed]
25. Baptista, P. Noble Metal Nanoparticles Applications in Cancer. *J. Drug Deliv.* **2012**, *2012*, 751075. [CrossRef]
26. Huang, X.; El-Sayed, M.A. Plasmonic photo-thermal therapy (PPTT). *Alexandria J. Med.* **2011**, *47*, 1–9. [CrossRef]
27. Khoury, C.G.; Norton, S.J.; Vo-Dinh, T. Investigating the plasmonics of a dipole-excited silver nanoshell: Mie theory versus finite element method. *Nanotechnology* **2010**, *21*, 315203. [CrossRef]
28. De Matteis, V.; Malvindi, M.A.; Galeone, A.; Brunetti, V.; De Luca, E.; Kote, S.; Pompa, P.P. Negligible particle-specific toxicity mechanism of silver nanoparticles: The role of Ag + ion release in the cytosol. *Nanomed. Nanotechnol. Biol. Med.* **2015**, *11*, 731–739. [CrossRef]
29. Foldbjerg, R.; Olesen, P.; Hougaard, M.; Anh, D.; Jürgen, H.; Autrup, H. PVP-coated silver nanoparticles and silver ions induce reactive oxygen species, apoptosis and necrosis in THP-1 monocytes. *Toxicol. Lett.* **2009**, *190*, 156–162. [CrossRef]
30. Lara, H.H.; Urbina, D.G.R.; Pierce, C.; Ribot, J.L.L.; Jiménez, M.J.A.; Yacaman, M.J. Effect of silver nanoparticles on Candida albicans biofilms: An ultrastructural study. *J. Nanobiotechnol.* **2015**, *13*, 91. [CrossRef]
31. Jalal, M.; Ansari, M.A.; Alzohairy, M.A. Biosynthesis of Silver Nanoparticles from Oropharyngeal Candida glabrata Isolates and Their Antimicrobial Activity against Clinical Strains of Bacteria and Fungi. *Nanomaterials* **2018**, *8*, 586. [CrossRef] [PubMed]
32. Panácek, A.; Kolár, M.; Vecerová, R.; Prucek, R.; Soukupová, J.; Krystof, V.; Hamal, P.; Zboril, R.K.L. Antifungal activity of silver nanoparticles against Candida spp. *Biomaterials* **2009**, *30*, 6333–6340. [CrossRef]

33. Kim, K.J.; Sung, S.; Moon, S.; Choi, J.; Kim, J.G.; Lee, D.G. Antifungal Effect of Silver Nanoparticles on Dermatophytes. *J. Microbiol. Biotechnol.* **2008**, *18*, 1482–1484. [PubMed]
34. Nobile, C.J.; Johnson, A.D. Candida albicans Biofilms and Human Disease. *Annu. Rev. Microbiol.* **2016**, *69*, 71–92. [CrossRef] [PubMed]
35. Roe, D.; Karandikar, B.; Bonn-savage, N.; Gibbins, B.; Roullet, J. Antimicrobial surface functionalization of plastic catheters by silver nanoparticles. *J. Antimicrob. Chemother.* **2008**, *61*, 869–876. [CrossRef] [PubMed]
36. Hasan, F.; Xess, I.; Wang, X.; Jain, N.; Fries, B.C. Biofilm formation in clinical Candida isolates and its association with virulence. *Microbes Infect.* **2009**, *11*, 753–761. [CrossRef] [PubMed]
37. Corrêa, J.M.; Mori, M.; Sanches, H.L.; Cruz, A.D.D.; Poiate, E.; Poiate, I.A.V.P. Silver Nanoparticles in Dental Biomaterials. *Int. J. Biomater.* **2015**, *2015*, 485275. [CrossRef] [PubMed]
38. Marques, R.; Figuerôa, S.; Yoshi, C.; Sugio, C.; Urban, V.M.; Neppelenbroek, K.H. Porosity, water sorption and solubility of denture base acrylic resins polymerized conventionally or in microwave Abstract. *J. Appl. Oral Sci.* **2018**, *26*, 1–7.
39. Al-fouzan, A.F.; Al-mejrad, L.A.; Albarrag, A.M. Adherence of Candida to complete denture surfaces in vitro: A comparison of conventional and CAD/CAM complete dentures. *J. Adv. Prosthodont.* **2017**, *9*, 402–408. [CrossRef] [PubMed]
40. Hazen, K.C. Participation of yeast cell surface hydrophobicity in adherence of Candida albicans to human epithelial cells. *Infect. Immun.* **1989**, *57*, 1894–1900. [PubMed]
41. Gleiznys, A.; Zdanavičienė, E.; Žilinskas, J. Candida albicans importance to denture wearers. A literature review. *Stomatologija* **2015**, *17*, 54–66. [PubMed]
42. Nair, V.V.; Karibasappa, G.N.; Dodamani, A.; Prashanth, V.K. Microbial contamination of removable dental prosthesis at different interval of usage: An in vitro study. *J. Indian Prosthodont. Soc.* **2016**, *16*, 346. [CrossRef] [PubMed]
43. Samaranayake, L.P. Experimental Oral Candidiasis in Animal Models. *Clin. Microbiol. Rev.* **2001**, *14*, 398–429. [CrossRef] [PubMed]
44. Lo, L.; Chaffin, W.L.A.J.; Marti, P.; Gozalbo, D. Cell Wall and Secreted Proteins of Candida albicans: Identification, Function, and Expression. *Microbiol. Mol. Biol. Rev.* **1998**, *62*, 130–180.
45. Lorraine Jones Paul O'Shea. The Electrostatic Nature of the Cell Surface of Candida albicans: A Role in Adhesion. *Exp. Mycol.* **1994**, *18*, 111–120. [CrossRef]
46. Chandra, J.; Patel, J.D.; Li, J.; Zhou, G.; Mukherjee, P.K.; McCormick, T.S.; Ghannoum, M.A. Modification of Surface Properties of Biomaterials Influences the Ability of Candida albicans To Form Biofilms. *Appl. Environ. Microbiol.* **2005**, *71*, 8795–8801. [CrossRef] [PubMed]
47. Mayahara, M.; Kataoka, R.; Arimoto, T.; Tamaki, Y. Effects of surface roughness and dimorphism on the adhesion of Candida albicans to the surface of resins: Scanning electron microscope analyses of mode and number of adhesions. *J. Investig. Clin. Dent.* **2014**, *5*, 307–312. [CrossRef] [PubMed]
48. Joint, T.; Implants, D. Maxillofacial Prosthetics Clinical evaluation of oral Candida in cancer chemotherapy patients. *Plast. Reconstr. Surg.* **1979**, *66*, 656.
49. Kho, H.; Lee, S.; Chung, S. Oral manifestations and salivary flow rate, pH, and buffer capacity in patients with end-stage renal disease undergoing hemodialysis. *Oral Surg. Oral Med. Oral Pathol. Oral Radiol. Endodontol.* **1999**, *88*, 316–319. [CrossRef]
50. Premkumar, J.; Ramani, P.; Chandrasekar, T.; Natesan, A.; Premkumar, P. Detection of species diversity in oral candida colonization and anti-fungal susceptibility among non-oral habit adult diabetic patients. *J. Nat. Sci. Biol. Med.* **2014**, *5*, 148–154. [CrossRef] [PubMed]
51. Avalos-borja, M.; Castro-longoria, E.; Vazquez-mun, R. Ultrastructural Analysis of Candida albicans When Exposed to Silver Nanoparticles. *PLoS ONE* **2014**, *9*, 108876. [CrossRef]
52. Lee, B.; Yun, S.J.; Choi, I. Silver nanoparticles induce reactive oxygen species-mediated cell cycle delay and synergistic cytotoxicity with 3-bromopyruvate in Candida albicans, but not in Saccharomyces cerevisiae. *Int. J. Nanomed.* **2019**, *14*, 4801–4816. [CrossRef]
53. Monteiro, D.R.; Takamiya, A.S.; Feresin, L.P.; Gorup, L.F.; Camargo, E.R.; De Carlos, A.; Barbosa, D.B. Silver colloidal nanoparticle stability: Influence on Candida biofilms formed on denture acrylic. *Medical* **2014**, *52*, 627–635. [CrossRef] [PubMed]
54. Miles, A.A.; Misra, S.S.; Irwin, J.O. The estimation of the bactericidal power of the blood. *J. Hyg.* **1938**, *38*, 732–749. [CrossRef] [PubMed]

55. Halbandge, S.D.; Jadhav, A.K.; Jangid, P.M.; Shelar, A.V.; Patil, R.H.; Karuppayil, S.M. Molecular targets of biofabricated silver nanoparticles in Candida albicans. *J. Antibiot.* **2019**, *72*, 640–644. [CrossRef] [PubMed]
56. Cascione, M.; De Matteis, V.; Mandriota, G.; Leporatti, S.; Rinaldi, R. Acute Cytotoxic Effects on Morphology and Mechanical Behavior in MCF-7 Induced by TiO2 NPs Exposure. *Int. J. Mol. Sci.* **2019**, *20*, 3594. [CrossRef] [PubMed]
57. Jacobsen, I.D.; Hube, B.; Jacobsen, I.D.; Hube, B. Candida albicans morphology: Still in focus. *Expert Rev. Anti Infect. Ther.* **2017**, *15*, 327–330. [CrossRef]
58. Journal, A.I.; Jalal, M.; Ansari, M.A.; Ali, S.G.; Haris, M. Anticandidal activity of bioinspired ZnO NPs: Effect on growth, cell morphology and key virulence attributes of Candida species. *Artif. Cells Nanomed. Biotechnol.* **2018**, *46*, 912–925. [CrossRef]
59. Durán, N.; Durán, M.; de Jesus, M.B.; Seabra, A.B.; Fávaro, W.J.; Nakazato, G. Silver nanoparticles: A new view on mechanistic aspects on antimicrobial activity. *Nanomedicine* **2016**, *12*, 789–799. [CrossRef]
60. Sudjana, A.N.; Carson, C.F.; Carson, K.C.; Riley, T.V.; Hammer, K.A. Candida albicans adhesion to human epithelial cells and polystyrene and formation of biofilm is reduced by sub-inhibitory Melaleuca alternifolia (tea tree) essential oil. *Med. Mycol.* **2012**, *50*, 863–870. [CrossRef]
61. Sherry, L.; Lappin, G.; O'Donnell, L.E.; Millhouse, E.; Millington, O.R.; Bradshaw, D.J.; Ramage, G. Viable Compositional Analysis of an Eleven Species Oral Polymicrobial Biofilm. *Front. Microbiol.* **2016**, *7*, 912. [CrossRef] [PubMed]

International Journal of
Molecular Sciences

MDPI

Review

The Role of Calix[n]arenes and Pillar[n]arenes in the Design of Silver Nanoparticles: Self-Assembly and Application

Pavel Padnya *, Vladimir Gorbachuk and Ivan Stoikov *

A.M. Butlerov' Chemistry Institute of Kazan Federal University, 18 Kremlevskaya Street, 420008 Kazan, Russia; leongard87@mail.ru

* Correspondence: padnya.ksu@gmail.com (P.P.); ivan.stoikov@mail.ru (I.S.); Tel.: +7-843-233-7241 (I.S.)

Received: 31 January 2020; Accepted: 18 February 2020; Published: 20 February 2020

Abstract: Silver nanoparticles (AgNPs) are an attractive alternative to plasmonic gold nanoparticles. The relative cheapness and redox stability determine the growing interest of researchers in obtaining selective plasmonic and electrochemical (bio)sensors based on silver nanoparticles. The controlled synthesis of metal nanoparticles of a defined morphology is a nontrivial task, important for such fields as biochemistry, catalysis, biosensors and microelectronics. Cyclophanes are well known for their great receptor properties and are of particular interest in the creation of metal nanoparticles due to a variety of cyclophane 3D structures and unique redox abilities. Silver ion-based supramolecular assemblies are attractive due to the possibility of reduction by "soft" reducing agents as well as being accessible precursors for silver nanoparticles of predefined morphology, which are promising for implementation in plasmonic sensors. For this purpose, the chemistry of cyclophanes offers a whole arsenal of approaches: exocyclic ion coordination, association, stabilization of the growth centers of metal nanoparticles, as well as in reduction of silver ions. Thus, this review presents the recent advances in the synthesis and stabilization of Ag (0) nanoparticles based on self-assembly of associates with Ag (I) ions with the participation of bulk platforms of cyclophanes (resorcin[4]arenes, (thia)calix[n]arenes, pillar[n]arenes).

Keywords: cyclophanes; resorcin[4]arenes; calix[n]arenes; thiacalix[n]arenes; pillar[n]arenes; self-assembly; silver nanoparticles

1. Introduction

Silver nanoparticles (AgNPs) are attractive nanomaterials, especially promising in such fields as colorimetric sensors, bactericidal materials and components of electrochemical sensors [1–3]. In contrast to gold nanoparticles, silver nanoparticles can be readily synthesized from relatively stable silver (I) salts using a wide range of reducing agents [4]. Moreover, silver nanoparticles find application as sterilizing nanomaterials in medicine. A unique feature of AgNPs is their slow release of silver (I) ions, which allows using them as bactericidal agents [5–7]. Silver nanoparticles are promising catalytically active nanomaterials, which can enhance some reactions for dye and drug synthesis [8,9].

These applications require surface modification of AgNPs that would allow to adjust their association with the target substrate or to offer higher selectivity towards association with bacterial cell walls. Depending on the application, AgNPs must be modified with different functionality. For electrochemical sensors and antibacterial nanomaterials, it is necessary to introduce functionality, providing AgNPs with selectivity of association [10]. However, the strategy of creating AgNP-based colorimetric sensors is different [11]. In order to obtain a wavelength shift in the presence of target a substrate, it is necessary to introduce functionalities that would not only bind to the target substrate but also induce aggregation of AgNPs [12].

One of the most promising strategies for creating selective nanoparticles is using supramolecular agents capable of forming host–guest complexes with the target substrate [13]. Cyclophanes are promising macrocyclic 3D host molecules, which are versatile building blocks for self-assembled materials [14–16]. Cyclophanes have been reported as selective host molecules for recognition of inorganic ions, and organic molecules and have been shown promising in biopolymer binding [17–22]. The vast opportunities for obtaining various functional derivatives and rich spatial geometry of cyclophanes offers the means necessary for achieving this goal [23].

This review summarizes the modern achievements in design and application of AgNPs functionalized with cyclophanes [24–129]. Several classes of cyclophanes were chosen: calix[n]arenes, their sulfur bridged analogue thiacalix[4]arenes, resorcin[4]arenes and pillar[n]arenes (Figure 1). Other cyclophanes are out of current review because such publications are scarce. While in this review we report recent findings in the field of cyclophane-functionalized AgNPs synthesis and application (Figure 2), our review has several key features. Specific attention is paid to comparing unique substrate recognition patterns that are inherent for each cyclophane type. Also, it is widely known that cyclophanes may form nanosized supramolecular associates with silver ions, and, on the other hand, there are a number of reports on the synthesis of silver nanoparticles in the presence of cyclophanes. While both are well known to the scientific community, to the best of our knowledge there have been no studies in which possible supramolecular self-assembly of cyclophane with silver ions prior to reduction would be investigated.

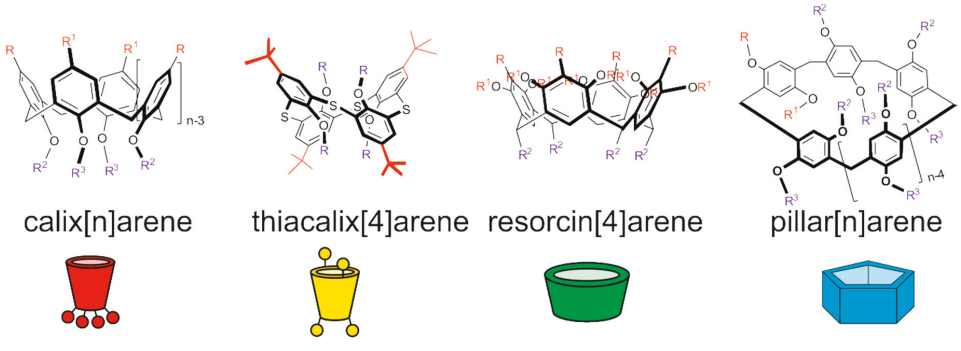

Figure 1. Structures and cartoon images of cyclophanes (calix[n]arenes, thiacalix[4]arenes, resorcin[4]arenes and pillar[n]arenes).

Using three-dimensional macrocyclic stabilizing agents at the stage of AgNPs synthesis provides unique means to adjust the sizes of nanoparticles at the growth stage, which is promising in the nanomaterial design field. Functionalization of AgNPs with cyclophanes allows achieving high selectivity towards various inorganic, organic and biomacromolecular substrates. It opens wide opportunities in developing novel selective antibacterial agents, surface-enhanced Raman scattering (SERS)-based colorimetric sensors and electrochemical sensors. The review presents achievements in cyclophane based AgNPs, which are especially promising for nanomedicine and diagnostics.

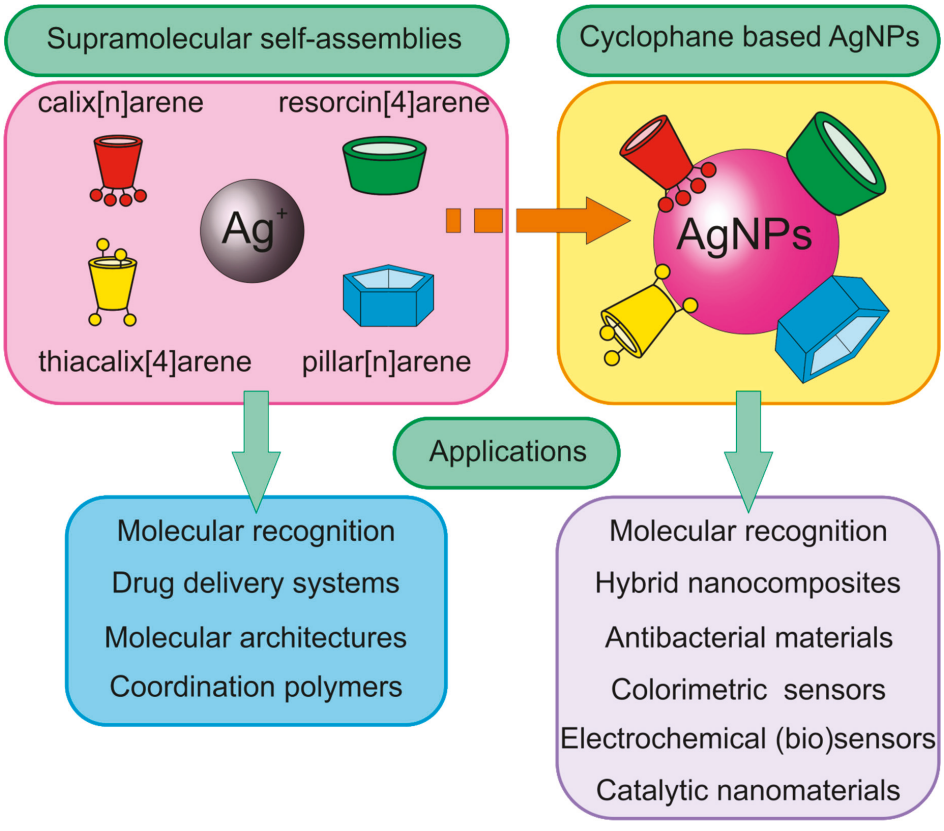

Figure 2. Application of supramolecular self-assemblies "cyclophane-Ag^+" and cyclophane based silver nanoparticles (AgNPs).

2. Supramolecular Self-Assembly of Calix[n]arenes with Ag(I) Ions and Calix[n]arene-Based AgNPs

Calix[n]arenes are the most wide-known cyclophane platforms. Most of the synthetic routes, patterns of substrate recognition and supramolecular self-assembly were realized on this platform for the first time and afterwards were successfully adapted to other cyclophanes. Ease of modification of lower and upper rims of calixarenes have made them versatile building blocks for supramolecular materials and surface modifiers for adjusting receptor and self-assembly properties of colloidal materials. Separate modification of upper and lower rims of calixarenes has become one of the common practices to obtain amphiphilic host molecules for Langmuir–Blodgett films and consequently for modification of nanoparticles, allowing to alter their lipophilicity [24].

2.1. Self-Assembly of Calix[n]arenes with Ag(I) Ions

Studying the self-assembly of calixarene derivatives with silver ions can help in understanding the role of calix[n]arene in the synthesis of AgNPs. Usually the role of calixarene is described as a stabilizer (Table 1). It is worth noting that most calixarene derivatives are poorly soluble in water, which complicates their use in the synthesis of AgNPs via the most common route (reduction with sodium borohydride). One approach to solve this problem is the creation of amphiphilic structures based on this cyclophane.

Tetrasubstituted amphiphilic calix[4]arene **CA-1** (Figure 3) containing alanine fragments on the upper rim and decyl groups on the lower rim was synthesized [25]. It was shown that macrocycle **CA-1** can self-assemble into various structures depending on the solvent pH. It forms a spherical structure at pH = 3 and a hollow, necklace-like structure of 500 nm diameter at pH 7. It has been shown that addition of silver ions leads to a three-dimensional dendrite nanostructure. The authors supposed that calix[4]arene **CA-1** acted as a stabilizer and shape controller in the diffusion-limited aggregation process. The obtained results can be used in the design of microelectronic devices or nanometer-scale electrodes.

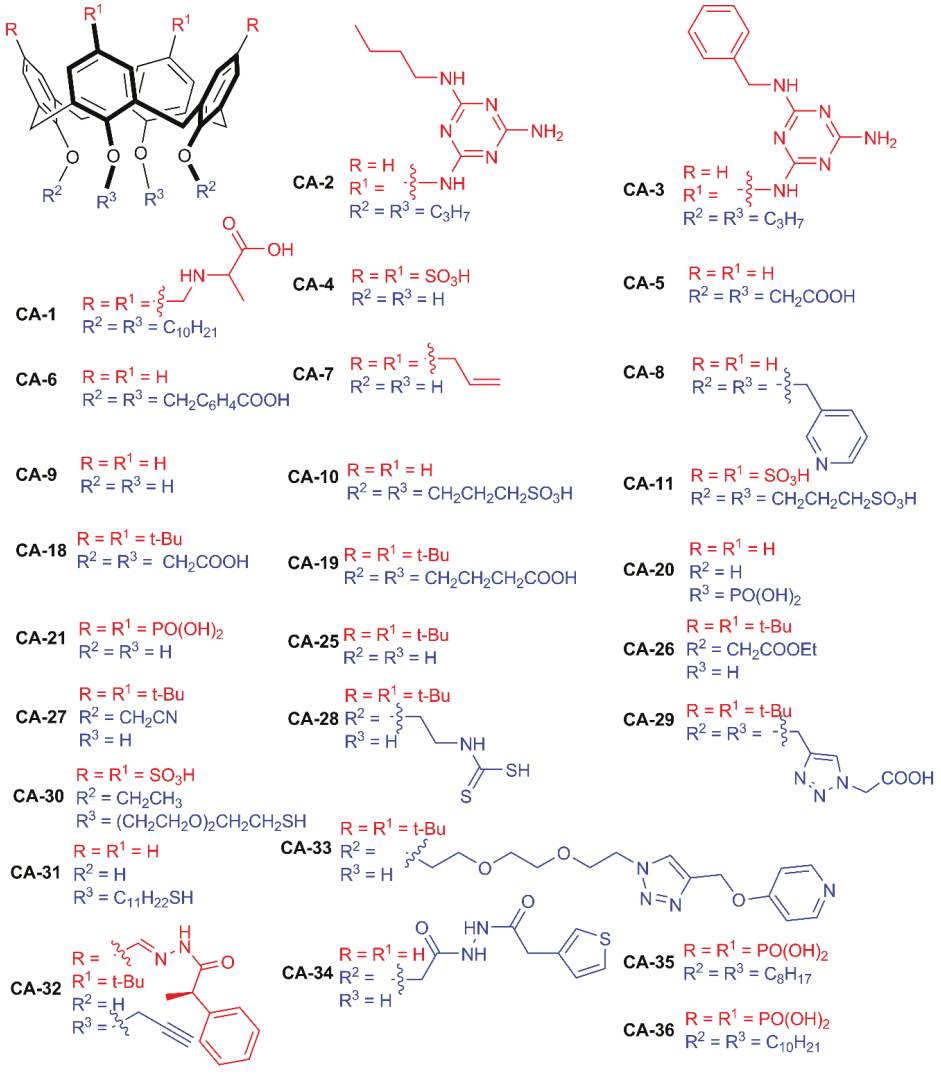

Figure 3. Structures of calix[4]arenes.

Table 1. Data on cyclophane-based silver nanoparticles (AgNPs) sizes, applications, target and comparison substrates.

Cyclophanes Studied	AgNPs Synthesis Method [1]	AgNPs Sizes (Method)	Surface Plasmon Resonance λ	Application, Target Substrate, SPR λ, nm in the Presence of Substrate [2]	Comparison Substrates	Lit.
CA-4, CA-10–CA-17	B ($NaBH_4$)	-	390 nm	CMC determination of cationic surfactants (CPB, CTAB) intensity of 390 nm band **CA-10**—decrease **CA-4**, **CA-11**—increase **CA-12–CA-17**—no changes	cetyl pyridium bromide, cetyl trimethyl ammonium bromide, *N*-octyl glucopyranoside.	[34]
CA-4, CA-10–CA-17	B ($NaBH_4$)	-	-	Structure-dependent inhibition of Gram+ and Gram− bacteria growth, anti-oxidant capacity, antibacterial effect against *E. coli*, *B. subtilis*	-	[35,36]
CA-4	B ($NaBH_4$)	~20 nm (TEM)	~380 nm	Multicolor response to nucleotides and desoxynucleotides	cytosine, guanine—540 nm, uracil—580 nm, thymine—590 nm, adenine—no changes, deoxy-adenosine, deoxy-guanosine—460 nm, deoxy-thymidine—520 nm, deoxy-cytidine—decoloration (grey colored solution)	[37]
CA-2, CA-3	B (electron beam)	**CA-2**: 2.3 ± 0.3 nm (TEM) **CA-3**: 2.1 ± 0.1 nm (TEM)	-	-	-	[26]
CA-4	B ($NaBH_4$)	~30 nm (TEM)	390 nm	540 nm (cytosine) 413 nm (water) oleic acid stabilized+calixarene;	-	[38]
CA-4	A ($NaBH_4$)	11.6 ± 3 nm (TEM)	407 nm (hexane) oleic acid stabilized	Oleic-stabilized particles become hydrophilic	-	[39]
CA-4	B ($NaBH_4$)	8.0 ± 1.0 nm (TEM)	394 nm	His ~ 500 nm	Alanine, valine, leucine, methionine, phenylalanine, histidine tyrosine, threonine, serine, proline, glutamic acid, aspartic acid	[40]
CA-4	B ($NaBH_4$)	~6–12 nm (TEM)	391 nm	450–600 nm (transition metal hydroxide particles at pH = 10)	Effectivity is: Ni^{2+} <Tb^{3+} ~Zn^{2+} <Cu^{2+} <Co^{2+}~Cd^{2+} << Pb^{2+}	[41]
CA-4, CA-15	A ($NaBH_4$)	**CA-4**: 8 nm (TEM) **CA-15**: 4 nm (TEM)	**CA-4**: 393 nm **CA-15**: 391 nm	**CA-4** Optunal ~ 500 nm **CA-15** -	iprodione, pyrimethanil, thiabendazole, optunal, parathion-methyl, methomyl and acetamiprid	[42]
CA-12	A ($NaBH_4$)	-	-	Three-component supramolecular system with dipyrene, discriminates; $H_2PO_4^-$	NaF, NaCl, NaBr, NaI, NaH_2PO_4, $NaHSO_3$, Na_2SO_4, $NaNO_3$, $NaNO_2$ and $NaHCO_3$	[43]
CA-12	B (KOH,400° C, H_2)	14.9 ±6.7 nm – AgNPs (TEM) 15.6 ± 9.1 nm – graphene nanocomposites (TEM)	-	Antibacterial activity against *S. aureus*, *E. Coli*	-	[44]
CA-4, CA-12, CA-15	B ($NaBH_4$)	**CA-4**: 4.5 nm (TEM) **CA-12**: 5 nm (TEM) **CA-15**: 8 nm (TEM)	400 nm 400 nm 400 nm	415 nm 410, 465 nm 410, 450, 490 nm (Saburopin)	increased Saburopin efficiency and stability.	[45]

Table 1. *Cont.*

Cyclophanes Studied	AgNPs Synthesis Method [1]	AgNPs Sizes (Method)	Surface Plasmon Resonance λ	Application, Target Substrate, SPR λ, nm in the Presence of Substrate [2]	Comparison Substrates	Lit.
CA-4, CA-10, CA-11, CA-18, CA-19, CA-20	$B(NaBH_4)$	-	**CA-4**: 390 nm **CA-10**: 390 nm **CA-11**: 380 nm **CA-18**: 420 nm **CA-19**: 400 nm **CA-20**: 400 nm	Chlorohexidine, gentamycine	chlorohexidine, chloramphenicol, gentamycine sulfate,	[46]
CA-4, CA-20	$B(NaBH_4)$	-	**CA-4**: 390 nm **CA-20**: 398 nm	**CA-4**: 398 nm (BSA), **CA-20**: 404 nm (BSA)	-	[47]
CA-21 CA-22 CA-23 CA-24	B (H_2) (pH = 9) 70 °C	**CA-21**: 2.1± 0.8 nm (TEM) **CA-22**: 2.9 ±1.3 nm (TEM) **CA-23**: 5 ± 3.6 nm (TEM) **CA-24**: 5.3± 2.4 nm (TEM)	~ 350, 390 nm	-	-	[48]
CA-25, CA-26, CA-27	A (NH_2OH·HCl)	~23 nm (TEM)	420 nm	436 nm (pyrene)	pyrene, triphenylene, benzo[c]phenantrene, anthracene, coronene, chrysene, dibenzoanthracene, rubicene	[50]
CA-28	A (sodium citrate or NH_2OH)	-	-	SERS (coronene)	pyrene, triphenylene, benzo[c]phenantrene, coronene	[51]
CA-25	B (ethylene-diamine)	9.4 nm (nanocrystalline) (TEM)	-	-	-	[54]
CA-12	$B(NaBH_4)$	7 nm (TEM)	393 nm	406 nm (Sanguinarine)	Enhancement of antibacterial activity	[55]
CA-29	A ($NaBH_4$, $C_{18}H_{37}NH_2$)	46.7 nm (DLS)	430 nm	430 nm (intensity increase)	$CoCl_2$, $NiCl_2$, $MnCl_2$, $Cd(NO_3)_2$, $AgNO_3$, $Cu(NO_3)_2$), $Pb(NO_3)_2$, $Hg(NO_3)_2$, $BaCl_2$	[56]
CA-30	A ($NaBH_4$)	52 nm (TEM)	422 nm	554 nm (Fe^{3+})	Zn Fe^{3+}, Cu^{2+}, Ca^{2+}, Co^{2+}, Mg^{2+}, Cd^{2+}, Ba^{2+}, Na^{+}, K^{+}, Mn^{2+}, Fe^{2+}, Pb^{2+}, Ni^{2+}, Pd^{2+}, Hg^{2+}, pepsin, cytochrome c, BSA, myoglobin	[57]
CA-31	A (interphase $NaBH_4$, $C_{12}H_{25}SH$)	3 ± 1 nm (TEM)	450 nm	580 nm (association with AuNPs)	AuNPs functionalized with pyridinium fragments	[58]
CA-33	$B(NaBH_4)$	9 nm (TEM)	~ 415 nm	~ 525 nm (N-Fmoc-L-aspartic acid)	N-Fmoc-L-aspartic acid, N-Fmoc-D-aspartic acid	[59]
CA-32	B (photo-reduction, 365 nm)	10 ± 1.0 nm (TEM)	364 nm	Fe^{3+} (414 nm)	Li^{+}, Na^{+}, K^{+}, Cs^{+}, Mg^{2+}, Ca^{2+}, Sr^{2+}, Ba^{2+}, Cr^{3+}, Fe^{3+}, Fe^{2+}, Cu^{2+}, Pb^{2+}, Ag+, Ni^{2+}, Mn^{2+}, Co^{2+}, Cd^{2+}, Zn^{2+}.	[60]
CA-34	B (photo-reduction with sunlight)	3-5 nm (TEM)	432 nm	432 nm, lower intensity (Hg^{2+})	Li^{+}, Na^{+}, K^{+}, Cs^{+}, Ca^{2+}, Mg^{2+}, Ba^{2+}, Cr^{3+}, Sr^{2+}, Co^{2+}, Ni^{2+}, Cd^{2+}, Zn^{2+}, Rb^{+}, Hg^{2+}, Pb^{2+}, Cu^{2+}	[61]
CA-21, CA-23, CA-24, CA-35, CA-36	B (photo-reduction, pH = 9, 365 nm)	**CA-21**: 3.6 ± 1.2 nm **CA-23**: 2.6 ± 0.8 nm **CA-24**: 2.6 ± 0.8 nm **CA-35**: 3.6 ± 1.2 nm **CA-36**: 3.6 ± 1.2 nm	**CA-21**: 400 nm **CA-23**: 400,485 nm **CA-24**: 400,485 nm **CA-35**: 400 nm **CA-36**: 400 nm	-	-	[62]

Table 1. *Cont.*

Cyclophanes Studied	AgNPs Synthesis Method [1]	AgNPs Sizes (Method)	Surface Plasmon Resonance λ	Application, Target Substrate, SPR λ, nm in the Presence of Substrate [2]	Comparison Substrates	Lit.
CA-37	B (gamma-irradiation)	1.55–0.5 nm in order $AgPF_6$ < $AgClO_4$ < AgOTf < $AgBF_4$ Bimetallic: 1 nm and 3 nm (HAADF-EDX-STEM)	410 nm	nitrothiophenol reduction	nitrothiophenol, nitrophenol	[63]
CA-12	B (electrochemical reduction)	~ 100 nm (TEM)	-	methyl parathion	PO_4^{3-}, SO_4^{2-}, CO_3^{2-}, NO^{3-}, *p*-nitrophenol, nitrobenzene	[64]
CA-25	B (electrochemical reduction)	40–70 nm (TEM)	-	nifedipine	dopamine, ascorbic acid, L-Dopa, epinephrine, tryptophan, L-cysteine, uric acid	[65]
CA-25, CA-38	B (electrochemical reduction)	~ 100–2000 nm (TEM)	-	flutamide	dopamine, ascorbic acid, L-Dopa, epinephrine, tryptophan, L-cysteine, uric acid	[66]
CA-39	B (electrochemical reduction)	70 nm (TEM)	-	electrochemical reduction of H_2O_2	-	[67]
CA-40, CA-41	Combination of C and B (electrochemical reduction with participation of cyclophane as reducing agent)	10 nm, height = 2 nm (AFM)	-	Photocatalytic degradation of methyl orange, methylene blue, rhodamine 6G chloride	-	[68,69]
TCA-3, TCA-8	B (reduction with DMF)	three-dimensional self-assembled monolayer (DMF) (1–13 nm; 46–622 nm	-	-	-	[92]
TCA-5	C	20 nm	~425 nm	~ 452 nm (histidine) ~414 nm (tryptophan)	valine, proline, arginine, cysteine, aspartic acid, glutamic acid, glutamine, leucine, methionine, phenylalanine, tryptophan, isoleucine, histidine	[93]
TCA-1	A	Two nanoclusters with 35 and 34 atoms	Ag36: 501, 336, 300 (shoulder) nm Ag35: 495, 336, 300 (shoulder) nm Ag34: 482, 336, 300 (shoulder) nm	-	-	[94]
TCA-27	C	4–6 nm (TEM)	-	Substrate depending on electrode composition: A: dopamine B: ochratoxin C: cholinesterase D: DNA damage	-	[95–98]
TCA-28	B (electrochemical reduction)	Micro-sized, contacted granules (TEM)	-	A: factors affecting DNA charge and structure (thermal denaturing, methylene blue intercalation, oxidative damage), thiocholline B: tryptophan	B: phenylalanine, histidine, cysteine, tyrosine	[99,100]

Table 1. *Cont.*

Cyclophanes Studied	AgNPs Synthesis Method [1]	AgNPs Sizes (Method)	Surface Plasmon Resonance λ	Application, Target Substrate, SPR λ, nm in the Presence of Substrate [2]	Comparison Substrates	Lit.
RA-1	A	45 ± 10 nm (DLS)	420 nm	519 nm (dimethoate)	dichlorvos, parathion, 2,4-D, dimethoate, hexaconazole, imidacloprid and monocrotophos	[104]
RA-2	A	20.9 ± 16.4 nm (TEM)	416 nm	reversible association with resorcinarene self-assembled microtubes	-	[105]
RA-3	B ($NaBH_4$)	2–3 nm (TEM)	-	doxorubicin	-	[106]
RA-4	B ($NaBH_4$)	4–6 nm (TEM)	429 nm	Cetyltrimethylammonium (phase transfer of AgNPs from water to chloroform upon interaction with surfactant)	-	[107]
RA-5	C	7 ± 1 nm (TEM)	406 nm	Fe^{3+} (fluorescence quenching at 560 nm), antibacterial activity against *E. coli*, *B. subtilis*, *S. aureus*, *B. megaterium*	Zn^{2+}, Cd^{2+}, Hg^{2+}, Co^{2+}, Cu^{2+}, Pb^{2+}, Cr^{3+}, V^{3+}	[108]
RA-6	C	5 ± 2 nm (TEM)	415 nm	Cd^{2+} (fluorescence quenching at 458 nm)	Zn^{2+}, Pb^{2+}, Co^{2+}, Cu^{2+}, Ba^{2+}, Cd^{2+}, Mn^{2+}, Hg^{2+}, Ca^{2+}, Mg^{2+}, Sr^{2+}, Ni^{2+}	[109]
RA7	C	15 ± 5 nm (TEM)	426 nm	Pb^{2+} (fluorescence quenching at 580 nm)	Cr^{3+}, Mn^{2+}, Fe^{3+}, Co^{2+}, Ni^{2+}, Cu^{2+}, Zn^{2+}, Cd^{2+}, Hg^{2+}	[110]
RA-8	C	7 ± 5 nm (TEM)	408 nm	420 nm (CT-DNA, S-DNA) Histidine (fluorescence quenching at 540 nm)	arginine, cysteine, aspartic acid, glutamic acid, glutamine, leucine, methionine, threonine, histidine, L-Dopa, tryptophan	[111]
RA-9	C	30 nm (TEM) 60 nm (AFM, DLS)	440 nm	Catalysis of nitrophenol reduction	-	[112]
PA-5	B ($NaBH_4$)	18.7 ± 2.18 nm (TEM)	400 nm	400 nm intensity decrease (Structural analogues of spermine **G3**)	spermine, ursol, tetraethylenepentamine, triethylenetetramine, ethanediamine, 1,12-dodecylamine and 1,6-hexamethylenediamine	[123]
PA-4	B ($NaBH_4$)	10 nm (TEM)	404 nm	456 nm (series of alkylidene- linked two paraquat units) binding is reversible upon addition of **PA-5**	-	[124]
PA-4	B ($NaBH_4$)	~10 nm (TEM)	394 nm	Electrochemical detection of paraquate	-	[125]
PA-6	B ($NaBH_4$ in the presence of SWCNT)	3–4 nm (TEM)	410 nm	Catalytic reduction of nitrophenol, catalytic degradation of methylene blue	-	[126]
PA-5	B ($NaBH_4$)	6.01 ± 0.94 nm (TEM)	400 nm	Electrochemical detection of paraquat	-	[127]
PA-7, **PA-8**	B ($NaBH_4$)	13.57 ± 2.18 nm (TEM)	400 nm	500 nm glutamic acid	lysine, arginine, histidine, glycine, glutamic acid, tyrosine, aspartic acid, threonine	[128]
PA-9	A (ligand-exchange), B (synthesis in the presence of cyclophane)	Ag_{29} nanoclusters For case B, formation of small nanoparticles is possible	330, 455, 513, 623, 700 nm	Photoluminiscence enhancement (810 nm, Neutral alkylamines; 650 nm, quaternary alkylammonium salts)	hexylamine, dodecaneamine, oleylamine, 1,8-diaminooctane trimethyloctadecylammonium bromide,	[129]

[1] A, pre-synthesized; B, reduced in the presence of cyclophane; C, cyclophane is used as reducing agent; [2] Application is not specified if AgNPs are used as the colorimetric sensor.

Double rosette assemblies of calix[4]arenes **CA-2** and **CA-3** with barbituric acid or cyanuric acid derivatives and silver were shown to reduce by electron beam at 200 keV *in situ* in conditions of a transmission electron microscopy (TEM) experiment [26]. Such method of reduction allows to obtain small monodisperse nanosized (d = 2 nm) AgNPs. The obtained results prove that association with cyclophanes allows to synthesize very small AgNPs.

Self-assembly of calix[6]arene containing imidazole groups on the lower rim and three sulfonato groups on the upper rim was studied [27]. It was shown that at concentrations of 10^{-4} M and higher, macrocycles formed multilamelar vesicles (50–250 nm diameter). Addition of silver (I) ions to the system leads to formation of nanomicelles with size of 2.5 nm. The authors suggest that the obtained micelles can be used in hosting of a guest, either in the calixarene core itself or in the heart of the assemblies.

Calixarenes upon self-assembly with silver ions can form not only micellar structures but highly regular networks of coordination polymers. It is caused by strict fixation of coordinating fragments relative to the macrocyclic rim. Possibility of functionalization of a macrocyclic platform with various functional groups, spacers and various conformations available for calixarenes has made them a versatile block for metal–organic frameworks with silver ions. For example, three component coordination polymers of silver ions with *p*-sulfonatocalix[4]arene **CA-4** and ethylenediamine were reported [28]. Similarly, carboxyl derivatives of calix[4]arene **CA-5** and **CA-6** [29], calix[4]arenes **CA-7** with allyl groups [30] and **CA-8** with pyridyl fragments [31] were shown to form regular crystalline structures. The last-mentioned material has been successfully used for recognition of nitrobenzene and photodegradation in aqueous solutions. There is an example of macrocycle **CA-5** and **CA-9** self-assembly in the presence of silver ions leading to the formation of dimeric capsules, which over time crystallize into three-dimensional molecular architecture [32].

The publications reporting self-assembled supramolecular nanostructures of calixarenes with silver ions are still scarce; however, considering the long period over which calixarenes have been known to the scientific community and intensely studied, it leads us to an indirect conclusion: such supramolecular association patterns are most likely uncommon for calixarenes. Molecular design approaches for creating supramolecular nanoparticles instead of regular three-dimensional MOFs (metal–organic frameworks) are unknown.

2.2. Synthesis and Application of Calix[n]arene-Based AgNPs

Calix[n]arene-based AgNPs have been synthesized using various methods [15,33]. The most commonly used approaches are chemical, electrochemical and photochemical reduction. Historically, the simplest and most studied method is chemical reduction (Table 1). Sodium borohydride is the most popular reducing agent (along with sodium citrate, hydrazine hydrate and molecular hydrogen). However, the choice of functional groups of substituents is a nontrivial task in the design of calixarene-based AgNPs. Basically, functional groups should allow association with AgNP surfaces. Especially in the case of calixarenes, the nature and geometry of functional groups (which are usually strictly preorganized by macrocyclic platform) dictate possible interaction with the target substrate. Therefore, this factor sufficiently limits all the possible substrate recognition patterns achieved for calixarenes, restricting possible functional groups to only those capable of interacting with AgNP surfaces. It could be overcome by introducing functional groups of different nature, but in practice (as we can see in articles listed below), mostly calixarenes modified with functional groups capable of association with AgNPs were reported.

2.2.1. Calix[n]arene-Based AgNPs Obtained Using Chemical Reduction

In supramolecular chemistry and in the chemistry of macrocyclic compounds, fragments of sulfonic acids usually are implemented to increase solubility in polar media (in water), giving surficial active properties and self-assembly based on acid–base or ionic interactions. In addition to mentioned directions, sulfonic acids are capable of coordinating some ions (e.g., silver ions) and can coordinate to

the surface of metallic silver (0) nanoparticles. Sulfonic acid derivatives of calixarene are capable not only to associate with silver ions but also with nanoparticles: silver nanoparticles functionalized with sulfonic acid derivatives of calix[n]arenes were reported.

Significant contribution in the synthesis and application of sulfonatocalix[n]arene-stabilized AgNPs was made by Prof. A. W. Coleman's group [33]. This group synthesized a number of sulfonic acid calixarene derivatives **CA-4** and **CA-10**–**CA-17** (Figure 4), which were used for surface modification of silver nanoparticles. Possibility of interacting sulfonatocalix[n]arene-based AgNPs with cationic, neutral and anionic surfactants was studied. It was shown that only *p*-sulfonatocalix[4]arene derivatives **CA-4** and **CA-11** interacted with cationic surfactants [34]. Toxicity of the nanoparticles obtained towards model pheochromocytoma neuronal-like cells was studied, and it was shown that synthesized nanoparticles were nontoxic up to 100 mg/mL concentration. It was shown that treatment of neural pheochromocytoma cells with such nanoparticles with calix[n]arenes leads to lowering of reactive oxygen species [35].

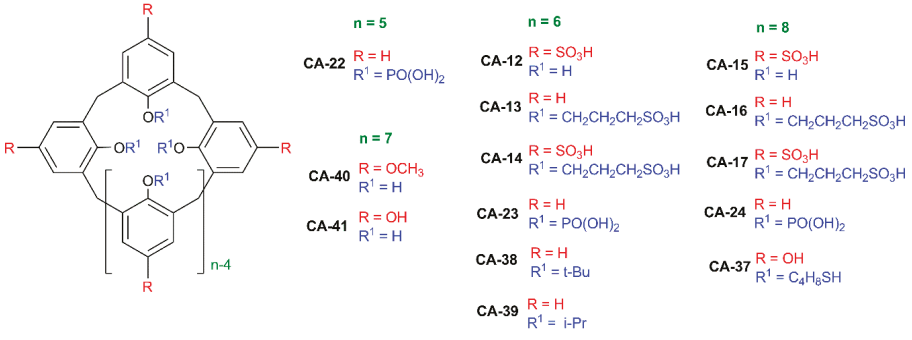

Figure 4. Structures of calix[n]arenes (n = 5–8).

It was shown that AgNPs capped with nine different sulphonated calix[n]arenes (**CA-4** and **CA-10**–**CA-17**) were tested for their antibacterial effects against *Bacillus subtilis* and *Escherichia coli* at concentration of 100 nM in calix[n]arene [36]. It was determined that antibacterial properties depend on the size of the macrocycle ring. It was shown that calixarenes (**CA-11**, **CA-14** and **CA-17**) with sulfonate groups on the lower and upper rims were active against Gram-negative bacteria. Derivatives of calix[6]arene **CA-13** containing sulfonate groups only on the lower rim has pronounced bactericidal activity.

It was reported [37] that interaction of *p*-sulfonatocalix[4]arene **CA-4** based AgNPs with nucleotides, nucleosides and desoxynucleosides leads to selective complexation, which is expressed by color change due to aggregate formation. There is a clear difference for purine and pyrimidine: for pyrimidine nucleotides, a new absorption band at 550 nm appears, and a color change from yellow to orange, red or pink is observed; for purine nucleotides, an absorption band is observed at 580–590 nm.

Molecular recognition of cytosine with *p*-sulphonatocalix[4]arene **CA-4** in solution, in the solid-state and on the surface of hybrid silver nanoparticles was studied [38]. It was found that the ratio of **CA-4**:cytosine changed depending on the state (from 1:1 in solution to 1:4 in solid phase). It was demonstrated that cytosine initiated aggregation of **CA-4**-based AgNPs.

Silver nanoparticles stabilized with oleic acid in organic solvents were obtained [39]. Adding of *p*-sulfonatocalix[4]arene **CA-4** to this system leads to formation of an inclusion complex of oleic acid and **CA-4**, which allows to transfer silver nanoparticles from the organic phase into the aqueous phase.

AgNPs modified with *p*-sulfonatocalix[4]arene **CA-4** were obtained by adding sodium borohydride to a mixture of **CA-4** and silver nitrate at room temperature for 5 min [40]. AgNP size was determined by TEM and was 8.0 ± 1.0 nm. A colorimetric sensor was made based on these AgNPs for detecting histidine

in water. High selectivity of this sensor allows to quantitatively determine histidine concentrations down to 5×10^{-6} M.

Presence of additional binding sites also opens new opportunities towards forming cascade composite structures based on inorganic materials. *p*-Sulfonatocalix[4]arene **CA-4**-modified AgNPs were synthesized by interaction of $AgNO_3$–calixarene mixture with $NaBH_4$ [41]. Solutions of nanoparticles obtained upon addition of metal ions at pH 10 have different colors. The authors explain such color diversity by the assembly size of **CA-4** AgNPs on the metal hydroxide crystals, which depend on the added metal species, leading to a different localized surface plasmon resonance band. Therefore, **CA-4**-AgNPs also may be used for discerning different metals by their color.

Highly stable AgNPs functionalized with *p*-sulfonatocalix[n]arenes **CA-4** ($n = 4$) and **CA-15** ($n = 8$) were obtained [42]. Interaction of the synthesized AgNPs with a number of pesticides (iprodione, pyrimethanil, thiabendazole, optunal, parathion-methyl, methomyl and acetamiprid) was investigated. It was shown that the AgNPs with calix[4]arene **CA-4** can be implemented as colorimetric probes to quantitatively determine optunal at concentrations down to 1×10^{-7} M.

Presence of a large flexible hydrophobic cavity in sulfonatocalix[6]arene **CA-12** opens the possibility of complexation with fluorescent ligands. Such double functionality opens the possibility of making three-component systems in which a fluorescent ligand acts as a bridge between cyclophane-modified silver nanoparticles [43]. A highly sensitive $H_2PO_4^-$ colorimetric sensor was developed based on self-assembly of **CA-12**-AgNPs with a dipyrene derivative. The authors report that this colorimetric sensor can also realize real-time quantitative detection for $H_2PO_4^-$ with a detection limit of 1×10^{-7} M.

Similarly, calixarene derivatives can be used for creating a graphene–AgNPs nanocomposite in a mixture of silver nitrate, graphene oxide and potassium hydroxide. Ag–graphene nanocomposites were synthesized by utilizing a continuous hydrothermal flow synthesis (in water overheated up to 450 °C, 24.1 MPa) process using sulfocalix[6]arene **CA-12** as an effective particle stabilizer [44]. The authors report low cytotoxicity and high activity against *Escherichia coli* (Gram-negative) and *Staphylococcus aureus* (Gram-positive) bacteria.

Modification of AgNPs with sulfonic acid derivatives of calixarenes **CA-4**, **CA-12** and **CA-15** also allows stabilizing enzymes [45]. It was shown that *p*-sulphonatocalix[8]arene **CA-15**-stabilized AgNPs can increase efficiency and stability of Saburopin (serpin enzyme from *Eubacterium saburreum* possessing proteolytic activities). The authors report that in the presence of **CA-15**–AgNPs, enzymes have a high inhibition effect in the pH range of 2–10 and in the temperature range of 10 to 40 °C, while remaining active even at 70 °C.

AgNPs were obtained using a series of anionic calix[4]arenes with sulfonate (**CA-4**, **CA-10** and **CA-11**), carboxylate (**CA-18** and **CA-19**) and phosphonate (**CA-20**) groups [46]. Selectivity of obtained nanoparticles was studied on a series of three active pharmaceutical ingredients (API): chlorhexidine (antiseptic), chloramphenicol (neutral antibiotic) and gentamycin sulfate (aminoglycosidic antibiotic). It was shown that affinity to APIs studied depended on the nature of calix[4]arene and API.

The binding of AgNPs modified with calix[4]arenes **CA-4** and **CA-20** with regard to various serum albumins (bovine, human, porcine and sheep serum albumins) has been studied by variable temperature fluorescence spectroscopy [47]. The studied albumins have different fluorescence quenching effects according to the nature of the anionic calixarene. The results obtained by the authors may help to discriminate among the different species.

AgNPs with diameter about 2 nm were obtained using *p*-phosphonated calix[n]arenes **CA-21** ($n = 4$), **CA-22** ($n = 5$), **CA-23** ($n = 6$) and **CA-24** ($n = 8$) as templates and surfactants for stabilization [48]. Hydrogen was used as a reducing agent. The authors show that the key factor affecting particle sizes and speed of reaction was the solution pH. The smallest monodisperse particles were obtained at pH = 12.

Due to preorganized hydrophobic cavity, one promising application of AgNPs functionalized with cyclophanes is their use for recognition of polycyclic aromatic hydrocarbons [49]. Calix[4]arenes (**CA-25**–**CA-27**)-modified AgNPs were investigated for affinity towards a series of polycyclic aromatic

hydrocarbons (PAHs) (pyrene, triphenylene, benzo[*c*]phenantrene, anthracene, coronene, chrysene, dibenzoanthracene and rubicene) [50]. AgNPs modified with disubstituted derivatives of calix[4]arene **CA-26** with two ester groups have selectivity towards polycyclic aromatic hydrocarbon guest systems bearing four benzene rings, mainly pyrene. It opens the opportunity for using functionalized calix[4]arenes in the design of highly sensitive and selective sensors of PAHs.

Dithiocarbamate calix[4]arene **CA-28** functionalized AgNPs were shown to detect traces of aromatic hydrocarbons using the surface-enhanced Raman scattering (SERS) method [51–53]. The effectiveness of this system was checked for a group of PAHs: pyrene, benzo[c]phenanthrene, triphenylene and coronene. High selectivity towards pyrene, benzo[c]phenanthrene and triphenylene containing four aromatic rings was demonstrated. For these compounds, affinity constants have close values, and detection limits are quite similar (10^{-7}, 10^{-8} M). In the case of coronene, the sensitivity was higher, which was explained by formation of a complex in which cavities of two calixarene molecules participated, leading to aggregation of nanoparticles.

Also, there are a series of articles reporting unsubstituted *p-tert*-butylcalix[n]arenes as AgNP stabilizers. A unique approach to the synthesis of AgNPs was developed [54] in a preassembled three-component Ag–ethylenediamine *p-tert*-butylcalix[4]arene **CA-25** coordination complex. Subsequent removal of amine under heating leads to reduction of Ag^+ ions and formation of Ag nanocrystals (d = 9.4 nm) with 29 Ag atoms in a single crystal.

AgNPs based on calix[6]arene **CA-12** with diameters of about 7 nm are capable of interacting with sanguinarine (antitumor, antibacterial, antioxidant and anti-inflammatory drugs) [55]. The nanoparticle–sanguinarine complex has shown to lower toxicity towards two cell lines (normal CHO and cancerous A549).

In the research group of Prof. D. Tian [56], AgNPs modified with the tetracarboxylate derivative of *p-tert*-butylcalix[4]arene **CA-29** in the 1,3-alternate conformation containing triazole spacers were obtained. A highly sensitive colorimetric sensor for Cu^{2+} was developed with the detection limit of 2.5×10^{-6} M. Moreover, the authors note that increasing Cu^{2+} concentration leads to increasing sizes of AgNPs and forming larger three-dimensional aggregates.

AgNPs modified by sulfonatocalixarene **CA-30** with thiol groups on the lower rim were prepared [57]. Obtained AgNPs were used for detecting trace concentrations of Fe^{3+} ions in aqueous medium. The sensor obtained has several advantages compared to reported colorimetric sensors: fast response time (<80 s) to ferric ions and long shelf-life (>4 weeks). The biosensor has been successfully applied to estimate ferric ions in human blood serum as well as in human hemoglobin.

Using thiol derivatives of cyclophanes for surface modification of metal nanoparticles can be considered as a more straightforward approach. AgNPs (d = 3 ± 1 nm) modified with disubstituted derivatives of calix[4]arene **CA-31** functionalized by thiol groups were obtained [58]. These nanoparticles were shown to be hosts for gold nanoparticles coated with 1-dodecanethiol and *N*-alkylpyridinium fragments. Specific recognition of pyridinium fragments of gold nanoparticles by **CA-31**-modified AgNPs was demonstrated by UV spectroscopy and dynamic light scattering (DLS) methods in dispersions.

While the abovementioned examples were limited to calixarenes functionalized with alkyl groups and fragments capable of interacting with AgNP surfaces, there are few examples of introducing functional fragments specific to target substrate recognition. Using chiral carboxylic acid fragments allows chiral substrate recognition while maintaining association to AgNPs surface. AgNPs based on chiral calix[4]arene **CA-32** containing R-mandelic acid fragments were obtained [59]. These AgNPs with diameters about 9 nm can differentiate N-Fmoc-d/l-aspartic acid (D-FAA and L-FAA), with higher sensitivity of chiral calixarene-modified AgNPs towards L-FAA. Several detection methods were compared, and DLS has been shown to be more sensitive to nanoparticle aggregation than UV spectroscopy (500-fold higher sensitivity of DLS method compared to UV spectroscopy).

Historically, calixarene is one of the first macrocyclic platforms that were used as a stabilizer in the synthesis of AgNPs. Most often, derivatives of calix[n]arenes containing charged sulfonate, carboxylate

and phosphonate groups are used for their functionalization. Keeping in mind that, especially for calixarenes, the nature of functional groups dictates selectivity, it definitely limits their potential as host molecules. The obtained calixarene-based AgNPs are used to design and create drug delivery systems, colorimetric sensors, antibacterial agents and separation and selective recognition of various biologically important substrates.

2.2.2. Calix[n]arene-Based AgNPs Obtained Using Photochemical Reduction

The photochemical synthesis method offers a reasonable potential for the synthesis of shape- and size-controlled calixarene-based AgNPs. It is also worth noting that the photochemical reduction method is environmentally friendly; therefore, this method can be attributed to "green chemistry". Excluding reducing agents from the reaction mixture simplifies the reduction of calixarene-silver ions, allowing to expect formation of AgNPs in a more associate–controlled fashion (Table 1).

Calixarene **CA-33** functionalized with two pyridyl groups linked to cyclophane with a triazole spacer [60] was found to selectively bind Fe^{3+} (1:1 stoichiometry ratio, $K = 5.35 \times 10^{-4}$ M^{-1}). Calixarene **CA-33** was used for synthesis of **CA-33**-AgNPs (diameter 10 ± 1 nm) by reduction of $AgNO_3$ in methanol using ultraviolet radiation (λ_{max} = 365 nm). A colorimetric sensor for Fe^{3+} was designed based on **CA-33** AgNPs. The authors report strong aggregation of **CA-33** AgNPs at higher concentrations of Fe^{3+}.

AgNPs (d~5 nm) were obtained using disubstituted calix[4]arene **CA-34** with hydrazide and thiophene fragments [61]. These nanoparticles were prepared by mixing a calixarene solution in methanol with aqueous solution of $AgNO_3$ in the ratio of $AgNO_3$/**CA-34** 1:15. The obtained reaction mixture was treated with sunlight. Temperature effects were studied at 20, 50 and 80 °C. It was shown that nanoparticle sizes did not depend on temperature significantly. Obtained nanoparticles can selectively recognize Hg^{2+} and Hg^0 in solution and vapor phases, respectively, with distinct color change. The detection limits reported for Hg^{2+} by UV–Vis and amperometry are 0.5 nM (0.1 ppb) and 10 nM (2 ppb), respectively.

AgNPs with diameters less than 5 nm were obtained by photochemical reduction of silver nitrate (1 mM) in water in the presence of *p*-phosphorylated calix[n]arenes **CA-21**, **CA-23**, **CA-24** and *O*-alkyl derivatives of **CA-21** (**CA-35** and **CA-36**) (0.25 mM) [62]. Photochemical reduction is one of the key methods of green chemistry. The experiment was conducted using a 100 W UV lamp emitting 365 nm light. At pH = 9, the size of obtained nanoparticles was 3.6 ± 1.2 nm.

Alkylthiol derivatives of calix[8]arene **CA-37** were used for modification of monometallic and bimetallic nanoparticles [63]. AgNPs were obtained by reducing Ag^+ in the presence of calix[8]arene **CA-37** in ethanol. In the results, small spherical nanoparticles were obtained with size dependence on silver salt concentration and counter ion. The structure of the calix[8]arenes and their anchoring on the AgNPs surface cause some accessibility to the surface of the AgNPs, which is very important for applications in catalysis. Potential catalytic applications of the obtained **CA-37** AgNPs were studied using the reduction of 4-nitrothiophenol as a model reaction.

It can be concluded that very small (5 nm or less) calixarene-based AgNPs can be obtained using the photochemical reduction method, which are smaller compared to AgNPs obtained by common chemical reduction route. Unfortunately, shapes and sizes of associates of calixarene with silver ions prior to reduction were not studied, while it could shed light on the effect of supramolecular association on size and morphology of the AgNPs formed. These results make this method very promising.

2.2.3. Calix[n]arene-Based AgNPs Obtained Using Electrochemical Reduction

The use of the electrochemical method for synthesis of AgNPs is one of the promising areas due to a number of advantages. Electrochemical methods make it possible to obtain nanoparticles with high purity using simple techniques, while controlling the particle size can be done by adjusting the current density or the applied potential. It is also worth noting that this method is environmentally friendly, since toxic chemical reducing agents are not used. On the other hand, the electrochemical

reduction proceeds in a heterogeneous environment (and with participation of AgNPs, resulting in their clustering), which leads to certain limitations of the method for size-control of the nanoparticles formed. Usually this method is implemented for constructing hybrid nanostructured electrochemical sensors, and introduction of AgNPs allows to increase sensitivity of electrodes.

Novel electrochemical sensors based on *p*-sulfonatocalix[6]arene **CA-12**-modified AgNPs coated glassy carbon electrode for methyl parathion as a model of nitroaromatic organophosphates were developed [64]. The obtained sensors can determine methyl parathion in the concentration range of 1×10^{-8} to 8×10^{-5} M with lower detection limit of 4.0×10^{-9} M. The authors report that reproducibility and stability of the sensor obtained was higher than those for enzyme-based electrodes.

AgNPs with diameters in a range of 40–70 nm were obtained by an electrochemical method using *p-tert*-butylcalix[4]arene **CA-25** on glassy carbon as the matrix [65]. The authors report that nifedipine (calcium channel blocker) can be detected in concentration range (0.8–60 μM) with detection limit at 0.72 μM. This electrode has a number of attractive properties: high stability, reproducibility of signal, high sensitivity, quick response and low detection limit.

AgNPs were synthesized on glassy carbon electrodes coated with *p-tert*-butylcalix[4]arene **CA-25** and *p-tert*-butylcalix[6]arene **CA-38** [66]. The authors demonstrate that the presence of calixarene on the electrode's surface allows to control nanoparticle sizes and to prevent agglomeration. Cyclic voltammetry has shown that AgNPs on glassy carbon electrode have pronounced catalytic activity to reduce flutamide, which is a widely used nonsteroidal anti-androgen drug in prostate cancer treatment. The modified electrode shows linear signal response in differential impulse voltammetry in a range 10–1000 μM with detection limit at 9.33 μM for flutamide.

An approach to synthesize AgNPs by electrochemical reduction of Ag^+ [67] on the glassy carbon electrode, modified with *p*-isopropylcalix[6]arene **CA-39** was reported. Obtained AgNPs were able to efficiently catalyze reduction of hydrogen peroxide.

An *in situ* synthesis route was reported [68] for preparation of a layer of AgNPs on the silicon surface using an immobilized supramolecular layer as silver ion reducing agent. First, *p*-methoxycalix[7]arene **CA-40** was covalently immobilized on the silicon surface, and 4-methoxyphenol fragments were demethylated to hydroquinone fragments. Then, AgNPs were immobilized into this layer by reducing with $Na_2S_2O_4$. AgNPs had plate-like morphology with a diameter of 10 nm and height of 2 nm. Repeating redox cycles of calix[7]hydroquinone **CA-41** can be implemented to vary sizes of plates in a range of 100 nm and more. Further study of AgNP properties in the same research group [69] was conducted, and it was shown that nanoparticles obtained were capable of photodegradation of various organic dyes (methyl orange, methylene blue and rhodamine chloride).

Thus, calixarene-based AgNPs obtained using the electrochemical method are mainly used as part of electrochemical sensors to determine biologically important substrates, and they can also be used as catalysts and components for photodegradation of dyes. Usually, electrochemical reduction leads to rather large sizes of AgNPs when compared to photoreduction and chemical reduction. On the other hand, the electrochemical method has definitely allowed to overcome several drawbacks of these methods: it allows to choose other groups for calixarene functionalization and using hydrophobic calixarenes.

3. Supramolecular Self-Assembly of Thiacalix[4]arenes with Ag(I) Ions and Thiacalix[4]arene-Based AgNPs

Among cyclophanes mentioned, thiacalixarenes are characterized by high conformational flexibility and larger sizes of macrocycles compared to calixarenes [70]. The unique feature of thiacalix[4]arenes is the presence of sulfur bridge atoms, which are capable of coordinating with transition metal ions, having high affinity to silver ions. For the most widespread representative of thiacalixarene-based synthetic platforms, *p-tert*-butylthiacalix[4]arene, three conformations are readily available (cone, partial cone and 1,3-alternate). This opens a unique possibility of distributing substituents on both sides from the macrocyclic rim, which in combination with introducing various

substituents allows to reach various substrate selectivities. Even more interesting is the applicability of this feature in various branches of material science and supramolecular chemistry. It allows to achieve unique association patterns, adjust polymer properties and vary aggregation of nanoparticles [71]. Due to the unique geometry of thiacalixarenes, they tend to form nanocage associates [72]. Therefore, in regard to silver ions and nanoparticles, thiacalixarenes are unique, allowing new patterns of self-assembly and nanoparticle functionalization.

3.1. Self-Assembly of Thiacalix[4]arenes with Ag(I) Ions

High affinity of silver ions and the presence of four sulfur bridge atoms, capable of coordinating silver ions, are among the key properties that have attracted the attention of the research community to thiacalixarenes. In the scientific group of Prof. M. W. Hosseini, molecular tectonics based on the formation of silver coordination networks by thiacalix[4]arene derivatives were investigated. The geometry of the final self-assembly was determined by both structural and coordination features of the organic tecton. The authors suggested that the obtained perspective molecular architectures can be used in catalysis, optics, electronics and magnetism [73–82].

While there are many reports on MOFs of silver-coordinated thiacalixarenes, it should be noted that additional coordinating sites (sulfur bridge atoms) can play dramatic roles in association with silver ions. For example, in contrast to any other cyclophanes [83], *p-tert*-butylthiacalix[4]arene **TCA-1** (Figure 5) can form a metal organic framework, where silver ions are coordinated by bridge groups. Therefore, when functionalized with additional groups capable of coordinating silver ions, these cyclophanes can have unique association behavior with silver ions (and other transition metal ions). Indeed, for thiacalixarenes, significant parts of publications are related to forming submicron and nanosized supramolecular associates in the presence of silver salts.

Thiacalixarene's ability of coordinating silver ions has opened the perfect opportunity for using them in electrochemical sensors for silver ion detection [84]. Associates of thiacalixarene derivatives **TCA-2** and **TCA-3** in cone, partial cone and 1,3-alternate conformations with silver ions form solid antimicrobial coatings [85].

Functionalization of thiacalixarene with propylsulfonate fragments (**TCA-4**, cone) allows to realize supramolecular self-assembly into unique shaped associates [86]. Sulfonate substituents are known as ligands for silver ions and, therefore, can provide additional coordination sites for silver ions, which is possibly the main reason of forming fractal associates. While self-assembly of propylsulfonate-functionalized (thia)calixarenes leads to formation of polydisperse submicron-sized micelles, in the presence of silver ions (equimolar ratio) polydispersity significantly decreases. In contrast, for calix[4]arene with similar functional fragments, the hydrodynamic diameter of the particles is 211.1 ± 11.6 nm (polydispersity index = 0.41 ± 0.01), and for the thiacalix[4]arene **TCA-4** it is 95 ± 7 nm (polydispersity index = 0.23 ± 0.01). The presence of additional coordinating sites greatly changes not only the self-associate sizes and stability but also their behavior: fractal associates are formed.

In the case of thiacalixarene three conformational isomers are readily accessible (cone, partial cone and 1,3-alternate). In some cases, conformation can play an interesting role in shape and morphology of associates with Ag^+. Alkylamide derivatives of thiacalixarene **TCA-2**, **TCA-3** and **TCA-5**–**TCA-10** were found to form associates with silver ions with different sizes and shapes as determined by atomic force microscopy (AFM), when interacting with silver ions. Most flat aggregates are formed in the case of 1,3-alternate stereoisomers (2 nm height), while the height of cone associates is 27 nm [87]. The associate sizes are in a range of 62.5–491.6 nm (determined by AFM), while the morphology of aggregates is more dependent on conformation of thiacalixarene derivatives: disk-shaped for partial cone and 1,3-alternate conformations and spherical or elongated structures for cone conformation are formed.

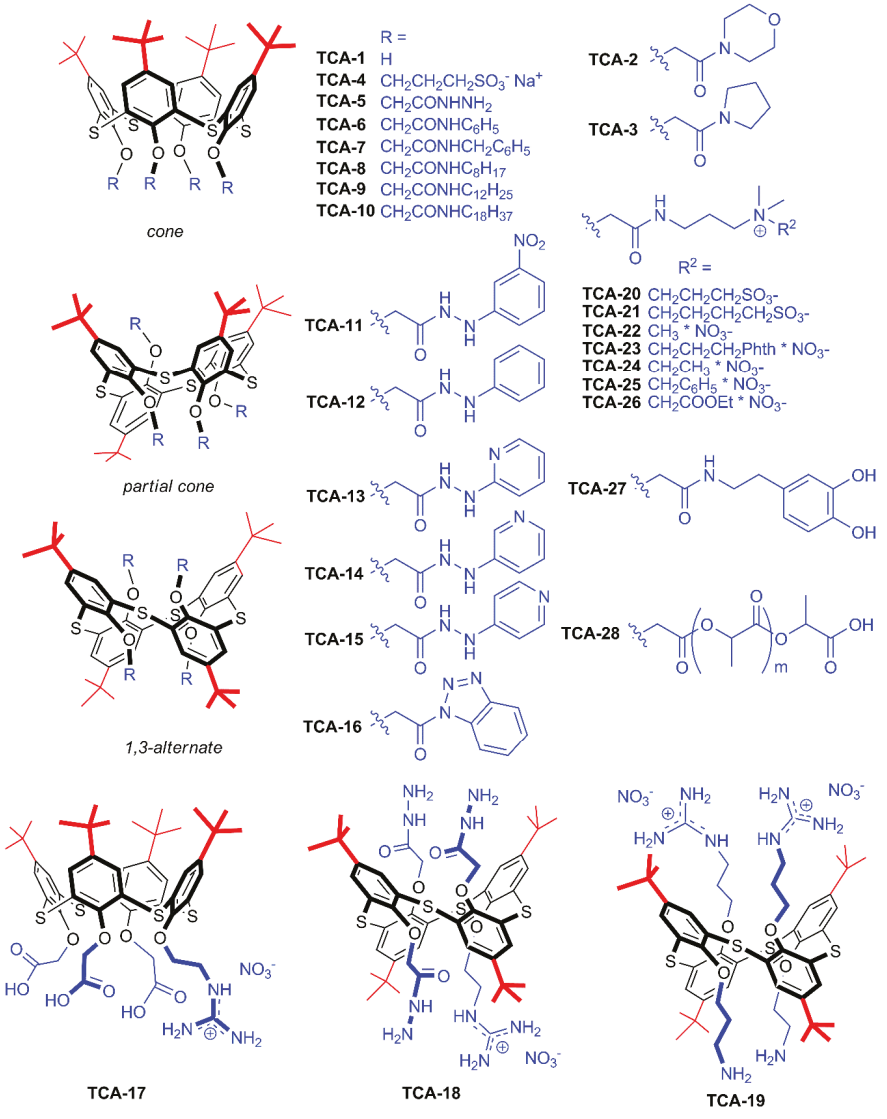

Figure 5. Structures of thiacalix[4]arenes.

High affinity to silver ions caused by bridging sulfur atoms allows introducing additional binding sites by lower rim functionalization while retaining association with silver ions. This allows not only to adjust morphology of supramolecular associates, but it also opens opportunity to use these associates as receptors. It was reported that associates of benzotriazole and arylhydrazide thiacalixarene derivatives with silver ions can interact with dicarboxylic acid, resulting in strong association dependency on the structure of dicarboxylic acid. It was reported that the sizes and morphology of arylhydrazide and benzotriazole derivatives of thiacalixarene **TCA-11–TCA-16** commutatively depend on the sequence of adding silver ions and dicarboxylic acid, and the size of three-component supramolecular associates significantly depends on the structure of dicarboxylic acids [88].

Functionalization of thiacalixarene with carboxylic, hydrazide and amino-groups along with 12 guanidine fragments (**TCA-17**–**TCA-19**) even more significantly enhances coordination with carboxylic acids [89]. Spherical associates of thiacalixarenes with silver ions change morphology upon addition of oxalic acid to granular aggregates.

Assembly of zwitterion-functionalized thiacalixarenes **TCA-20** and **TCA-21** with silver ions not only increased the hydrophilicity of resulting associates, but it also demonstrated significant dependence of supramolecular associate sizes on the length of the spacer connecting the quaternary ammonium fragment to the sulfonate group (197 and 332 nm for propanesulfonic **TCA-20** and butanesulfonic **TCA-21** derivatives) [90].

Adding positively charged fragments to thiacalixarene structures **TCA-22**–**TCA-26** opens the route to creating three-component associates with dye molecule (fluorescein), which allows fluorimetric detection of bovine serum albumin (BSA). Sizes of supramolecular associates with silver ions and fluorescein in the range of 10–67 nm are comparable with sizes of associates with silver ions only (8–88 nm). Among cyclophanes studied, three-component systems based on methyl-ammonium **TCA-22** and phthalimidopropyl-ammonium **TCA-23** derivatives have the highest affinity to bovine serum albumin [91].

Thus, the presence of bridging sulfur atoms, as well as functional groups of substituents, is a fundamental factor in the design and creation of supramolecular systems based on silver cations and derivatives of thiacalix[4]arene. Among functional groups, amide, hydrazide and pyridinium groups can be distinguished. The choice of such substituents is explained from the point of view of the Pearson acid–base concept: the "soft" silver cation more effectively interacts with the "soft" bridging sulfur atom, as well as substitute fragments, and several variants of the coordination of silver ions with thiacalix[4]arene molecules can be suggested (Figure 6). The obtained systems can be used for targeted drug delivery and selective recognition of proteins, amino acids and hydroxyl acids.

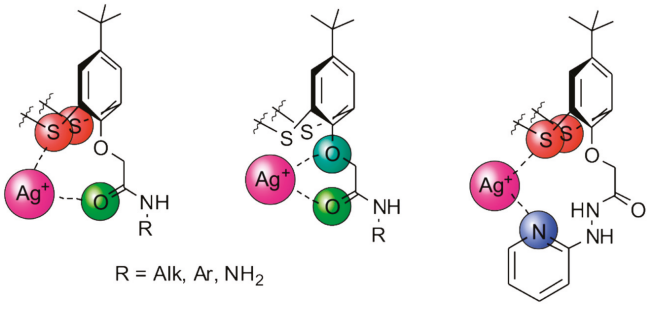

Figure 6. Possible coordination of silver ions with amide derivatives of thiacalix[4]arene.

3.2. Synthesis and Application of Thiacalix[4]arene-Based AgNPs

While there is a number of publications reporting self-assembly of thiacalixarenes with silver ions, unfortunately there are only several reports on reduction of self-assembled structures to AgNPs (Table 1).

It was shown that self-assembly of **TCA-3** and **TCA-8** with $AgNO_3$ under laser irradiation (633 nm) in DMF led to formation of thiacalixarene-coated silver nanoparticles [92]. It was shown that temperature (varied in a range of 2–50 °C) had significant impact on the size of nanoparticle aggregates: average size increased with increasing temperature. The largest associates of AgNPs were observed for **TCA-3** in partial cone conformation.

A hydrazide derivative of thiacalixarene **TCA-5** was shown to reduce silver ions in the work of Prof. V. K. Jain's research group [93]. Relatively uniform 20 nm spherical AgNPs were formed over a pH range of 5–9. The interaction behavior of **TCA-5** AgNPs with different amino acids was

investigated using spectrophotometry and spectrofluorimetry. Among the amino acids tested, only tryptophan and histidine showed fluorescence quenching and fluorescence enhancement, respectively. **TCA-5** AgNPs were reported to effectively reduce the levels of Gram-positive bacteria, Gram-negative bacteria and fungi.

Due to the unique affinity to silver ions, the tendency of thiacalixarenes to form nanocages is especially promising as protection for silver nanoclusters. Nonfunctionalized *p-tert*-butylthiacalix[4]arene **TCA-1** has been shown as an effective protecting agent for silver nanoclusters (containing 35 and 34 Ag atoms) [94].

Dopamine is a known reducing agent of silver ions. It was shown that the tetradopamide derivative of thiacalixarene, **TCA-27,** can chemically reduce silver ions. There are certain similarities with reports of Prof. V. K. Jain's research group: reduction proceeds slowly starting with the formation of associates with silver ions with their further reduction to form 4–6 nm particles. Chemical reduction takes several hours, and the obtained coating is more uniform and acts as more effective electrochemical sensing nanomaterial when compared to electrochemically reduced silver salt on the **TCA-27**-coated electrode. With variations in other components of electrochemical sensors, these nanoparticles were successfully used for dopamine [95] and ochratoxin determination [96]. This approach has allowed to obtain electrochemical sensors for cholinesterase, where quaternary ammonium derivatives of thiacalixarene **TCA-22–TCA-24** act as cholinesterase inhibitors [97]. The same nanostructures were implemented for impedimetric detection of DNA damage in sensors containing neutral red [98].

Electrochemical reduction of silver ions on electrodes coated with thiacalixarene-functionalized oligolactic acid **TCA-28** in cone, partial cone and 1,3-alternate conformations has allowed to obtain hybrid nanomaterials, where morphology of silver particles was shown to depend on thiacalixarene's conformation. Electrochemical reduction of silver ions has allowed to obtain tree-like nanostructured metallic materials. These materials were shown to act as effective electrochemical sensors [99]. The SEM (scanning electron microscopy) micrographs show the formation of spherical particles mostly in contact with each other and amalgamated into submicron-sized structures. Electrostatic assembling of DNA on films allows the detection of specific interactions. Silver dendrites deposited on films offer detection of cholinesterase substrate. These nanomaterials were used in electrochemical sensors, allowing to detect 0.1 to 100 μM of tryptophan with the limit of detection down to 0.03 μM [100]. No interference with oxidation of other amino acids (phenylalanine, histidine, cysteine and tyrosine) was found. The electrochemical sensor developed was validated in the determination of tryptophan sedative medication "Formula of calmness" in the presence of vitamins B5 and B6.

Summing up the discussed material, thiacalixarenes are unique building blocks for supramolecular assembly with silver ions, easily allowing to create three-component assemblies. Thiacalixarenes, due to efficient interaction with silver ions, are very promising stabilizing agents for silver nanomaterials, which would act both as nanostructure-directing agents and stabilizers for prolonged performance of silver nanoparticle (or nanocluster)-based devices.

4. Synthesis and Application of Resorcin[4]arene-Based AgNPs

Resorcinarenes are different from other metacyclophanes because of their possibility of functionalizing bridge fragments (forming "lower rim") by using functional aldehydes at the macrocyclization stage of their synthesis. Presence of eight OH groups forming the upper rim and absence of diverse conformations make their host–guest properties quite specific: they tend to form dimeric capsules enclosing the target substrate due to interactions between eight substituents of each cyclophane molecule [101]. It is especially useful for colloidal plasmonic sensors in which SERS is dependent on nanoparticle aggregation, and in the presence of the target substrate the capsule is formed, which leads to nanoparticle aggregation [102]. (Thia)crown derivatives of resorcinarene are an exception to this rule: such functionalities distort resorcinarene symmetry and present efficient cation binding functional groups. Therefore, such resorcinarene derivatives tend to form crystalline structures, which can differ depending on solvent or thiacrown fragment structure [103], and are out of

the scope of our review. To the best of our knowledge, there are no reports on particles obtained by supramolecular self-assembly of resorcinarene derivatives with silver ions.

Similarly to calixarenes and thiacalixarenes, sulfonate derivatives of resorcinarenes can be used for modification of AgNPs (Table 1). Modification of AgNPs (d = 38 ± 5 nm) with *p*-sulfonatoresorcinarene **RA-1** (Figure 7) was reported leading to the formation of larger (d = 45 ± 10 nm) particles that aggregate in the presence of dimethoate (leading to formation of submicron-sized associates, d = 734 nm) [104]. Selective recognition of dimethoate among structurally close dichlorvos, parathion, 2,4-D, dimethoate, hexaconazole, imidacloprid and monocrotophos, was demonstrated.

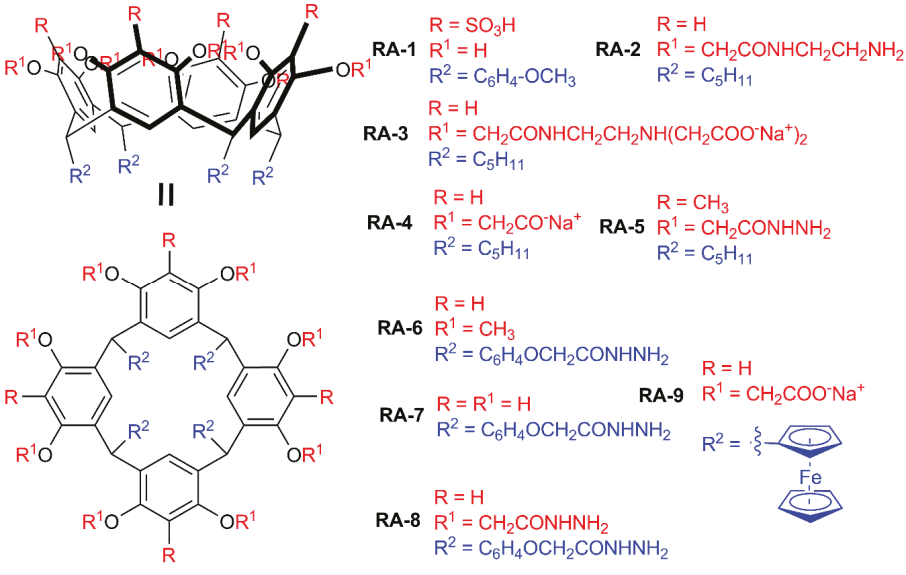

Figure 7. Structures of resorcin[4]arenes.

The presence of eight spatially preorganized functional groups can lead to interesting association behaviors of resorcinarenes. Resorcinarene **RA-2** functionalized with amidoethlyamine fragments has an affinity to the silver nanoparticles surface (which is unusual for amines), which allows to use its self-associates as a supramolecular template for creating hybrid nanomaterial with AgNPs [105]. The authors describe using submicron-sized tubular self-associates of **RA-2** for self-assembly with silver nanoparticles (d = 20.9 ± 16.4 nm). Such assembly is reversible: treatment of resulting hybrid nanomaterials with ultrasound leads to release of AgNPs.

While it is known that substrate encapsulation is often accompanied by formation of dimeric capsules of resorcinarenes, it should be noted that aggregation of resorcinarene molecules on the surface of AgNPs also can assist encapsulation. Such an effect was reported for **RA-3** (derivative of **RA-2** functionalized with 20 carboxylate fragments) [106]: efficiency of doxorubicin binding significantly increased in the case of **RA-3** associated on AgNPs surface, compared to free **RA-3** (95% and 82% of doxorubicin was bound at equimolar **RA-3**:doxorubicin by **RA-3**-AgNPs and **RA-3** solution, respectively). Also, it should be noted that **RA-3** acts as surface-stabilizer of AgNPs synthesized via the sodium borohydride reduction route in the presence of **RA-3,** leading to formation of small-sized nanoparticles (2–3 nm as defined by TEM).

Octacarboxylate derivatives of resorcinarene **RA-4** were also successfully used as a stabilizer in silver ion reduction [107]. **RA-4** increases the affinity of AgNPs formed to the cationic surfactant cetyltrimethylammonium bromide, acting both as host and counter ion. This effect allows to extract nanoparticles into chloroform phase from water.

In a series of reports by Prof. V. K. Jain's group, hydrazide derivatives of resorcinarene were used for reducing silver salts to AgNPs. An octahydrazide derivative of resorcinarene **RA-5** was successfully used to reduce silver nitrate [108]. Obtained luminescent nanoparticles (d = 7 ± 1 nm) showed pronounced antibacterial activity and were stable in wide range of temperatures (10–50 °C) and pH (4–10). Dispersions were stable at room temperature for 120 days. Also, selectivity towards Fe^{3+} ions was shown (over Zn^{2+}, Cd^{2+}, Hg^{2+}, Co^{2+}, Cu^{2+}, Pb^{2+}, Cr^{3+} and V^{3+}). Antibacterial activity was studied on *Escherichia coli*, *Bacillus megaterium*, *Staphylococcus aureus* and *Bacillus subtilis*. The authors explained the antibacterial activity by a two-step mechanism: adsorption of AgNPs to the cell wall and diffusion of silver ions through cell walls.

Resorcinarene **RA-6** was used for reducing silver ions: four hydrazide moieties in bridge fragments acted as reducer [109]. Resulting AgNPs (d = 5 ± 2 nm) have selectivity towards Cd^{2+}. Substitution of eight methoxy groups in **RA-6** with hydroxyl fragments in compound **RA-7** switched AgNPs selectivity [110]. **RA-7**-AgNPs (d = 15 ± 5 nm) selective to Pb^{2+} ions were obtained.

Selectivity towards metal ions was not only demonstrated for AgNPs resulting from reducing Ag^{+} with hydrazide derivatives of resorcinarenes. For example, AgNPs (7 ± 5 nm) were obtained using dodecahydrazide derivatives of resorcinarene **RA-8** as a reducing agent for $AgNO_3$. [111]. Obtained **RA-8** AgNPs are sensitive towards histidine in the concentration range of 10 nM–10 μM. **RA-8** AgNPs interact with DNA and show free radical scavenging activity.

Not only hydrazide derivatives of resorcinarene can be used for reducing silver salts. Ferrocene derivatives of resorcinarene **RA-9** form associates which are capable of reducing silver ions into AgNPs [112]. Also, presence of ferrocene fragments provides nanoparticles with catalytic activity in oxidizing *p*-aminophenol to *p*-nitrophenol. Obtained AgNPs have a diameter of 30 nm according to TEM. The thick shell of resorcinarene leads to differences among TEM-defined sizes, and the diameter was determined by AFM and DLS (~60 nm).

In summing up this section, while resorcinarenes have similar cavity shapes, the selectivity of resorcinarenes can be easily adjusted by varying upper rim substituents and bridge fragments. The tendency to form dimeric capsules in the presence of a substrate is extremely favorable for creating AgNPs-based colorimetric sensors. While a significant fraction of resorcinarene derivatives were used for direct synthesis of AgNPs from silver ions, this should not be regarded as a feature specific to resorcinarene derivatives, and most likely there are no obstacles to using similar strategies or similar substituents with other cyclophanes. The use of resorcinarene-based AgNPs mainly consists in the selective recognition of cations and biomolecules in an aqueous solution.

5. Supramolecular Self-Assembly of Pillar[n]arenes with Ag(I) Ions and Pillar[n]arene-Based AgNPs

Pillar[n]arenes are a relatively novel class of *para*-cyclophanes, which was first described in 2008 [113]. These macrocycles attract special interest of researchers due to possibility of creating unique supramolecular systems based on them [114]. Pillararenes have a number of attractive features, such as synthetic accessibility, planar chirality and a tube-shaped three-dimensional structure, which provides an electron-donor cavity and the possibility of stringing elongated acyclic and planar cyclic guest fragments. Due to these unique properties, developing novel functional organo-inorganic nanomaterials based on pillararenes is especially attractive [115]. The key feature of pillar[5]arenes compared to other cyclophanes is the combination of a wide range of synthetically accessible functional fragments inherent for calixarenes and resorcinarenes with the possibility of forming pseudo-rotaxanes, rotaxanes and poly-pseudo-rotaxanes [116,117]. The presence of metal ions in supramolecular architectures allows to adjust their properties and provides them with unique optical, magnetic and electric properties [118].

Therefore, substrate recognition in the case of pillararenes strongly depends on substrate geometry: a higher affinity is observed if the substrate fits inside the cavity of pillararene. While using aggregation-induced shift of the absorption band in substrate recognition is a common practice for creating selective AgNP-based sensors, in the case of pillararenes the pattern of interaction with

substrate can be in sharp contrast to other cyclophanes. For the other abovementioned cyclophanes ((thia)calixarenes, resorcinarenes), the substrate fits inside the cyclophane binding site or molecular cage formed by several cyclophane molecules (e.g., dimeric capsules of resorcinarenes). On the contrary, in the case of pillararene–AgNPs, interaction with substrate may effectively induce AgNPs aggregation even if only some of its fragments are "inserted" into pillar-shaped cavities of pillararenes (Table 1).

5.1. Self-Assembly of Pillar[n]arenes with Ag(I) Ions

There are some publications that report formation of pillararene-Ag^+ host–guest complexes [119]. Monosubstituted pillar[5]arene with a pyridine group **PA-1** (Figure 8) is capable of forming dimers in the presence of silver ions, forming supramolecular polymer in the presence of a homoditopic guest [120]. The polymer obtained can reversibly bind H_2S or I^- in chloroform. The authors suppose that the proposed material can be used for creating advanced sensor materials.

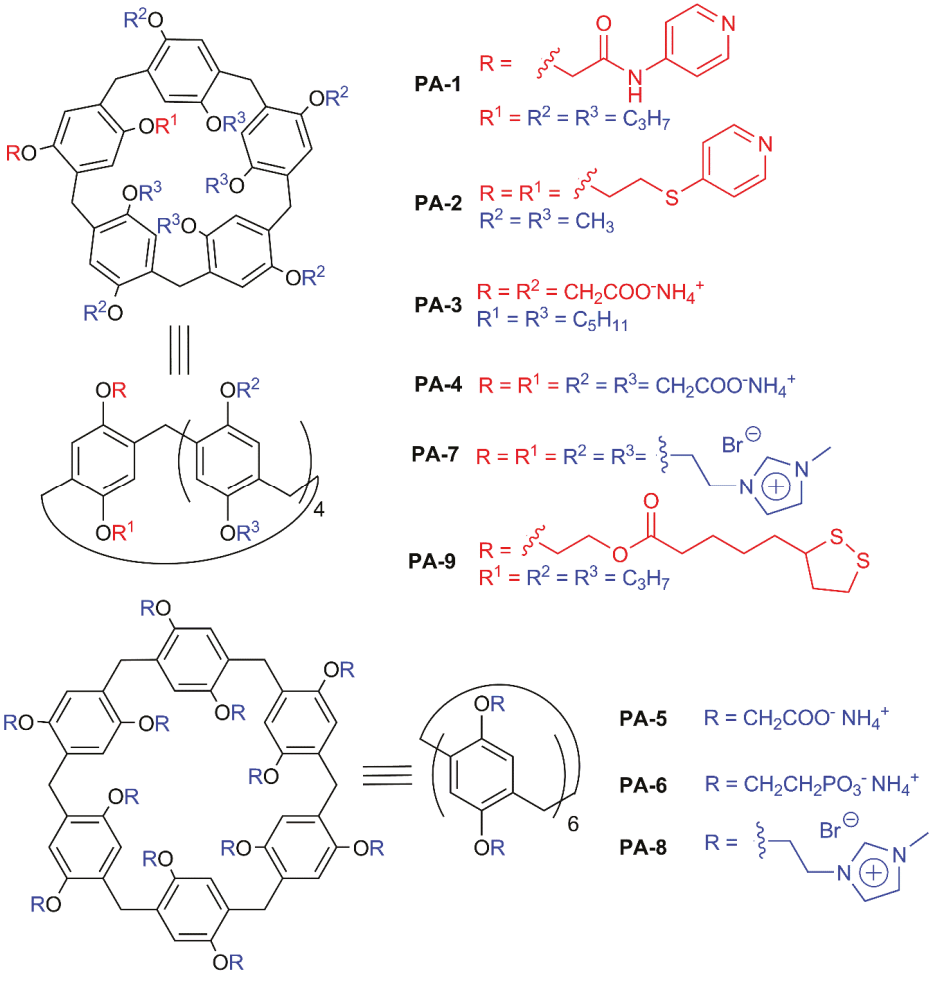

Figure 8. Structures of pillar[n]arenes.

1D-coordinated polymer based on disubstituted pillar[5]arene **PA-2** containing thiopyridyl moieties and silver cations was formed [121]. Upon addition of α,ω-dicyanoalkanes [$CN(CH_2)_nCN$,

n = 2–8] (Figure 9) to that supramolecular system, 1D and 2D poly-pseudo-rotaxanes are formed (Figure 10). The length of α,ω-dicyanoalkane significantly affects the structures of corresponding polypseudorotoxanes: 1D poly-pseudo-rotaxane is formed with $CN(CH_2)_2CN$ (**G1**). In the case of $CN(CH_2)_8CN$ (**G2**), 2D poly-pseudo-rotaxane is formed, in which the same guest is forming both threads and crosslinks. The authors report that results obtained allow to create poly-pseudo-rotaxane based inorganic/organic hybrid materials, incorporating macrocyclic components.

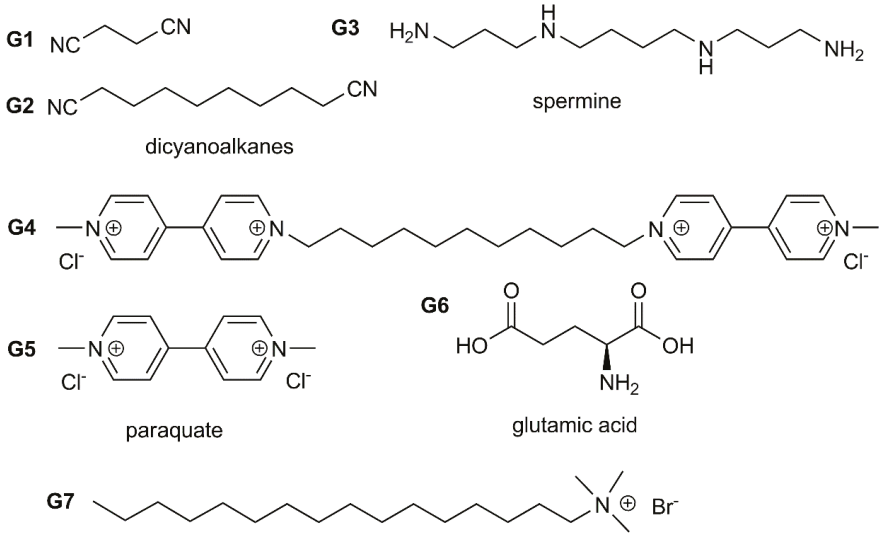

Figure 9. Structures of guest molecules for recognition using pillar[n]arene-based AgNPs.

Amphililic pillar[5]arene containing carboxylate charged fragments on one site of the macrocyclic rim and lipophilic pentyl groups **PA-3** does not form associates in water, but adding silver ions leads to dendrite structures [122]. Stoichiometry, structure, sizes and morphology of associates formed are studied by a complex of methods (DLS, TEM, SEM).

Unfortunately, there are few publications on the self-assembly of pillar[n]arenes and silver cations, perhaps due to the fact that pillararenes are a new class of *para*-cyclophanes. However, the possibility of pillararenes to form poly-pseudo-rotaxane structures with silver cations opens up prospects for the creation of new materials with unique physical properties.

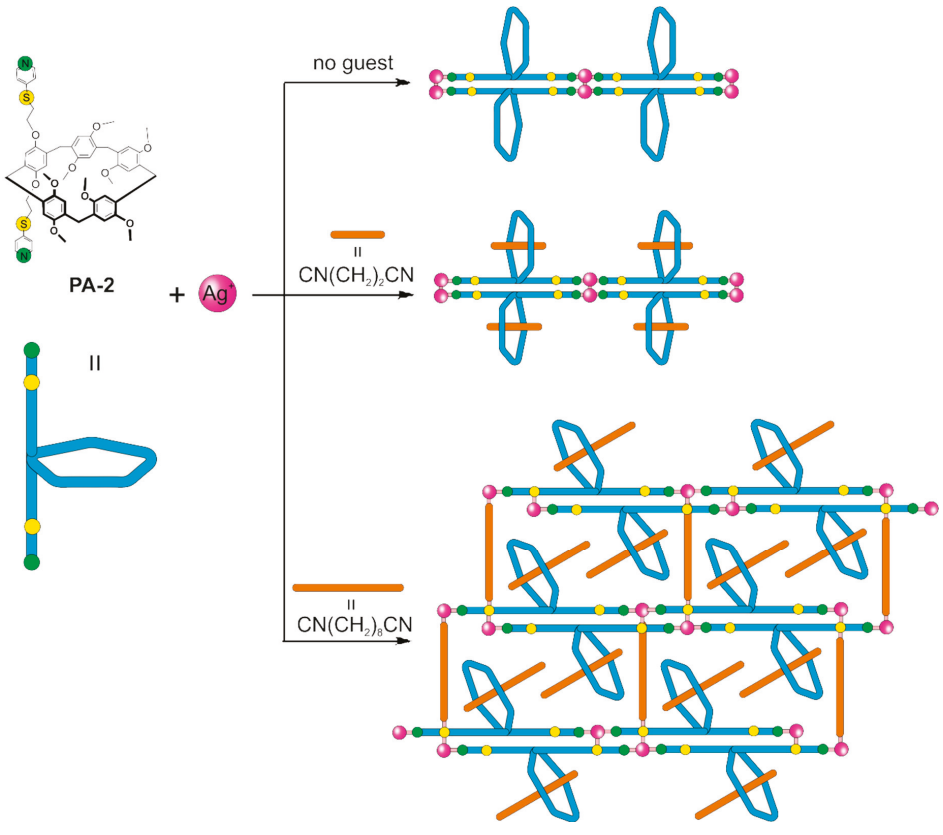

Figure 10. Cartoon representation of molecular architectures obtained by self-assembly of pillar[5]arene **PA-2**, silver ions and **G1** and **G2** guest molecules.

5.2. Synthesis and Application of Pillar[n]arene-Based AgNPs

Pillar[n]arene-modified AgNPs combine electronic, thermal and catalytic properties of metal nanoparticles with the ability of molecular recognition of various guests fitting into the pillararene cavity (Figure 9). The tendency to form complexes with substrates having long fragments fitting into the pillararene cavity was described above. In a fashion similar to individual pillararene molecules, if the substrate has several such fragments, formation of the complex results in aggregation of AgNPs.

In Prof. M. Xue's group, AgNPs modified by decacarboxylate pillararene **PA-4** and dodecacarboxylate pillar[6]arene **PA-5** were synthesized. Synthesis of AgNPs stabilized with a water-soluble derivative of pillar[5]arene **PA-4** with narrow size distribution (18.7 ± 2.18 nm) was reported [123]. Nanoparticles were obtained by reducing silver nitrate (10 mM) with $NaBH_4$ (50 mM) in the presence of varying concentrations of **PA-4**. Optimal concentration of **PA-4** (0.4 mM) was defined. Obtained nanoparticles were stable at high temperatures over long time periods. AgNPs interact with spermine **G3** and its structural analogues leading to aggregation-induced sedimentation. Pillararene **PA-4**-based AgNPs are capable of interacting with water-soluble guest molecules containing two paraquate fragments **G4** [124]. Adding of dodecacarboxylate **PA-5** leads to the concurrent process of guest binding with **PA-5,** which leads to disaggregation of **PA-4**-stabilized AgNPs. The authors show that disaggregated nanoparticles can be used repeatedly: centrifugation allows to separate **PA-4**-stabilized AgNPs and to redisperse them in water.

Further studies with decacarboxylate derivatives of **PA-4-**stabilized **AgNPs** are reported [125], and an electrochemical sensor has been developed, allowing detection of paraquate **G5** (PQ) herbicide (highly toxic for humans). In this work, **PA-4**-stabilized AgNPs were immobilized on graphene surface. Glassy carbon electrodes modified with hybrid material obtained demonstrate pronounced sensitivity towards PQ. They show good current response toward PQ, with limit of detection for PQ of 1.0×10^{-8} M. Such synergism is explained by complementarity of the pillar[5]arene cavity towards PQ.

A green and facile approach towards synthesis of small AgNPs (3–4 nm) on a single-walled carbon nanotube surface (SWCNT) modified with pillar[6]arene **PA-6** containing 12 phosphate groups was described [126]. Nanoparticles were obtained by adding aqueous solution of $AgNO_3$ (10.0 mM) to a dispersion of **PA-6**-SWCNT, following with slow addition of $NaBH_4$ (0.1 M). Obtained AgNPs show higher activity towards reduction of 4-nitrophenol and methylene blue degradation compared to analogous catalysts. Highly sensitive electrochemical sensors based on obtained nanoparticles for PQ detection has been developed. The authors report these results as a promising approach to create highly effective catalytic nanomaterials for organic dye degradation and detection of highly toxic herbicides.

The same research group obtained AgNPs functionalized with pillar[6]arene **PA-5** containing 12 carboxylate groups [127], which were cast on 2D covalent organic framework (COF) composite. The obtained hybrid material has high sensitivity towards PQ. Electrodes based on this material can detect 0.01–50 μM PQ with a detection limit of 0.014 μM.

AgNPs stabilized with water-soluble pillar[5]arene **PA-7** and pillar[6]arene **PA-8** containing 10 and 12 imidazolium fragments were obtained [128]. The concentration ratio of **PA-8** to $AgNO_3$ varied, the optimal ratio was [**PA-8**]/[$AgNO_3$] = 0.15, at which AgNPs size was 13.57 ± 2.18 nm. It was shown that **PA-8**-stabilized AgNPs can be used as colorimetric sensor for selective detection of glutamic acid **G6** in water (in a row of lysine, arginine, histidine, glycine, glutamic acid, tyrosine, aspartic acid and threonine). In the presence of glutamic acid, the colloid system color changes from yellow to red (detection limit = 2.8×10^{-6} M). It should be noted that the pillar[5]arene derivative **PA-7** does not show such selectivity. This work is a good illustration of the pillararene-specific pattern of substrate recognition: substrate (or its fragment) should "fit" in the pillararene cavity for selective and efficient recognition.

Silver nanoclusters were modified by monosubstituted pillar[5]arene **PA-9** with fragments of lipolic acid obtained both by straight synthesis in the presence of **PA-9** and by ligand exchange [129]. It was shown that they were stable at room temperature over a four-month period. Obtained nanoclusters interact with neutral (alkylamine) and charged quaternary ammonium (**G7)** guest molecules, which lead to the formation of spherical aggregates with unique optical properties. The authors report that while alkylamines produced a 30-fold photoluminescence enhancement, positively charged quaternary ammonium molecules induced an approximately 2000-fold photoluminescence enhancement that can be perceived by the naked eye.

For summing up the publications mentioned, it is interesting to compare pillararene-functionalized AgNPs to AgNPs modified with other cyclophanes, in contrast to (thia)calixarenes: complexation with guest molecule, to a larger extent, is guided by "fitting" guest molecule fragments into the macrocyclic cavity rather than by the nature and number of substituents. In contrast to resorcinarenes where substrates should usually fit into the cavity of dimeric capsules to induce AgNPs aggregation, for pillararenes it is enough to form inclusion complexes incorporating fragments of the substrate inside pillararene cavities. It would be intriguing to see multisensor systems based on these different patterns which would allow to effectively discern over a wide range of structurally related substrates. While AgNPs functionalized with resorcinarene derivatives would most likely bind those guest molecules which are best fit for dimeric capsules, pillararene-functionalized AgNPs would more effectively aggregate in the presence of guest molecules containing alkyl and aryl groups, fitting inside cavities of single pillararene molecules.

6. Conclusions

This review summarizes recent progress in self-assembly of cyclophanes with silver cations and in the design, synthesis and application of cyclophane-based silver nanoparticles until 2020. Various strategies are used to create silver nanoparticles such as modifying, functionalizing, templating, reducing and stabilizing. As mentioned in the above publications, the choice of functional groups of cyclophanes for modification of AgNPs is quite similar. On the other hand, each class of macrocycles (calix[n]arene, thiacalix[4]arene, resorcin[4]arene, pillar[n]arene) offers unique patterns of interacting with the substrate. For example, significant differences in organic substrates that are recognized by resorcinarene-modified AgNPs and pillararene-modified AgNPs are observed. Thiacalixarenes prove promising for Ag nanocluster stabilization and for creating supramolecular ensembles with silver ions, which encourages their use in supramolecular templating of AgNPs formed by reduction.

The obtained nanoparticles are used for recognition of various biomolecules in aqueous media, namely amino acids, hydroxyl acids, proteins and nucleic acids. Based on cyclophane-capped silver nanoparticles, electrochemical and colorimetric sensors were created for the selective determination of heavy metal cations (Cu^{2+}, Fe^{3+}, Hg^{2+}, Cd^{2+}, Pb^{2+}), anions ($H_2PO_4^-$, I^-), amino acids (histidine, aspartic acid, tryptophan, glutamic acid), polycyclic aromatic hydrocarbons and pesticides. Therefore, we can conclude that over the last years cyclophanes have opened new and interesting opportunities for selective substrate recognition (based on unique patterns of substrate-induced aggregation). Depending on substrate structure, cyclophane type and functionality can be successfully devised. While it was shown that silver nanoparticles can be successfully prepared in the presence of any cyclophane mentioned above, it is still intriguing to study the relation between silver ion aggregation with cyclophane and the sizes of AgNPs formed. Unfortunately, this field is still waiting to bloom.

It is certain that cyclophane-based silver nanoparticles will find application in many areas of life. Cyclophane-functionalized AgNPs have proven promising for medicine and diagnostic fields. The tendency of cyclophanes to form supramolecular assemblies with various substrates allows using them in constructing AgNP-based colorimetric sensors due to substrate-induced nanoparticle aggregation. Depending on the macrocyclic platform and functionalization, cyclophanes are selective to a wide range of substrates. This possibility of adjusting association behavior ranges from small inorganic and organic substrates, and allows creating AgNPs with adjustable cytotoxicity towards different bacteria. A different pattern is implemented in electrochemical sensors: differences in affinity towards substrates allow achieving a selective response towards small-sized substrates. The use of cyclophanes for silver nanocluster stabilization is emerging. Also, there are future prospects for use of cyclophane–silver ion assemblies as templates for Ag(0) nanomaterial designs due to manifold morphologies of associates formed with silver ions. It can be concluded that, in the nearest future, cyclophane-modified AgNPs and silver nanomaterials will find applications in nanoelectronics.

Author Contributions: Conceptualization, writing—review and editing, supervision, I.S.; investigation, writing—original draft preparation, P.P. and V.G.; funding acquisition, project administration, P.P. All authors have read and agreed to the published version of the manuscript.

Funding: We gratefully acknowledge the support for this paper by the Russian Science Foundation grant (No. 19-73-10134).

Conflicts of Interest: The authors declare no conflicts of interest. The funders had no role in the design of the study; in the collection, analyses, or interpretation of data; in the writing of the manuscript, or in the decision to publish the results.

Abbreviations

AgNPs	Silver nanoparticles
CA	Calixarene
TCA	Thiacalixarene
PA	Pillararene
RA	Resorcinarene
TEM	Transmission electron microscopy

API	Active pharmaceutical ingredient
PAHs	Polycyclic aromatic hydrocarbons
SERS	Surface-enhanced Raman scattering
DLS	Dynamic light scattering
D-FAA	N-Fmoc-D-aspartic acid
L-FAA	N-Fmoc-L-aspartic acid
ppb	Parts per billion
AFM	Atomic force microscopy
BSA	Bovine serum albumin
DMF	Dimethylformamide
DNA	Deoxyribonucleic acid
SEM	Scanning electron microscopy
PQ	Paraquat
SWCNT	Single-walled carbon nanotube
COF	Covalent organic framework
MOF	Metal–organic framework

References

1. Sabela, M.; Balme, S.; Bechelany, M.; Janot, J.M.; Bisetty, K. A review of gold and silver nanoparticle-based colorimetric sensing assays. *Adv. Eng. Mater.* **2017**, *19*, 1700270. [CrossRef]
2. Chandraker, K.; Nagwanshi, R.; Jadhav, S.K.; Ghosh, K.K.; Satnami, M.L. Antibacterial properties of amino acid functionalized silver nanoparticles decorated on graphene oxide sheets. *Spectrochim. Acta Part A Mol. Biomol. Spectrosc.* **2017**, *181*, 47–54. [CrossRef] [PubMed]
3. Malekzad, H.; Zangabad, P.S.; Mirshekari, H.; Karimi, M.; Hamblin, M.R. Noble metal nanoparticles in biosensors: Recent studies and applications. *Nanotechnol. Rev.* **2017**, *6*, 301–329. [CrossRef] [PubMed]
4. Montes-García, V.; Pérez-Juste, J.; Pastoriza-Santos, I.; Liz-Marzán, L.M. Metal nanoparticles and supramolecular macrocycles: A tale of synergy. *Chem. A Eur. J.* **2014**, *20*, 10874–10883. [CrossRef] [PubMed]
5. Wong, K.K.; Liu, X. Silver nanoparticles—The real "silver bullet" in clinical medicine? *MedChemComm* **2010**, *1*, 125–131. [CrossRef]
6. Burdușel, A.C.; Gherasim, O.; Grumezescu, A.M.; Mogoantă, L.; Ficai, A.; Andronescu, E. Biomedical applications of silver nanoparticles: An up-to-date overview. *Nanomaterials* **2018**, *8*, 681. [CrossRef]
7. Hamouda, R.A.; Hussein, M.H.; Abo-elmagd, R.A.; Bawazir, S.S. Synthesis and biological characterization of silver nanoparticles derived from the cyanobacterium Oscillatoria limnetica. *Sci. Rep.* **2019**, *9*, 1–17. [CrossRef]
8. Lee, S.H.; Jun, B.H. Silver Nanoparticles: Synthesis and application for nanomedicine. *Int. J. Mol. Sci.* **2019**, *20*, 865. [CrossRef]
9. Rasheed, T.; Bilal, M.; Li, C.; Nabeel, F.; Khalid, M.; Iqbal, H.M. Catalytic potential of bio-synthesized silver nanoparticles using Convolvulus arvensis extract for the degradation of environmental pollutants. *J. Photochem. Photobiol. B Biol.* **2018**, *181*, 44–52. [CrossRef]
10. Zhang, X.F.; Liu, Z.G.; Shen, W.; Gurunathan, S. Silver nanoparticles: Synthesis, characterization, properties, applications, and therapeutic approaches. *Int. J. Mol. Sci.* **2016**, *17*, 1534. [CrossRef]
11. Hussain, M.; Nafady, A.; Avcı, A.; Pehlivan, E.; Nisar, J.; Sherazi, S.T.H.; Balouch, A.; Shah, M.R.; Almaghrabi, O.A.; Ul-Haq, M.A. Biogenic silver nanoparticles for trace colorimetric sensing of enzyme disrupter fungicide vinclozolin. *Nanomaterials* **2019**, *9*, 1604. [CrossRef] [PubMed]
12. Kailasa, S.K.; Singhal, R.K.; Basu, H.; Park, T.J. Surface-modified metal nanoparticles for recognition of toxic organic molecules. In *Handbook of Nanomaterials in Analytical Chemistry*; Elsevier: London, UK, 2020; pp. 415–432. [CrossRef]
13. Wu, Z.; Song, N.; Menz, R.; Pingali, B.; Yang, Y.W.; Zheng, Y. Nanoparticles functionalized with supramolecular host–guest systems for nanomedicine and healthcare. *Nanomedicine* **2015**, *10*, 1493–1514. [CrossRef]
14. Akiba, U.; Minaki, D.; Anzai, J.I. Host-guest chemistry in layer-by-layer assemblies containing calix[n]arenes and cucurbit[n]urils: A review. *Polymers* **2018**, *10*, 130. [CrossRef] [PubMed]
15. Kongor, A.R.; Mehta, V.A.; Modi, K.M.; Panchal, M.K.; Dey, S.A.; Panchal, U.S.; Jain, V.K. Calix-based nanoparticles: A review. *Top. Curr. Chem.* **2016**, *374*, 28. [CrossRef] [PubMed]
16. Sanabria Español, E.; Maldonado, M. Host–guest recognition of pesticides by calixarenes. *Crit. Rev. Anal. Chem.* **2019**, *49*, 383–394. [CrossRef] [PubMed]

17. Padnya, P.L.; Andreyko, E.A.; Mostovaya, O.A.; Rizvanov, I.K.; Stoikov, I.I. The synthesis of new amphiphilic *p-tert*-butylthiacalix[4]arenes containing peptide fragments and their interaction with DNA. *Organ. Biomol. Chem.* **2015**, *13*, 5894–5904. [CrossRef] [PubMed]
18. Yakimova, L.; Padnya, P.; Tereshina, D.; Kunafina, A.; Nugmanova, A.; Osin, Y.; Evtugyn, V.; Stoikov, I. Interpolyelectrolyte mixed nanoparticles from anionic and cationic thiacalix[4]arenes for selective recognition of model biopolymers. *J. Mol. Liq.* **2019**, *279*, 9–17. [CrossRef]
19. Mostovaya, O.A.; Gorbachuk, V.V.; Bazanova, O.B.; Gerasimov, A.V.; Evtugyn, V.G.; Osin, Y.N.; Myakushev, V.D.; Rizvanov IKh Stoikov, I.I. Thiacalixarene "knot" effect on protein binding by oligolactic acid particles. *Mater. Chem. Front.* **2019**, *3*, 292–300. [CrossRef]
20. Shu, X.; Xu, K.; Hou, D.; Li, C. Molecular Recognition of Water-soluble pillar[n]arenes towards biomolecules and drugs. *Isr. J. Chem.* **2018**, *58*, 1230–1240. [CrossRef]
21. Español, E.S.; Villamil, M.M. Calixarenes: Generalities and their role in improving the solubility, biocompatibility, stability, bioavailability, detection, and transport of biomolecules. *Biomolecules* **2019**, *9*, 90. [CrossRef]
22. Späth, A.; König, B. Molecular recognition of organic ammonium ions in solution using synthetic receptors. *Beilstein J. Org. Chem.* **2010**, *6*, 32. [CrossRef] [PubMed]
23. Li, Z.; Li, X.; Yang, Y.W. Photoactive nanoparticles capped with macrocycles as platforms and hosts. In *Photoactive Inorganic Nanoparticles*; Elsevier: London, UK, 2019; pp. 139–167. [CrossRef]
24. Kim, H.J.; Lee, M.H.; Mutihac, L.; Vicens, J.; Kim, J.S. Host–guest sensing by calixarenes on the surfaces. *Chem. Soc. Rev.* **2012**, *41*, 1173–1190. [CrossRef]
25. Cho, E.J.; Kang, J.K.; Han, W.S.; Jung, J.H. Stimuli-responsive supramolecular nanostructure from amphiphilic calix[4]arene and its three-dimensional dendritic silver nanostructure. *Langmuir* **2008**, *24*, 5229–5232. [CrossRef] [PubMed]
26. Kinge, S.; Crego-Calama, M.; Reinhoudt, D. Silver nanoparticles from hydrogen-bonded supramolecular scaffolds. *New J. Chem.* **2008**, *32*, 2071–2073. [CrossRef]
27. Houmadi, S.; Coquiere, D.; Legrand, L.; Faure, M.C.; Goldmann, M.; Reinaud, O.; Remita, S. Architecture-controlled "SMART" calix[6]arene self-assemblies in aqueous solution. *Langmuir* **2007**, *23*, 4849–4855. [CrossRef] [PubMed]
28. Li, J.; Zhang, S.; Chen, Y.G.; Du, X.; Yu, H.; Yu, J. Supramolecular compounds with coordination polymeric chains of Ag ions, *p*-sulfonatocalix[4]arene and ethylenediamine. *J. Incl. Phenom. Macrocycl. Chem.* **2015**, *81*, 485–491. [CrossRef]
29. Park, K.M.; Lee, E.; Park, C.S.; Lee, S.S. Tube-type coordination polymers: Two-and four-silver (i)-mediated linear networking of calix[4]arene tetracarboxylates. *Inorg. Chem.* **2011**, *50*, 12085–12090. [CrossRef]
30. Shi, Q.; Luo, W.Z.; Li, B.; Xie, Y.P.; Zhang, T. Versatile architectures of silver (i) organometallic polymers with tetra-allyl functionalized calix[4]arene fine-tuned by distinct Anions. *Cryst. Growth Des.* **2015**, *16*, 493–498. [CrossRef]
31. Liu, L.L.; Chen, J.; Yu, C.X.; Lv, W.X.; Yu, H.Y.; Cui, X.Q.; Liu, L. A novel Ag (I)-calix[4]arene coordination polymer for the sensitive detection and efficient photodegradation of nitrobenzene in aqueous solution. *Dalton Trans.* **2017**, *46*, 178–185. [CrossRef]
32. Zheng, G.L.; Li, Y.Y.; Deng, R.P.; Song, S.Y.; Zhang, H.J. Self-assembly of guest-induced calix[4]arene nanocapsules into three-dimensional molecular architecture. *CrystEngComm* **2008**, *10*, 658–660. [CrossRef]
33. Tauran, Y.; Kim, B.; Coleman, A.W. Bio-applications of calix[n]arene capped silver nanoparticles. *J. Nanosci. Nanotechnol.* **2015**, *15*, 6308–6326. [CrossRef]
34. Tauran, Y.; Brioude, A.; Shahgaldian, P.; Cumbo, A.; Kim, B.; Perret, F.; Coleman, A.W.; Montasser, I. Calix-arene silver nanoparticles interactions with surfactants are charge, size and critical micellar concentration dependent. *Chem. Commun.* **2012**, *48*, 9483–9485. [CrossRef] [PubMed]
35. Stephens, E.K.; Tauran, Y.; Coleman, A.W.; Fitzgerald, M. Structural requirements for anti-oxidant activity of calix [n] arenes and their associated anti-bacterial activity. *Chem. Commun.* **2015**, *51*, 851–854. [CrossRef] [PubMed]
36. Boudebbouze, S.; Coleman, A.W.; Tauran, Y.; Mkaouar, H.; Perret, F.; Garnier, A.; Brioude, A.; Kim, B.; Maguin, E.; Rhimi, M. Discriminatory antibacterial effects of calix[n]arene capped silver nanoparticles with regard to Gram positive and Gram negative bacteria. *Chem. Commun.* **2013**, *49*, 7150–7152. [CrossRef] [PubMed]

37. Tauran, Y.; Grosso, M.; Brioude, A.; Kassab, R.; Coleman, A.W. Colourimetric and spectroscopic discrimination between nucleotides and nucleosides using *para*-sulfonato-calix[4]arene capped silver nanoparticles. *Chem. Commun.* **2011**, *47*, 10013–10015. [CrossRef]
38. Tauran, Y.; Rhimi, M.; Ueno, R.; Grosso, M.; Brioude, A.; Janneau, E.; Suwinska, K.; Kassab, R.; Shahgaldian, P.; Cumbo, A.; et al. Cytosine: Para-sulphonato-calix[4]arene assemblies: In solution, in the solid-state and on the surface of hybrid silver nanoparticles. *J. Incl. Phenom. Macrocycl. Chem.* **2013**, *77*, 213–221. [CrossRef]
39. Chen, M.; Ding, W.; Kong, Y.; Diao, G. Conversion of the surface property of oleic acid stabilized silver nanoparticles from hydrophobic to hydrophilic based on host−guest binding interaction. *Langmuir* **2008**, *24*, 3471–3478. [CrossRef]
40. Xiong, D.; Chen, M.; Li, H. Synthesis of *para*-sulfonatocalix[4]arene-modified silver nanoparticles as colorimetric histidine probes. *Chem. Commun.* **2008**, *7*, 880–882. [CrossRef]
41. Abe, N.; Iki, N. Multi-coloration of calixarene-coated silver nanoparticles for the visual discrimination of metal elements. *Anal. Sci.* **2017**, *33*, 1141–1145. [CrossRef]
42. Xiong, D.; Li, H. Colorimetric detection of pesticides based on calixarene modified silver nanoparticles in water. *Nanotechnology* **2008**, *19*, 465502. [CrossRef]
43. Hu, R.; Long, G.; Chen, J.; Yin, Y.; Liu, Y.; Zhu, F.; Feng, J.; Mei, Y.; Wang, R.; Xue, H.; et al. Highly sensitive colorimetric sensor for the detection of $H_2PO_4^-$ based on self-assembly of *p*-sulfonatocalix[6]arene modified silver nanoparticles. *Sens. Actuators B Chem.* **2015**, *218*, 191–195. [CrossRef]
44. Kellici, S.; Acord, J.; Vaughn, A.; Power, N.P.; Morgan, D.J.; Heil, T.; Facq, S.P.; Lampronti, G.I. Calixarene assisted rapid synthesis of silver-graphene nanocomposites with enhanced antibacterial activity. *ACS Appl. Mater. Interfaces* **2016**, *8*, 19038–19046. [CrossRef] [PubMed]
45. Akermi, N.; Mkaouar, H.; Kriaa, A.; Jablaoui, A.; Soussou, S.; Gargouri, A.; Coleman, A.W.; Perret, F.; Maguin, E.; Rhimi, M. *para*-Sulphonato-calix[n]arene capped silver nanoparticles challenge the catalytic efficiency and the stability of a novel human gut serine protease inhibitor. *Chem. Commun.* **2019**, *55*, 8935–8938. [CrossRef] [PubMed]
46. Perret, F.; Tauran, Y.; Suwinska, K.; Kim, B.; Chassain-Nely, C.; Boulet, M.; Coleman, A.W. Molecular recognition and transport of active pharmaceutical ingredients on anionic calix[4]arene-capped silver nanoparticles. *J. Chem.* **2012**, *2013*, 1–9. [CrossRef]
47. Tauran, Y.; Brioude, A.; Kim, B.; Perret, F.; Coleman, A. Anionic calixarene-capped silver nanoparticles show species-dependent binding to serum albumins. *Molecules* **2013**, *18*, 5993–6007. [CrossRef]
48. Hartlieb, K.J.; Saunders, M.; Raston, C.L. Templating silver nanoparticle growth using phosphonated calixarenes. *Chem. Commun.* **2009**, *21*, 3074–3076. [CrossRef]
49. Tauran, Y.; Brioude, A.; Coleman, A.W.; Rhimi, M.; Kim, B. Molecular recognition by gold, silver and copper nanoparticles. *World J. Biol. Chem.* **2013**, *4*, 35. [CrossRef]
50. Leyton, P.; Sanchez-Cortes, S.; Garcia-Ramos, J.V.; Domingo, C.; Campos-Vallette, M.; Saitz, C.; Clavijo, R.E. Selective molecular recognition of polycyclic aromatic hydrocarbons (PAHs) on calix [4] arene-functionalized Ag nanoparticles by surface-enhanced Raman scattering. *J. Phys. Chem. B* **2004**, *108*, 17484–17490. [CrossRef]
51. Guerrini, L.; Garcia-Ramos, J.V.; Domingo, C.; Sanchez-Cortes, S. Functionalization of Ag nanoparticles with dithiocarbamate calix [4] arene as an effective supramolecular host for the surface-enhanced Raman scattering detection of polycyclic aromatic hydrocarbons. *Langmuir* **2006**, *22*, 10924–10926. [CrossRef]
52. Guerrini, L.; Garcia-Ramos, J.V.; Domingo, C.; Sanchez-Cortes, S. Self-assembly of a dithiocarbamate calix[4]arene on Ag nanoparticles and its application in the fabrication of surface-enhanced Raman scattering based nanosensors. *Phys. Chem. Chem. Phys.* **2009**, *11*, 1787–1793. [CrossRef]
53. Guerrini, L.; Garcia-Ramos, J.V.; Domingo, C.; Sanchez-Cortes, S. Sensing polycyclic aromatic hydrocarbons with dithiocarbamate-functionalized Ag nanoparticles by surface-enhanced Raman scattering. *Anal. Chem.* **2009**, *81*, 953–960. [CrossRef] [PubMed]
54. Brown, P.O.; Enright, G.D.; Ripmeester, J.A. Nanocrystalline Ag from supramolecular stabilization of metals in 4-tert-butylcalix[4]arene lattices. *Chem. Asian J.* **2006**, *1*, 529–535. [CrossRef] [PubMed]
55. Mehra, C.; Gala, R.; Kakatkar, A.; Kumar, V.; Khurana, R.; Chatterjee, S.; Kumar, N.N.; Barooah, N.; Bhasikuttan, A.C.; Mohanty, J. Cooperative enhancement of antibacterial activity of sanguinarine drug through p-sulfonatocalix[6]arene functionalized silver nanoparticles. *Chem. Commun.* **2019**, *55*, 14275–14278. [CrossRef] [PubMed]

56. Nsengiyuma, G.; Hu, R.; Li, J.; Li, H.; Tian, D. Self-assembly of 1,3-alternate calix[4]arene carboxyl acids-modified silver nanoparticles for colorimetric Cu^{2+} sensing. *Sens. Actuators B Chem.* **2016**, *236*, 675–681. [CrossRef]
57. Pandya, A.; Sutariya, P.G.; Lodha, A.; Menon, S.K. A novel calix[4]arene thiol functionalized silver nanoprobe for selective recognition of ferric ion with nanomolar sensitivity via DLS selectivity in human biological fluid. *Nanoscale* **2013**, *5*, 2364–2371. [CrossRef] [PubMed]
58. Vita, F.; Boccia, A.; Marrani, A.G.; Zanoni, R.; Rossi, F.; Arduini, A.; Secchi, A. Calix[4]arene-functionalised silver nanoparticles as hosts for pyridinium-loaded gold nanoparticles as guests. *Chem. A Eur. J.* **2015**, *21*, 15428–15438. [CrossRef]
59. Sun, Y.; Zhao, H.; Boussouar, I.; Zhang, F.; Tian, D.; Li, H. Highly sensitive chiral sensing by calix[4]arene-modified silver nanoparticles via dynamic light scattering. *Sens. Actuators B Chem.* **2015**, *216*, 235–239. [CrossRef]
60. Zhan, J.; Wen, L.; Miao, F.; Tian, D.; Zhu, X.; Li, H. Synthesis of a pyridyl-appended calix[4]arene and its application to the modification of silver nanoparticles as an Fe^{3+} colorimetric sensor. *New J. Chem.* **2012**, *36*, 656–661. [CrossRef]
61. Vyas, G.; Bhatt, S.; Paul, P. Synthesis of calixarene-capped silver nanoparticles for colorimetric and amperometric detection of mercury (Hg^{II}, Hg^{0}). *ACS Omega* **2019**, *4*, 3860–3870. [CrossRef]
62. Hartlieb, K.J.; Martin, A.D.; Saunders, M.; Raston, C.L. Photochemical generation of small silver nanoparticles involving multi-functional phosphonated calixarenes. *New J. Chem.* **2010**, *34*, 1834–1837. [CrossRef]
63. Ray, P.; Clément, M.; Martini, C.; Abdellah, I.; Beaunier, P.; Rodriguez-Lopez, J.L.; Huc, V.; Remita, H.; Lampre, I. Stabilisation of small mono-and bimetallic gold–silver nanoparticles using calix[8]arene derivatives. *New J. Chem.* **2018**, *42*, 14128–14137. [CrossRef]
64. Bian, Y.; Li, C.; Li, H. *para*-Sulfonatocalix[6]arene-modified silver nanoparticles electrodeposited on glassy carbon electrode: Preparation and electrochemical sensing of methyl parathion. *Talanta* **2010**, *81*, 1028–1033. [CrossRef] [PubMed]
65. Baghayeri, M.; Namadchian, M.; Karimi-Maleh, H.; Beitollahi, H. Determination of nifedipine using nanostructured electrochemical sensor based on simple synthesis of Ag nanoparticles at the surface of glassy carbon electrode: Application to the analysis of some real samples. *J. Electroanal. Chem.* **2013**, *697*, 53–59. [CrossRef]
66. Ahmadi, F.; Raoof, J.B.; Ojani, R.; Baghayeri, M.; Lakouraj, M.M.; Tashakkorian, H. Synthesis of Ag nanoparticles for the electrochemical detection of anticancer drug flutamide. *Chin. J. Catal.* **2015**, *36*, 439–445. [CrossRef]
67. Raoof, J.B.; Ojani, R.; Hasheminejad, E.; Rashid-Nadimi, S. Electrochemical synthesis of Ag nanoparticles supported on glassy carbon electrode by means of p-isopropyl calix[6]arene matrix and its application for electrocatalytic reduction of H_2O_2. *Appl. Surf. Sci.* **2012**, *258*, 2788–2795. [CrossRef]
68. Zhou, R.; Teo, S.; Srinivasan, M.P. In situ formation of silver nanoparticle layer by supramolecule-directed assembly. *Thin Solid Films* **2014**, *550*, 210–219. [CrossRef]
69. Zhou, R.; Srinivasan, M.P. Photocatalysis in a packed bed: Degradation of organic dyes by immobilized silver nanoparticles. *J. Environ. Chem. Eng.* **2015**, *3*, 609–616. [CrossRef]
70. Tian, H.W.; Liu, Y.C.; Guo, D.S. Assembling features of calixarene-based amphiphiles and supra-amphiphiles. *Mater. Chem. Front.* **2020**, *4*, 46–98. [CrossRef]
71. Mostovaya, O.A.; Gorbachuk, V.V.; Padnya, P.L.; Vavilova, A.A.; Evtugyn, G.A.; Stoikov, I.I. Modification of Oligo-and Polylactides With Macrocyclic Fragments: Synthesis and Properties. *Front. Chem.* **2019**, *7*, 554. [CrossRef]
72. Bi, Y.; Du, S.; Liao, W. Thiacalixarene-based nanoscale polyhedral coordination cages. *Coord. Chem. Rev.* **2014**, *276*, 61–72. [CrossRef]
73. Kozlova, M.N.; Ferlay, S.; Solovieva, S.E.; Antipin, I.S.; Konovalov, A.I.; Kyritsakas, N.; Hosseini, M.W. Molecular tectonics: On the formation of 1-D silver coordination networks by thiacalixarenes bearing nitrile groups. *Dalton Trans.* **2007**, *44*, 5126–5131. [CrossRef] [PubMed]
74. Bourlier, J.; Hosseini, M.W.; Planeix, J.M.; Kyritsakas, N. Molecular tectonics: Generation of 1-D interdigitated and 2-D interwoven helical silver coordination networks by oligoethylene glycol based tectons bearing two benzonitrile moieties. *New J. Chem.* **2007**, *31*, 25–32. [CrossRef]

75. Kozlova, M.N.; Ferlay, S.; Kyritsakas, N.; Hosseini, M.W.; Solovieva, S.E.; Antipin, I.S.; Konovalov, A.I. Molecular tectonics: 3-D organisation of decanuclear silver nanoclusters. *Chem. Commun.* **2009**, *18*, 2514–2516. [CrossRef] [PubMed]
76. Ovsyannikov, A.; Lang, M.N.; Ferlay, S.; Solovieva, S.E.; Antipin, I.S.; Konovalov, A.I.; Kyritsakas, N.; Hosseini, M.W. Molecular tectonics: Pyridyl containing thiacalix[4]arene based tectons for the generation of 2-and 3-D silver coordination networks. *Dalton Trans.* **2013**, *42*, 116–126. [CrossRef]
77. Ovsyannikov, A.; Ferlay, S.; Solovieva, S.E.; Antipin, I.S.; Konovalov, A.I.; Kyritsakas, N.; Hosseini, M.W. Molecular tectonics: Anion control of dimensionality and connectivity in meta-pyridyl appended tetramercaptotetrathiacalix[4]arene based silver coordination networks. *Dalton Trans.* **2014**, *43*, 158–165. [CrossRef]
78. Hosseini, M.W. Molecular tectonics an approach to crystal enginee. In *Applications of Supramolecular Chemistry*; Taylor & Francis Group: London, UK, 2012; pp. 231–254. [CrossRef]
79. Ovsyannikov, A.S.; Epifanova, N.A.; Popova, E.V.; Kyritsakas, N.; Ferlay, S.; Hosseini, M.W.; Latypov, S.h.K.; Solovieva, S.E.; Konovalov, A.I. Template synthesis of tetrakis-triazolylthiacalix[4]arene in the cone conformation and supramolecular structure of its hexanuclear complex with Ag (I). *Macroheterocycles* **2014**, *7*, 189–195. [CrossRef]
80. Ovsyannikov, A.S.; Ferlay, S.; Solovieva, S.E.; Antipin, I.S.; Konovalov, A.I.; Kyritsakas, N.; Hosseini, M.W. Molecular tectonics: Silver coordination networks based on tetramercaptothiacalix[4]arene in 1,3-alternate conformation bearing four nitrile groups. *Russ. Chem. Bull.* **2015**, *64*, 1955–1962. [CrossRef]
81. Ovsyannikov, A.S.; Noamane, M.H.; Abidi, R.; Ferlay, S.; Solovieva, S.E.; Antipin, I.S.; Konovalov, A.I.; Kyritsakas Hosseini, M.W. Molecular tectonics: Dimensionality and geometry control of silver coordination networks based on pyrazolyl appended thiacalixarenes. *CrystEngComm* **2016**, *18*, 691–703. [CrossRef]
82. Noamane, M.H.; Ferlay, S.; Abidi, R.; Kyritsakas, N.; Hosseini, M.W. Discrete di-and tetranuclear silver complexes based on ortho-imino-or ortho-amino-methylpyridyl-appended p-tert-butylcalix [4] arene or *p-tert*-butylthiacalix[4]arene in 1,3-alternate conformation. *Eur. J. Inorg. Chem.* **2017**, *2017*, 3327–3336. [CrossRef]
83. Sýkora, J.; Himl, M.; Stibor, I.; Císařová, I.; Lhoták, P. Unique self-assembly patterns based on thiacalix[4]arene–silver interactions. *Tetrahedron* **2007**, *63*, 2244–2248. [CrossRef]
84. Evtugyn, G.A.; Stoikov, I.I.; Beljyakova, S.V.; Shamagsumova, R.V.; Stoikova, E.E.; Zhukov, A.Y.; Antipin, I.S.; Budnikov, H.C. Ag selective electrode based on glassy carbon electrode covered with polyaniline and thiacalix[4]arene as neutral carrier. *Talanta* **2007**, *71*, 1720–1727. [CrossRef] [PubMed]
85. Galitskaya, P.; Fomin, V.; Stoikov, I.; Andreyko, E.; Selivanovskaya, S. Antimicrobial activity of nanoparticles fromsolid phase supramolecular assembliesbased on stereoisomers of *p-tert*-butylthiacalix[4]arene with silver cations. *Int. J. Pharm. Technol.* **2016**, *8*, 15048–15053.
86. Yakimova, L.S.; Gilmanova, L.H.; Evtugyn, V.G.; Osin, Y.N.; Stoikov, I.I. Self-assembled fractal hybrid dendrites from water-soluble anionic (thia)calix[4]arenes and Ag^{+}. *J. Nanoparticle Res.* **2017**, *19*, 173. [CrossRef]
87. Stoikov, I.I.; Yushkova, E.A.; Bukharaev, A.A.; Biziaev, D.A.; Selivanovskaya, S.Y.; Chursina, M.A.; Antipin, I.S.; Konovalov, A.I.; Zharov, I. Self-assembly of *p-tert*-butylthiacalix[4]arenes and metal cations into nanoscale three-dimensional particles. *J. Phys. Org. Chem.* **2012**, *25*, 1177–1185. [CrossRef]
88. Yushkova, E.A.; Stoikov, I.I.; Zhukov, A.Y.; Puplampu, J.B.; Rizvanov, I.K.; Antipin, I.S.; Konovalov, A. Heteroditopic *p-tert*-butylthiacalix[4]arenes for creating supramolecular self-assembles by cascade or commutative mechanisms. *RSC Adv.* **2012**, *2*, 3906–3919. [CrossRef]
89. Andreyko, E.A.; Puplampu, J.B.; Ignacio-De Leon, P.A.; Zharov, I.; Stoikov, I.I. *p-tert*-Butylthiacalix[4]arenes containing guanidinium groups: Synthesis and self-assembly into nanoscale aggregates. *Supramol. Chem.* **2019**, *31*, 473–483. [CrossRef]
90. Yakimova, L.S.; Padnya, P.L.; Kunafina, A.F.; Nugmanova, A.R.; Stoikov, I.I. Sulfobetaine derivatives of thiacalix[4]arene: Synthesis and supramolecular self-assembly of submicron aggregates with Ag^{I} cations. *Mendeleev Commun.* **2019**, *29*, 86–88. [CrossRef]
91. Andreyko, E.A.; Padnya, P.L.; Stoikov, I.I. Supramolecular self-assembly of water-soluble nanoparticles based on amphiphilic *p-tert*-butylthiacalix[4]arenes with silver nitrate and fluorescein. *Colloids Surf. A Physicochem. Eng. Asp.* **2014**, *454*, 74–83. [CrossRef]

92. Stoikov, I.I.; Yushkova, E.A.; Antipin, I.S.; Konovalov, A.I. Synthesis of silver and lithium sub-micro-and nanoparticles coated with derivatives of *p-tert*-butylthiacalix[4]arenes. *J. Nanoparticle Res.* **2011**, *13*, 6603–6611. [CrossRef]
93. Darjee, S.M.; Bhatt, K.D.; Panchal, U.S.; Jain, V.K. Scrupulous recognition of biologically important acids by fluorescent "turn off-on" mechanism of thaicalix reduced silver nanoparticles. *Chin. Chem. Lett.* **2017**, *28*, 312–318. [CrossRef]
94. Guan, Z.J.; Zeng, J.L.; Nan, Z.A.; Wan, X.K.; Lin, Y.M.; Wang, Q.M. Thiacalix[4]arene: New protection for metal nanoclusters. *Sci. Adv.* **2016**, *2*, e1600323. [CrossRef] [PubMed]
95. Evtugyn, G.A.; Shamagsumova, R.V.; Sitdikov, R.R.; Stoikov, I.I.; Antipin, I.S.; Ageeva, M.V.; Hianik, T. Dopamine sensor based on a composite of silver nanoparticles implemented in the electroactive matrix of calixarenes. *Electroanalysis* **2011**, *23*, 2281–2289. [CrossRef]
96. Evtugyn, G.; Porfireva, A.; Sitdikov, R.; Evtugyn, V.; Stoikov, I.; Antipin, I.; Hianik, T. Electrochemical aptasensor for the determination of ochratoxin A at the Au electrode modified with Ag nanoparticles decorated with macrocyclic ligand. *Electroanalysis* **2013**, *25*, 1847–1854. [CrossRef]
97. Evtugyn, G.A.; Shamagsumova, R.V.; Padnya, P.V.; Stoikov, I.I.; Antipin, I.S. Cholinesterase sensor based on glassy carbon electrode modified with Ag nanoparticles decorated with macrocyclic ligands. *Talanta* **2014**, *127*, 9–17. [CrossRef] [PubMed]
98. Kuzin, Y.; Porfireva, A.; Stepanova, V.; Evtugyn, V.; Stoikov, I.; Evtugyn, G.; Hianik, T. Impedimetric detection of DNA damage with the sensor based on silver nanoparticles and neutral red. *Electroanalysis* **2015**, *27*, 2800–2808. [CrossRef]
99. Gorbatchuk, V.V.; Porfireva, A.V.; Stepanova, V.B.; Kuzin, Y.I.; Evtugyn, V.G.; Shamagsumova, R.V.; Stoikov, I.I.; Evtugyn, G.A. Co-polymers of oligolactic acid and tetrasubstituted thiacalix[4]arenes as a new material for electrochemical sensor development. *Sens. Actuators B Chem.* **2017**, *246*, 136–145. [CrossRef]
100. Porifreva, A.V.; Gorbatchuk, V.V.; Evtugyn, V.G.; Stoikov, I.I.; Evtugyn, G.A. Glassy carbon electrode modified with silver nanodendrites implemented in polylactide-thiacalix[4]arene copolymer for the electrochemical determination of tryptophan. *Electroanalysis* **2018**, *30*, 641–649. [CrossRef]
101. Kobayashi, K.; Yamanaka, M. Self-assembled capsules based on tetrafunctionalized calix[4]resorcinarene cavitands. *Chem. Soc. Rev.* **2015**, *44*, 449–466. [CrossRef]
102. Wei, H.; Abtahi, S.M.H.; Vikesland, P.J. Plasmonic colorimetric and SERS sensors for environmental analysis. *Environ. Sci. Nano* **2015**, *2*, 120–135. [CrossRef]
103. Salorinne, K.; Lopez-Acevedo, O.; Nauha, E.; Häkkinen, H.; Nissinen, M. Solvent driven formation of silver embedded resorcinarene nanorods. *CrystEngComm* **2012**, *14*, 347–350. [CrossRef]
104. Menon, S.K.; Modi, N.R.; Pandya, A.; Lodha, A. Ultrasensitive and specific detection of dimethoate using ap-sulphonato-calix [4] resorcinarene functionalized silver nanoprobe in aqueous solution. *RSC Adv.* **2013**, *3*, 10623–10627. [CrossRef]
105. Sun, Y.; Yao, Y.; Yan, C.G.; Han, Y.; Shen, M. Selective decoration of metal nanoparticles inside or outside of organic microstructures via self-assembly of resorcinarene. *ACS Nano* **2010**, *4*, 2129–2141. [CrossRef] [PubMed]
106. Ermakova, A.M.; Morozova, J.E.; Shalaeva, Y.V.; Syakaev, V.V.; Nizameev, I.R.; Kadirov, M.K.; Antipin, I.S.; Konovalov, A.I. Calixresorcinarene-capped silver nanoparticles as new supramolecular hybrid nanocontainers. *Mendeleev Commun.* **2017**, *27*, 335–337. [CrossRef]
107. Ermakova, A.M.; Morozova, J.E.; Shalaeva, Y.V.; Syakaev, V.V.; Nizameev, I.R.; Kadirov, M.K.; Antipin, I.S.; Konovalov, A.I. The supramolecular approach to the phase transfer of carboxylic calixresorcinarene-capped silver nanoparticles. *Colloids Surf. A Physicochem. Eng. Asp.* **2017**, *524*, 127–134. [CrossRef]
108. Makwana, B.A.; Vyas, D.J.; Bhatt, K.D.; Jain, V.K.; Agrawal, Y.K. Highly stable antibacterial silver nanoparticles as selective fluorescent sensor for Fe^{3+} ions. *Spectrochim. Acta Part A Mol. Biomol. Spectrosc.* **2015**, *134*, 73–80. [CrossRef] [PubMed]
109. Makwana, B.A.; Vyas, D.J.; Bhatt, K.D.; Darji, S.; Jain, V.K. Novel fluorescent silver nanoparticles: Sensitive and selective turn off sensor for cadmium ions. *Appl. Nanosci.* **2016**, *6*, 555–566. [CrossRef]

110. Mishra, D.; Kongor, A.; Panchal, M.; Modi, K.; Jain, V. Resorcinarene-embedded stable silver nanoparticles: A fluorescent nanoprobe for Pb (II) in water. *Int. J. Res. Appl. Sci. Eng. Technol.* **2018**, *6*, 1360–1370. [CrossRef]
111. Makwana, B.A.; Darjee, S.; Jain, V.K.; Kongor, A.; Sindhav, G.; Rao, M.V. A comparative study: Metal nanoparticles as fluorescent sensors for biomolecules and their biomedical application. *Sens. Actuators B Chem.* **2017**, *246*, 686–695. [CrossRef]
112. Sergeeva, T.Y.; Samigullina, A.I.; Gubaidullin, A.T.; Nizameev, I.R.; Kadirov, M.K.; Mukhitova, R.K.; Ziganshina, A.Y.; Konovalov, A.I. Application of ferrocene-resorcinarene in silver nanoparticle synthesis. *RSC Adv.* **2016**, *6*, 87128–87133. [CrossRef]
113. Ogoshi, T.; Kanai, S.; Fujinami, S.; Yamagishi, T.A.; Nakamoto, Y. para-Bridged symmetrical pillar[5]arenes: Their Lewis acid catalyzed synthesis and host–guest property. *J. Am. Chem. Soc.* **2008**, *130*, 5022–5023. [CrossRef]
114. Tan, L.L.; Yang, Y.W. Molecular recognition and self-assembly of pillarenes. *J. Incl. Phenom. Macrocycl. Chem.* **2015**, *81*, 13–33. [CrossRef]
115. Song, N.; Yang, Y.W. Hybrid Materials Based on Pillararenes. In *Pillararenes*; Royal Society of Chemistry: London, UK, 2015; pp. 229–262. [CrossRef]
116. Yang, K.; Chao, S.; Zhang, F.; Pei, Y.; Pei, Z. Recent advances in the development of rotaxanes and pseudorotaxanes based on pillar[n]arenes: From construction to application. *Chem. Commun.* **2019**, *55*, 13198–13210. [CrossRef] [PubMed]
117. Nazarova, A.A.; Padnya, P.L.; Gilyazeva, A.I.; Khannanov, A.A.; Evtugyn, V.G.; Kutyreva, M.P.; Klochkov, V.V.; Stoikov, I.I. Supramolecular motifs for the self-assembly of monosubstituted pillar[5]arenes with an amide fragment: From nanoparticles to supramolecular polymers. *New J. Chem.* **2018**, *42*, 19853–19863. [CrossRef]
118. Zhang, C.W.; Chen, L.J.; Yang, H.B. Pillarene-involved metallic supramolecular nanostructures. *Chin. J. Chem.* **2015**, *33*, 319–328. [CrossRef]
119. Hua, B.; Shao, L.; Zhang, Z.; Liu, J.; Huang, F. Cooperative silver ion-pair recognition by peralkylated pillar[5]arenes. *J. Am. Chem. Soc.* **2019**, *141*, 15008–15012. [CrossRef] [PubMed]
120. Wang, P.; Ma, J.; Xia, D. AH_2S and I^- dual-responsive supramolecular polymer constructed via pillar[5]arene-based host–guest interactions and metal coordination. *Org. Chem. Front.* **2018**, *5*, 1297–1302. [CrossRef]
121. Lee, E.; Park, I.H.; Ju, H.; Kim, S.; Jung, J.H.; Habata, Y.; Lee, S.S. Formation of a pillar[5]arene-based two-dimensional poly-pseudo-rotaxane: Threading and crosslinking by the same guest molecules. *Angew. Chem. Int. Ed.* **2019**, *58*, 11296–11300. [CrossRef]
122. Yao, Y.; Wei, P.; Yue, S.; Li, J.; Xue, M. Amphiphilic pillar[5]arenes: Influence of chemical structure on self-assembly morphology and application in gas response and λ-DNA condensation. *RSC Adv.* **2014**, *4*, 6042–6047. [CrossRef]
123. Yao, Y.; Zhou, Y.; Dai, J.; Yue, S.; Xue, M. Host–guest recognition-induced color change of water-soluble pillar[5]arene modified silver nanoparticles for visual detection of spermine analogues. *Chem. Commun.* **2014**, *50*, 869–871. [CrossRef]
124. Yao, Y.; Jie, K.; Zhou, Y.; Xue, M. Reversible assembly of silver nanoparticles driven by host–guest interactions based on water-soluble pillar[n]arenes. *Chem. Commun.* **2014**, *50*, 5072–5074. [CrossRef]
125. Sun, J.; Guo, F.; Shi, Q.; Wu, H.; Sun, Y.; Chen, M.; Diao, G. Electrochemical detection of paraquat based on silver nanoparticles/water-soluble pillar[5]arene functionalized graphene oxide modified glassy carbon electrode. *J. Electroanal. Chem.* **2019**, *847*, 113221. [CrossRef]
126. Zhao, G.; Gao, Z.; Li, H.; Liu, S.; Chen, L.; Zhang, R.; Guo, H. Controlled assembly of Ag nanoparticles on the surface of phosphate pillar[6]arene functionalized single-walled carbon nanotube for enhanced catalysis and sensing performance. *Electrochim. Acta* **2019**, *318*, 711–719. [CrossRef]
127. Tan, X.; Zhang, Z.; Cao, T.; Zeng, W.; Huang, T.; Zhao, G. Control assembly of pillar[6]arene-modified Ag nanoparticles on covalent organic framework surface for enhanced sensing performance toward paraquat. *ACS Sustain. Chem. Eng.* **2019**, *7*, 20051–20059. [CrossRef]

128. Yao, Y.; Jie, K.; Zhou, Y.; Xue, M. Water-soluble pillar[6]arene stabilized silver nanoparticles: Preparation and application in amino acid detection. *Tetrahedron Lett.* **2014**, *55*, 3195–3199. [CrossRef]
129. Muhammed, M.A.H.; Cruz, L.K.; Emwas, A.H.; El-Zohry, A.M.; Moosa, B.; Mohammed, O.F.; Khashab, N.M. Pillar[5]arene-stabilized silver nanoclusters: Extraordinary stability and luminescence enhancement induced by host–guest interactions. *Angew. Chem.* **2019**, *131*, 15812–15817. [CrossRef]

International Journal of
Molecular Sciences

MDPI

Article

Array-Based Screening of Silver Nanoparticle Mineralization Peptides

Masayoshi Tanaka [1], Shogo Saito [1], Reo Kita [2], Jaehee Jang [3], Yonghyun Choi [3], Jonghoon Choi [3] and Mina Okochi [1,*]

[1] Department of Chemical Science and Engineering, Tokyo Institute of Technology, 2-12-1, O-okayama, Meguro-ku, Tokyo 152-8552, Japan; tanaka.m.bn@m.titech.ac.jp (M.T.); saito.s.bc@m.titech.ac.jp (S.S.)
[2] School of Science; Tokyo Institute of Technology, 2-12-1, O-okayama, Meguro-ku, Tokyo 152-8552, Japan; kita@stat.phys.titech.ac.jp
[3] School of Integrative Engineering, Chung-Ang University, Seoul 06974, Korea; jjaeh95@gmail.com (J.J.); dydgus5057@gmail.com (Y.C.); jonghoonc@gmail.com (J.C.)
* Correspondence: okochi.m.aa@m.titech.ac.jp; Tel.: +81-3-5734-2116

Received: 21 February 2020; Accepted: 26 March 2020; Published: 30 March 2020

Abstract: The use of biomolecules in nanomaterial synthesis has received increasing attention, because they can function as a medium to produce inorganic materials in ambient conditions. Short peptides are putative ligands that interact with metallic surfaces, as they have the potential to control the synthesis of nanoscale materials. Silver nanoparticle (AgNP) mineralization using peptides has been investigated; however, further comprehensive analysis must be carried out, because the design of peptide mediated-AgNP properties is still highly challenging. Herein, we employed an array comprising 200 spot synthesis-based peptides, which were previously isolated as gold nanoparticle (AuNP)-binding and/or mineralization peptides, and the AgNP mineralization activity of each peptide was broadly evaluated. Among 10 peptides showing the highest AgNP-synthesis activity (TOP10), nine showed the presence of EE and E[X]E (E: glutamic acid, and X: any amino acid), whereas none of these motifs were found in the WORST25 (25 peptides showing the lowest AgNP synthesis activity) peptides. The size and morphology of the particles synthesized by TOP3 peptides were dependent on their sequences. These results suggested not only that array-based techniques are effective for the peptide screening of AgNP mineralization, but also that AgNP mineralization regulated by peptides has the potential for the synthesis of AgNPs, with controlled morphology in environmentally friendly conditions.

Keywords: AgNP; peptide array; biomineralization; green synthesis

1. Introduction

Different metallic nanoparticles, such as silver nanoparticles (AgNPs), have received marked attention in various fields including molecular labeling [1], sensing [2], microbiocidal activities [3], and catalysis [4]. To expand the characteristics of these molecules, such as optical, electronic, and catalytic properties, numerous studies have focused on the regulation of AgNP synthesis. However, the controlled synthesis of AgNPs, especially in an aqueous solution through a green synthesis course, is still challenging. Hence, it is necessary to develop a technique to synthesize AgNPs, controlling their morphology, size, and properties [5,6].

Biological molecules directed at the synthesis of metallic nanoparticles have received great attention in recent years, due to their potential as green and economic synthesis methods [7–9]. Whereas various biological molecules, including pigments, nucleic acids and proteins are utilized for nanoparticle synthesis and functionalization [7–13], peptides also comprise promising ligand molecules that bind, not only metallic ions, but also metallic crystals. This is because variants are designed

abundantly from combinations using amino acids with various physicochemical properties through chemical synthesis [14–18]. Among a wide range of functional peptides, catalytic peptides used for nanoparticle synthesis regulation, named mineralization peptides, have commonly been isolated from peptides that are strongly bound to target crystals [14–16]. Considering the chemical equilibrium of crystalline nanoparticles and their metallic ions in solution, it has been suggested that the strong binding of peptides stabilizes the crystals, resulting in a shift in the equilibrium from an ionic state towards that of the crystal; specifically, target crystal mineralization is mediated by peptide addition. AgNP mineralization by peptides has been investigated for the development of an AgNP-synthesis technique in ambient conditions [19,20]; however, detailed analyses of peptide directed-AgNP property design are still required.

In this research area, one of the limitations is the number of known AgNP mineralization peptides. To evaluate the mineralization mechanism, additional AgNP-mineralization peptides are required. Among the various techniques used for peptide screening (e.g., phage display library, cell surface display library, ribosome library), coherent membrane-supported peptide array libraries based on spot-synthesis are known to have different advantages, such as ease of peptide sequence identification (DNA sequencing is not necessary), chemical synthesis without a biological organism, and the gain of mineralization activity data from positive (high-mineralization peptides) to negative (weak- or null-mineralization) with amino acid sequences [21,22]. In a previous study, we developed a technique to screen nanoparticle-binding peptides using the peptide array technique [23–26]. Among them, gold nanoparticle (AuNP)-binding peptides were isolated through the design of an array based on variations in the amino acid frequency, informed by empirical results of their binding assays [25]. This simple strategy resulted in approximately 1800 peptides with various AuNP-binding affinities.

In this study, we explored the green synthesis of AgNPs, using peptides without any environmentally hostile chemicals (e.g., $NaBH_4$). To investigate the AgNP mineralization by peptides, peptide array technology was used to identify a list of mineralization peptides with various physicochemical properties. The peptide library was designed from an AuNP-binding peptide, previously reported, because many of these peptide sequences revealed AuNP mineralization activity [15,25]. To expand the potential for other nanoparticle synthesis, the top 200 AuNP-binding peptides were herein evaluated in terms of AgNP mineralization activity.

2. Results

2.1. Screening of AgNP Mineralization Peptide Using Peptide Array Consisting of AuNP-Binding Peptides

To screen various types of AgNP mineralization peptides, AgNP mineralization properties of the top 200 (TOP200) high AuNP-binding peptide sequences (Table S1 in [15]) were investigated. Based on the result shown in Figure 1a, approximately 50 AgNP mineralization peptides were isolated using the peptide array. After a 7-h incubation of the peptide array in an aqueous solution of 50 mM $AgNO_3$ in MilliQ water, individual peptide array spots were observed to change color, indicative of AgNP mineralization. The mineralization profiles using a peptide array with the same peptide library were not identical to the results of an AuNP mineralization evaluation previously reported [15]. From this observation, the mineralization mechanism associated with peptides seems to be different between AuNP and AgNP mineralization. The observed colors were yellowish and consistent at all mineralizing peptide spots, except those of peptide 64 (AESEHEWEVA) and 112 (NWELEEHSAS) (Figure 1a), showing an orange-yellow color.

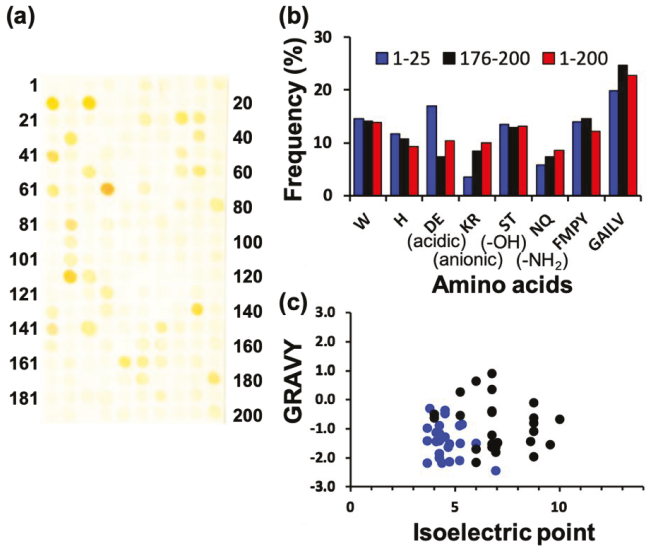

Figure 1. Screening of silver nanoparticle (AgNP) mineralization peptides using peptide array consisting of AuNP-binding peptides. (**a**) Representative image of peptide array after biomineralization reaction by soaking in $AgNO_3$-containing solution for 7 h. (**b**) Amino acid frequencies for high-mineralization peptides (TOP25) and low-mineralization peptides (WORST25), based on the brightness evaluation from each peptide spot using ImageJ. (**c**) Physicochemical properties of high- and low-mineralization peptides. Physicochemical properties of high-binding TOP25 peptides (blue circle) and worse binding WORST25 peptides (black circle), based on pI and GRAVY (the grand average of hydropathy) values. The latter is considered the average hydropathy value for all amino acids in a peptide sequence; therefore, high GRAVY values denote hydrophobicity.

In addition, comparative analyses of amino acid frequencies and sequences among the TOP25 peptides are shown in Figure 1b. Comparing the amino acid frequency with the average of all 200 library peptides, results indicated a significantly higher proportion of acidic amino acids, including aspartic acid (D) and glutamic acid (E) monomers in AgNP mineralization peptides, whereas these were notably reduced in the bottom 25 (WORST25) peptides. It is probable that this results from the negative charge of amino acids, which can interact with Ag^+. In terms of other minerals of magnetite and hydroxyapatites, the importance of these amino acids has also been reported; however, the mechanisms are still controversial [22–24]. Therefore, these residues could comprise a prerequisite for all AgNP biomineralization peptides. The importance of acidic amino acids was also supported by the plot analysis of peptide physicochemical properties (Figure 1c). Almost all peptides were found in a region of hydrophilicity and a low isoelectric point (pI), whereas the bottom 25 (WORST25) peptides were widely spread in the chart. The amino acid frequency and physicochemical properties of AgNP mineralization peptides were different from those of AuNP mineralization peptides (Figure S1). A tryptophan residue was clearly an important amino acid for AuNP mineralization, and the pI and hydropathy values did not appear to coincide with the Au mineralization activity. A detailed investigation based on these differences would contribute to the elucidation of metallic nanoparticle mineralization peptides and their sequence design to control particle properties.

In the image of the peptide array after AgNP mineralization activity evaluation, peptides demonstrating strong Ag mineralization are signified by a low summed color intensity value. The TOP10 peptides (re-named AgMP1–10; Ag mineralization peptide 1–10) and the WORST10 are listed with their physicochemical properties in Tables 1 and 2, respectively. Interestingly, nine peptides of the TOP10 peptide sequences were found to have a unique motif, specifically EE and E[X]E (E: glutamic

acid, and X: any amino acid), whereas none of these motifs were found in the WORST10 peptides (Tables 1 and 2). The motif collectively possessing glutamic acids would be an important factor for AgNP mineralization by peptides.

Table 1. List of Ag mineralization peptides (TOP10) screened, and their physical properties.

Peptide No.	Sequence	Mineralization Activity [1]	pI [2]	GRAVY2 [2]
AuP64 (AgMP1)	AESEHEWEVA	162.9	4.09	−1.11
AuP13 (AgMP2)	EEPHWEEMAA	168.2	4.09	−1.42
AuP11 (AgMP3)	PEESQEGWMA	168.2	3.67	−1.4
AuP112 (AgMP4)	NWELEEHSAS	169.4	4.24	−1.41
AuP139 (AgMP5)	ETEWLGHETL	174.7	4.24	−0.88
AuP41 (AgMP6)	WSEETEMWPL	177.8	3.67	−0.97
AuP82 (AgMP7)	WQENSMEENW	183.9	3.67	−2.17
AuP180 (AgMP8)	HWWWEHEMEH	185.1	5.22	−2.09
AuP165 (AgMP9)	EGSDHPSWNQ	186.0	4.35	−2.17
AuP28 (AgMP10)	PEEGPHSLWH	186.3	5.23	−1.49

[1] Using Image quant software, the mineralization activity of each peptide was determined through the quantitative analysis of spot color intensity for peptide array images. Average values for peptide spots are shown from triplicate independent experiments. [2] Based on the ProtParam tool in ExPASy (http://web.expasy.org/protparam/), the isoelectric point (pI) and the grand average of the hydropathy value (GRAVY) were shown.

Table 2. List of Ag mineralization peptides (WORST10) screened and their physical properties.

Peptide No.	Sequence	Mineralization Activity [1]	pI [2]	GRAVY [2]
AuP77	YWASHKHWWW	221.2	8.61	−1.42
AuP173	WMMWGWVHEI	221.6	5.24	0.27
AuP65	TQWHEWHWYQ	221.9	5.98	−2.16
AuP155	NWTHWSTTQH	222.0	6.92	−1.81
AuP137	VHYGSQIEWG	222.7	5.24	−0.53
AuP95	AHALWIWHKT	223.0	8.76	−0.09
AuP125	TTWHGFPWAG	223.1	6.74	−0.42
AuP74	VLWRHEWAWK	223.1	8.75	−0.80
AuP116	WHHWAQGWHG	223.5	7.02	−1.48
AuP117	YEAVSTTWQS	224.0	4.00	−0.62

[1] Using Image quant software, the mineralization activity of each peptide was determined through the quantitative analysis of spot color intensity for peptide array images. Average values for peptide spots are shown from triplicate independent experiments. [2] Based on the ProtParam tool in ExPASy (http://web.expasy.org/protparam/), the isoelectric point (pI) and the grand average of the hydropathy value (GRAVY) are shown.

2.2. *Ag Nanoparticle Synthesis by Screened Mineralization Peptides*

The AgNP mineralization activity of the top three (TOP3) peptides (AgMP1; AESEHEWEVA, AgMP2; EEPHWEEMAA, and AgMP3; PEESQEGWMA) was further investigated for use in the one-pot green synthesis of AgNPs in aqueous solution. Herein, in the presence of different peptide and $AgNO_3$ concentrations, AgNP mineralization was demonstrated (Figure 2). Particle synthesis by AgMP1 and AgMP2 was confirmed easily by the naked eye, and orange/yellow pigments derived from synthesized AgNPs were observed, whereas no color change was found in the presence of AgMP3 or without peptide. Therefore, it was shown that for the identified peptides, at least two can function in AgNP mineralization. In addition, according to the increase in peptide and $AgNO_3$ concentrations, the increase in absorbance signals at 450 nm, indicative of AgNP mineralization, was found in the presence of AgMP1 and AgMP2, whereas no significant change was found in the presence of AgMP3 and in the absence of peptide. When the reaction was conducted with 5 mM of each peptide (AgMP1 and AgMP2) and 50 mM $AgNO_3$, maximum absorbance signals were observed.

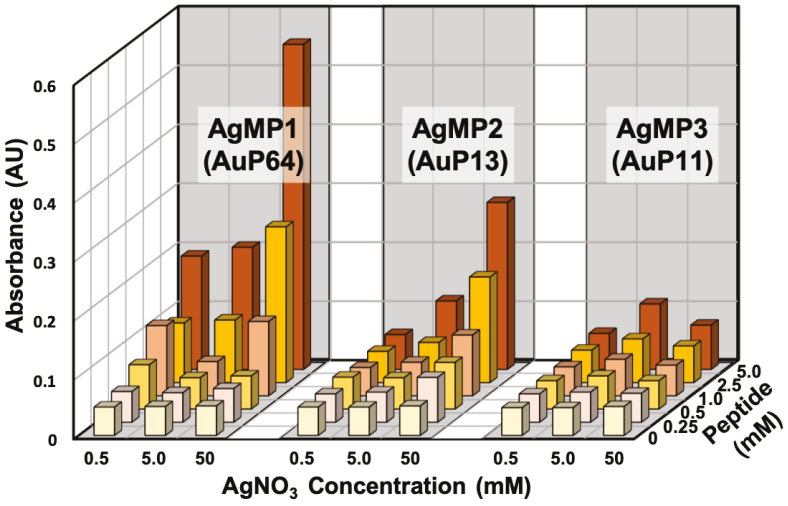

Figure 2. Silver nanoparticle (AgNP) synthesis using the top three (TOP3) screened peptides (AgMP1, AgMP2, and AgMP3) from the peptide array. Mineralization was evaluated based on absorbance intensity (450 nm) in the presence of different concentrations of peptides (0, 0.25, 0.5, 1.0, 2.5, and 5.0 mM) and $AgNO_3$ (0.5, 5.0, and 50 mM).

To further characterize the mineralization mediated by peptides, time-course analyses of AgNP synthesis were performed, showing gradual AgNP synthesis (Figure 3). Clearly, different absorbance spectra were obtained by using AgMP1 and AgMP2, whereas no significant absorbance was found in the negative control (without peptide). The solution containing AgNPs synthesized by AgMP1 had two absorbance peaks at 420 nm and one broad peak at approximately 490 nm. The AgMP2-based solution revealed one broad absorbance peak at 450 nm. These spectra are expected to be derived from localized surface plasmon resonance (LSPR) by synthesized AgNPs. As the LSPR wavelength depends on the shape, size, and agglomeration state [25–27], it was suggested that the synthesized AgNPs have different characteristics.

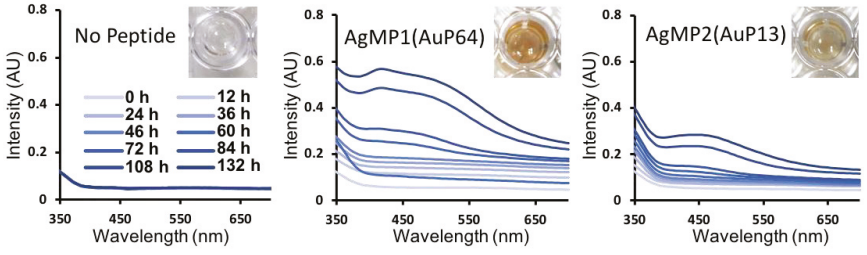

Figure 3. Time-dependent changes in absorption spectra of silver nanoparticles (AgNPs) synthesized by screened peptides, including AgMP1(AuP64) and AgMP2(AuP13). The mineralization was monitored until 132 h in the presence of each mineralization peptide (5 mM) and $AgNO_3$ (50 mM). Images of solutions containing AgNPs synthesized by each peptide at 132 h are included.

2.3. Transmission Electron Microscopic (TEM) Observation of AgNPs Synthesized by Screened Mineralization Peptides

A TEM observation of synthesized AgNPs by each peptide (AgMP1 and AgMP2) was conducted (Figure S2). These two solutions contained two types of particles, large agglomerate and small spherical particles. Interestingly, the morphologies of agglomerate particles were obviously different in each

sample. In the presence of AgMP1, large agglomerates made by vertically overlapping nanoplates (mainly triangle nanoplates) with sizes of 250 nm to 1 μm were found. To the best of our knowledge, there are no reports of a silver agglomerate with this unique morphology. In general, the triangle silver nanoplate revealed absorbance at 420 nm and the red-shifted region [27,28]. Therefore, two absorbance peaks at 420 and 490 nm might be observed in the solution containing AgNPs synthesized by AgMP1. In addition, as an increased absorbance in the whole range of wavelengths was found, the aggregation of biomineralized AgNPs seems to have occurred. This was supported by TEM observation; large agglomerates were found in the solution. From the size evaluation of more than 350 randomly selected AgNPs, the size of small spherical nanoparticles was 19.1 ± 9.3 nm. The AgNPs synthesized by AgMP2 showed large agglomerates with a coral morphology and a smaller size range than that of AgNPs derived from AgMP1 (200 to 750 nm). The small spherical nanoparticles were also smaller (4.9 ± 2.4 nm) than the AgNPs synthesized by AgMP1.

3. Discussion

Using a list of AuNP-binding peptides synthesized on a peptide array, AgNP mineralization activity was evaluated. As a result, more than 50 AgNP mineralization peptides were effectively isolated (Figure 1). This is probably because Au and Ag have similar metallic properties and the utilized peptide library contains a large number of tryptophan molecules, which could play an important role as electron donors for particle formation. The result obtained here suggests that the 200 peptides have potential for the synthesis of other nanoparticles. However, the AgNP mineralization activity of isolated peptides was not consistent with that of AuNPs. This was very interesting because this observation reveals the potential of peptide isolation for metallic species-specific mineralization, through further comparative studies with other metals.

From the sequence analysis of isolated AgNP mineralization peptides, EE and E[X]E (E: glutamic acid, and X: any amino acid) motifs were found. For this kind of analysis, it is beneficial to use peptide array technology, because the activity information could be obtained from all peptides, whereas it is difficult to use a positive screening technique including phage display library-based screening. In addition, the results indicated that the AgMP1 and AgMP2 peptides have two and three EE and E[X]E (E: glutamic acid, and X: any amino acid) motifs in their sequence, respectively, whereas AgMP3 has only one. This observation suggested that the number of EE and E[X]E (E: glutamic acid, and X: any amino acid) motifs is important for peptide-based AgNP mineralization in solution.

As shown in Figure 3, the AgNP mineralization reaction was still occurring, even after 132 h. In the case of AuNP mineralization, when G1 (ETGHHIWEWM) and B3 (ASHQWAWKWE) peptides were used, AuNPs of 2.6 ± 1.2 nm and 34.7 ± 6.7 nm were synthesized, respectively [15]. Interestingly, the reaction for smaller particle synthesis with an irregular shape reached a plateau within 10 min, whereas the synthesis of larger particles with unique morphologies, including triangle nanoplate and decahedron particles, required approximately 12 h [15]. As AgNPs with unique morphologies were also observed after long reaction times in this study, the difference in reaction kinetics seems to be a key factor for the formation of different sizes and morphologies of AgNPs, as discussed in a previous study on AuNP synthesis regulation [29–31]. In addition, further investigation of the interaction between peptides and specific crystal facets should be performed to elucidate the morphological regulation, because various biological molecules bound to a specific crystal surface are suggested to contribute to morphological regulation in the biomineralization process [32–36].

In conclusion, using a peptide array comprising an AuNP-binding peptide library, AgNP mineralization peptide screening was performed and identified approximately 50 different peptide candidates. From these sequence analyses, some unique characteristics, including amino acid frequency and physicochemical properties with a unique sequence motif, specifically EE and E[X]E (E: glutamic acid, and X: any amino acid), were found. Interestingly, among the TOP3 AgNP mineralization peptides isolated from the peptide array, two peptides (named AgMP1 and AgMP2) were revealed to possess AgNP-synthesis activity resulting in different morphologies. Moreover, it should be noted that although

detailed analyses were only performed for two peptides screened in this study, the investigation could be expanded to the entire array of peptides. A comprehensive analysis using various peptides might contribute to the elucidation of AgNP mineralization by peptides and peptide design for morphologically controlled AgNP synthesis through a one-pot green course. The investigation of particle properties of each AgNP synthesized by the peptides might also lead to particle applications in various fields.

4. Materials and Methods

4.1. Peptide Array Synthesis Using Spot Technology

We used a cellulose membrane (grade 542; Whatman, Maidstone, UK), activated by β-alanine as the N-terminal basal spacer, as reported previously [37,38]. With a peptide auto-spotter (ResPepSL; Intavis AG, Köln, Germany), each activated Fmoc amino acid (0.5 M) was spotted on the membrane, as per the manufacturer's instructions. After adding the first amino acid residue, the remaining amino groups were blocked with 4% acetic anhydride. The membrane, deprotected with 20% piperidine in N,N′-dimethylformamide (DMF), was subsequently washed thoroughly with DMF, followed by ethanol at each amino acid elongation process. After the final deprotection step, side-chain-protecting groups were deprotected using a solution of m-cresol:thioanisol:ethandithiol:trifluoroacetic acid (1:6:3:40) for 3 h. The membranes were finally carefully washed with diethyl ether and ethanol and dried.

4.2. Screening of AgNP Mineralization Peptides Using Peptide Array

To screen AgNP mineralization peptides, 200 AuNP-binding and/or mineralization peptides were synthesized on a cellulose membrane. The synthesized membrane was incubated in an aqueous solution of 500 mM $AgNO_3$ in MilliQ water under fluorescent light. After incubation for 7 h, individual peptide array spots were observed to change color, indicative of AgNP mineralization. After washing twice with MilliQ water, the mineralization activity of each peptide was evaluated quantitatively, based on the color intensity derived from AgNP mineralization activity onto peptide spots. This was measured from digitized images of the peptide array after the mineralization experiment (ImageQuant TL software, GE Healthcare, Tokyo, Japan).

4.3. AgNP Synthesis and Characterization Using Screened Mineralization Peptides

To evaluate the effects of AgNP mineralization peptides on AgNP synthesis in free aqueous solution (not on the peptide array), chemically synthesized and purified peptides were added to the reaction solution. The peptide was synthesized following the standard Fmoc-based solid-phase protocol, with a Respep SL automatic peptide synthesizer (Intavis AG, Köln, Germany). Briefly, Fmoc protected amino acid residues were applied to the TentaGel Resin stepwise for elongation of the peptide chain. The synthesized peptide was deprotected with 20% piperidine in DMF and cleaved from the scaffold resin by the cleavage cocktail containing TFA, water, thioanisole, phenol, EDT, and TIPS (82.5:5:5:2.5:1). Peptides were precipitated in cold diethyl ether and dissolved in 30% acetonitrile for storage in a form of freeze-dried powder. Purification was performed with an ODS-80TS column (Tosoh Corp., Tokyo, Japan) and a high-performance liquid chromatography (HPLC) system (LC-20AR, CBM-20A, SIL-20AC, CTO-20AC, SPD-20AV, Shimadzu Corp., Kyoto, Japan), before measuring the molecular weight by matrix assisted laser desorption/ionization mass spectrometry (AXIMA-CFRPlus, Shimadzu Corp.) (Figure S3). The final purity of the peptide was confirmed to be > 85% using an ODS-100Z column (Tosoh Corp.) and the HPLC system (Shimadzu Corp.)

Three different peptides comprising three AgMPs screened using a peptide array (AgMP1; AESEHEWEVA, AgMP2; EEPHWEEMAA, and AgMP3; PEESQEGWMA) were investigated. The peptide powders were dissolved in 100% DMSO (100 mM peptide). After confirming that DMSO did not affect Ag mineralization, different volumes of the peptide solution were added to $AgNO_3$ containing MilliQ water for Ag mineralization evaluation.

TEM analysis was performed using a Hitachi H7650 microscope (Hitachi, Tokyo, Japan), operating at a working voltage of 100 kV. Specimens were prepared through the drop-casting of 1.5 µL of the sample dispersion onto a formvar-coated 200-mesh Cu grid (Nisshin EM, Tokyo, Japan) and washed with MilliQ water twice. The average sizes (± SD) of nanoparticles were obtained by manually counting >350 randomly selected particles in TEM images. UV-vis optical absorbance of the AgNPs was delineated using a microtiter plate reader (PowerScan 4, DS Pharma Biomedical Co., Ltd., Osaka, Japan).

Supplementary Materials: Supplementary materials can be found at http://www.mdpi.com/1422-0067/21/7/2377/s1.

Author Contributions: Study conceptualization, M.T., J.C., and M.O.; Methodology, S.S., R.K., J.J., and Y.C.; investigation, M.T., S.S., R.K., J.J., Y.C., J.C., and M.O.; resources, M.T. and M.O.; writing—original draft preparation, M.T. and S.S.; writing—review and editing, M.T., S.S., J.J., Y.C., J.C., and M.O.; supervision, M.O.; project administration, M.T., J.C. and M.O.; funding acquisition, M.T., J.C., and M.O. All authors have read and agreed to the published version of the manuscript.

Funding: This research was supported by a Grant-in-Aid for Scientific Research from Ministry of Education, Sports, Science and Technology, Japan, No. 18H01795, 18K18970 and 18K04848. This work was partially supported by the Cross-ministerial Strategic Innovation Promotion Program (SIP), from the Cabinet Office, Government of Japan. M.T. is appreciative of funds from the Iketani Science and Technology Foundation and the Royal Society UK, under the Newton International Fellowships scheme.

Conflicts of Interest: The authors declare no conflict of interest.

Abbreviations

AgNP	Silver nanoparticle
AgMP	Silver mineralization peptide
AuNP	Gold nanoparticle
DMF	N,N′-dimethylformamide
pI	Isoelectric point

References

1. Zhao, L.J.; Yu, R.J.; Ma, W.; Han, H.X.; Tian, H.; Qian, R.C.; Long, Y.T. Sensitive detection of protein biomarkers using silver nanoparticles enhanced immunofluorescence assay. *Theranostics* **2017**, *7*, 876–883. [CrossRef] [PubMed]
2. Okochi, M.; Kuboyama, M.; Tanaka, M.; Honda, H. Design of a dual-function peptide probe as a binder of angiotensin II and an inducer of silver nanoparticle aggregation for use in label-free colorimetric assays. *Talanta* **2015**, *142*, 235–239. [CrossRef] [PubMed]
3. Jang, J.; Choi, Y.; Tanaka, M.; Choi, J. Development of silver/graphene oxide nanocomposites for antibacterial and antibiofilm applications. *J. Ind. Eng. Chem.* **2019**, *83*, 46–52. [CrossRef]
4. Huard, D.J.E.; Demissie, A.; Kim, D.; Lewis, D.; Dickson, R.M.; Petty, J.T.; Lieberman, R.L. Atomic structure of a fluorescent Ag_8 cluster templated by a multistranded DNA scaffold. *J. Am. Chem. Soc.* **2019**, *141*, 11465–11470. [CrossRef] [PubMed]
5. Syafiuddin, A.; Salmiati; Salim, M.R.; Beng Hong Kueh, A.; Hadibarata, T.; Nur, H. A review of silver nanoparticles: Research trends, global consumption, synthesis, properties, and future challenges. *J. Chin. Chem. Soc.* **2017**, *64*, 732–756. [CrossRef]
6. Lee, S.H.; Jun, B.H. Silver nanoparticles: Synthesis and application for nanomedicine. *Int. J. Mol. Sci.* **2019**, *20*, 865. [CrossRef]
7. Tarannum, N.; Divya; Gautam, Y.K. Facile green synthesis and applications of silver nanoparticles: A state-of-the-art review. *RSC Adv.* **2019**, *9*, 34926–34948. [CrossRef]
8. Srikar, S.K.; Giri, D.D.; Pal, D.B.; Mishra, P.K.; Upadhyay, S.N. Green synthesis of silver nanoparticles: A review. *Green Sustain. Chem.* **2016**, *6*, 34–56. [CrossRef]
9. Rafique, M.; Sadaf, I.; Rafique, M.S.; Tahir, M.B. A review on green synthesis of silver nanoparticles and their applications. *Artif. Cells Nanomed. Biotechnol.* **2017**, *45*, 1272–1291. [CrossRef]
10. Kasyanenko, N.; Varshavskii, M.; Ikonnikov, E.; Tolstyko, E.; Belykh, R.; Sokolov, P.; Bakulev, V.; Rolich, V.; Lopatko, K. DNA modified with metal nanoparticles: Preparation and characterization of ordered metal-DNA nanostructures in a solution and on a substrate. *J. Nanomater.* **2016**, *2016*, 3237250. [CrossRef]

11. Zagorovsky, K.; Chou, L.Y.T.; Chan, W.C.W. Controlling DNA-nanoparticle serum interactions. *Proc. Natl. Acad. Sci. USA* **2016**, *113*, 13600–13605. [CrossRef] [PubMed]
12. Li, H.; Rothberg, L. Colorimetric detection of DNA sequences based on electrostatic interactions with unmodified gold nanoparticles. *Proc. Natl. Acad. Sci. USA* **2004**, *101*, 14036–14039. [CrossRef] [PubMed]
13. Gurme, S.T.; Aware, C.B.; Surwase, S.N.; Chavan, C.S.; Jadhav, J.P. Synthesis of melanin mediated silver nanoparticles from Aeromonas sp. SNS using response surface methodology: Characterization with the biomedical applications and photocatalytic degradation of brilliant green. *J. Polym. Environ.* **2019**, *27*, 2428–2438. [CrossRef]
14. Hatanaka, T.; Matsugami, A.; Nonaka, T.; Takagi, H.; Hayashi, F.; Tani, T.; Ishida, N. Rationally designed mineralization for selective recovery of the rare earth elements. *Nat. Commun.* **2017**, *8*, 15670. [CrossRef] [PubMed]
15. Tanaka, M.; Takahashi, Y.; Roach, L.; Critchley, K.; Evans, S.D.; Okochi, M. Rational screening of biomineralisation peptides for colour-selected one-pot gold nanoparticle syntheses. *Nanoscale Adv.* **2019**, *1*, 71–75. [CrossRef]
16. Maeda, Y.; Makhlynets, O.V.; Matsui, H.; Korendovych, I.V. Design of catalytic peptides and proteins through rational and combinatorial approaches. *Annu. Rev. Biomed. Eng.* **2016**, *18*, 311–328. [CrossRef]
17. Vallee, A.; Humblot, V.; Pradier, C.-M. Peptide interactions with metal and oxide surfaces. *Acc. Chem. Res.* **2010**, *43*, 1297–1306. [CrossRef]
18. Tang, Z.; Palafox-Hernandez, J.P.; Law, W.-C.; Hughes, Z.E.; Swihart, M.T.; Prasad, P.N.; Knecht, M.R.; Walsh, T.R. Biomolecular recognition principles for bionanocombinatorics: An integrated approach to elucidate enthalpic and entropic factors. *ACS Nano* **2013**, *7*, 9632–9646. [CrossRef]
19. Carter, C.J.; Ackerson, C.J.; Feldheim, D.L. Unusual reactivity of a silver mineralizing peptide. *ACS Nano* **2010**, *4*, 3883–3888. [CrossRef]
20. Belser, K.; Slenters, T.V.; Pfumbidzai, C.; Upert, G.; Mirolo, L.; Fromm, K.M.; Wennemers, H. Silver nanoparticle formation in different sizes induced by peptides identified within split-and-mix libraries. *Angew. Chem. Int. Ed.* **2009**, *48*, 3661–3664. [CrossRef]
21. Frank, R. The SPOT-synthesis technique: Synthetic peptide arrays on membrane supports–principles and applications. *J. Immunol. Methods* **2002**, *267*, 13–26. [CrossRef]
22. Frank, R. Spot-synthesis: An easy technique for the positionally addressable, parallel chemical synthesis on a membrane support. *Tetrahedron* **1992**, *48*, 9217–9232. [CrossRef]
23. Okochi, M.; Sugita, T.; Furusawa, S.; Umetsu, M.; Adschiri, T.; Honda, H. Peptide array-based characterization and design of ZnO-high affinity peptides. *Biotechnol. Bioeng.* **2010**, *106*, 845–851. [CrossRef] [PubMed]
24. Okochi, M.; Ogawa, M.; Kaga, C.; Sugita, T.; Tomita, Y.; Kato, R.; Honda, H. Screening of peptides with a high affinity for ZnO using spot-synthesized peptide arrays and computational analysis. *Acta Biomater.* **2010**, *6*, 2301–2306. [CrossRef]
25. Tanaka, M.; Hikiba, S.; Yamashita, K.; Muto, M.; Okochi, M. Array-based functional peptide screening and characterization of gold nanoparticle synthesis. *Acta Biomater.* **2017**, *1*, 13–26. [CrossRef]
26. Kuboyama, M.; Kato, R.; Okochi, M.; Honda, H. Screening for silver nanoparticle-binding peptides by using a peptide array. *Biochem. Eng. J.* **2012**, *66*, 73–77. [CrossRef]
27. Si, G.; Shi, W.; Li, K.; Ma, Z. Synthesis of PSS-capped triangular silver nanoplates with tunable SPR. *Colloids Surfaces A Physicochem. Eng. Asp.* **2011**, *380*, 257–260. [CrossRef]
28. Wijaya, Y.N.; Kim, J.; Choi, W.M.; Park, S.H.; Kim, M.H. A systematic study of triangular silver nanoplates: One-pot green synthesis, chemical stability, and sensing application. *Nanoscale* **2017**, *9*, 11705–11712. [CrossRef]
29. Xiong, Y.; McLellan, J.M.; Chen, J.; Yin, Y.; Li, Z.Y.; Xia, Y. Kinetically controlled synthesis of triangular and hexagonal nanoplates of palladium and their SPR/SERS properties. *J. Am. Chem. Soc.* **2005**, *127*, 17118–17127. [CrossRef]
30. Le Beulze, A.; Duguet, E.; Mornet, S.; Majimel, J.; Tréguer-Delapierre, M.; Ravaine, S.; Florea, I.; Ersen, O. New insights into the side-face structure, growth aspects, and reactivity of Ag_n nanoprisms. *Langmuir* **2014**, *30*, 1424–1434. [CrossRef]
31. Alloyeau, D.; Dachraoui, W.; Javed, Y.; Belkahla, H.; Wang, G.; Lecoq, H.; Ammar, S.; Ersen, O.; Wisnet, A.; Gazeau, F.; et al. Unravelling kinetic and thermodynamic effects on the growth of gold nanoplates by liquid transmission electron microscopy. *Nano Lett.* **2015**, *15*, 2574–2581. [CrossRef] [PubMed]

32. Yamagishi, A.; Tanaka, M.; Lenders, J.J.M.; Thiesbrummel, J.; Sommerdijk, N.A.J.M.; Matsunaga, T.; Arakaki, A. Control of magnetite nanocrystal morphology in magnetotactic bacteria by regulation of *mms7* gene expression. *Sci. Rep.* **2016**, *6*, 29785. [CrossRef] [PubMed]
33. Yamagishi, A.; Narumiya, K.; Tanaka, M.; Matsunaga, T.; Arakaki, A. Core amino acid residues in the morphology-regulating protein, Mms6, for intracellular magnetite biomineralization. *Sci. Rep.* **2016**, *6*, 35670. [CrossRef] [PubMed]
34. Grohe, B.; O'Young, J.; Ionescu, D.A.; Lajoie, G.; Rogers, K.A.; Karttunen, M.; Goldberg, H.A.; Hunter, G.K. Control of calcium oxalate crystal growth by face-specific adsorption of an osteopontin phosphopeptide. *J. Am. Chem. Soc.* **2007**, *129*, 14946–14951. [CrossRef]
35. Ndao, M.; Ash, J.T.; Stayton, P.S.; Drobny, G.P. The role of basic amino acids in the molecular recognition of hydroxyapatite by statherin using solid state NMR. *Surf. Sci.* **2010**, *604*, L39–L42. [CrossRef]
36. Deshpande, A.S.; Beniash, E. Bioinspired synthesis of mineralized collagen fibrils. *Cryst. Growth Des.* **2008**, *8*, 3084–3090. [CrossRef]
37. Tanaka, M.; Suwatthanarak, T.; Arakaki, A.; Johnson, B.R.G.; Evans, S.D.; Okochi, M.; Staniland, S.S.; Matsunaga, T. Enhanced tubulation of liposome containing cardiolipin by MamY protein from magnetotactic bacteria. *Biotechnol. J.* **2018**, *13*, e1800087. [CrossRef]
38. Alvin, A.W.L.; Tanaka, M.; Okochi, M. Characterization of particulate matter binding peptides screened from phage display. *J. Biosci. Bioeng.* **2017**, *123*, 621–624. [CrossRef]

International Journal of
Molecular Sciences

MDPI

Article

Photochemical Printing of Plasmonically Active Silver Nanostructures

Marcin Szalkowski [1,2], Karolina Sulowska [1], Martin Jönsson-Niedziółka [3], Kamil Wiwatowski [1], Joanna Niedziółka-Jönsson [3], Sebastian Maćkowski [1,*] and Dawid Piątkowski [1]

1 Institute of Physics, Faculty of Physics, Astronomy and Informatics, Nicolaus Copernicus University in Toruń, Grudziadzka 5, 87-100 Torun, Poland; marszal@fizyka.umk.pl (M.S.); sulowska@doktorant.umk.pl (K.S.); kamilw@doktorant.umk.pl (K.W.); dapi@fizyka.umk.pl (D.P.)
2 Institute of Low Temperature and Structure Research, Polish Academy of Sciences, Okolna 2, 50-422 Wrocław, Poland
3 Institute of Physical Chemistry, Polish Academy of Sciences, Kasprzaka 44/52, 01-224 Warszawa, Poland; martinj@ichf.edu.pl (M.J.-N.); jniedziolka@ichf.edu.pl (J.N.-J.)
* Correspondence: mackowski@fizyka.umk.pl

Received: 29 February 2020; Accepted: 13 March 2020; Published: 16 March 2020

Abstract: In this paper, we demonstrate plasmonic substrates prepared on demand, using a straightforward technique, based on laser-induced photochemical reduction of silver compounds on a glass substrate. Importantly, the presented technique does not impose any restrictions regarding the shape and length of the metallic pattern. Plasmonic interactions have been probed using both Stokes and anti-Stokes types of emitters that served as photoluminescence probes. For both cases, we observed a pronounced increase of the photoluminescence intensity for emitters deposited on silver patterns. By studying the absorption and emission dynamics, we identified the mechanisms responsible for emission enhancement and the position of the plasmonic resonance.

Keywords: silver nanostructures; silver islands film; silver deposition; metal enhanced luminescence

1. Introduction

Metallic nanostructures can modify the spectral properties of quantum emitters localized in their vicinity. When both the distance and the spectral relations between them are properly chosen, absorption and emission rates can be significantly enhanced [1–3]. Modern chemical synthesis methods enable to control and tailor the spectral properties of the metallic nanoparticles. By changing sizes and shapes of nanoparticles (spheres, rods, triangles, stars, rings, wires, etc.), spectral positions of the resonance peak can be shifted across a broad spectral range, from ultraviolet to near-infrared [4,5]. The position of the plasmon resonance can be additionally controlled by changing the type of material that the particle is made of [6]. Presently, noble metals like silver and gold are the most widely used. Since metallic nanoparticles are usually synthesized using wet chemistry techniques, their optical properties are inevitably affected by particle size/shape dispersion. Thus, the optical properties of a particular nanoparticle can only be investigated using advanced experimental techniques, based on single-molecule detection [7], and in the case of macroscopic experiments, only a statistically averaged response from the sample can be probed.

Among plasmonically active platforms, silver islands films (SIFs) play an important role. The SIF substrate consists of randomly deposited silver islands, formed during a reduction reaction of silver nitrate on glass [8,9]. The synthesis is quite straightforward and low-cost, and such substrates have been shown to exhibit strong plasmonic properties. Namely, they can modify transition rates of nearby emitters. It has been shown, for instance, that quantum dots deposited on SIFs feature emission enhancement factors of about 5 [10], whereas even 200-fold fluorescence enhancement has been recently

observed for photosynthetic complexes deposited on SIFs [11]. Besides fluorescence microscopy, SIFs have also been applied to increase the sensitivity of Raman [12] and TIRF microscopy [13]. Nonetheless, with respect to the metallic nanoparticles, SIFs feature some disadvantages. First of all, due to a high degree of sample inhomogeneity, the spatial distribution of islands as well as their sizes and shapes are random and cannot be controlled. In addition, the method of SIF fabrication implies in principle that the whole substrate is covered with silver islands, limiting their use as high optical contrast substrates.

In this work, we demonstrate that silver nanostructures fabricated using a laser-induced photochemical reaction [14,15] are plasmonically active for both Stokes and anti-Stokes emitters. The method, in contrast to the wet chemistry SIF preparation, uses a tightly focused laser beam to initialize the reaction. Depending on the resolution of the optical system, the paths can feature submicrometer widths with practically no restrictions regarding their shapes and sizes. Scanning electron microscopy images confirm island-like morphology of the paths. The results of fluorescence microscopy on the other hand, indicate that these silver nanostructures can enhance the optical response of two qualitatively different emitters: peridinin-chlorophyll-proteins (PCPs) and rare-earths doped nanocrystals (NCs). PCP complexes are efficient natural proteins responsible for efficient light harvesting complexes [16,17], while the up-converting NCs allow conversion of the light from the infrared to the visible [18]. Experimentally measured enhancements are of the order of 5–7, and both an increase of absorption as well as radiative emission rates contribute to this remarkable effect. The demonstration that such high quality plasmonically-active patterns of arbitrary shape can be used for enhancing the optical response of organic and inorganic materials opens a way to implement these structures for optoelectronic and sensing devices.

2. Results and Discussion

The influence of silver islands, fabricated using the photochemical approach on the optical properties of emitters, was evaluated for both Stokes and anti-Stokes nanostructures, i.e., photoactive protein, peridinin-chlorophyll-protein, and rare-earth doped nanocrystals, respectively.

2.1. Photoactive Protein

Peridinin-chlorophyll-protein is a well-known light-harvesting complex. It consists of eight optically active peridinin molecules and two chlorophylls [19]. Its absorption spectrum is dominated by a broad band localized between 400 and 550 nm, attributed to the electric-dipole transition in peridinins and absorption of the chlorophylls via the Soret band (Figure 1a). Additional absorption at 655 nm comes from chlorophylls. The emission can be activated either via peridinins, which transfer the excitation energy to the chlorophylls, or via chlorophyll absorption bands. The Stokes-shifted emission of the PCP is observed at 670 nm and it is characterized by a monoexponential decay profile, as shown in Figure 1b.

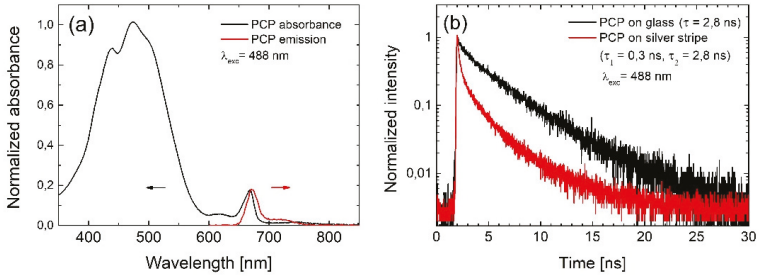

Figure 1. (**a**) Absorption and emission spectra of peridinin-chlorophyll-protein (PCP) complexes. (**b**) Photoluminescence decay transients acquired for PCPs deposited on glass (black line) and silver stripes (red line).

The sample was prepared by spin-coating (3000 rpm for 1 min) the aqueous solution of PCP (2 μg/mL) on a glass substrate with previously deposited silver stripes. Experiments were carried out using wide-field fluorescence microscopy and confocal fluorescence microscopy for determining the intensities and decay curves of PCP emission, respectively. The wide-field microscope (Eclipse Ti-S, Nikon, Japan) was equipped with an oil immersion objective (Plan Apo 60× NA = 1.4, Nikon, Japan), a set of LED illuminators, and an EMCCD camera (iXon, Andor, UK) mounted in the detection channel. The confocal microscope used the same objective, picosecond excitation lasers (BDL-SMN series, Becker&Hickl, Germany), and fast detection based on time correlated single photon counting system (SPC-130-EMN, Becker&Hickl, Germany) coupled with single photon counting module (ID100, ID Quantique, Switzerland).

Emission intensity maps obtained for four excitation wavelengths of 405 nm, 480 nm, 535 nm, and 630 nm, are displayed in Figure 2. The broad absorption spectrum of PCP complexes makes it possible to use a range of excitation wavelengths, an approach often applied for studying plasmonic interactions in similar systems [20]. The sequence of excitation wavelengths was reversed (from 630 nm to 405 nm) in order to minimize any influence of photobleaching, which is expected to be the strongest for shorter wavelengths. The fluorescence intensity maps indicate homogeneous distribution of the PCP complexes across the surface, except for one agglomerate. There were two important observations: (1) the emission intensity of PCP complexes placed in the vicinity of the silver stripes was considerably higher than elsewhere, and (2) the scale of this enhancement depended on the excitation wavelength. Both results confirm that silver islands fabricated using the photochemical approach not only can be printed on the surface with remarkable accuracy, but also that these structures are plasmonically active. In other words, they can be used for controlling the optical properties of emitters located at their proximity. Calculated enhancement factors are equal to approximately 2 for 405 nm, 3 for 480 nm, 2.5 for 535 nm, and around 1.5 for 630 nm. It is known that spatial localization of the electromagnetic field by metallic nanoparticles may result in plasmon enhanced absorption in nearby emitters [21]. Indeed, the results of fluorescence imaging indicate that photochemically deposited silver stripes enhance the PCP absorption, and that this effect is wavelength-dependent, with the maximum enhancement detected for 480 nm, which corresponds approximately to the plasmon resonance.

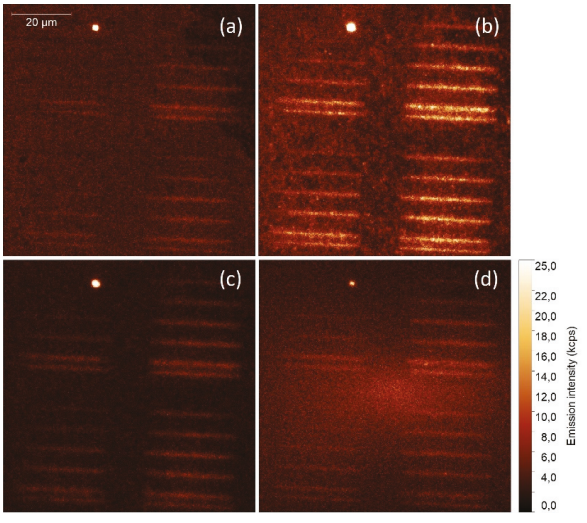

Figure 2. Photoluminescence intensity maps acquired for PCP complexes deposited on a glass substrate with photochemically deposited silver stripes. Excitation wavelengths of: (**a**) 405 nm, (**b**) 480 nm, (**c**) 535 nm, and (**d**) 630 nm were used with the excitation power of 100 μW.

In addition to enhancing the absorption, metallic nanostructures may also—under appropriate geometrical and spectral conditions—influence the radiative properties of the emitters. In order to probe this process, we compared fluorescence transients measured of PCP complexes deposited on silver stripes and on glass. For the excitation, we used picosecond lasers operating at 405 nm, 488 nm, and 630 nm. The emission was extracted using a bandpass filter (670/10 nm), matching the emission of PCP chlorophylls. The comparison plotted in Figure 1b confirms that interaction with silver stripes indeed affect the emission of chlorophyll in the protein. In contrast to the reference, the decay measured for PCPs on silver stripes consists of two components: a fast one of about 0.3 ns, and a slow one of about 2.8 ns, referring to the emission from isolated PCPs. The presence of the fast component indicates an increase of the emission rates due to the interaction with the silver stripes, known as Purcell effect [22]. In this process, the probability of spontaneous emission is increased due to modified local density of states, caused by the presence of the metallic nanoparticles [23]. Higher probability of the spontaneous emission leads to more absorption–emission cycles realized in a second by a single emitter, and thus contributes to the emission enhancement. The slow component, however, indicates that some PCP complexes are not coupled to the silver stripe—probably because of larger separation from the stripe—and decay with the rate of the reference. We found no measurable dependence of the emission dynamics on the excitation wavelength.

2.2. Up-Converting Nanocrystals

Erbium-ytterbium doped $NaYF_4$ nanocrystals were synthesized by wet chemistry, as described elsewhere [24]. They exhibit efficient anti-Stokes luminescence, commonly referred to as energy transfer up-conversion emission [25]. In this system, Yb^{3+} plays the role of a donor, whereas Er^{3+} is the acceptor of the energy. The mechanism of the energy conversion involves several electronic states of erbium and is presented in Figure 3. Nanocrystals excited at 980 nm show visible up-conversion emission lines, centered at 550 and 660 nm, assigned to the $^2H_{11/2}+^4S_{3/2}\rightarrow{}^4I_{15/2}$ and $^4F_{9/2}\rightarrow{}^4I_{15/2}$ electric-dipole transitions in Er^{3+} ions, respectively (Figure 4a) [25]. Typical photoluminescence transient acquired at 660 nm for a single NC on glass is presented in Figure 4b. The transient has a bi-exponential character, and can be globally described by the averaged time constant of about 120 µs [25].

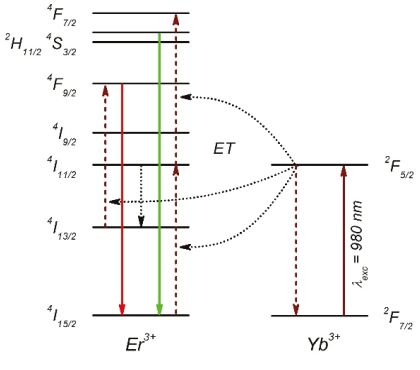

Figure 3. Simplified energy diagram of Er^{3+} and Yb^{3+}. Dotted arrows illustrate energy transfer and other non-radiative processes leading to the up-conversion photoluminescence (green and red lines).

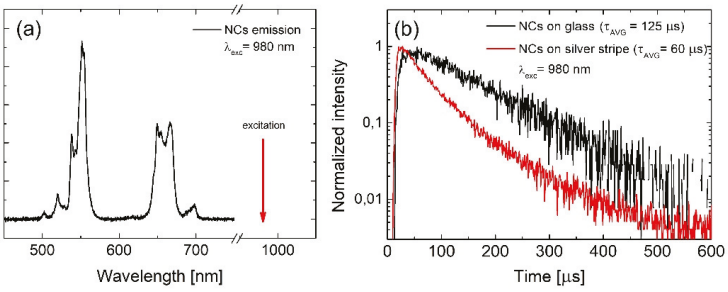

Figure 4. (**a**) Absorption and emission spectra of $NaYF_4:Er^{3+}/Yb^{3+}$ nanocrystals. (**b**) Photoluminescence transients acquired for nanocrystals deposited on glass (black line) and silver stripes (red line).

Nanocrystals, with an average diameter of about 30 nm, were dispersed in chloroform, where they form an optically stable colloid. A quantity of 10 μL of the NCs colloid (10 mg/mL) was spin-coated (3000 rpm for 1 min) on a glass substrate with previously fabricated silver stripes, as presented in Figure 5a. The concentration of the colloid was optimized to obtain a close to homogeneous layer of the nanocrystals on the sample surface. To fabricate the metallic nanostructure, we applied the same protocol of silver deposition; however, the exposure time was in this the same for each stripe (200 ms). For measuring luminescence of NCs, we used a confocal microscope (Eclipse Ti-S, Nikon, Japan) equipped with an oil immersion objective (Plan Apo 60× NA = 1.4, Nikon, Japan), a 10 mW excitation laser operating at 980 nm, and a single photon counting module (SPCM-AQR-16, Perkin Elmer, Canada). As the up-conversion is a more power-demanding process, we used a confocal excitation and detection scheme in order to assure for sufficient power densities. Photoluminescence intensity map acquired for a 660 nm emission is displayed in Figure 5b. The NCs are distributed rather homogeneously on the substrate, and similarly as for the PCP complexes, NCs placed in the vicinity of the silver stripes feature a much stronger emission compared with the reference. Indeed, there are some very bright emission spots, which we attribute to the emission originating from nanocrystals placed in the optimal positions with respect to the silver islands. In this case, the enhancement factor reaches values of about 6. The intensity of the up-conversion emission depends quadratically on the excitation power. Thus, if enhanced absorption appears, it leads to a greater enhancement factor than observed for Stokes-like emitters. Importantly, the emission pattern recorded for the second emission band of the NCs (550 nm) is identical, and show similar enhancement factor.

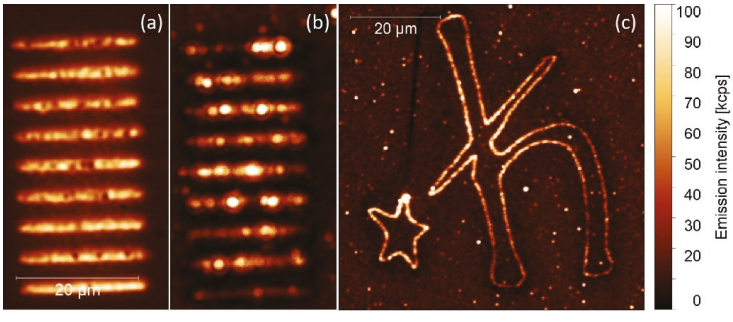

Figure 5. (**a**) Silver paths visualized by a confocal microscope. (**b**) Photoluminescence intensity maps acquired from nanocrystals (NCs) deposited on a silver-decorated glass substrate, and (**c**) from NCs deposited on arbitrarily shaped metallic structures. The excitation wavelength was 980 nm.

In analogy to the experiments carried out for the photoactive protein, PCP, in the case of the up-converting NCs, we have also performed time-resolved luminescence measurements in order to

demonstrate the influence of metallic nanostructures on the radiative processes. For the excitation, an electrically modulated laser operating at 980 nm generating pulses of about 1 μs in width was used. A typical transient collected from NCs deposited onto the silver stripes is presented in Figure 4b. While, similarly to the reference, the decay features a bi-exponential character, the global average decay time was found to be considerably shorter, namely 60 μs. We attribute the reduction of the decay constant to the increase of the emission rate due to the Purcell effect. Two-fold increase of the emission rate is not sufficient to account for the observed enhancement factors; thus, we can conclude that both processes are responsible to a similar degree for the enhancement of the emission intensity of up-converting NCs deposited over the silver stripes.

One of the key advantages of the photochemical approach described in this work concerns the ability of printing an arbitrarily shaped plasmonically active pattern. In Figure 5c, we present a luminescence image measured for up-converting NCs deposited over a 60 μm high symbol of the Dirac constant. The structure was prepared within a couple of minutes with the exposure time of 100 ms for each point. The emission was collected for the 660 nm band of the NCs upon excitation at 980 nm. In accordance with the previous results, the emission of the NCs is also strongly enhanced due to the coupling with metallic nanostructures. Indeed, the enhancement factors amount to approximately 5.

3. Materials and Methods

Plasmonically active metallic nanostructures have been prepared on glass substrates using a confocal fluorescence microscope (Eclipse Ti-S, Nikon, Tokyo, Japan), equipped with a continuous-wave laser operating at 405 nm. A high numerical aperture oil immersion objective (Plan Apo 60× NA = 1.4, Nikon, Tokyo, Japan) ensured a small, diffraction-limited diameter of the laser spot (~200 nm) for precise spatial localization of the deposited material. Subsequently, a glass coverslip (#1, Carl Roth, Neunkirchen, Germany), previously cleaned in a Hellmanex II (Hellma, Müllheim, Germany) solution, was mounted on an XY piezoelectric stage of the microscope. Then, 10 μL of a freshly prepared 2 mmol solution of silver nitrate ($AgNO_3$, >99%, Sigma-Aldrich, St. Louis, MO, USA) mixed in 1:1 proportion with 2 mmol of trisodium citrate (NaCit, >99%, Acros, Merelbeke, Belgium) was placed on top of the coverslip (Figure 6). The laser, providing an optical power of about 1 mW, which was sufficient to activate the photochemical reaction, was illuminating the sample while moving the piezoelectric stage. The duration of the reaction was controlled by the laser operation time, triggered and synchronized with the movement of the piezoelectric stage by a computer. After the photochemical deposition of silver was completed, the substrate was rinsed in distilled water and dried under ambient condition. In order to avoid silver oxidation, the substrates were used within 24 h from preparation.

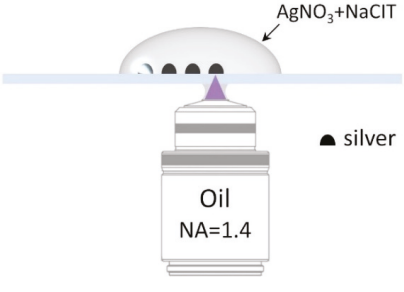

Figure 6. Geometry of the photochemical deposition of silver on a glass substrate. The glass coverslip is mounted above the microscope objective, while a droplet of $AgNO_3$ and NaCit is deposited on top. A laser (λ_{exc} = 405 nm) focused on the substrate activates the deposition of silver.

Substrates fabricated using the photochemical approach were characterized with wide-field microscopy and scanning electron microscopy (SEM). In Figure 7, we show a wide-field microscopy transmission image, where silver stripes grouped in four areas are visible. The stripes within each area

were obtained with varied exposure time per step during the fabrication. The exposure time for the first stripe was 50 ms per step of the piezoelectric stage (s = 200 nm), increasing by 50 ms for each subsequent stripe.

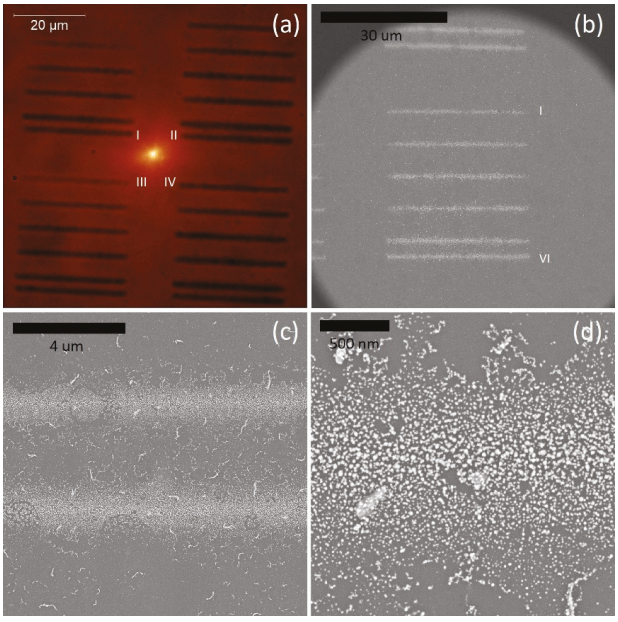

Figure 7. Photochemically synthesized silver islands observed with (**a**) a wide-field optical microscope in transmission mode, and (**b**–**d**) a scanning electron microscope.

On the other hand, the areas were obtained with a different delay time following the movement of the stage. This parameter, defined as delay time, was equal to 10 ms for the first area, 50 ms for the second, and 100 and 150 ms for the remaining two areas. The optical and SEM images (taken using a FEI Nova NanoSEM 450 scanning electron microscope) reveal the influence of both parameters on the morphology of the stripes: for the shortest time and the lowest excitation power of the laser, we found no formation of a distinguished metallic stripe. In contrast, for all other parameter pairings, a clear line emerged, which we associated with photochemical deposition of silver nanostructures. In order to gain insight into the morphology of the stripes, the same sample was analyzed using SEM, as shown in Figure 7b–d. The stripes, regardless of the particular combination of photodeposition parameters, feature an island-like morphology. With the exception of some defects, the islands are rather uniform, with diameters of a few tens of nanometers. We also observe that our approach yields a relatively well controlled distribution of silver within the stripe, as the achieved width of the stripes was of about 1 µm, and the interface between silver islands and the bare glass substrate is also rather sharp. An increase of the exposure time had little influence on the size of silver islands; however, it resulted in an increase of their surface density. Such dimensions, together with the sharp border, make these silver stripes highly promising in the context of applying them for studying plasmonically enhanced photoluminescence.

4. Conclusions

In this work, we demonstrate that silver islands deposited photochemically on glass substrates exhibit a strong plasmonic activity for both Stokes and anti-Stokes emitters. From the fabrication point of view, using this approach, we can precisely define positions of silver stripes, which are characterized

with widths of about 1 micrometer. Importantly, in the case of photoactive proteins and rare-earth doped nanocrystals we find a strong increase of the emission intensity. This effect is attributed to enhanced absorption and emission rates (Purcell effect) of these emitters, as a result of the interaction with silver stripes. By correlating the laser illumination with the position of the piezoelectric stage, a pattern of any arbitrary shape can be obtained from the photochemically deposited silver islands. The strong plasmonic activity, together with the ability to control positioning, renders these unique structures potentially applicable for optoelectronic, photovoltaic, and sensory devices.

Author Contributions: Formal analysis, D.P.; Funding acquisition, S.M. and D.P.; Investigation, M.S., K.S., M.J.-N., K.W., and D.P.; Project administration, D.P.; Supervision, S.M.; Writing—original draft, S.M. and D.P.; Writing—review and editing, J.N.-J., M.J.-N. and S.M. All authors have read and agreed to the published version of the manuscript.

Funding: This research was partially financed by the National Science Centre (Poland) within the grants 2016/21/B/ST3/02276, 2017/27/B/ST3/02457, 2016/22/E/ST5/00531, and 2017/26/E/ST3/00209, project 3/DOT/2016 funded by the City of Gdynia, and project nr POWR.03.05.00-00-Z302/17 "Universitas Copernicana Thoruniensis In Futuro" (2018-2022).

Acknowledgments: We thank Marcin Nyk for providing the nanocrystals. Inspiring discussions with Anatoliy Pinchuk are gratefully acknowledged.

Conflicts of Interest: The authors declare no conflict of interest.

References

1. Bharadwaj, P.; Anger, P.; Novotny, L. Nanoplasmonic enhancement of single-molecule fluorescence. *Nanotechnology* **2007**, *18*, 044017. [CrossRef]
2. Mauser, N.; Piatkowski, D.; Mancabelli, T.; Nyk, M.; Mackowski, S.; Hartschuh, A. Tip Enhancement of Upconversion Photoluminescence from Rare Earth Ion Doped Nanocrystals. *ACS Nano* **2015**, *9*, 3617–3626. [CrossRef] [PubMed]
3. Bharadwaj, P.; Novotny, L. Spectral dependence of single molecule fluorescence enhancement. *Opt. Express* **2007**, *15*, 14266. [CrossRef] [PubMed]
4. Wiley, B.J.; Im, S.H.; Li, Z.-Y.; McLellan, J.; Siekkinen, A.; Xia, Y. Maneuvering the Surface Plasmon Resonance of Silver Nanostructures through Shape-Controlled Synthesis. *J. Phys. Chem. B* **2006**, *110*, 15666–15675. [CrossRef] [PubMed]
5. Eustis, S.; El-Sayed, M.A. Why gold nanoparticles are more precious than pretty gold: Noble metal surface plasmon resonance and its enhancement of the radiative and nonradiative properties of nanocrystals of different shapes. *Chem. Soc. Rev.* **2006**, *35*, 209–217. [CrossRef]
6. Giannini, V.; Fernández-Domínguez, A.I.; Heck, S.C.; Maier, S.A. Plasmonic Nanoantennas: Fundamentals and Their Use in Controlling the Radiative Properties of Nanoemitters. *Chem. Rev.* **2011**, *111*, 3888–3912. [CrossRef]
7. Lakowicz, J.R. *Principles of Fluorescence Spectroscopy*, 3rd ed.; Springer: Amsterdam, The Netherland, 2006; ISBN 978-0-387-31278-1.
8. Aslan, K.; Leonenko, Z.; Lakowicz, J.R.; Geddes, C.D. Annealed silver-island films for applications in metal-enhanced fluorescence: Interpretation in terms of radiating plasmons. *J. Fluoresc.* **2005**, *15*, 643–654. [CrossRef]
9. Ciszak, K.K.; Olejnik, M.; Strzelecki, J.; Krajnik, B.; Piątkowski, D.; Hofmann, E.; Mackowski, S. Influence of Plasmon Resonance in Silver Island Film on the Optical Properties of Peridinin-Chlorophyll-Protein Light-Harvesting Complexes. *Acta Phys. Pol. A* **2012**, *122*, 275–278. [CrossRef]
10. Ray, K.; Badugu, R.; Lakowicz, J.R. Metal-Enhanced Fluorescence from CdTe Nanocrystals: A Single-Molecule Fluorescence Study. *J. Am. Chem. Soc.* **2006**, *128*, 8998–8999. [CrossRef]
11. Czechowski, N.; Lokstein, H.; Kowalska, D.; Ashraf, K.; Cogdell, R.J.; Mackowski, S. Large plasmonic fluorescence enhancement of cyanobacterial photosystem I coupled to silver island films. *Appl. Phys. Lett.* **2014**, *105*, 043701. [CrossRef]
12. Turrell, G.; Corset, J. *Raman Microscopy: Developments and Applications*; Academic Press: Cambridge, MA, USA, 1996; ISBN 978-0-08-054025-2.

13. Staiano, M.; Matveeva, E.G.; Rossi, M.; Crescenzo, R.; Gryczynski, Z.; Gryczynski, I.; Iozzino, L.; Akopova, I.; D'Auria, S. Nanostructured Silver-Based Surfaces: New Emergent Methodologies for an Easy Detection of Analytes. *ACS Appl. Mater. Interfaces* **2009**, *1*, 2909–2916. [CrossRef]
14. Geddes, C.D.; Parfenov, A.; Lakowicz, J.R. Photodeposition of Silver Can Result in Metal-Enhanced Fluorescence. *Appl. Spectrosc.* **2003**, *57*, 526–531. [CrossRef] [PubMed]
15. Jiang, K.; Spendier, K.; Pinchuk, A.O. *Laser-Directed Deposition of Silver Nanostructures*; Boardman, A.D., Ed.; SPIE: Washington, DC, USA, 2014; p. 916314.
16. Kleima, F.J.; Wendling, M.; Hofmann, E.; Peterman, E.J.G.; van Grondelle, R.; van Amerongen, H. Peridinin Chlorophyll a Protein: Relating Structure and Steady-State Spectroscopy. *Biochemistry* **2000**, *39*, 5184–5195. [CrossRef]
17. Mackowski, S. Hybrid nanostructures for efficient light harvesting. *J. Phys. Condens. Matter* **2010**, *22*, 193102. [CrossRef] [PubMed]
18. Shang, Y.; Hao, S.; Yang, C.; Chen, G. Enhancing Solar Cell Efficiency Using Photon Upconversion Materials. *Nanomaterials* **2015**, *5*, 1782–1809. [CrossRef] [PubMed]
19. Olejnik, M.; Krajnik, B.; Kowalska, D.; Twardowska, M.; Czechowski, N.; Hofmann, E.; Mackowski, S. Imaging of fluorescence enhancement in photosynthetic complexes coupled to silver nanowires. *Appl. Phys. Lett.* **2013**, *102*, 083703. [CrossRef]
20. Szalkowski, M.; Olmos, J.D.J.; Buczyńska, D.; Maćkowski, S.; Kowalska, D.; Kargul, J. Plasmon-induced absorption of blind chlorophylls in photosynthetic proteins assembled on silver nanowires. *Nanoscale* **2017**, *9*, 10475–10486. [CrossRef]
21. Anger, P.; Bharadwaj, P.; Novotny, L. Enhancement and quenching of single-molecule fluorescence. *Phys. Rev. Lett.* **2006**, *96*, 113002. [CrossRef]
22. Purcell, E.M. Spontaneous Emission Probabilities at Radio Frequencies. *Phys. Rev.* **1946**, *69*, 681.
23. Barnes, W. Fluorescence near interfaces: The role of photonic mode density. *J. Mod. Opt.* **1998**, *45*, 661–699. [CrossRef]
24. Kumar, R.; Nyk, M.; Ohulchanskyy, T.Y.; Flask, C.A.; Prasad, P.N. Combined Optical and MR Bioimaging Using Rare Earth Ion Doped NaYF4 Nanocrystals. *Adv. Funct. Mater.* **2009**, *19*, 853–859. [CrossRef]
25. Piatkowski, D.; Hartmann, N.; Macabelli, T.; Nyk, M.; Mackowski, S.; Hartschuh, A. Silver nanowires as receiving-radiating nanoantennas in plasmon-enhanced up-conversion processes. *Nanoscale* **2015**, *7*, 1479–1484. [CrossRef] [PubMed]

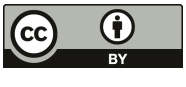

International Journal of
Molecular Sciences

MDPI

Review

Silver Island Film for Enhancing Light Harvesting in Natural Photosynthetic Proteins

Dorota Kowalska [1,*], Marcin Szalkowski [1,2], Karolina Sulowska [1], Dorota Buczynska [3], Joanna Niedziolka-Jonsson [3], Martin Jonsson-Niedziolka [3], Joanna Kargul [4], Heiko Lokstein [5] and Sebastian Mackowski [1,*]

1 Institute of Physics, Faculty of Physics, Astronomy and Informatics, Nicolaus Copernicus University in Torun, Grudziadzka 5, 87-100 Torun, Poland; marszal@fizyka.umk.pl (M.S.); sulowska@doktorant.umk.pl (K.S.)
2 Institute of Low Temperature and Structure Research, Polish Academy of Sciences, Okolna 2, 50-422 Wrocław, Poland
3 Institute of Physical Chemistry, Polish Academy of Sciences, Kasprzaka 44/52, 01-224 Warszawa, Poland; dbuczynska@ichf.edu.pl (D.B.); jniedziolka@ichf.edu.pl (J.N.-J.); martinj@ichf.edu.pl (M.J.-N.)
4 Solar Fuels Laboratory, Centre of New Technologies, University of Warsaw, Banacha 2C, 02-097 Warsaw, Poland; j.kargul@cent.uw.edu.pl
5 Department of Chemical Physics and Optics, Charles University, Ke Karlovu 3, 12116 Prague, Czech Republic; lokstein@karlov.mff.cuni.cz
* Correspondence: dorota@fizyka.umk.pl (D.K.); mackowski@fizyka.umk.pl (S.M.)

Received: 29 February 2020; Accepted: 30 March 2020; Published: 1 April 2020

Abstract: The effects of combining naturally evolved photosynthetic pigment–protein complexes with inorganic functional materials, especially plasmonically active metallic nanostructures, have been a widely studied topic in the last few decades. Besides other applications, it seems to be reasonable using such hybrid systems for designing future biomimetic solar cells. In this paper, we describe selected results that point out to various aspects of the interactions between photosynthetic complexes and plasmonic excitations in Silver Island Films (SIFs). In addition to simple light-harvesting complexes, like peridinin-chlorophyll-protein (PCP) or the Fenna–Matthews–Olson (FMO) complex, we also discuss the properties of large, photosynthetic reaction centers (RCs) and Photosystem I (PSI)—both prokaryotic PSI core complexes and eukaryotic PSI supercomplexes with attached antenna clusters (PSI-LHCI)—deposited on SIF substrates.

Keywords: SIF; photosynthetic complexes; biohybrid structures; MEF

1. Introduction

Among the grand challenges for science in the 21st century, environmental pollution together with a possible energy crisis and the necessity for developing new renewable energy sources stand out as the most critical [1,2]. All of them are, in fact, branches of the same tree, since a considerable part of pollution and degradation of the environment originates from the combustion of fossil fuels. In this regard, developing sources of clean energy seems to be the prerequisite to address and fix (at least partially) these important issues [2–4]. Most renewable energy sources are powered by the sun—directly or indirectly; its radiation energy induces fluctuations of air pressure, which result in winds, as well as water circulation in natural environment [5–7]. Both of these natural sources have been used for electric power generation. However, in the case of approaches based on secondary effects of solar activity, significant energy losses are unavoidable, since at each step of the energy conversion chain, a fraction is dissipated as heat. Thus, in order to use the solar energy more efficiently, the direct conversion of solar energy seems to be the approach of choice [3,4,8–10]. Currently available

solar cells, based on the photoelectric effect in crystalline materials (mainly silicon), reach conversion efficiencies up to 26%. The values are limited, for instance, by low efficiency of absorption in the infrared region of the solar spectrum [10–14]. Possible ways of improvement can be inspired by nature—naturally evolved pigment–protein complexes forming the energy conversion apparatus in photosynthetic organisms are able to carry out charge separation. Moreover, they achieve remarkably high ratios of separated charges per captured photon, which can be close to unity [15,16]. This high efficiency originates from the optimization of nanoscale cofactor arrangements over billions of years of evolution. Furthermore, analogously to the processes taking place in photosynthesis-performing organisms, which use captured solar energy for biosynthesis of carbohydrates, biomimetic solar cells should be able to generate not only photovoltage, but simple organic fuels as well [4,8].

One of the key issues related to developing solar energy conversion devices concerns the improvement of the absorption rate [9,17], conversion efficiency [18], stability of the working modules [19] and selectivity of the catalytic reactions in the case of solar-to-chemical devices. With respect to increasing and/or tuning the absorption of natural and artificial photosynthetic molecular systems, encouraging results have been achieved using metallic nanostructures [9,20–23]. These nanostructures exhibit a unique property associated with collective oscillations of electrons induced by electromagnetic waves: so-called plasmons [9,17]. It has been shown in numerous reports that plasmons excited in metallic nanostructures can affect the optical properties of emitters placed in their vicinity (at distances of up to tens of nm). This interaction, however, is generally rather complex, with the net result ranging from strongly enhanced fluorescence (due to increase of local electric field intensity or the Purcell effect) to fluorescence quenching and energy dissipation [9,17,24]. Indeed, plasmonic effects depend on several parameters, such as the relation between the optical spectra of metallic nanostructures and emitters, as well as their geometrical arrangement, particularly the distance between the components [9,21,24,25]. Therefore, by changing sizes or shapes of metallic nanoparticles, it is possible to tune the position of the plasmon resonance to match the optical spectra of emitters [9,21,26]. Additionally, the geometry of the hybrid photosynthetic structure can be tested and optimized for achieving the required functionality [27–31]. Within the infinite variety of metallic nanostructures, in the context of photosynthetic hybrid devices, Silver Island Film (SIF) [25] seems to be close to the optimal choice. First of all, SIFs can be deposited in a rather straightforward way on large substrates, overcoming the necessity of using expensive techniques, such as electron beam lithography or evaporation approaches. In addition, SIF structures feature very broad absorption spectra associated with the plasmon resonance in islands of varied size. In this way, plasmon resonances can affect the optical properties of natural and artificial photosynthetic complexes within an exceptionally broad spectral range.

In this review, we present the results of comprehensive studies carried out for a variety of photosynthetic complexes either solely responsible for the absorption of the solar energy, or those which participate in photochemistry (charge separation and electron transfer) upon coupling to SIF structures. A schematic representation of a hybrid photosynthetic nanostructure and the effect of plasmonic interactions between SIFs and photosynthetic complexes are presented in Figure 1. For clarity's sake, the selected hybrid systems are described in order of increasing complexity and the number of chlorophyll *a* (Chl *a*) molecules. Finally, to show the influence of SIF chemistry and morphology, hybrid structures containing Photosystem I (PSI)—the photosynthetic supercomplex with the largest number of Chl *a* molecules—and SIF substrates fabricated with different approaches are presented.

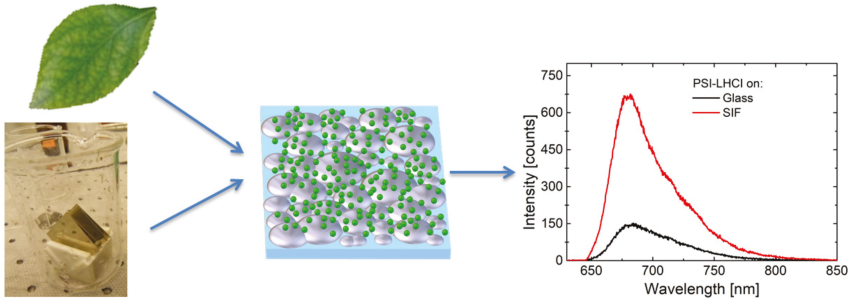

Figure 1. Schematic concept of a hybrid photosynthetic nanostructure and the effect of plasmonic interactions between Silver Island Film (SIF) and photosynthetic proteins.

1.1. Photosynthetic Complexes

The light-harvesting peridinin-chlorophyll-protein (PCP) from the dinoflagellate *Amphidinium carterae* [20] in its native form is a trimer, where each of the monomers comprises eight peridinin molecules and two Chls *a* embedded in a protein scaffold [20,32–34]. As shown in Figure 2b, the absorption spectrum of PCP (black) features a band in the range from ~400 to 550 nm due to peridinins, while Chl *a* molecules absorb light in the Soret band (with a maximum around 440 nm) and in the Q_y region from 600 to 670 nm. The fluorescence spectrum of PCP (red) has a maximum at the wavelength of 673 nm, which corresponds to the emission of Chl *a*. The small size of PCP, together with its rather simple structure, renders this complex a very good model system for studying the interactions in plasmonic (bio)hybrid nanostructures.

The reaction center (RC) from *Chlorobaculum* (*C.*) *tepidum* is an example of a much larger complex, as compared to PCP, although its detailed structure is not known at present. It contains bacteriochlorophyll *a* (BChl *a*), Chls *a*, and carotenoid molecules [35–40]. The contribution of each type of pigment is visible in the absorption spectrum (Figure 2d). This RC can be associated with one or several Fenna–Matthews–Olson (FMO) protein complexes [39,41], whose absorption spectrum is shown in Figure 2c. The structure of the FMO complex is known, FMO forms trimers, each monomer contains seven (or eight) BChl *a* molecules, very strongly coupled to each other [23,42–46]. Fingerprints of FMO absorption can be recognized in the RC absorption spectrum (cf. Figure 2c,d). FMO acts not only as light-harvesting complex, but also takes part in transferring energy from the outer antenna complexes (chlorosomes) to the RCs [43,44].

The analogue to the RC from *C. tepidum* in higher plants, algae, and cyanobacteriais a very large pigment–protein complex, Photosystem I (PSI). PSI is the key component of the oxygenic photosynthetic apparatus [15], since it converts photon energy to separated charges, which are used for the biosynthesis of organic molecules, like sugars [4,8,16]. While there are differences in the structures of antenna systems of PSI in different organisms, photosystem cores, adapted and optimized during evolution, are largely conserved [15]. In this work we use eukaryotic PSI complex with its peripheral light-harvesting antenna (PSI-LHCI supercomplex) from a red microalga *Cyanidioschyzon merolae*. Medium resolution structures of this supercomplex have been recently reported [47–49]. The red algal PSI-LHCI supercomplex is a monomer binding up to 210 Chl *a* molecules and up to 54 carotenoids [47]. Absorption and emission spectra of this protein are presented in Figure 2e. In addition, we studied the PSI complex from *Thermosynechococcus* (*T.*) *elongatus*, also with a known crystal structure [50–52]. Each of the monomers forming the PSI trimer binds 96 Chl *a*, and 22 carotenoids [50–52]. Absorption and emission spectra of PSI are shown in Figure 2f.

The experimental studies described in this work concern large ensemble of photosynthetic complexes, giving the results a strong generality component, in particular regarding the influence of plasmon excitations on energy transfer pathways and activation of natively blind pigments in multichromophoric PSI.

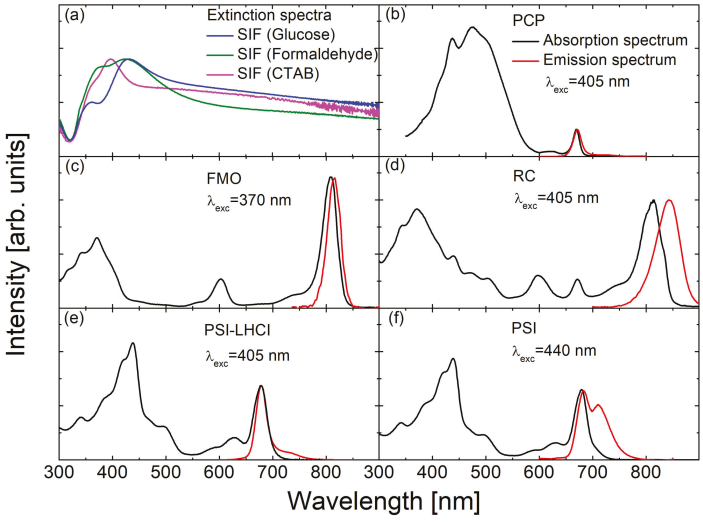

Figure 2. Optical characterization of the SIF substrates (**a**) and the pigment–protein complexes: peridinin-chlorophyll-protein (PCP) (**b**), Fenna–Matthews–Olson (FMO) (**c**), reaction centers (RC) (**d**), Photosystem I with attached antenna clusters (PSI-LHCI) supercomplex (**e**), and Photosystem I (PSI) complex (**f**). Absorption spectra are marked in black; emission spectra are shown in red. Excitation wavelengths are also given in each case.

1.2. Silver Island Films

SIF structure typically consists of irregular silver islands, around 50–200 nm in size, deposited randomly on a substrate [53]. There are several methods of SIF preparation with an approach based on wet chemistry being the most feasible for potential applications. Synthesis of SIFs is in general rather fast, requires no sophisticated experimental setups, and it is also relatively inexpensive—small amounts of ingredients are needed to prepare solutions necessary for depositing SIFs over large substrates. Since SIF is a planar structure, it can be easily adapted into a solar energy-converting device, which often is designed in a form of flat panels, where all components are arranged in a layer-by-layer geometry. Furthermore, by varying the parameters of the chemical reactions, one can control the properties of the SIFs, especially the density of silver islands on the substrate can be tuned. Thus, the transparency of the electrode may be regulated. All these features are advantageous for designing solar energy converting devices. Preparation of SIFs using wet chemistry is, however, characterized by relatively low reproducibility. It is challenging to produce structures with identical morphology of the islands (sizes, density, etc.), which translates into differences in the optical properties. Some of these factors are averaged out since the sizes of silver islands and proteins are less than 100 nm, and the interactions related to plasmonic coupling occur oneven smaller length scales.

For most of the results presented in this survey, a wet-chemistry SIF preparation was used, in which glucose was added at the last stage [25]. This straightforward and low-cost method allows us to prepare SIF substrates with varying density of silver islands, which can be tuned by reaction parameters, such as temperature or time. Scanning electron microscopy (SEM) pictures of the obtained SIF substrates are presented in Figure 3a. Although plasmonic SIF substrates fabricated using this approach have been widely applied in metal-enhanced fluorescence studies [22,23,41,53], some of the glucose used in the synthesis tends to adhere to the SIF surface forming a layer. This may be sufficiently thin to allow for efficient plasmonic interactions; however, it may still form a barrier for chemical functionalization of the surface and controlled immobilization of emitters. This layer may be removed by heating, but such a treatment can also influence the SIF morphology. The preparation of SIFs is also possible by reduction of

silver nitrate by formaldehyde (Figure 3b) in basic solution. The preparation time is significantly longer (two hours in dark vs. several minutes) and the substrates exhibit lower densities of silver islands and somewhat reduced homogeneity as compared to SIF (glucose). On the other hand, since formaldehyde evaporates at room temperature, it is possible to prepare contamination-free SIF substrates, thus opening ways for their functionalization. Preparation of SIF (using cetyltrimethylammonium bromide, CTAB) is more complex (Figure 3c) [54]. In this method, a two-step procedure is applied: first, carefully cleaned substrates were immersed in a pre-prepared aqueous solution of ~4-nm-sized Ag colloids and incubated for two hours [54,55]. Afterwards, the substrates were transferred from the seed solution to a growth solution containing CTAB, in which during overnight incubation silver islands can develop [54,55]. However, this method also leaves some contamination by CTAB.

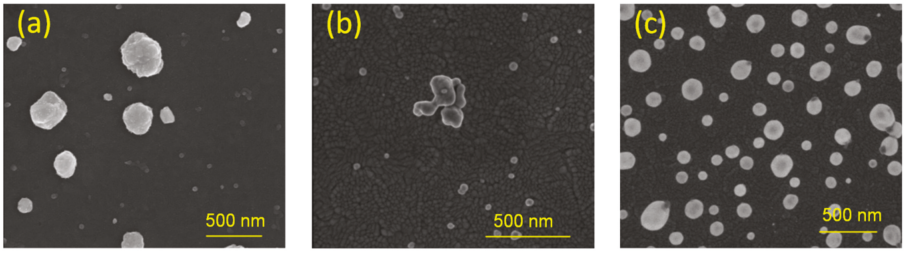

Figure 3. Scanning electron microscopy images of SIF substrates prepared with wet-chemistry methods, using glucose (**a**), formaldehyde (**b**) and cetyltrimethylammonium bromide (CTAB) (**c**). The scale bar is 500 nm.

One of the most important parameters of SIF substrates from the point of view of using them as plasmonically active building blocks for hybrid nanostructures is the spectral position and shape of the plasmon resonance. Typical extinction spectra of the used substrates are shown in Figure 2a. In the case of SIF (glucose) and SIF (formaldehyde), blue and green lines are used, respectively. The maximum of the resonance peak is at ~ 430 nm, while for SIF (CTAB) it is blue-shifted to 400 nm. Nevertheless, in every case the resonance peak is very broad, covering not only the visible range, but also a substantial wing reaching the near IR. This is promising, since solar cells employing plasmonic effects should be optimized for higher efficiency under typical solar radiation, which has the highest intensity in the visible range [10,46]. Lastly, these broad optical spectra of SIF substrates overlap rather well with the absorption spectra of many photosynthetic complexes.

In the following, we present selected results of using SIFs for engineering the optical properties of photosynthetic complexes, both simple antenna complexes, as well as large, complex photosystems. The basic effect, common for such hybrid structures, is a strong enhancement of the fluorescence intensity of the respective fluorophores. The determined enhancement factors (EFs) of fluorescence reach values as high as 300.

2. Methods

Absorption spectra of the SIF structures and photosynthetic complexes in solution were obtained using a Cary 50 spectrophotometer, while fluorescence spectra were recorded using a Fluorolog-3 spectrofluorometer (JobinYvon). Spectrally and time-resolved fluorescence measurements with high spatial resolution were performed using a home-built confocal fluorescence microscope, as described previously [22,23,41]. In a typical experiment, after acquiring a fluorescence map, a few tens of emission spectra were measured in order to gain statistically relevant information. Particularities regarding the experimental approach and analysis of the results are specified in each section devoted to the actual photosynthetic complex studied.

3. The Effect of SIF on the Optical Properties of Photosynthetic Complexes

3.1. Simple Photosynthetic Antenna Complexes

The concept of introducing SIF structures as substrates for enhancing the optical properties of organic dyes was postulated and experimentally demonstrated by the group of J. Lakowicz [17,25,53,56]. In these studies, a comparatively simple description of the interactions in such a system was presented, together with an extensive discussion of possible applications of the plasmonic excitations for controlling the radiative properties of fluorophores. In 2007 the group of J. Lakowicz reported a 9-fold increase in fluorescence emission intensity and up to a 7-fold decrease in emission lifetime for phycobiliproteins deposited on SIFs [57]. In the next year, a study followed, in which the results of ensemble and single-molecule spectroscopy of peridinin−chlorophyll−protein (PCP) deposited on SIF were described [20]. The key result of this study was the observation of strongly enhanced emission and absorption of these complexes through plasmonic interactions with SIF. It was shown that the measured values of the EFs depend on the excitation wavelength, which, in the case of even this rather simple photosynthetic complex, is indicative of exciting different molecules bound to the complex. As shown in Figure 4, in the case of peridinin excitation, at 532 nm, an average EF of 6 is achieved. In contrast, direct excitation into the absorption band of Chls results in somewhat stronger increase of fluorescence intensity, which amounts to 8.5 (Figure 4b). This may be a counterintuitive observation, as the values of EFs are lower in the case of excitation closer to the maximum of the plasmon resonance in the SIF layer. However, it seems to be due to the multichromophoric character of such photosynthetic complexes. When Chls are excited directly, the only interaction that plays a role in determining the actual EF values is the interaction between these molecules and the plasmon excitations. On the other hand, excitation at 532 nm populates excited states of peridinin, which upon absorption of light can transfer excitation energy to Chl molecules [58]. In other words, plasmon excitations in the SIF layer may influence excitation of peridinin molecules, emission of Chl molecules as well as the dynamics of the excitation energy transfer between them. Hence, importantly, for multichromophoric and interacting systems such as photosynthetic complexes, the description of the influence of plasmon excitation on their optical properties is more complex. This is not only a direct consequence of the relation between the spectral properties of the metallic nanostructure and the complexes, but also of inter-pigment interactions. One critical consequence of this observation concerns the requirement for using spectrally selective spectroscopy to study and understand the effects of plasmonic enhancement in photosynthetic hybrid nanostructures, as even in such a simple complex as PCP the inter-pigment interactions can be clearly demonstrated.

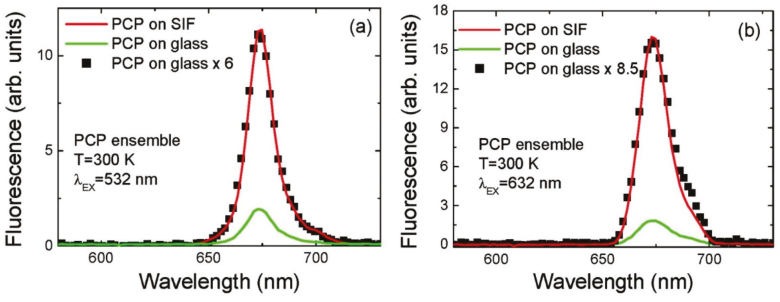

Figure 4. (**a**) Average fluorescence emission spectra measured for PCP ensembles on bare glass (green) and SIF-coated coverslips (red) excited at 532 nm. Black points correspond to the spectrum measured for PCP on glass multiplied by a factor of six. (**b**) Average fluorescence emission spectra measured for PCP ensembles on bare glass (green) and SIF-coated coverslips (red) excited at 632 nm. Black points correspond to the spectrum measured for PCP on glass multiplied by a factor of 8.5. "Reprinted (adapted) with permission from [20]. Copyright (2020) American Chemical Society."

Another observation that is typical for hybrid nanostructures based on SIFs (or other metallic nanoparticles) is a much broader distribution of fluorescence intensities collected at different spots on the sample. First of all, in the case of a layer of emitters deposited on glass, the distribution of emission intensities is usually rather narrow, indicating homogeneity of the layer. Introducing plasmonic interactions broadens the distribution [59]. On the other hand, the strength of plasmonic interactions depends strongly on the distance between emitters and metallic nanostructures. This will induce additional dispersion of fluorescence intensity. Namely, the complexes placed at the optimal distance to the SIF layer the intensity can be enhanced even by a few orders of magnitude, while those located very close to the metallic surface show decreased emission intensity (quenching). Indeed, the emission measured for the latter is less not only in comparison with those in the optimal distance, but also with the average intensity measured for the reference structure [58]. Another important contribution to broadening of fluorescence intensities may come from the sizes of the pigment–protein complexes themselves, which can be large enough to experience variations of plasmon-induced influence on the optical properties of pigments even within a single complex. This is not the case for PCP, which is approximately 4 nm in size, and it can be assumed that all of the pigments within the complex interact with the plasmons in SIF with comparable strength. However, large photosystems, which bind tens or even hundreds pigments, feature dimensions exceeding 10 nm [60], which is sufficient to observe effects associated with differences in plasmonic interactions within these complexes [16,22,30,31,41,61–66].

The influence of plasmonic excitations on the distribution of measured fluorescence intensities can be visualized using the results obtained for the light-harvesting FMO complex: In this work, layers with two different concentrations of the FMO protein were deposited on SIF [23]. The FMO concentrations were corresponding to optical densities of 0.25 and 0.05 for the c_1 and c_2, respectively. For both concentrations the emission intensity was considerably enhanced for the SIF-containing samples, as shown in Figure 5. Comparison of the average emission spectrum (Figure 5a) and histograms of emission intensities extracted from 50 spectra of FMO, both on glass (black) and SIF (blue and red) substrates, respectively, yields average enhancement factors of 40. At the same time, maximum values of a 60-fold increase of total emission intensity were observed, apparently for optimal distances and orientations of FMO with respect to the silver islands.

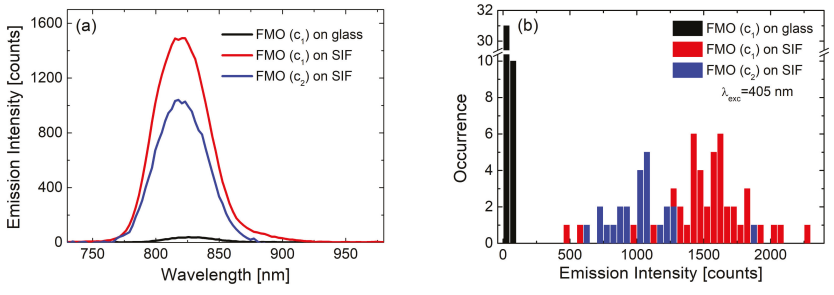

Figure 5. (**a**) Comparison between the emission spectra of FMO on glass (black line for concentration c_1) and on SIF (red line and blue line for concentration c_1 and c_2 respectively) excited at 405 nm; (**b**) corresponding histograms of the maximum emission intensities of FMO on glass (black bars) and on SIF (blue and red bars).

These are remarkably high values for relatively simple, non-specifically oriented light-harvesting complexes. Indeed, the EFs observed for FMO deposited on SIFs are approximately one order of magnitude higher than for PCP. Similarly, as in the case of PCP, the spectrum of the FMO complex deposited on a SIF layer is essentially unaffected by the presence of the metallic nanostructure. This indicates that the protein is intact and intra-protein energy transfer pathways are efficient. Combining steady-state fluorescence spectroscopy with time-resolved experiments, in which fluorescence dynamics

are probed, provides information about the dominant mechanism responsible for the enhancement of fluorescence intensity. These experiments were carried out in the same way as collecting of fluorescence spectra: many fluorescence decay curves were measured for FMO deposited on SIFs and glass substrates. As can be seen in Figure 6, the shapes of typical fluorescence decay curves of FMO deposited on both glass (black) and SIFs (red) are, essentially, similar. This observation is further corroborated by analyzing the decay curves using bi-exponential fitting. Histograms of the extracted decay constants are compared in Figure 6b. As no measurable effect of plasmonic excitations on the fluorescence dynamics is observed, it can be concluded that in the case of FMO complexes deposited on SIFs, the primary mechanism of fluorescence enhancement is associated with an increase of FMO absorption upon coupling with plasmon excitations in the SIF layer.

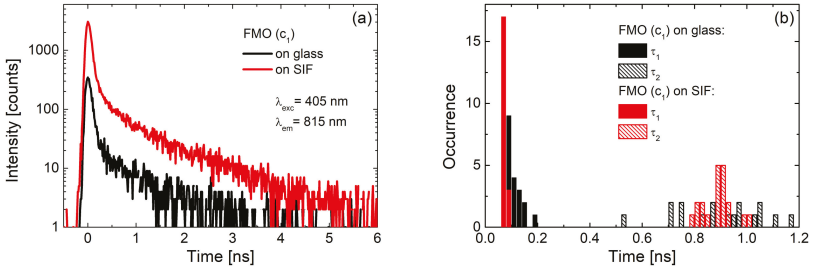

Figure 6. Results of time-resolved experiments for the c_1 concentration of FMO: (**a**) fluorescence decay curves of FMO on glass (black) and on SIF (red) and (**b**) histograms of fluorescence lifetimes of FMO deposited on glass (black bars) and on SIF (red bars).

The contribution of the FMO complexes to the optical response of FMO-containing RCs is clearly visible in the experiment, in which RCs from *C. tepidum* were deposited on a SIF layer [41]. As already pointed out, in order to detect the influence of plasmonic excitations on the components of the photosynthetic complexes, it is necessary to measure the optical response as a function of the excitation wavelength. In particular, in these experiments, several excitation wavelengths across the absorption spectrum of the RCs (tuned into different cofactors) were used. These included: 405 nm (tuned into Chl *a* and BChl *a*), 485 nm (tuned to carotenoids), 589 nm (tuned to Bchl *a* within FMO) and 640 nm (tuned to Chl *a*). The fluorescence intensity of RC emission was enhanced upon depositing the complex on a SIF layer, however, a remarkable variation of the shapes of the emission spectra was found as a function of the excitation wavelength. Therefore, in this case, the EFs were calculated for narrow, 20-nm-wide intervals across the spectrum. After this, averaged enhancement factors were calculated for each slice of emission and excitation wavelength combination. Figure 7a summarizes the results of the analysis in the form of a 3D graph, where average EFs as a function of the excitation wavelength are displayed for emission stripes. The lowest EF values were found for excitation at 405 nm (8). However, for other excitation wavelengths, EFs reached considerably higher values, often being in the range of several tens. The actual EF value might be related to the excitation wavelength and corresponding shape of the plasmon resonance of the SIF. Indeed, the shape of the extinction spectrum can be assigned to the efficiency of inducing plasmon excitations in the metallic nanostructure, and to the strength of the interaction [67]. At the same time, changes in the emission spectra as a function of the excitation wavelength point towards spectrally selective coupling with respect to the pigments in the RC complex that are excited.

An interesting effect is observed when distributions of EFs measured for different excitation wavelengths are compared. In a standard system of a simple complex, such as PCP, we can expect a Gaussian distribution of the measured fluorescence intensities and a resulting Gaussian distribution of the EFs. Moreover, as already discussed, such a distribution is expected to be considerably broader than the analogous distribution for a reference (where complexes are deposited on a glass substrate).

Indeed, for most of the excitation wavelengths used in this experiment, we observe close to normal distributions of fluorescence intensities and EFs. Upon exiting individual cofactors within the RCs (Chl *a*, BChl *a* or Car), in spite of the observed distribution of fluorescence intensities, the patterns remain unchanged: a strong increase of fluorescence intensity is measured due to interaction with plasmonic excitations and the corresponding distribution of EFs can be approximated with a single Gaussian [41].

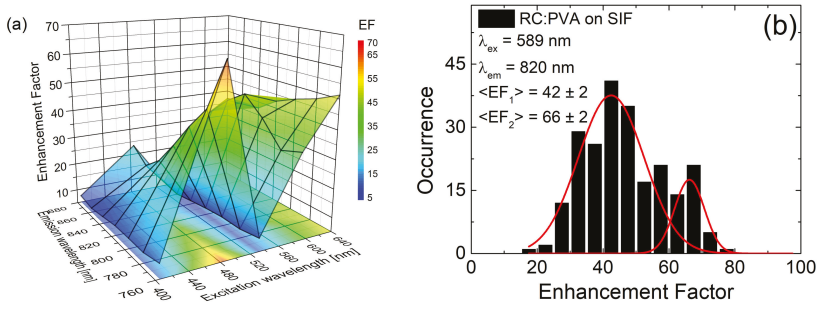

Figure 7. (**a**) Three-dimensional graph of enhancement factors (EFs) of emission intensities of *Chlorobaculum tepidum* RCs in function of excitation and emission wavelength; (**b**) histogram of EFs of RCs deposited on SIF (black bars) calculated for excitation at 589 nm and emission at 820 nm. Bimodal normal functions, fitted to the calculated EFs are shown (red lines) in the figure.

A qualitatively different behavior is observed for *C. tepidum* RCs deposited on SIFs upon excitation at 589 nm. For this excitation, the distribution of EFs exhibits a bimodal character, as can be seen in Figure 7b, where two maxima can be distinguished with values of around 40 and 70. Despite the fact that the detailed structure of the RC is not known yet, it is possible to understand the origin of such a bimodal EF distribution. The band at 589 nm corresponds almost exclusively to FMO absorption. Moreover, the observed EFs are comparable to those measured for FMO-only structures deposited on SIF. Therefore, the bimodal distribution of the measured fluorescence intensities (and the corresponding EFs) can be attributed to variations in the efficiency of plasmonic interactions with the RCs and FMO complexes attached to the RCs. Namely, one of the peaks can be related to direct interaction between RCs and plasmons in SIF (70-fold enhancement), while the other (40-fold enhancement) originates from the interaction between plasmons and FMO complexes.

3.2. SIF Substrates Obtained with Different Methods of Wet-Chemistry

The interaction between emitters and metallic nanostructures strongly depends on the distance between them. Moreover, shapes and sizes of metallic nanoparticles, as well as their density (in other words, the coverage of silver islands on the substrate), also have an impact on the measured behavior. In order to elucidate these effects, three SIF substrates were fabricated, using different methods of wet-chemistry. After this, the SIF substrates were covered with photosynthetic complexes: PSI-LHCI from *C. merolae* and PSI from *T. elongatus*. All SIF substrates used in these studies were semi-transparent, characterized by comparatively low density of silver islands. Such SIF structures allow for observation of plasmonic effects, due to relatively high transparency. Moreover, they can be considered for various applications, like sensor platforms or substrates for biohybrid solar cells. On the other hand, high transparency of SIF substrates may result in weaker interactions with fluorophores: In contrast to dense, non-transparent SIF substrates, one has to take into account the actual spatial arrangement of the sample, the sizes of silver islands and complexes as well as their relative distances. The size of the silver islands is around 50–200 nm [22,53], while photosystems, despite being relatively large supercomplexes, are roughly one order of magnitude smaller. Thus, when silver islands are deposited sparsely on the surface, many complexes deposited between them are at distances exceeding

the typical range of plasmonic interactions (Figure 8). Therefore, in such samples it is necessary to consider not only the vertical dimension (i.e., the thickness of the protein layer(s) and how far PSI is placed from the SIF metallic surface), but also the horizontal dimension (which is the relative density of silver islands compared to their sizes and the sizes of the complexes). As a result, although there can be some PSI complexes placed at optimal distances to silver islands, thus exhibiting strong enhancement of emission, the overall fluorescence may remain unchanged reduced due to a much larger number of PSI complexes unaffected by plasmonic excitations in the SIF layer. Both vertical and horizontal spatial arrangements might cause differences in the observed macroscopic results, when averaged over the observed sample area resulting in different fluorescence intensities or changes in fluorescence dynamics [17,25,56].

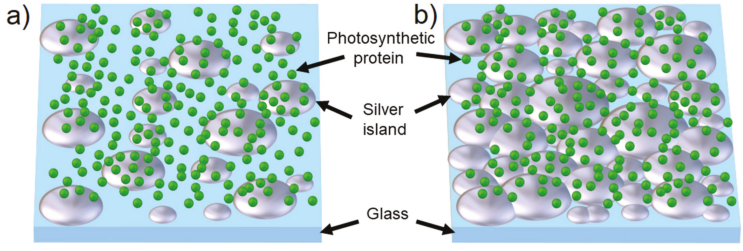

Figure 8. Schematic concept of the difference between semi-transparent (**a**) and dense (**b**) SIF layers in biohybrid nanostructure. The concentration of photosynthetic complexes is the same for both samples.

Fluorescence intensity enhancements of PSI-LHCI were compared for SIF substrates fabricated with all three preparation methods, namely SIF (glucose), SIF (formaldehyde) and SIF (CTAB). Two excitation wavelengths, 405 nm and 570 nm, were used in this experiment, tuned to the spectral regions corresponding to Chl *a* and carotenoid absorption bands, respectively. Moreover, at 405 nm PSI-LHCI absorption is high, while it is low at 570 nm. Furthermore, these two excitation wavelengths have different intensities in the plasmon resonance spectrum. Average fluorescence spectra obtained with 405 nm excitation for PSI-LHCI on glass (black), SIF (glucose) (red), SIF (formaldehyde) (blue) and SIF (CTAB) (green) are presented in Figure 9a, with the corresponding histograms of emission intensities shown in Figure 9b. The determined averaged EFs are relatively low: five, five and one, respectively. In the case of the excitation at 570 nm, the following EFs were achieved: seven, one and 0.2, respectively.

Analogous experiments to those described above for the PSI- LHC supercomplex were carried out for PSI from *T. elongatus*. Although the trimeric PSI binds more Chl *a* molecules than the red algal PSI-LHCI supercomplex, its interaction with plasmonic SIF substrates seems to result in similar EF values. In this experiment, the same excitation wavelengths of 405 nm and 570 nm were used. These also correspond to (high) Chl *a* absorption and absorption of carotenoids. The averaged values of EFs extracted for the excitation wavelength of 405 nm are five, three and one for SIF (glucose), SIF (formaldehyde) and SIF (CTAB), respectively. On the other hand, excitation at 570 nm yields EF values of eight, 12 and 0.8 for SIF (glucose), SIF (formaldehyde) and SIF (CTAB), respectively.

It is clearly visible that the results depended strongly on the substrate type used for assembly of the hybrid nanostructure. In particular, for SIF (CTAB), the measured values exhibit essentially no enhancement of PSI fluorescence intensity when compared to the glass substrate (when excited at 405 nm) or even a reduction of fluorescence signal (for excitation at 570 nm). This may be caused, as mentioned before, by residual layers of contaminants and variations in the density of silver islands deposition, for example. It might also be connected to, for example, different hydrophobic properties of the SIFs, which can affect deposition of spin-casted PSI over the metallic nanostructure.

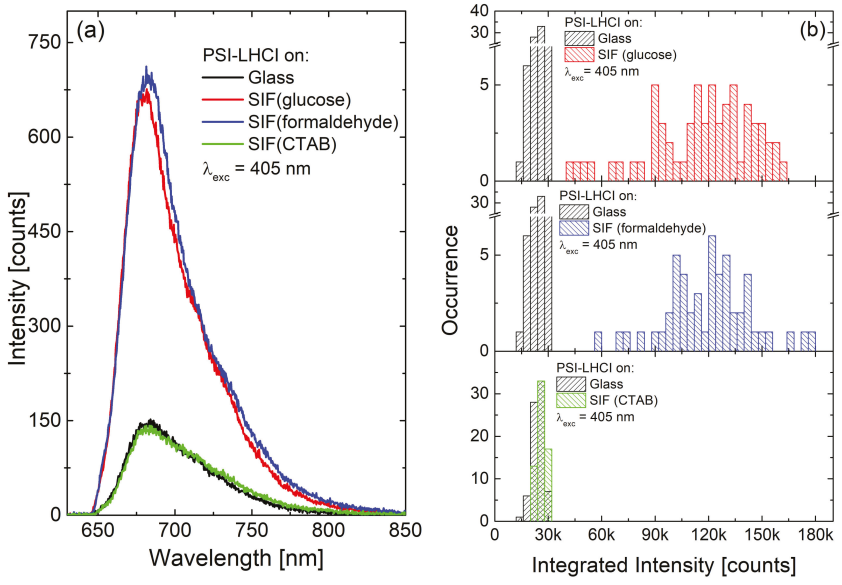

Figure 9. Emission spectra (**a**) and histograms of emission intensities (**b**) of *Cyanidioschyzon merolae* PSI-LHCI supercomplex: on glass (black), SIF (glucose) (red), SIF (formaldehyde) (blue), and SIF (CTAB) (green), the excitation wavelength is 405 nm.

3.3. Maximum Enhancement Factors

The final sequence of experiments focused on studying the interactions between photosynthetic complexes and plasmonic excitations in SIF substrates concerns PSI from *T. elongatus* (with the highest number of Chl *a* molecules) deposited on an opaque, very dense SIF (glucose) [22]. In such a structure, stronger enhancements might be expected.

A three-dimensional graph of experimentally determined EFs as a function of the excitation wavelength is displayed in Figure 10. The EFs were determined for 20-nm wide spectral bands across the emission spectrum, since a clear dependence of the emission spectrum on the excitation wavelength was observed. Similarly to the case of the RCs, the EFs strongly depend on the excitation wavelength, with measured EFs of around 200 (for excitation at 640 nm, i.e., when excited directly into Chl *a* Q_y transition). Furthermore, maximum enhancements in the order of ~400, are detected when PSI complexes were excited at 580 nm, a region characterized by very low absorption. At the same time, fluorescence decays indicate no substantial change in the fluorescence dynamics of plasmon-coupled PSI as compared to the reference. There are at least two origins of such large enhancements of the optical response of multichromophoric systems deposited on a SIF layer: First of all, the SIF substrate used for this experiment was very dense, which implies that the large majority of the PSI complexes are located in the proximity of the islands, enabling efficient coupling. Such an increase of the fraction of interacting PSI complexes should readily result in increase of the global fluorescence intensity, which is the average over the size of the laser spot at the sample surface.

Besides the geometrical structure of sample, there is also the possibility of plasmon-induced activation of (additional) intramolecular excitation energy transfer pathways for PSI complexes that are sufficient to close to the SIF layer. In other words, such large values of EFs may suggest that PSI functionality might also be influenced by plasmon coupling. In such a large multichromophoric assembly like the PSI trimer binding 300 Chls *a*, new energy transfer pathways can be activated in an amplified electromagnetic field provided by plasmons in the SIF layer. While an increase of

fluorescence intensity is not the actual aim (but rather increased electron transfer), it gives an insight into the processes associated with coupling these complex systems with plasmonic excitations in SIF. An improvement of the absorption rate, combined with the activation of absorption in normally "blind" regions, as well as the improvement of intrinsic excitation energy transfer pathways, empower the prospect of incorporating SIF into PSI-based energy converting devices.

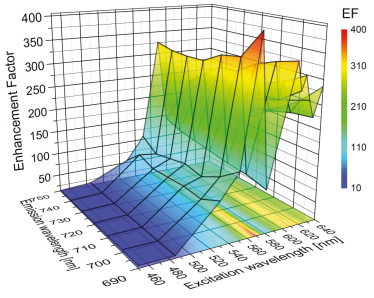

Figure 10. Three-dimensional representation of EFs of emission intensities of *Thermosynechococcus elongatus* PSI complex as a function of excitation and emission wavelengths.

4. Conclusions and Future Prospects

Table 1 summarizes EFs measured for all photosynthetic complexes considered in this study. It is conspicuous that the achieved results are characterized by a very broad distribution of EF values, which range from nearly no or weak interactions, to very large increases fluorescence intensity due to plasmonic effects.

Table 1. Summarized EFs for all considered complexes.

Complex	SIF	λ_{exc} [nm]	EF
PCP [20]	(glucose) semi-transparent	532 (632)	6 (8.5)
FMO [23]	(glucose) dense	405	40
RC [41]	(glucose) dense	405–640	up to 60
PSI-LHCI	(glucose) semi-transparent	405 (570)	5 (7)
	(formaldehyde) semi-transparent		5 (1)
	(CTAB) semi-transparent		1 (0.2)
PSI	(glucose) semi-transparent	405 (570)	5 (8)
	SIF (formaldehyde) semi-transparent		3 (12)
	(CTAB) semi-transparent		1 (0.8)
PSI [22]	(glucose) dense	450–640	up to 400

The presented results show the dominant effects observed in the interaction of photosynthetic complexes with plasmonic excitations and the main features of these hybrid systems, which make them very interesting as an inspiration for designing organic solar cells. Fluorescence of various complexes can be considerably enhanced from (relatively) simple light-harvesting complexes to large charge separation-performing photosystems. Properties of SIF substrates can be tuned depending on the requirements—selected methods allow for, e.g., control of silver islands deposition density, influencing SIF-covered electrode transparency. Moreover, as a substrate for SIFs, numerous surfaces can be used: those especially important for photovoltaic applications would be indium-tin oxide (ITO) or fluorine doped tin oxide (FTO).

Importantly, the hybrid structures composed of photosynthetic complexes and SIFs can still be improved in order to optimize the desired plasmonic effects. Besides the density of silver islands deposition, controlled oriented/unidirectional attachment of the complexes onto the SIFs would be desired. Indeed, since the distance between the interacting components is crucial for plasmon-based effects, the key parameter for enhanced functionality is the spatial arrangement of the components. Achieving a proper distance between the complexes and the silver surface by using specific linkers, can allow for the obtaining of the maximum possible enhancements (with distances of approximately 10–12 nm [24,68]). Unidirectional deposition would not be so critical for small, simple complexes binding only a few fluorophores, as in this case homogeneous interaction may be assumed. On the other hand, for large complexes comprising tens or hundreds of photoactive cofactors, their sizes are comparable to the distances of optimal plasmonic interactions. Thus, for photosynthetic complexes such as PSI, subpopulations of chromophores embedded in the protein scaffold can interact with plasmons in SIF with considerably different strength, resulting in efficient quenching, strong enhancements or no interaction at all. In this respect, the oriented attachment of photosynthetic complexes may assure the same distance, leading to uniform interaction with the metallic surface. Additionally, when all complexes are attached to SIF in a controlled way, no free-standing, non-interacting molecules would be present, thus limiting any averaging effects.

There are several promising concepts related to using different materials, which can act as transparent conducting electrodes, like graphene, TiO_2 or ITO [63,69–72], and different complexes that perform light-harvesting, charge separation and charge transfer [4,8,9,16,28,29,73]. At the same time, plasmonic nanomaterials, like SIFs or nanowires, seem to be excellent structures for improving the performance of photosynthetic materials, not only in terms of enhancing the optical properties, but also their charge transfer properties, leading to increased photocurrent generation. Indeed, despite the increased complexity of the whole biohybrid device, the latter was recently reported [74] for bacterial RCs immobilized on rough silver surfaces resulting in plasmonic-enhanced photocurrent generation.

Author Contributions: S.M. conceived and designed the experiments; M.S., K.S. and D.B. performed the experiments and analysed the data; J.K. and H.L. provided photosynthetic complexes as well as contributed in manuscript editing; J.N.-J. and M.J.-N. carried out SEM measurements; D.K. and S.M. wrote the paper. All authors have read and agreed to the published version of the manuscript.

Funding: K.S. was supported by project nr POWR.03.05.00-00-Z302/17 "Universitas Copernicana Thoruniensis In Futuro" (2018-2022) and by the National Science Centre (Poland) within the grant 2017/27/B/ST3/02457. S.M. was supported by the National Science Centre (Poland) within the grant 2016/21/B/ST3/02276. DK, MSz gratefully acknowledge support from the Polish National Centre for Research and Development (grant no. DZP/POLTUR-1/50/2016). D.B., J.N.-J. were supported by the National Science Centre (Poland) within the grant 2016/22/E/ST5/00531. H.L. was supported by the Charles University Research Centre program (UNCE/SCI/010). J.K. gratefully acknowledges the support from the Polish National Centre for Research and Development (grant no. DZP/POLTUR-1/50/2016, agreement no. 5/POLTUR-1/2016) and the Polish National Science Centre (grants no. UMO-2014/15/B/NZ1/00975 and UMO-2017/27/B/ST5/00472).

Conflicts of Interest: The authors declare no conflict of interest.

References

1. Voloshin, R.A.; Rodionova, M.V.; Zharmukhamedov, S.K.; Hou, H.J.M.; Shen, J.-R.; Allakhverdiev, S.I. Components of Natural Photosynthetic Apparatus in Solar Cells. In *Applied Photosynthesis—New Progress*; Najafpour, M.M., Ed.; InTech: London, UK, 2016; ISBN 978-953-51-2267-8.
2. Stephens, E.; Ross, I.L.; Mussgnug, J.H.; Wagner, L.D.; Borowitzka, M.A.; Posten, C.; Kruse, O.; Hankamer, B. Future prospects of microalgal biofuel production systems. *Trends Plant Sci.* **2010**, *15*, 554–564. [CrossRef]
3. Cogdell, R. Can photosynthesis provide a "biological blueprint" for the design of novel solar cells? *Trends Biotechnol.* **1998**, *16*, 521–527. [CrossRef]
4. Janna Olmos, J.D.; Kargul, J. Oxygenic photosynthesis: Translation to solar fuel technologies. *Acta Soc. Bot. Pol.* **2014**, *83*, 423–440. [CrossRef]
5. Johansson, T.B. *Renewable Energy: Sources for Fuels and Electricity*; Island Press: Washington, DC, USA, 1993; ISBN 978-1-55963-138-9.
6. Panwar, N.L.; Kaushik, S.C.; Kothari, S. Role of renewable energy sources in environmental protection: A review. *Renew. Sustain. Energy Rev.* **2011**, *15*, 1513–1524. [CrossRef]
7. Twidell, J.; Weir, T. *Renewable Energy Resources*; Routledge: London, UK, 2015; ISBN 978-1-317-66037-8.
8. Janna Olmos, J.D.; Kargul, J. A quest for the artificial leaf. *Int. J. Biochem. Cell Biol.* **2015**, *66*, 37–44. [CrossRef]
9. Mackowski, S. Hybrid nanostructures for efficient light harvesting. *J. Phys. Condens. Matter* **2010**, *22*, 193102. [CrossRef]
10. Blankenship, R.E.; Tiede, D.M.; Barber, J.; Brudvig, G.W.; Fleming, G.; Ghirardi, M.; Gunner, M.R.; Junge, W.; Kramer, D.M.; Melis, A.; et al. Comparing Photosynthetic and Photovoltaic Efficiencies and Recognizing the Potential for Improvement. *Science* **2011**, *332*, 805–809. [CrossRef]
11. Green, M.A. The path to 25% silicon solar cell efficiency: History of silicon cell evolution. *Prog. Photovolt. Res. Appl.* **2009**, *17*, 183–189. [CrossRef]
12. Green, M.A.; Emery, K.; Hishikawa, Y.; Warta, W.; Dunlop, E.D. Solar cell efficiency tables (Version 45). *Prog. Photovolt. Res. Appl.* **2015**, *23*, 1–9. [CrossRef]
13. Richards, B.S. Enhancing the performance of silicon solar cells via the application of passive luminescence conversion layers. *Sol. Energy Mater. Sol. Cells* **2006**, *90*, 2329–2337. [CrossRef]
14. Atwater, H.A.; Polman, A. Plasmonics for improved photovoltaic devices. *Nat. Mater.* **2010**, *9*, 205–213. [CrossRef] [PubMed]
15. Kargul, J.; Janna Olmos, J.D.; Krupnik, T. Structure and function of photosystem I and its application in biomimetic solar-to-fuel systems. *J. Plant Physiol.* **2012**, *169*, 1639–1653. [CrossRef] [PubMed]
16. Ocakoglu, K.; Krupnik, T.; van den Bosch, B.; Harputlu, E.; Gullo, M.P.; Olmos, J.D.J.; Yildirimcan, S.; Gupta, R.K.; Yakuphanoglu, F.; Barbieri, A.; et al. Photosystem I-based Biophotovoltaics on Nanostructured Hematite. *Adv. Funct. Mater.* **2014**, *24*, 7467–7477. [CrossRef]
17. Lakowicz, J.R. Radiative Decay Engineering: Biophysical and Biomedical Applications. *Anal. Biochem.* **2001**, *298*, 1–24. [CrossRef]
18. Sugiyama, M.; Fujii, K.; Nakamura, S. *Solar to Chemical Energy Conversion: Theory and Application*; Springer International Publishing: Basel, Switzerland, 2016; ISBN 978-3-319-25400-5.
19. Zhao, F.; Ruff, A.; Rögner, M.; Schuhmann, W.; Conzuelo, F. Extended Operational Lifetime of a Photosystem-Based Bioelectrode. *J. Am. Chem. Soc.* **2019**, *141*, 5102–5106. [CrossRef]
20. Mackowski, S.; Wörmke, S.; Maier, A.J.; Brotosudarmo, T.H.P.; Harutyunyan, H.; Hartschuh, A.; Govorov, A.O.; Scheer, H.; Bräuchle, C. Metal-Enhanced Fluorescence of Chlorophylls in Single Light-Harvesting Complexes. *Nano Lett.* **2008**, *8*, 558–564. [CrossRef]
21. Schmidt, M.; Mackowski, S. Theoretical studies of excitation dynamics in a peridinin-chlorophyll-protein coupled to a metallic nanoparticle. *Open Phys.* **2011**, *9*, 47–51. [CrossRef]
22. Czechowski, N.; Lokstein, H.; Kowalska, D.; Ashraf, K.; Cogdell, R.J.; Mackowski, S. Large plasmonic fluorescence enhancement of cyanobacterial photosystem I coupled to silver island films. *Appl. Phys. Lett.* **2014**, *105*, 043701. [CrossRef]
23. Szalkowski, M.; Ashraf, K.U.; Lokstein, H.; Mackowski, S.; Cogdell, R.J.; Kowalska, D. Silver island film substrates for ultrasensitive fluorescence detection of (bio)molecules. *Photosynth. Res.* **2016**, *127*, 103–108. [CrossRef]

24. Bharadwaj, P.; Novotny, L. Spectral dependence of single molecule fluorescence enhancement. *Opt. Express* **2007**, *15*, 14266–14274. [CrossRef]
25. Lakowicz, J.R.; Shen, Y.; D'Auria, S.; Malicka, J.; Fang, J.; Gryczynski, Z.; Gryczynski, I. Radiative Decay Engineering: 2. Effects of Silver Island Films on Fluorescence Intensity, Lifetimes, and Resonance Energy Transfer. *Anal. Biochem.* **2002**, *301*, 261–277. [CrossRef] [PubMed]
26. Ashraf, I.; Konrad, A.; Lokstein, H.; Skandary, S.; Metzger, M.; Djouda, J.M.; Maurer, T.; Adam, P.M.; Meixner, A.J.; Brecht, M. Temperature dependence of metal-enhanced fluorescence of photosystem I from Thermosynechococcus elongatus. *Nanoscale* **2017**, *9*, 4196–4204. [CrossRef] [PubMed]
27. Badura, A.; Kothe, T.; Schuhmann, W.; Rögner, M. Wiring photosynthetic enzymes to electrodes. *Energy Environ. Sci.* **2011**, *4*, 3263–3274. [CrossRef]
28. Ciesielski, P.N.; Faulkner, C.J.; Irwin, M.T.; Gregory, J.M.; Tolk, N.H.; Cliffel, D.E.; Jennings, G.K. Enhanced Photocurrent Production by Photosystem I Multilayer Assemblies. *Adv. Funct. Mater.* **2010**, *20*, 4048–4054. [CrossRef]
29. LeBlanc, G.; Gizzie, E.; Yang, S.; Cliffel, D.E.; Jennings, G.K. Photosystem I Protein Films at Electrode Surfaces for Solar Energy Conversion. *Langmuir* **2014**, *30*, 10990–11001. [CrossRef]
30. Frolov, L.; Wilner, O.; Carmeli, C.; Carmeli, I. Fabrication of Oriented Multilayers of Photosystem I Proteins on Solid Surfaces by Auto-Metallization. *Adv. Mater.* **2008**, *20*, 263–266. [CrossRef]
31. Carmeli, I.; Lieberman, I.; Kraversky, L.; Fan, Z.; Govorov, A.O.; Markovich, G.; Richter, S. Broad Band Enhancement of Light Absorption in Photosystem I by Metal Nanoparticle Antennas. *Nano Lett.* **2010**, *10*, 2069–2074. [CrossRef]
32. Polívka, T.; Hofmann, E. Structure-Function Relationship in Peridinin-Chlorophyll Proteins. In *The Structural Basis of Biological Energy Generation*; Hohmann-Marriott, M.F., Ed.; Springer: Dordrecht, The Netherlands, 2014; Volume 39, pp. 39–58. ISBN 978-94-017-8741-3.
33. Carbonera, D.; Valentin, M.; Spezia, R.; Mezzetti, A. The Unique Photophysical Properties of the Peridinin-Chlorophyll-a-Protein. *Curr. Protein Pept. Sci.* **2014**, *15*, 332–350. [CrossRef]
34. Schulte, T.; Johanning, S.; Hofmann, E. Structure and function of native and refolded peridinin-chlorophyll-proteins from dinoflagellates. *Eur. J. Cell Biol.* **2010**, *89*, 990–997. [CrossRef]
35. Takaichi, S.; Nippon, M.S.; Ohoka, H. Pigment composition in the reaction center complex from the thermophilic green sulfur bacterium, *Chlorobium tepidum*: Carotenoid glucoside esters, menaquinone [Vitamine K] and chlorophylls. *Plant Cell Physiol. Jpn.* **1999**, *40*, 691–694. [CrossRef]
36. Tsukatani, Y.; Miyamoto, R.; Itoh, S.; Oh-Oka, H. Function of a PscD subunit in a homodimeric reaction center complex of the photosynthetic green sulfur bacterium *Chlorobium tepidum* studied by insertional gene inactivation. Regulation of energy transfer and ferredoxin-mediated NADP+ reduction on the cytoplasmic side. *J. Biol. Chem.* **2004**, *279*, 51122–51130. [PubMed]
37. Frigaard, N.-U.; Chew, A.G.M.; Li, H.; Maresca, J.A.; Bryant, D.A. *Chlorobium tepidum*: Insights into the structure, physiology, and metabolism of a green sulfur bacterium derived from the complete genome sequence. *Photosynth. Res.* **2003**, *78*, 93–117. [CrossRef] [PubMed]
38. Azai, C.; Kim, K.; Kondo, T.; Harada, J.; Itoh, S.; Oh-oka, H. A heterogeneous tag-attachment to the homodimeric type 1 photosynthetic reaction center core protein in the green sulfur bacterium *Chlorobaculum tepidum*. *Biochim. Biophys. Acta* **2011**, *1807*, 803–812. [CrossRef] [PubMed]
39. He, G.; Niedzwiedzki, D.M.; Orf, G.S.; Zhang, H.; Blankenship, R.E. Dynamics of Energy and Electron Transfer in the FMO-Reaction Center Core Complex from the Phototrophic Green Sulfur Bacterium *Chlorobaculum tepidum*. *J. Phys. Chem. B* **2015**, *119*, 8321–8329. [CrossRef]
40. Rémigy, H.W.; Stahlberg, H.; Fotiadis, D.; Müller, S.A.; Wolpensinger, B.; Engel, A.; Hauska, G.; Tsiotis, G. The reaction center complex from the green sulfur bacterium *Chlorobium tepidum*: A structural analysis by scanning transmission electron microscopy. *J. Mol. Biol.* **1999**, *290*, 851–858. [CrossRef]
41. Maćkowski, S.; Czechowski, N.; Ashraf, K.U.; Szalkowski, M.; Lokstein, H.; Cogdell, R.J.; Kowalska, D. Origin of bimodal fluorescence enhancement factors of *Chlorobaculum tepidum* reaction centers on silver island films. *FEBS Lett.* **2016**, *590*, 2558–2565. [CrossRef]
42. Olson, J.M. The FMO protein. In *Discoveries in Photosynthesis*; Govindjee, B.J.T., Gest, H., Allen, J.F., Eds.; Advances in Photosynthesis and Respiration; Springer: Dordrecht, The Netherlands, 2005; pp. 421–427. ISBN 978-1-4020-3323-0.

43. Olson, J.M. Chlorophyll Organization and Function in Green Photosynthetic Bacteria*. *Photochem. Photobiol.* **1998**, *67*, 61–75. [CrossRef]
44. Blankenship, R.E.; Olson, J.M.; Miller, M. Antenna Complexes from Green Photosynthetic Bacteria. In *Anoxygenic Photosynthetic Bacteria*; Blankenship, R.E., Madigan, M.T., Bauer, C.E., Eds.; Advances in Photosynthesis and Respiration; Springer: Dordrecht, The Netherlands, 1995; pp. 399–435. ISBN 978-0-7923-3681-5.
45. Matthews, B.W.; Fenna, R.E. Structure of a green bacteriochlorophyll protein. *Acc. Chem. Res.* **1980**, *13*, 309–317. [CrossRef]
46. Blankenship, R.E. *Molecular Mechanisms of Photosynthesis*; Wiley-Blackwell: Hoboken, NJ, USA, 2014; ISBN 978-1-4051-8976-7.
47. Haniewicz, P.; Abram, M.; Nosek, L.; Kirkpatrick, J.; El-Mohsnawy, E.; Olmos, J.D.J.; Kouřil, R.; Kargul, J.M. Molecular Mechanisms of Photoadaptation of Photosystem I Supercomplex from an Evolutionary Cyanobacterial/Algal Intermediate. *Plant Physiol.* **2018**, *176*, 1433–1451. [CrossRef]
48. Antoshvili, M.; Caspy, I.; Hippler, M.; Nelson, N. Structure and function of photosystem I in Cyanidioschyzon merolae. *Photosynth. Res.* **2018**, *139*, 499–508. [CrossRef]
49. Pi, X.; Tian, L.; Dai, H.-E.; Qin, X.; Cheng, L.; Kuang, T.; Sui, S.-F.; Shen, J.-R. Unique organization of photosystem I-light-harvesting supercomplex revealed by cryo-EM from a red alga. *Proc. Natl. Acad. Sci. USA* **2018**, *115*, 4423–4428. [CrossRef] [PubMed]
50. Jordan, P.; Fromme, P.; Witt, H.T.; Klukas, O.; Saenger, W.; Krauss, N. Three-dimensional structure of cyanobacterial photosystem I at 2.5 A resolution. *Nature* **2001**, *411*, 909–917. [CrossRef] [PubMed]
51. Fromme, P.; Melkozernov, A.; Jordan, P.; Krauss, N. Structure and function of photosystem I: Interaction with its soluble electron carriers and external antenna systems. *FEBS Lett.* **2003**, *555*, 40–44. [CrossRef]
52. Grotjohann, I.; Fromme, P. Structure of cyanobacterial photosystem I. *Photosynth. Res.* **2005**, *85*, 51–72. [CrossRef]
53. Aslan, K.; Leonenko, Z.; Lakowicz, J.R.; Geddes, C.D. Annealed Silver-Island Films for Applications in Metal-Enhanced Fluorescence: Interpretation in Terms of Radiating Plasmons. *J. Fluoresc.* **2005**, *15*, 643–654. [CrossRef]
54. Chang, G.; Zhang, J.; Oyama, M.; Hirao, K. Silver-Nanoparticle-Attached Indium Tin Oxide Surfaces Fabricated by a Seed-Mediated Growth Approach. *J. Phys. Chem. B* **2005**, *109*, 1204–1209. [CrossRef]
55. Jana, N.R.; Gearheart, L.; Murphy, C.J. Wet chemical synthesis of silver nanorods and nanowiresof controllable aspect ratio. *Chem. Commun.* **2001**, 617–618. [CrossRef]
56. Lakowicz, J.R. Radiative decay engineering 5: Metal-enhanced fluorescence and plasmon emission. *Anal. Biochem.* **2005**, *337*, 171–194. [CrossRef]
57. Chowdhury, M.H.; Ray, K.; Aslan, K.; Lakowicz, J.R.; Geddes, C.D. Metal-Enhanced Fluorescence of Phycobiliproteins from Heterogeneous Plasmonic Nanostructures. *J. Phys. Chem. C Nanomater. Interfaces* **2007**, *111*, 18856–18863. [CrossRef]
58. Mackowski, S.; Wörmke, S.; Brotosudarmo, T.H.P.; Jung, C.; Hiller, R.G.; Scheer, H.; Bräuchle, C. Energy Transfer in Reconstituted Peridinin-Chlorophyll-Protein Complexes: Ensemble and Single-Molecule Spectroscopy Studies. *Biophys. J.* **2007**, *93*, 3249–3258. [CrossRef]
59. Ray, K.; Badugu, R.; Lakowicz, J.R. Metal-Enhanced Fluorescence from CdTe Nanocrystals: A Single-Molecule Fluorescence Study. *J. Am. Chem. Soc.* **2006**, *128*, 8998–8999. [CrossRef] [PubMed]
60. Qin, X.; Suga, M.; Kuang, T.; Shen, J.-R. Photosynthesis. Structural basis for energy transfer pathways in the plant PSI-LHCI supercomplex. *Science* **2015**, *348*, 989–995. [CrossRef] [PubMed]
61. Brecht, M.; Hussels, M.; Nieder, J.B.; Fang, H.; Elsässer, C. Plasmonic interactions of photosystem I with Fischer patterns made of Gold and Silver. *Chem. Phys.* **2012**, *406*, 15–20. [CrossRef]
62. Nabiev, I.; Rakovich, A.; Sukhanova, A.; Lukashev, E.; Zagidullin, V.; Pachenko, V.; Rakovich, Y.P.; Donegan, J.F.; Rubin, A.B.; Govorov, A.O. Fluorescent Quantum Dots as Artificial Antennas for Enhanced Light Harvesting and Energy Transfer to Photosynthetic Reaction Centers. *Angew. Chem. Int. Ed.* **2010**, *49*, 7217–7221. [CrossRef] [PubMed]
63. Feifel, S.C.; Stieger, K.R.; Lokstein, H.; Lux, H.; Lisdat, F. High photocurrent generation by photosystem I on artificial interfaces composed of π-system-modified graphene. *J. Mater. Chem. A* **2015**, *3*, 12188–12196. [CrossRef]

64. Stieger, K.R.; Feifel, S.C.; Lokstein, H.; Lisdat, F. Advanced unidirectional photocurrent generation via cytochrome c as reaction partner for directed assembly of photosystem I. *Phys. Chem. Chem. Phys.* **2014**, *16*, 15667. [CrossRef]
65. Carmeli, I.; Mangold, M.; Frolov, L.; Zebli, B.; Carmeli, C.; Richter, S.; Holleitner, A.W. A Photosynthetic Reaction Center Covalently Bound to Carbon Nanotubes. *Adv. Mater.* **2007**, *19*, 3901–3905. [CrossRef]
66. Hatazaki, S.; Sharma, D.K.; Hirata, S.; Nose, K.; Iyoda, T.; Kölsch, A.; Lokstein, H.; Vacha, M. Identification of Short- and Long-Wavelength Emitting Chlorophylls in Cyanobacterial Photosystem I by Plasmon-Enhanced Single-Particle Spectroscopy at Room Temperature. *J. Phys. Chem. Lett.* **2018**, *9*, 6669–6675. [CrossRef]
67. Anger, P.; Bharadwaj, P.; Novotny, L. Enhancement and Quenching of Single-Molecule Fluorescence. *Phys. Rev. Lett.* **2006**, *96*, 113002. [CrossRef]
68. Szalkowski, M.; Olmos, J.D.J.; Buczyńska, D.; Maćkowski, S.; Kowalska, D.; Kargul, J. Plasmon-induced absorption of blind chlorophylls in photosynthetic proteins assembled on silver nanowires. *Nanoscale* **2017**, *9*, 10475–10486. [CrossRef]
69. LeBlanc, G.; Winter, K.M.; Crosby, W.B.; Jennings, G.K.; Cliffel, D.E. Integration of Photosystem I with Graphene Oxide for Photocurrent Enhancement. *Adv. Energy Mater.* **2014**, *4*, 1301953. [CrossRef]
70. Mershin, A.; Matsumoto, K.; Kaiser, L.; Yu, D.; Vaughn, M.; Nazeeruddin, M.K.; Bruce, B.D.; Graetzel, M.; Zhang, S. Self-assembled photosystem-I biophotovoltaics on nanostructured TiO_2 and ZnO. *Sci. Rep.* **2012**, *2*, 234. [CrossRef] [PubMed]
71. Ciornii, D.; Riedel, M.; Stieger, K.R.; Feifel, S.C.; Hejazi, M.; Lokstein, H.; Zouni, A.; Lisdat, F. Bioelectronic Circuit on a 3D Electrode Architecture: Enzymatic Catalysis Interconnected with Photosystem I. *J. Am. Chem. Soc.* **2017**, *139*, 16478–16481. [CrossRef] [PubMed]
72. Stieger, K.R.; Feifel, S.C.; Lokstein, H.; Hejazi, M.; Zouni, A.; Lisdat, F. Biohybrid architectures for efficient light-to-current conversion based on photosystem I within scalable 3D mesoporous electrodes. *J. Mater. Chem. A* **2016**, *4*, 17009–17017. [CrossRef]
73. Kondo, M.; Iida, K.; Dewa, T.; Tanaka, H.; Ogawa, T.; Nagashima, S.; Nagashima, K.V.P.; Shimada, K.; Hashimoto, H.; Gardiner, A.T.; et al. Photocurrent and electronic activities of oriented-His-tagged photosynthetic light-harvesting/reaction center core complexes assembled onto a gold electrode. *Biomacromolecules* **2012**, *13*, 432–438. [CrossRef]
74. Friebe, V.M.; Delgado, J.D.; Swainsbury, D.J.K.; Gruber, J.M.; Chanaewa, A.; van Grondelle, R.; von Hauff, E.; Millo, D.; Jones, M.R.; Frese, R.N. Plasmon-Enhanced Photocurrent of Photosynthetic Pigment Proteins on Nanoporous Silver. *Adv. Funct. Mater.* **2016**, *26*, 285–292. [CrossRef]

MDPI
St. Alban-Anlage 66
4052 Basel
Switzerland
Tel. +41 61 683 77 34
Fax +41 61 302 89 18
www.mdpi.com

International Journal of Molecular Sciences Editorial Office
E-mail: ijms@mdpi.com
www.mdpi.com/journal/ijms

MDPI
St. Alban-Anlage 66
4052 Basel
Switzerland

Tel: +41 61 683 77 34
Fax: +41 61 302 89 18

www.mdpi.com

ISBN 978-3-03943-205-9